

THÈSE

Pour obtenir le grade de

DOCTEUR DE L'UNIVERSITÉ DE GRENOBLE

Spécialité : **Physique de la matière condensée et du rayonnement**

Arrêté ministériel : 7 août 2006

Présentée par

Martina Flöser

Thèse dirigée par **Régis Mélin**
et codirigée par **Serge Florens**

préparée au sein de l'**Institut Néel**
et de l'**Ecole Doctorale de Physique de Grenoble**

From Local to Non-Local Transport : Percolation in Quantum Hall Systems Cross-Correlations in Superconducting Hybrid Structures

Thèse soutenue publiquement le **1er Octobre 2012**,
devant le jury composé de :

M. Thierry Champel

Chargé de recherche, Laboratoire de Physique et Modélisation des Milieux Condensés, Co-Encadrant

M. Pascal Degiovanni

Directeur de recherche, Ecole Normale Supérieure de Lyon, Rapporteur

M. Benoît Douçot

Directeur de recherche, Laboratoire de Physique Théorique et Hautes Energies, Rapporteur

M. Ferdinand Evers

Professeur des universités, Karlsruher Institut für Technologie, Examineur

M. Serge Florens

Chargé de recherche, Institut Néel, Co-Directeur de thèse

M. Ulf Gennser

Directeur de recherche, Laboratoire de photonique et de nanostructures, Examineur

M. Régis Mélin

Directeur de recherche, Institut Néel, Directeur de thèse

Mme Julia Meyer

Professeur des universités, Université Joseph Fourier, Grenoble, Présidente



Acknowledgements

I would like to thank ...

- ... my three supervisors who guided my research during the last three years:
 - Régis Mélin my “Directeur de thèse” with whom I worked on the part about superconducting hybrid structures. During my master’s thesis, he aroused my enthusiasm for solid state physics and motivated me to start with this thesis.
 - Serge Florens my “Co-Directeur de thèse” with whom I worked on transport in the quantum Hall regime.
 - Thierry Champel who became over the collaboration with Serge Florens my second “Co-Directeur de thèse”.
- The chance to work closely together with three persons allowed me to learn about physics and how to do good research from different points of view. Thank you for all you taught me and for the all the time you spent discussing with me.
- ... the members of my thesis committee Ferdinand Evers, Ulf Gennser, Julia Meyer and especially the readers Pascal Degiovanni and Benoît Douçot for having accepted this task.
- ... Benjamin Piot for the collaboration which led to chapter three of this thesis and for answering my questions concerning the experiments on the quantum Hall effect.
- ... Denis Feinberg for a lot of discussions about superconducting hybrid structures.
- ... Vincent Renard for sending us his data.
- ... the administrative staff of the Néel institute.
- ... François Lefloch for helpful discussions and explanations concerning experiments on superconducting hybrid structures.
- ... Axel Freyn from who I learned a lot about writing and testing computer programs and making the computer do what I want no matter if using Mathematica, Pyx, Latex or any other program. Thank you for also being a friend and for cheering me up if my thesis work threatened to frustrate me.
- ... all the other students and postdocs from the “Theorie et Nano” group, Mathias Cabrera Cano, Soumya Bera, Jascha Ulrich, Gaston Hornecker and Matthieu Vert. Without you, lunch breaks would have been much less fun.
- ... Claire Hilaire, Marie-Luise Menzel and my other flatmates, my friends Maelle Morgant and Delphine Pierron and the members of the “Orchestre de Nôtre Dame” who made me feel at home in Grenoble.
- ... my parents, my brother and my sister for their love and support.

Contents

From Local to Non-Local Quantum Transport	9
Résumé substantiel en français	13
I. Transport in the Regime of the Quantum Hall Effect	21
1. The Integer Quantum Hall Effect	23
1.1. History and Phenomenology	23
1.2. Realisation of Two Dimensional Electron Gases	24
1.3. Landau Levels	26
1.4. Localization	28
1.5. Where Do the Hall Steps Come From ?	32
1.6. Further Complications to Consider	34
1.7. Perturbation Expansion in the Disorder Potential	35
1.8. The Gradient Expansion of the Disorder Potential	39
1.9. The "Classical" Percolation Model	40
1.10. The Chalker-Coddington Model	40
1.11. The Two Phase Model	41
1.12. Summary	43
2. Diagrammatic Approach for the Classical Percolation Regime of Quantum Hall Transitions	45
2.1. Percolation Arguments for the Critical Exponent	46
2.2. The Effective Medium Approach	50
2.3. Systematic Expansion at Strong Dissipation	53
2.4. Form of the Potential Correlations	55
2.5. Application to the Quantum Hall Effect	58
2.6. Creation of the Diagrams	60
2.7. Evaluation of the Diagrams	61
2.8. Extrapolation to the Regime of Small Dissipation	65
2.9. Summary	69

3. Classical Percolating Transport: Theory and Experiment	71
3.1. Estimation of the Local Ohmic Conductivity from Phonon Scattering	71
3.2. Reexpressing the Effective Longitudinal Conductivity with the Poisson Summation Formula	75
3.3. High Temperature Magnetic Field Dependence	77
3.4. Temperature Dependence of the Peak Conductivity	78
3.5. Experimental Data	79
3.5.1. Longitudinal Magneto-Conductance	80
3.5.2. Temperature Dependence of the Peak Conductivity	82
3.6. Outlook towards Lower Temperatures	86
3.7. Summary	89
4. Transmission Coefficient through a Saddle Point	91
4.1. The Exact Solution to the Saddle Point Tunneling Problem	92
4.2. The Vortex Green's Function Formalism	94
4.3. Tunneling over Saddle Points in an Ordinary Two Dimensional Electron Gas	99
4.4. Vortex Green's Functions for Graphene	104
4.5. Transmission Coefficients for Graphene	107
4.6. Summary	110
 II. Conductance and Differential Current Cross-Correlations in Three-Terminal Normal Conductor-Superconductor-Normal Conductor Hybrid Structures	 113
5. Introduction to Normal Conductor-Superconductor Hybrid Structures	115
5.1. Charge Transfer Processes at Interfaces between Normal Conductors and Superconductors	115
5.2. Einstein-Podolsky-Rosen Experiments with Electrons	117
5.3. Conductance in Three-Terminal Normal Metal-Superconductor-Normal Metal Devices	120
5.4. Noise and Current Cross-Correlations	125
5.5. Summary	128
6. Three-Terminal Normal Metal-Superconductor-Normal Metal Hybrid Structures	129
6.1. The Model	129
6.2. Calculation of the Scattering Matrix with the approach of Blonder, Tinkham and Klapwijk	131
6.3. Components of Conductance and Current Cross-Correlations	135
6.4. Positive Cross-Correlations without CAR	137

6.5. Reflectionless Tunneling	140
6.6. Multiple Barriers	142
6.7. Summary	146
7. The Ballistic System	149
7.1. Resonances in a Fabry-Perot Interferometer	149
7.2. The Tunnel Regime	153
7.3. Increasing the Interface Transparency	159
7.4. Could these Effects Be Observed Experimentally?	167
7.5. Summary	168
Conclusion and Outlook	169
List of Publications	173
A. Self-Consistent Diagrammatic Approach to the Effective Longitudinal Conductivity	175
B. Components of Current Cross-Correlations	181

From Local to Non-Local Quantum Transport

In physics, transport is the generic term for the motion of charge, mass or energy in response to a non-equilibrium situation. In my thesis, I study two very different systems with remarkable transport properties: Two dimensional electron gases under a strong perpendicular magnetic field showing the quantum Hall effect and superconducting hybrid structures. Common to both systems is the important role of quantum effects leading to regimes of dissipationless transport.

In quantum Hall systems, quantum mechanics manifests itself clearly in the conductance quantization. The transverse Hall conductance does not increase linearly with the magnetic field, as would be expected classically, but in steps of integer multiples of e^2/h . The longitudinal conductance features peaks at the magnetic field values of the plateau transitions in the Hall conductance and drops by several orders of magnitude everywhere else. The study of noise and current cross-correlations in normal metal-superconductor hybrid structures reveals other aspects of quantum mechanics: the quantization of charge, interference effects and the statistics of the charge carriers. The noise at tunnel barriers is proportional to the charge per carrier and it doubles if a superconductor, where charge is transported in Cooper pairs, is involved. At the interfaces between the different electrodes, the stream of incoming charge carriers is divided into a transmitted and a reflected stream. The interference of streams having taken different ways leads to noise and current cross-correlations. They are especially rich in superconducting hybrid structures which couple electron and hole channels. In non-interacting purely fermionic systems, current cross-correlations are always negative. However, they can become positive in the presence of a superconductor.

The quantum Hall effect has a well established application in metrology, where it is used to maintain the resistance standard. The high precision needed in metrology is one motivation for further theoretical research, as one needs to know all factors which limit the quantization of the Hall plateaus. The edge states of quantum Hall samples are ballistic conducting channels that provide a possibility to perform with electrons interference experiments well known from optics. The idea of an electronic equivalent to a quantum optics experiment is also a motivation for studying three-terminal superconducting hybrid structures: One hopes to use them as a source of entangled electrons for Einstein-Podolski-Rosen experiments.

While in a classical framework position is a well defined quantity, in quantum

mechanical systems wave functions are spread and non-local effects are possible. The local or non-local nature of transport phenomena depends on the relation between the coherence length and other relevant length scales of the system. We study local transport in quantum Hall systems at high temperature. There, electron-phonon scattering destroys phase coherence on a length scale much shorter than the length scale on which the disorder potential varies and the transport problem becomes purely classical. Nevertheless, transport stays far from trivial. The current profile is highly inhomogeneous and leads in the presence of extremely weak dissipation to a percolation problem. One aim of this work is to develop theoretical tools to address this difficult transport problem and to make predictions that can be confronted to experiments.

At lower temperatures transport becomes non-local as tunnel effects start to play a role. Here, wave functions pass as evanescent waves through classically insurmountable potential barriers leading to a finite probability that the particle propagates at the opposite side of the barrier. As a first step towards non-local transport, we consider tunneling of located wave packets in the quantum Hall regime.

Another beautiful manifestation of non-local transport can be found in three-terminal normal metal-superconductor-normal metal hybrid structures where the length of the superconductor separating the two normal metal electrodes is shorter or of the order of the coherence length of the superconductor. A voltage applied between one normal electrode and the superconductor leads to a current in the second normal electrode. Besides conductance, current cross-correlations are often studied, amongst others because positive cross-correlations are an indication of entanglement. In this context, we want to know if reflectionless tunneling, an effect that leads to an enhancement of the conductance over an normal metal-superconductor interface in the presence of disorder, can enhance positive current cross-correlations. The conductance and the current cross-correlations are always a sum of several microscopic processes leading us to the question if electronic Fabry-Perot interferometers can be used to filter these different processes.

Outline

My thesis consists of two parts “Transport in the Regime of the Quantum Hall Effect” and “Conductance and Differential Current Cross-Correlations in Three-Terminal Normal Conductor-Superconductor-Normal Conductor Hybrid Structures” the former containing four the later three chapters.

The **first chapter** is a general introduction to the quantum Hall effect. First, the basic concepts of Landau levels and localization by disorder are introduced leading to an intuitive explanation of the quantum Hall effect. Afterwards, some more sophisticated theories that can throw light on specific aspects of the quantum Hall effect are presented.

In the **second chapter**, we study the high temperature regime of the quantum Hall effect. We develop a diagrammatic technique based on an effective medium approach to calculate the conductance as a function of the local conductivity tensor. In this regime transport is dominated by classical percolation.

In the **third chapter**, we derive expressions for the conductance in function of experimentally controllable quantities and compare our theoretical predictions to recent experiments.

In the **fourth chapter**, we study quantum tunneling over saddle points from the scattering of semi-coherent state wave packets. This method allows us in particular to address analytically saddle points in the scalar potential in graphene.

The second part starts with the **fifth chapter**, which is an introduction to three-terminal normal conductor-superconductor-normal conductor (NSN) hybrid structures. After explaining the charge transfer processes that can occur on the interfaces between normal conductors and superconductors, I give an introduction to Einstein-Podolski-Rosen experiments which have inspired research on three-terminal NSN-structure motivated by proposals to use them as a source of entangled electrons. It is followed by an overview of experiments probing non-local conductance and a discussion about what we can learn from current cross-correlations.

In the **sixth chapter**, metallic systems are studied in a one-dimensional model where multi-dimensional behavior is simulated qualitatively by mode averaging. We address the question whether an effect similar to reflectionless tunneling could enhance positive cross-correlations in three-terminal normal conductor-superconductor-normal conductor hybrid structure with additional barriers in the normal conducting electrodes.

In the **seventh chapter**, we turn towards a ballistic model. Here, additional barriers lead to Fabry-Perot oscillations, which can at small but finite bias serve to separate the different contributions of the conductance and of the differential current cross-correlations.

The thesis ends with a summary and propositions for further work regarding both topics addressed.

Résumé substantiel en français

Transport quantique local et non-local

Dans le contexte de la physique, le transport est le terme générique désignant le mouvement de charge, de masse ou d'énergie en réaction à une situation hors équilibre. Dans ma thèse, j'étudie deux systèmes très différents avec des propriétés de transport remarquables : les gaz d'électrons bidimensionnels sous fort champ magnétique perpendiculaire montrant l'effet Hall quantique et les structures hybrides supraconductrices. Ces deux systèmes ont en commun le rôle important de la mécanique quantique amenant à des régimes de transport sans dissipation.

Dans les systèmes à effet Hall quantique, la mécanique quantique se manifeste clairement par la quantification de la conductance de Hall. En effet, la conductance transverse ne croît pas linéairement avec le champ magnétique, comme attendu classiquement, mais en marches multiples entières de e^2/h . La conductance longitudinale affiche des maxima aux champs magnétiques correspondants aux transitions entre plateaux dans la conductance de Hall et chute de plusieurs ordres de grandeur partout ailleurs. L'étude du bruit et des corrélations croisées en courant dans des structures hybrides métal normal-supraconducteur montrent d'autres aspects de la mécanique quantique : la quantification de la charge, les effets d'interférence et la statistique des porteurs de charge. Le bruit sur une barrière tunnel est proportionnel à la charge par porteur et se double en présence d'un supraconducteur où la charge est transportée par les paires de Cooper. Aux interfaces entre les différentes électrodes, le flot des porteurs de charge incidents est divisé dans un flot transmis et dans un flot réfléchi. Le bruit et les corrélations croisées en courant sont le résultat de l'interférence entre des flots ayant pris des chemins différents. Ces corrélations sont particulièrement riches dans les structures hybrides supraconductrices qui couplent les canaux d'électrons et les canaux de trous.

L'effet Hall quantique a une application bien établie en métrologie où il est utilisé pour maintenir le standard de résistance. La précision élevée nécessaire pour des applications métrologiques est une motivation pour la poursuite de la recherche théorique, parce qu'il est nécessaire de connaître tous les facteurs limitant la quantification des plateaux de Hall. Les états de bord des échantillons de Hall sont des canaux balistiques avec lesquels une version électronique des expériences d'interférence bien connues de l'optique peut être réalisée. L'idée d'un équivalent électronique des expériences de l'optique quantique est aussi une motivation pour

étudier les structures hybrides supraconductrices à trois terminaux : on espère les utiliser comme source d'électrons intriqués dans des expériences de type Einstein-Podolski-Rosen.

Tandis que dans un cadre classique la position est une quantité bien définie, en mécanique quantique les fonctions d'onde donnent seulement une distribution de probabilité pour la position, et des effets non-locaux sont possibles. La nature locale ou non-locale d'un phénomène de transport dépend de la relation entre la longueur de cohérence et les autres échelles pertinentes du système. Nous étudions le transport local dans un système de Hall quantique à des températures élevées. Dans cette situation, la diffusion électron-phonon détruit la cohérence de phase sur des échelles beaucoup plus courtes que l'échelle sur laquelle le potentiel de désordre varie et le problème de transport devient purement classique. Néanmoins, le transport reste hautement non-trivial. Le profil de courant est fortement inhomogène et entraîne en présence d'une dissipation extrêmement faible un problème de percolation. Un but de ce travail est de développer des outils théoriques pour adresser ce problème de transport difficile et de faire des prédictions qui peuvent être confrontées aux résultats expérimentaux.

Pour des températures plus basses, le transport devient non-local, parce que l'effet tunnel entre en jeu : des fonctions d'onde évanescentes passent des barrières classiquement infranchissables et donnent lieu à une probabilité finie pour une particule de se propager du côté opposé. Comme première étape vers le transport non-local, nous étudions le passage par effet tunnel d'un paquet d'onde localisé à travers une barrière unique dans le régime de l'effet Hall quantique.

Une autre manifestation impressionnante du transport non-local peut être trouvée dans des structures conducteur normal-supraconducteur-conducteur normal à trois terminaux où la longueur du supraconducteur séparant les deux électrodes normales est plus courte que (ou de l'ordre de) la longueur de cohérence du supraconducteur. Une tension appliquée entre la première électrode normale et le supraconducteur entraîne un courant dans la deuxième électrode. En plus de la conductance, les corrélations croisées en courant sont souvent étudiées, entre autre parce qu'un signe positif des corrélations croisées est un indice pour l'intrication. Dans ce contexte, nous souhaitons savoir si la réflexion d'Andreev résonante (reflectionless tunneling), un processus qui augmente la conductance sur une interface métal normal-supraconducteur en présence de désordre, peut amplifier des corrélations croisées positives. La conductance et les corrélations croisées en courant sont toujours une somme de plusieurs effets microscopiques, ce qui nous amène à la question de savoir si des interféromètres de Fabry-Pérot électroniques peuvent être utilisés pour filtrer ces différents processus.

Résumé par chapitre

Introduction à l'effet Hall quantique

Le premier chapitre donne une introduction générale à l'effet Hall quantique. Après la description de la phénoménologie, quelques remarques historiques et une digression sur la réalisation physique des gaz des électrons bidimensionnels, l'effet Hall quantique est expliqué de manière intuitive : pour l'effet Hall quantique deux ingrédients sont essentiels : le champ magnétique intense qui fait naître la structure particulière du spectre en niveaux de Landau et le potentiel de désordre qui localise la plupart des électrons. La localisation peut déjà être comprise à partir de la solution de l'équation de mouvement newtonienne classique. Sous champ magnétique perpendiculaire et en présence d'un potentiel, le mouvement des électrons peut être décomposé dans le mouvement cyclotron autour d'un centre de guidage et le mouvement de dérive de ce centre de guidage. Il s'avère que le centre de guidage suit les lignes équipotentiels du potentiel de désordre. Ainsi, un électron se trouvant sur une ligne équipotentielle entourant un sommet ou une dépression est localisé. Seulement les électrons sur les lignes équipotentiels percolant à travers le système sont délocalisés. Les électrons localisés ne contribuent pas au transport macroscopique et sont à l'origine des plateaux de Hall et des régions de faible conductance longitudinale. Tandis que les électrons délocalisés sont la raison pour la transition entre les plateaux et les pics dans la conductance longitudinale.

Ensuite, je présente quelques théories plus élaborées et leur limitations. Cette partie montre que l'explication de l'effet Hall quantique est loin d'être triviale et que beaucoup de pièces du puzzle sont encore à trouver.

Dans les chapitres suivants, je présente mes deux pièces du puzzle : Une théorie du transport pour le régime de haute température de l'effet Hall quantique et la détermination analytique du coefficient de transmission d'un point selle pour le potentiel scalaire dans le graphène à partir de paquets d'ondes.

Approche diagrammatique pour le régime de percolation classique des transitions de Hall quantique

Dans le deuxième chapitre, nous étudions le régime de haute température de l'effet Hall quantique, où l'énergie thermique est plus élevée que les fluctuations typiques du potentiel de désordre. À ces températures, la diffusion électron-phonon détruit la cohérence de phase des électrons sur une échelle plus courte que la longueur de corrélation du potentiel de désordre et la loi d'Ohm peut être utilisée dans sa version locale. Les variations aléatoires du potentiel de désordre créent des fluctuations fortes dans les composantes de Hall de la conductivité locale. La densité de courant suit les lignes équipotentiels, ce qui crée un problème de percolation. Expérimentalement, la densité de courant et le champ électrique local sont difficiles à mesurer et l'expérience de transport typique donne seulement accès aux quantités spatialement moyennées. Pour cette raison, nous souhaitons calculer la conductivité effective σ_e , une quantité

qui est à un facteur géométrique près identique à la conductance, à partir de la conductivité locale. L'approche de milieu effectif dans la version développée par Stroud [1] permet de calculer la conductivité effective sous forme d'un développement en puissances des fluctuations de la conductivité. Si la conductivité longitudinale locale σ_0 est grande par rapport aux fluctuations de la conductivité de Hall, la conductivité effective peut facilement être trouvée en arrêtant le développement perturbatif dès que la précision souhaitée est atteinte. Cependant, les échantillons de Hall se trouvent dans la limite opposée de fortes fluctuations où l'application de la théorie de perturbation est impossible. En se basant sur des arguments de la théorie de la percolation, Simon and Halperin [2] et Isichenko et al. [3] conjecturent que la conductivité effective longitudinale σ_L^e s'annule comme $\sigma_L^e \propto \sigma_0^{1-\kappa}$ dans la limite $\sigma_0 \rightarrow 0$, avec l'exposant critique $\kappa = 10/13$. Nous accédons à ce régime de fortes fluctuations en trois étapes. D'abord, nous développons un formalisme diagrammatique qui nous permet de générer systématiquement les termes de la série. Ensuite, nous calculons avec une combinaison d'étapes analytiques et numériques les diagrammes de la série jusqu'à l'ordre six dans le nombre des boucles. Finalement, en supposant que la conductivité effective s'annule avec une loi d'échelle dans la limite de faible dissipation et de fortes fluctuations, nous extrapolons la conductivité effective du régime de faibles fluctuations jusqu'au régime de fortes fluctuations avec un approximant de Padé. L'extrapolation donne pour l'exposant critique $\kappa \approx 0,767 \pm 0,002$.

En conclusion, avec cette combinaison de calculs diagrammatiques et d'extrapolation, nous sommes capables de décrire le passage entier du régime dissipatif jusqu'au régime de percolation. De plus nous confirmons par une méthode purement microscopique l'exposant critique κ qui était auparavant seulement conjecturé par des arguments heuristiques.

Transport percolatif classique : Théorie et expérience

Dans le troisième chapitre, nous dérivons les dépendances de la conductivité effective longitudinale avec la température et le champ magnétique. Utilisant l'estimation du temps de diffusion entre électrons et phonons par Zhao and Feng [4], nous déduisons que la conductivité ohmique locale σ_0 est indépendante du champ magnétique et croît linéairement avec la température. Pour des températures élevées ($k_B T \gg \hbar \omega_c$) et des champs magnétiques assez forts pour invalider le régime de Drude, nous trouvons que la conductivité effective longitudinale suit la loi d'échelle $\sigma_L^e \propto B^{-\kappa}$. Pour évaluer la dépendance en température, il faut connaître la valeur du potentiel chimique. Aux valeurs magnétiques où la conductance longitudinale présente un pic et la conductivité de Hall passe d'un plateau à l'autre, le potentiel chimique est donné par $\mu = \hbar \omega_c (n + 1/2)$. Pour la conductivité effective sur les pics nous trouvons une formule analytique qui décrit la passage entre deux régimes distinct : pour des températures élevées $k_B T > \hbar \omega_c / 4$ nous sommes dans un régime purement classique et $\sigma_L^{\text{peak}} \propto T^{1-\kappa}$. Pour $k_B T < \hbar \omega_c / 4$ les niveaux de Landau commencent à se former

et $\sigma_L^{\text{peak}} \propto T^{1-2\kappa}$.

Nous comparons ces formules avec des expériences menées par B. Piot *et al.* [5] au Laboratoire National des Champs Magnétiques Intenses (LNCMI) à Grenoble et par V. Renard *et al.* (en partie publié en [6]). Il est difficile d'extraire l'exposant κ de la dépendance en champ magnétique, car B doit être assez large pour être dans le régime de l'effet Hall quantique, mais en même temps assez petit pour que $k_B T \gg \hbar \omega_c$ soit satisfait. Pour la dépendance en température la forme globale des courbes mesurées est en très bonne correspondance avec la prédiction théorique. Cependant, les valeurs de κ trouvées expérimentalement sont légèrement plus petites que la prédiction théorique.

Coefficient de transmission d'un point selle dans le potentiel électrostatique dans le régime de l'effet Hall quantique

Dans le quatrième chapitre, nous quittons le régime semi-classique et considérons un problème purement quantique : le passage à travers un point selle par l'effet tunnel. Les points selles sont importants tant à l'échelle macroscopique, où ils servent pour décrire les points contact quantiques définis par des électrodes, qu'à l'échelle microscopique où les points selles dans le potentiel de désordre sont les premiers endroits où une description classique échoue. Pour des gaz d'électrons bidimensionnels ordinaires, Fertig et Halperin [7] ont déterminé le coefficient de transmission de manière exacte à partir de la diffusion des ondes planes. Nous développons une méthode alternative, basée sur des fonction Green de vortex [8–10]. En principe, il s'agit d'une théorie de diffusion avec des paquets d'onde formés par des états semi-cohérent. Le grand avantage de notre méthode est qu'elle peut aussi être appliquée au graphène pour lequel une solution analytique exacte n'existe pas encore. Une fois la transmission connue, la formule de Landauer-Büttiker permet de remonter à la conductance. Les points selles asymétriques ont une influence différente sur la conductance dans les gaz d'électrons bidimensionnels ordinaires et dans graphène. Dans un gaz d'électrons bidimensionnel ordinaire, l'asymétrie cause seulement une légère modification de la longueur des plateaux de conductivité qui sera expérimentalement difficile à mesurer. Pour le graphène, les points selles asymétriques brisent la symétrie particule-trou de la conductance, c'est à dire la courbe de conductance pour des énergies positive et négative sera asymétrique.

Introduction aux structures hybrides supraconductrices

Avec le cinquième chapitre commence la deuxième partie de la thèse. Il donne une introduction aux processus non-triviaux de transfert de charge entre des conducteurs normaux et des supraconducteurs, passe en revue des propositions d'utiliser une structure conducteur normal-supraconducteur-conducteur normal (NSN) à trois terminaux comme source de paires d'Einstein-Podolski-Rosen, présente en suite des expériences sondant la conductance non-locale des structures NSN et montre finalement pourquoi il est intéressant d'étudier les corrélations croisées en courant.

Si un électron arrive à une interface entre un conducteur normal et un supraconducteur avec une énergie plus petite que le gap supraconducteur, son passage direct dans le supraconducteur est prohibé par l'absence d'états à un électron dans le supraconducteur. Le transfert de charge est cependant possible par réflexion d'Andreev. Dans ce processus, l'électron arrivant à l'interface crée une paire électron-trou. Les deux électrons forment une paire de Cooper qui passe dans le supraconducteur et le trou retourne dans le conducteur normal. Dans une structure hybride avec plusieurs contacts normaux séparés d'une distance de l'ordre de la longueur de cohérence du supraconducteur, deux processus additionnels jouent un rôle : le cotunneling élastique et la réflexion d'Andreev croisée. Dans un processus de cotunneling élastique, l'électron traverse le supraconducteur par l'effet tunnel. Le processus de réflexion d'Andreev croisée ressemble au processus de réflexion d'Andreev direct, avec la différence que le trou n'est pas retransmis dans l'électrode de provenance de l'électron, mais dans une autre électrode.

Structures hybrides métal normal-supraconducteur-métal normal à trois terminaux

Le sixième chapitre commence avec une description du modèle utilisé, suivi d'une proposition pour décomposer les corrélations croisées en courant en analogie à la décomposition du courant dans les contributions AR, CAR et EC. Après, l'effet de réflexion d'Andreev résonante (reflectionless tunneling) est présenté, parce qu'il donne la motivation pour l'étude d'une structure NNSNN, c'est à dire une structure NSN avec deux barrières additionnelles, qui forme la partie principale de ce chapitre. Le but de notre étude est de savoir, si un effet similaire à la réflexion Andreev résonante (reflectionless tunneling) peut amplifier des corrélations croisées en courant positives. Nous étudions un modèle unidimensionnel avec la théorie de diffusion. La matrice de diffusion est évaluée avec la méthode de Blonder, Tinkham and Klapwijk [11] par adaptation des fonctions d'onde. Le formalisme de Anantram et Datta [12] permet de passer des éléments de la matrice de diffusion au courant et aux corrélations croisées de courant. Dans notre modèle à une dimension, le courant et les corrélations croisées sont très sensibles aux distances entre les barrières. Dans des systèmes balistiques à un canal, les barrières multiples agissent comme un interféromètre de Fabry-Pérot. Cet aspect sera étudié en détail au chapitre suivant. Mais dans un système multidimensionnel avec plus d'un mode de transmission, les oscillations dans des modes différents sont indépendantes et la conductance totale ne dépend que de la moyenne de ces oscillations. Pour imiter qualitativement un comportement multidimensionnel avec un modèle à une dimension, nous moyennons les distances entre les barrières sur une période.

La conductance à travers une interface métal normal-supraconducteur (NS) peut être significativement amplifiée en remplaçant le métal normal par un semi-conducteur désordonné. Melsen et Beenakker [13] ont reproduit cet effet appelé réflexion d'Andreev résonante (reflectionless tunneling) en utilisant une barrière additionnelle

comme un simple modèle de désordre.

L'étude de la structure NNSNN montre que, si la barrière entre les électrodes normales et le supraconducteur est une barrière tunnel, ajouter une deuxième barrière augmente fortement la partie AR du courant comme dans la structure NS. Cependant, les composantes EC et CAR et les corrélations croisées en courant sont peu influencées. La réflexion d'Andreev résonante est la conséquence d'une interférence constructive, qui a seulement lieu si les électrons et les trous impliqués acquièrent une phase exactement opposés sur leur chemin à travers le système. Dans un système où la phase est moyennée, ceci est seulement possible si les électrons et les trous ont le même vecteur d'onde et s'ils voient le même environnement. C'est pourquoi les barrières additionnelles ont peu d'influence sur les processus non-locaux EC et CAR où la particule entre d'un côté et quitte la structure de l'autre côté. Si la même tension est appliquée sur les deux électrodes normales, les corrélations croisées sont dans notre modèle positives. Ces corrélations positives ne peuvent pas être amplifiées par l'effet de réflexion d'Andreev résonant.

Le système balistique

Dans le septième chapitre, nous étudions toujours un système NNSNN, mais cette fois-ci en supposant que le transport dans les électrodes normales est balistique. Les barrières multiples agissent comme des interféromètres de Fabry-Pérot et nous voulons savoir si cet effet peut être utilisé pour filtrer les différents processus microscopiques contribuant à la conductivité et aux corrélations croisées en courant. La réponse à cette question est positive, au moins d'un point de vue théorique. Dans la limite d'énergie nulle, les résonances pour EC et CAR coïncident. Cependant, pour des énergies plus élevées, mais toujours beaucoup plus petites que le gap, le vecteur d'onde pour les électrons est différent du vecteur d'onde pour les trous. En conséquence, les longueurs de résonance sont différentes, et ceci permet de séparer l'effet CAR et EC, ainsi que les différentes contributions aux corrélations croisées.

Conclusion

Nous avons développé un formalisme diagrammatique basé sur un modèle de conductivité locale qui nous permet de calculer la conductivité longitudinale effective dans le régime de haute température de l'effet Hall quantique. Notre formalisme relie le domaine de fluctuations spatiales faibles, qui est déjà bien décrit par une théorie de perturbation au premier ordre, jusqu'au régime de fortes fluctuations qui était jusqu'à présent inaccessible et où les échantillons de Hall sont normalement classés. Pour le transport dans un gaz d'électrons bidimensionnels sous fort champ magnétique, deux effets jouent un rôle important : le mouvement de dérive suivant les lignes équipotentielles percolant à travers l'échantillon et la diffusion électron-phonon qui permet de traverser des points selles qui forment des goulots d'étranglement

pour le transport. Une signature des effets de percolation est l'exposant critique κ . Sa valeur était auparavant conjecturée à partir d'arguments qualitatifs. Notre formalisme permet de le calculer microscopiquement.

Nous avons comparé nos résultats avec des expériences récentes et avons trouvé un bon accord général.

Dans le régime de basse température de l'effet Hall quantique nous avons étudié la passage par effet tunnel à travers des points selles par la diffusion des paquets d'ondes formés par des états semi-cohérents. Nous avons analytiquement calculé le coefficient de transmission d'un point selle pour le potentiel scalaire dans le graphène et avons trouvé que les points selles asymétriques brisent la symétrie particule-trou de la conductance.

Nous avons étudié l'influence des barrières additionnelles sur la conductance (non-locale) et sur les corrélations croisées dans des structures conducteur normal-supraconducteur-conducteur normal à trois terminaux pour répondre à deux questions. Dans les systèmes où la phase est moyennée, la réflexion d'Andreev résonante peut-elle amplifier les corrélations croisées du courant positives dans le régime tunnel? Dans les systèmes balistiques, les interféromètres Fabry-Pérot peuvent-ils filtrer les différents processus dont la conductance et les corrélations croisées sont composées? La réponse à la première question est négative : la réflexion d'Andreev résonante n'amplifie pas les corrélations croisées positives dans le régime tunnel. La réponse à la deuxième question est positive : Si une tension beaucoup plus petite que le gap mais finie est appliquée, les différents processus dans le régime tunnel peuvent clairement être distingués.

Part I.

Transport in the Regime of the Quantum Hall Effect

1. The Integer Quantum Hall Effect

1.1. History and Phenomenology

During the winter of 1980, Klaus von Klitzing studied anomalies in the Hall resistance and magneto-resistance of a two dimensional electron gas in the inversion layer of a silicon MOSFET. To his surprise, the Hall resistance of his sample was not proportional to the magnetic field, but featured steps as the data shown in figure 1.1b. Even though von Klitzing was not the first to see these steps, he was the first to realize that the Hall resistance on the plateaus is always an integer fraction of the constant $R_K = h/e^2$, which carries now his name.

Already in Klaus von Klitzing's very first experiment, the relative uncertainty of the plateau values was better than 10^{-5} [14]. Nowadays, the reproducibility of R_K is confirmed within some parts in 10^{10} , and its determination in terms of SI units has an uncertainty of one part in 10^7 [15]. The universality of the Hall plateaus makes it possible to apply them as a resistance standard, which is much more reliable than the wire resistors used before 1990.

The discovery of the quantum Hall effect was not possible until the late seventies as only then the techniques existed to meet the experimental conditions: the sample fabrication technology to build the semiconductor heterostructures containing a two dimensional electron gas, strong enough magnets to produce the needed high magnetic field (typically 2-10T) and the cooling technique to reach the low temperatures (typically below 1K).

There is to date no complete microscopic theory which describes the behavior of a two dimensional electron gas for the whole range of magnetic fields, temperature, and disorder configurations and could satisfyingly explain all aspects of the quantum Hall effect. In this first introductory chapter, I will first give some arguments which will lead us to a rough understanding of the phenomenology of the quantum Hall effect. Afterwards, I will present some more sophisticated theories, which can put light on specific aspects of the quantum Hall effect.

Charged particles moving in a magnetic field feel the Lorentz force, which deflects them orthogonally to their initial motion and to the magnetic field. Resistivity and conductivity become thus matrices which read in the two dimensional isotropic case:

$$\hat{\rho} = \begin{pmatrix} \rho_L & \rho_H \\ -\rho_H & \rho_L \end{pmatrix} \text{ and } \hat{\sigma} = \begin{pmatrix} \sigma_L & -\sigma_H \\ \sigma_H & \sigma_L \end{pmatrix} = \hat{\rho}^{-1} = \frac{1}{\rho_L^2 + \rho_H^2} \begin{pmatrix} \rho_L & -\rho_H \\ \rho_H & \rho_L \end{pmatrix}. \quad (1.1)$$

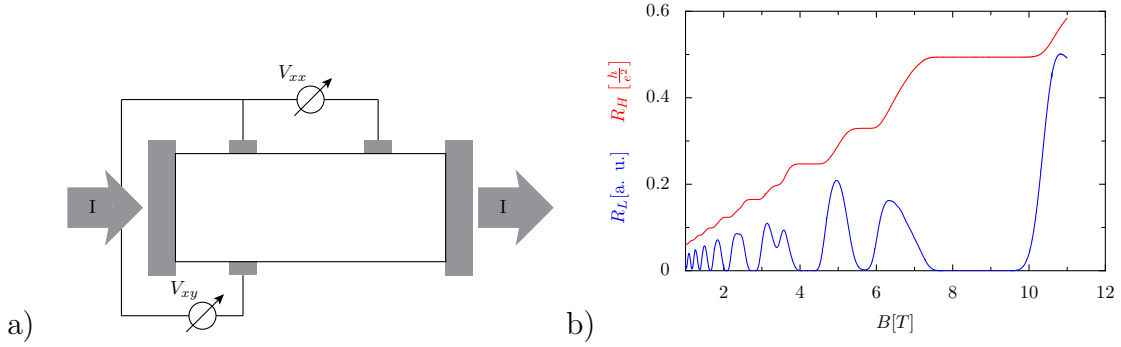


Figure 1.1.: a) Schematic of a Hall bar. b) Typical form of the Hall resistance R_H and the longitudinal resistance R_L as a function of the magnetic field. (data by B. Piot et al. [5])

The diagonal elements of these matrices are called longitudinal or Ohmic resistivity/ conductivity and the off-diagonal elements Hall resistivity/ conductivity. Figure 1.1a shows a schematic of a Hall bar, a rectangular structure containing a two dimensional electron gas with several contacts. Often, there is a gate under the Hall bar by which the density of the electron gas can be changed. In a typical Hall measurement, this Hall bar is placed in a magnetic field perpendicular to its surface and a constant current is forced through the sample. The voltages in direction of the current (longitudinal voltage $V_L = V_{xx}$) and perpendicular to it (Hall voltage $V_H = V_{xy}$) are measured while varying either the magnetic field or the gate voltage. As the system is two dimensional, the Hall resistance, the quotient of Hall voltage and current is equal to the Hall resistivity $\rho_H = R_H = U_H/I$. The sample dimensions are not needed to get the Hall resistivity, ensuring the accurate determination of R_K . The longitudinal resistivity is given by $\rho_L = R_L(L_x/L_y) = (V_L/I)(L_x/L_y)$ and contains geometrical prefactors.

The phenomenon called the quantum Hall effect is that the Hall resistivity as a function of magnetic field or electron density is quantized in integer fractions of the constant $R_K = h/e^2$ and the longitudinal resistance is extremely small, except in regions where the Hall resistance changes from one plateau to the next. Expressed in terms of the conductance, this means that the Hall conductance features steps which are integer multiples of e^2/h and the longitudinal conductance is, as the longitudinal resistance, extremely small, except at the plateau transitions, owing to equation (1.1).

1.2. Realisation of Two Dimensional Electron Gases

To see the quantum Hall effect, one needs a two dimensional electron gas. As a theoretician, it is easy to limit electron motion to a plane. But let us have a look how

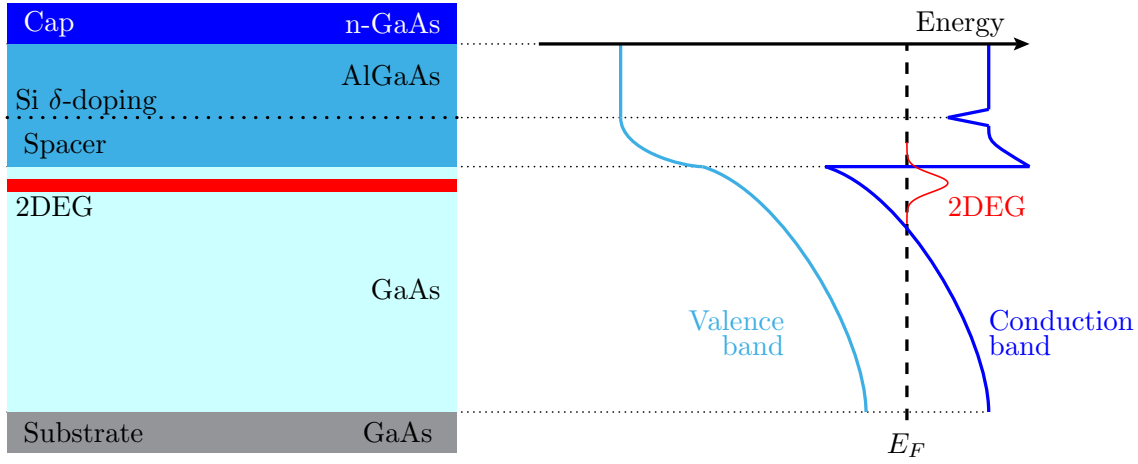


Figure 1.2.: Left: Schematic of the layers in a GaAs/AlGaAs heterostructure with two dimensional electron gas (2DEG), right: energy of the conduction and valence band

experimentalists create a two dimensional electron gas. Most commonly, samples are either Si-MOSFETs or GaAs/GaAlAs heterostructures.

A Si-MOSFET consists of a p-doped silicon substrate, covered with a thin silicon oxide layer and on top of it an aluminum gate electrode. Charging the aluminum electrode positively bends the conduction band of the silicon substrate downwards. Once it is bend under the Fermi level, electrons are trapped at the interface between the silicon and the silicon oxide layer: The electrons cannot enter the silicon oxide layer, as it is an isolator, and they cannot enter the bulk of the silicon substrate, as the band inversion exists only close to the aluminum electrode. Si-MOSFETs have the advantage, that the density of the electron gas can be easily controlled by the applied gate voltage.

In the second case undoped GaAs is covered first by a thin undoped GaAlAs layer, the spacer, and then by n doped GaAlAs. Often, all dopants are in one plane, which is called δ -doping. GaAlAs has a bigger gap between valence and conduction bands than GaAs, and, due to the doping, its Fermi level lies higher. When GaAlAs and GaAs are brought in contact, electrons supplied by the n doped GaAlAs will wander to the GaAs side, to equal the Fermi levels. Positively charged ionized donor atoms stay on the GaAlAs side and play the same role which was in the Si-MOSFET played by the positively charged gate electrode: They bend the conduction band of the GaAs downwards and lead to inversion close to the interface to the GaAlAs layer. As the conduction band of GaAlAs lies much higher in energy than the downwards bend conduction band of GaAl, the electrons are again trapped at the interface. Two dimensional electron gases created in GaAs/GaAlAs heterostructure have the advantage of high mobility.

In the above discussed cases, the two dimensional electron gas is deeply buried in the semiconductor heterostructure. Using a different strategy, the authors of [16] managed to create a two dimensional electron gas on the surface of InSb by depositing Cesium atoms on it. This allowed them to investigate a surface electron gas by scanning tunnel spectroscopy, which gives directly access to the local density of states. On their images (see figure 1.4) the drift states, which are, depending on energy, more or less localized, are clearly visible.

Another conducting material, which is naturally two dimensional, is graphene. Graphene is a planar allotrop of carbon with linear energy spectrum. It shows an half integer quantum Hall effect different from the one presented so far. Most parts of this thesis deal with ordinary two dimensional electron gases. But the calculation in chapter 4 are also applied to graphene and I will explain some of the peculiarities of graphene in section 4.4.

1.3. Landau Levels

In this paragraph, which follows [17], we want to get some insight into the density of states of the two dimensional electron gases under a perpendicular magnetic field, understand what Landau levels are and estimate their degeneracy.

We suppose the electron gas to be confined to the (x, y) -plane and the magnetic field to point in z -direction perpendicular to the electron gas. To start simple, we neglect disorder, Zeeman coupling and the confining potentials. We suppose the electrons to be free particles. Then, they are described by the Hamiltonian

$$\hat{\mathcal{H}}_0 = \frac{1}{2m^*} \left(\mathbf{p} - \frac{e}{c} \mathbf{A}(\mathbf{r}) \right)^2 = \frac{\hat{\mathbf{P}}^2}{2m^*}, \quad (1.2)$$

where m^* is the effective mass, $e = -|e|$ the electron charge, \mathbf{A} the vector potential and \mathbf{P} the canonical momentum¹ conjugate to \mathbf{r} .

In order to bring the Hamiltonian into a familiar form with dimensionless operators, we introduce the cyclotron frequency ω_c and the magnetic length l_B :

$$\omega_c = \frac{|e|B}{m^*c} \quad l_B = \sqrt{\frac{\hbar c}{|e|B}} \quad (1.3)$$

and change to the ladder operators defined by:

$$\hat{a} := \frac{1}{\sqrt{2}} \frac{l_B}{\hbar} (P_x + iP_y), \quad \hat{a}^\dagger := \frac{1}{\sqrt{2}} \frac{l_B}{\hbar} (P_x - iP_y). \quad (1.4)$$

1. i. e. $\frac{d}{dt} \mathbf{r} = \frac{\mathbf{P}}{m^*}$

These ladder operators obey the usual bosonic commutator relation $[\hat{a}, \hat{a}^\dagger] = 1$ and the Hamiltonian takes the familiar form of an harmonic oscillator

$$\hat{\mathcal{H}}_0 = \hbar\omega_c \left(\hat{a}^\dagger \hat{a} + \frac{1}{2} \right) \quad (1.5)$$

with the well known energy spectrum

$$E_n = \hbar\omega_c \left(n + \frac{1}{2} \right), \quad n > 0. \quad (1.6)$$

The energy levels of this spectrum are called Landau levels. The corresponding states are highly degenerate. In realistic systems, there is always a disorder potential which lifts the degeneracy partially and broadens the Landau levels, leading to the density of states schematically presented in figure 1.5.

There are many different sets of eigenstates for H_0 , depending on boundary conditions. One example are the vortex eigenstates, which are the basis for the Green's function formalism used in chapter 4 and will be presented there. Here, we will have a closer look at the states of the Landau basis and use them to estimate the number of states per Landau level and surface. We choose periodic boundary conditions in x -direction and the Landau gauge, where $\mathbf{A} = -By\mathbf{u}_x$ with \mathbf{u}_x an unitary vector in x -direction. The Hamiltonian is now

$$\hat{\mathcal{H}} = \frac{p_y^2}{2m^*} + \frac{1}{2m^*} \left(p_x + \frac{e}{c}By \right)^2. \quad (1.7)$$

As the Hamiltonian does not depend on x we search the eigenstates under the form

$$\Psi_n(x, y) = \frac{1}{\sqrt{L_x}} e^{ik_x x} \psi_{n,k_x}(y), \quad (1.8)$$

where ψ_{n,k_x} solves

$$\left[\frac{p_y^2}{2m^*} + \frac{m^*\omega_c^2}{2} (y - l_B^2 k_x)^2 \right] \psi_{n,k_x} = E_{n,k_x} \psi_{n,k_x}, \quad (1.9)$$

which we recognize as the Schrödinger equation for the one-dimensional harmonic oscillator with equilibrium position $Y_{k_x} = l_B^2 k_x$. Its eigenfunctions are the normalized shifted Hermite polynomials

$$\psi_{n,k_x}(y) = \frac{1}{\sqrt{2^n n! \pi^{\frac{1}{2}} l_B}} e^{-\frac{(y - Y_{k_x})^2}{2l_B^2}} H_n \left(\frac{y - Y_{k_x}}{l_B} \right). \quad (1.10)$$

$$\text{with } H_n(x) = (-1)^n e^{x^2} \frac{d^n}{dx^n} e^{-x^2}. \quad (1.11)$$

2. $[p_x, p_y] = [A_x, A_y] = 0$, $[A_j, p_k] = i\hbar \frac{\partial A_j}{\partial k}$ with $j, k \in \{x, y\}$ and $[\text{rot}\mathbf{A}]_z = \frac{\partial A_y}{\partial x} - \frac{\partial A_x}{\partial y} = B = [\mathbf{B}]_z$

In order to estimate the degeneracy, let us count the number N of states per Landau level on a surface $L_x L_y$. Let L_x be the sample length in x -direction. Due to the periodic boundary conditions $\Psi_n(x, y) = \Psi_n(x + L_x, y)$, which tells us $k_x = (2\pi/L_x)k$ with k an integer. For states centered in the interval $[0, L_y]$, the inequality $0 < Y_{kx} < L_y$ has to hold. As $Y_{kx} = l_B^2 k_x = (2\pi l_B^2/L_x)k$, we have the inequality $2\pi l_B^2 < L_x L_y$ and the number of states in the square $L_x L_y$ is $N = (L_x L_y)/(2\pi l_B^2) = |e| L_x L_y B/(\hbar c)$. Knowing the degeneracy, we can define the filling factor ν as the ratio of electron density n_e and the number of states per Landau level and surface

$$\nu = \frac{n_e}{2\pi l_B^2}. \quad (1.12)$$

Experimentally, there are two ways of seeing conductance steps: either by varying the voltage of a gate under the sample or by varying the magnetic field. Both can be traced back to a variation of the filling factor ν . With the gate voltage, the electron density is changed. A change in the magnetic field changes the degeneracy, *i. e.* the number of states available in the system.

1.4. Localization

In this section, we want to get a qualitative understanding of the way disorder localizes the electron states. To this end, we first study the classical motion of electrons under a magnetic field following [18]. Afterwards, we turn to a quantum mechanical description and add, still following [17], an electric field to the Hamiltonian (1.2) of the last section.

The classical motion of an electron with charge e in presence of an electric field \mathbf{E} and a magnetic field \mathbf{B} is governed by the Lorentz force $\mathbf{F} = e(\mathbf{E} + (\mathbf{v}/c) \times \mathbf{B})$. For an electron constrained to the (x, y) -plane under a constant magnetic field $\mathbf{B} = B\mathbf{u}_z$ the Newtonian equation of motion reads

$$\frac{d^2}{dt^2} \begin{pmatrix} x \\ y \end{pmatrix} = \frac{|e|B}{m^*c} \frac{d}{dt} \begin{pmatrix} -y \\ x \end{pmatrix} \quad (1.13)$$

Introducing the cyclotron frequency ω_c and the complex notation $z = x + iy$ the equation of motion can be rewritten in the form

$$\frac{d^2}{dt^2} z = i\omega_c \frac{d}{dt} z. \quad (1.14)$$

with the solution

$$z(t) = z_0 + r e^{i\omega_c t}. \quad (1.15)$$

The electron performs a cyclotron motion, *i. e.* it moves on a circle around z_0 called the guiding center with radius $|r| = |v|/\omega_c$ given by the initial velocity v and the

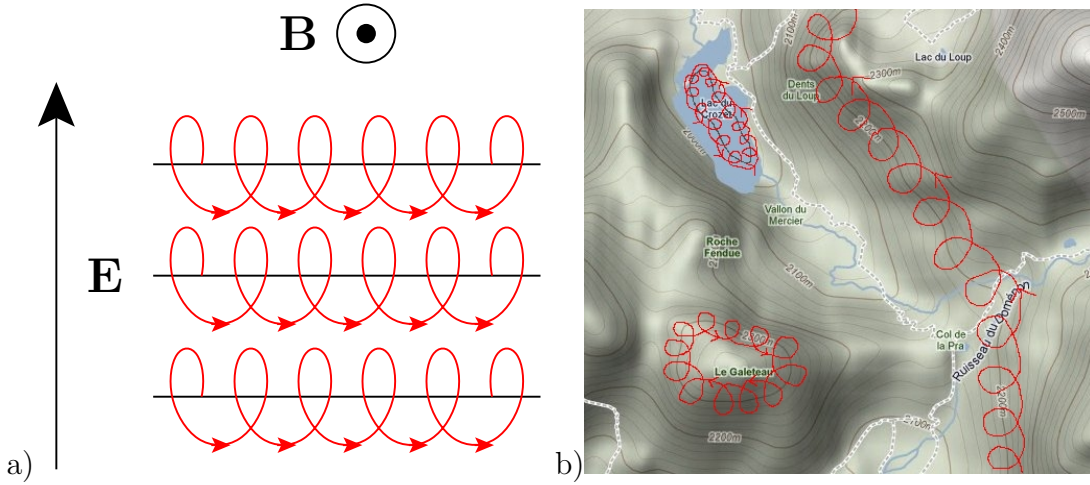


Figure 1.3.: a) Trajectory of a classical electron in a uniform electric and magnetic field. b) Analogy between electric equipotential lines and contour lines with examples for localized trajectories around mountain tops and valleys and extended states which traverse the whole system. (The underlying map has been taken from Google Maps.)

cyclotron frequency. If an electric field $\mathbf{E} = \mathcal{E}\mathbf{u}_y$ is added, the equation of motion and its solution becomes

$$\frac{d^2}{dt^2}z = i\omega_c \frac{d}{dt}z - i\frac{e\mathcal{E}}{m^*}, \quad z(t) = z_0 + re^{i\omega_c t} + c\frac{\mathcal{E}}{B}t. \quad (1.16)$$

The electron trajectory is represented in figure 1.3a: In addition to the cyclotron motion, the guiding center drifts perpendicular to the electric field or, in other words, it follows the equipotential lines of the electric potential Φ defined as $\mathbf{E} = -\nabla\Phi$. The drift velocity is given by $\mathbf{v}_d = c\mathbf{E} \times \mathbf{B}/B^2$ for a general electric field. The radius of the cyclotron motion is inversely proportional to the magnetic field. If the electron moves in a slowly spatially varying electrostatic potential $V(\mathbf{r}) = e\Phi(\mathbf{r})$ (where slowly varying means $|\partial_j \partial_k V| \ll m^*\omega_c^2, j, k \in \{x, y\}$) the guiding center motion is given by

$$\frac{d}{dt}\mathbf{R} = \frac{c}{e} \frac{\mathbf{B} \times \nabla V}{B^2} \quad (1.17)$$

and thus the guiding center drifts along the equipotential lines of $V(\mathbf{r})$. In a smoothly varying potential landscape, this leads to two different kinds of trajectories: Closed ones for guiding centers following an equipotential line around a local maximum or minimum of the potential, and open ones with energy close to the mean value of the potential, percolating through the system. An intuitive way of thinking of the equipotential lines is to identify them with contour lines of a topographic map as shown in figure 1.3b. There are electron trajectories which cycle infinitely around the same mountain tops or lakes and there are trajectories leading over passes which run through the whole area.

1. The Integer Quantum Hall Effect

Let us get back to the quantum mechanical description. As in the classical case, we introduce an electric field pointing in y -direction. This means adding a potential $V(y) = -e\mathcal{E}y$ to the Hamiltonian which is most easily done in Landau gauge. The Hamiltonian is now

$$\hat{\mathcal{H}} = \frac{p_y^2}{2m^*} + \frac{1}{2m^*} \left(p_x + \frac{e}{c}By \right)^2 - e\mathcal{E}y \quad (1.18)$$

and does not depend on x . So we search again the solution under the form of equation (1.8). This time ψ_{n,k_x} has to solve

$$\left[\frac{p_y^2}{2m^*} + \frac{1}{2m^*} \left(\hbar k_x + \frac{e}{c}By \right)^2 - e\mathcal{E}y \right] \psi_{n,k_x} = E_{n,k_x} \psi_{n,k_x}. \quad (1.19)$$

Completing the square in order to absorb the term linear in y and using the new variables $v_d = c\mathcal{E}/B$ and $Y_{k_x} = k_x l_B^2 - v_d/\omega_c$ the Hamiltonian takes the form of equation (1.9) shifted by $\Delta E = Y_{k_x}|e|\mathcal{E} + (m^*/2)v_d^2$ and with equilibrium position Y_{k_x} :

$$\left[\frac{\hat{p}_y^2}{2m^*} + \frac{m^*}{2}\omega_c^2 (y - Y_{k_x})^2 + Y_{k_x}|e|\mathcal{E} + \frac{m^*}{2}v_d^2 \right] \psi_{n,k_x} = E_{n,k_x} \psi_{n,k_x}. \quad (1.20)$$

Therefore the energy eigenvalues are

$$E_{n,k_x} = \left(n + \frac{1}{2} \right) \hbar\omega_c + Y_{k_x}|e|\mathcal{E} + \frac{m^*}{2}v_d^2 \quad (1.21)$$

$$= \left(n + \frac{1}{2} \right) \hbar\omega_c + V(Y_{k_x}) + \frac{l_B^2}{2\hbar\omega_c} |\nabla V|^2 = E_n(Y_{k_x}). \quad (1.22)$$

The disorder potential lifts the degeneracy of the states in one Landau level. The eigenfunctions are still given by (1.10) with the only difference that now $Y_{k_x} = k_x l_B^2 - v_d/\omega_c$. It is interesting to notice that these wave functions are localized on a length scale of l_B along the y -direction, but are extended in the x -direction. This means they follow, as the classical guiding centers, the electric equipotential lines. This will also stay true for potentials with more complex spatial dependence, as long as they are slowly varying. As the kinetic energy of electrons can only change in steps of $\hbar\omega_c$, the potential energy cannot change continuously either due to energy conservation. The only way of changing the potential energy is by tunneling. Except for states close to saddle points, the distances between states is typically much larger than the characteristic width l_B of the electronic wave functions and the electrons have to stay on their equipotential line.

It seems now plausible that there are two kinds of states: localized ones and extended ones. A beautiful experimental confirmation of the existence of localized and delocalized states are the scanning tunneling spectroscopy measurements of [16]

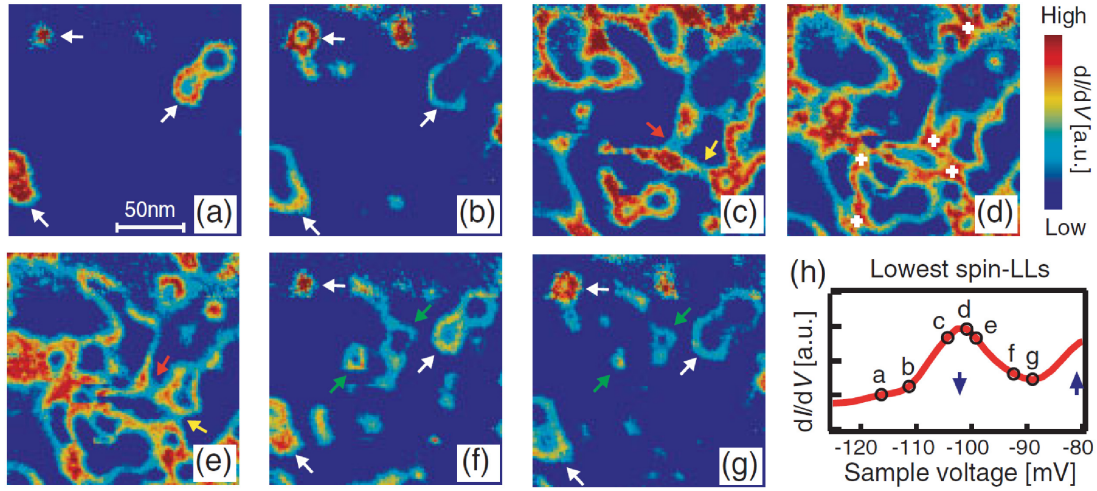


Figure 1.4.: Density of states of a two dimensional InSb surface electron gas in the quantum Hall regime ($B = 12T$, $T = 0.3K$) measured by scanning tunneling spectroscopy [16]. From a) to g) the sample voltage is increased (see h)) allowing to probe the density of states at different energies. In figure a), at low energy, the density of states is located in valleys of the potential landscape. In figure b) at slightly higher energy, the density of states is still localized in the same valleys, but has moved outwards. In d) the density of states percolates the entire sample. f) and g) shows the density of states of the lowest spin level localized around mountain tops. The valleys reappear as now also the density of states of the second spin level is probed.

(see figure 1.4). The eigenenergies of the extended states are approximately the energies of the original Landau levels, *i. e.* they are at the center of the disorder broadened Landau band. These two kinds of states are marked in the sketch of the electron density of states in figure 1.5. It is intuitively clear, that only states that are extended from one edge of the sample to the other can contribute to the macroscopic conductance.

Let us calculate the current carried by one of the eigenstates. In general the current operator is

$$\hat{\mathbf{j}} = \frac{e}{m^*} \hat{\mathbf{P}}. \quad (1.23)$$

It is useful to introduce the latter operators

$$\hat{b} = \frac{1}{\sqrt{2}} \left(\sqrt{\frac{m^* \omega_c}{\hbar}} (y - Y_{k_x}) + i \frac{1}{\sqrt{m^* \hbar \omega_c}} p_y \right), \quad (1.24)$$

$$\hat{b}^\dagger = \frac{1}{\sqrt{2}} \left(\sqrt{\frac{m^* \omega_c}{\hbar}} (y - Y_{k_x}) - i \frac{1}{\sqrt{m^* \hbar \omega_c}} p_y \right) \quad (1.25)$$

and express the current operators by them

$$\hat{j}_x = \frac{e}{m^*} \left(p_x + \frac{e}{c} B y \right) = -e \sqrt{\frac{\hbar \omega_c}{2m^*}} (\hat{b} + \hat{b}^\dagger) + e v_d, \quad (1.26)$$

$$\hat{j}_y = \frac{e}{m^*} p_y = i e \sqrt{\frac{\hbar \omega_c}{2m^*}} (\hat{b}^\dagger - \hat{b}). \quad (1.27)$$

Using the orthogonality of the eigenstates of the harmonic oscillator, their expectation values are readily evaluated

$$j_x^{n,k_x} = \int dx \int dy \Psi_{n,k_x}^* \hat{j}_x \Psi_{n,k_x} = e v_d = e \frac{\partial E_{n,k}}{\hbar \partial k_x}, \quad (1.28)$$

while j_y^{m,k_y} is zero.

Every state is carrying a current $\hat{\mathbf{j}} = e v_d \mathbf{u}_x$ and as in the classical case, the current density follows the equipotential lines.

1.5. Where Do the Hall Steps Come From ?

As last ingredient for a phenomenological explanation of the quantum Hall effect, we need the Hall conductance of a Landau level whose localized states are completely filled. To calculate it, we use the edge state approach: In a Hall bar, as the one depicted in figure 1.1, the confining potential will strongly rise on the lower and

upper edge, leading to delocalized edge states which go through the sample. We suppose the disorder potential to trap all states in the bulk of the sample. The disorder potential will deform the edge states slightly, but not change the amount of current they can carry. The electric field will point in positive y -direction on the lower edge and in negative y -direction on the upper edge, leading to drift currents $\hat{\mathbf{j}}_{n,|k_x|}^{\text{lower}} = -|ev_d|\mathbf{u}_x$ on the lower edge and $\hat{\mathbf{j}}_{n,-|k_x|}^{\text{upper}} = |ev_d|\mathbf{u}_x$ on the upper edge. If there is no difference in the occupation of states on the upper and the lower side, $\hat{\mathbf{j}}^{\text{lower}}$ and $\hat{\mathbf{j}}^{\text{upper}}$ cancel each other exactly.

If there is a Hall voltage V_H , a difference in the chemical potentials of the upper and the lower edge $eV_H = \mu_l - \mu_u$ arises. The current carried by one Landau level is the current carried by the edge states times their occupation probability $n_{n,k_x} = n_F(E_{n,k_x} - \mu_{k_x})$ where n_F is the Fermi function. At zero temperature the contribution of one Landau level to the Hall conductivity reads

$$\sigma_H^n = \lim_{\mathcal{E} \rightarrow 0} \frac{1}{L_y \mathcal{E}} \sum_{k_x} j_x^{n,k_x} n_{n,k_x} = \lim_{\mathcal{E} \rightarrow 0} \frac{e}{\hbar L_y \mathcal{E}} \int \frac{dk_x}{2\pi} \frac{\partial E_{n,k_x}}{\partial k_x} n_{n,k_x} \quad (1.29)$$

$$= \lim_{\mathcal{E} \rightarrow 0} \frac{e}{\hbar} \frac{1}{L_y \mathcal{E}} \int_{\mu_l}^{\mu_u} dE_{n,k_x} = \lim_{\mathcal{E} \rightarrow 0} \frac{e}{\hbar} \frac{\mu_u - \mu_l}{L_y \mathcal{E}} = \lim_{\mathcal{E} \rightarrow 0} \frac{e^2}{\hbar} \frac{(-V_H)}{L_y \mathcal{E}} = \frac{e^2}{\hbar}. \quad (1.30)$$

From this expression, we can read the contribution to the Hall conductivity of one Landau level $\sigma_H^n = e^2/\hbar$.

One could now jump to the conclusion that the direct generalization of equation (1.30) to all Landau levels

$$G_H = \frac{e^2}{h} \sum_n n_F(E_n - \mu) \quad (1.31)$$

would already be the desired quantized conductance formula. But this is wrong: $\sum_n n_F(E_n - \mu)$ is nothing else but the filling factor ν and so

$$G_H = \nu \frac{e^2}{h} = \frac{n_e}{2\pi l_B^2} \frac{e^2}{h} = \frac{|e|n_e c}{B}. \quad (1.32)$$

This is the classical result. The conductance increases linearly with the electron density n_e . There are no steps. To understand the conductance quantization, we have to argument with the localized and delocalized states illustrated in figure 1.5. At low temperatures electron states are filled successively with increasing electron density, starting by the states with the lowest energy. At very low filling factors, all electrons are in localized states and both, the longitudinal and the Hall conductance, are zero. With increasing filling factor, the conducting states around $(1/2)\hbar\omega_c$ will be filled. The Hall conductance rises, until the conducting states are filled. The conductance will then have reached the value of $\sigma_H = e^2/\hbar$ that we have calculated as the contribution of one Landau level in equation (1.30). If the electron density increases

1. The Integer Quantum Hall Effect

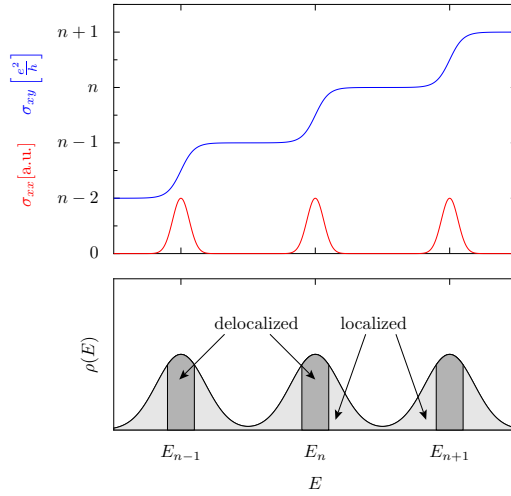


Figure 1.5: Lower figure: Schematics of the density of states in the regime of the quantum Hall effect in presence of disorder. Dark gray areas stand for extended, conducting states, light gray areas for localized, non-conducting states.

Upper figure: Resulting longitudinal (σ_{xx}) and Hall (σ_{xy}) conductance.

further, electrons are placed into non-conducting states. The Hall conductance stays on its plateau value, until the next bunch of extended states is reached and so on. The longitudinal conductance decreases as soon as half of the conducting states are filled, because states with opposite k_x -values cancel each other and completely filled bands do not contribute to the macroscopic longitudinal conductance.

1.6. Further Complications to Consider

It is generally believed that the integer quantum Hall effect can be explained in an effective one body image: The one body Hamiltonian $\hat{\mathcal{H}} = 1/(2m^*)(\hat{\mathbf{p}} - (e/c)\hat{\mathbf{A}}(\hat{\mathbf{r}}))^2 + \hat{V}(\hat{\mathbf{r}})$, where $\hat{V}(\hat{\mathbf{r}})$ is the potential created by disorder and the confinement, captures qualitatively the whole physics of the integer quantum Hall effect. But, to achieve quantitative agreement with experimental data, it is, depending on the studied temperature, magnetic field and density range, necessary to take electron-electron and electron-phonon interactions into account.

Electrons appear in two spin species. So the degeneracy and the conductivity have to be multiplied by two. If one measures for example the Hall conductance at low magnetic fields in a regime where spin cannot be resolved, one will only see conductance plateaus at even integer values.

The spin couples by the Zeeman effect to the external magnetic field. This leads to an energy shift of $E_z = \pm(1/2)g\mu_B B$, where μ_B is the Bohr magneton. The Zeeman effect in itself is usually small, because the g-factors and the effective masses m^* which give the ratio of the Zeeman energy to the energy scale of the Landau levels $\Delta E_z/\Delta E_n = g\mu_B B/(\hbar\omega_c) = gm^*/(2m_e)$ are small. For example in GaAs $g = 0.43$ [19], $m^*/m_e = 0.067$ [19] leading to $\Delta E_z/\Delta E_n = 0.014 \ll 1$. It can be taken into account, by calculating the quantities one is interested in separately for both spin species and adding them with the appropriate Zeeman shift. However, there are

exchange interaction effects between the two spin species [20]. Phenomenologically, the effect of the exchange interaction can be described with an effective g-factor which depends on magnetic field, electron density and temperature. The effective g-factors are typically of the order of 10 [21] and no longer negligible. They make quantitative analysis of experimental data difficult, because they have to be determined by a self consistent calculation taking disorder and electron-electron interaction into account. As electrons are charged particles, they interact via Coulomb forces. It is in general believed that a mean-field description is enough to describe these interaction effects in the regime of the integer quantum Hall effect. In the limit of zero temperature, interaction leads to the separation of the two dimensional electron gas into “compressible” and “incompressible” regions [22–24]. In a “compressible” region, there is a Landau band at the Fermi energy. Electrons can be redistributed without energy costs and are arranged to screen the external potential perfectly, resulting in strong spatial fluctuations of the electron density and a constant effective potential. In an “incompressible” region the Fermi energy falls into a gap between Landau bands. Electron redistribution being energetically not possible, there is no screening of the fluctuating external potential and the electron density is constant. The incompressible regions are destroyed for increasing temperatures and can be safely ignored if $k_B T / (\hbar \omega_c)$ is bigger than a few percents [25].

Let us consider in what follows only the one body problem. For the arguments I have given so far to explain the quantum Hall effect the disorder potential is important, as it provides the localization mechanism, but has not yet been treated microscopically. In the following sections, I will present some more sophisticated theories to deal with the disorder potential.

1.7. Perturbation Expansion in the Disorder Potential

As the eigenstates and eigenvalues of the Hamiltonian $\hat{\mathcal{H}}_0$ (see equation (1.2)) for a free particle in a magnetic field are known, it is a natural idea to gain insight in the behavior of the full Hamiltonian

$$\hat{\mathcal{H}} = \hat{\mathcal{H}}_0 + \hat{V} \quad (1.33)$$

via a perturbation theory in the potential \hat{V} describing the disorder. The impurities causing the disorder are distributed randomly. Most experiments probe macroscopic quantities, which are only sensible to the average disorder. Therefore, most theoretical treatments do not aim to solve the problem for one specific realization of disorder, but average somewhere over all possible disorder configuration. Usually the disorder averaged Green’s function is calculated, whose imaginary part gives the density of states and which is a starting point to calculate the conductivity using the Kubo formula. Tsuneya Ando was a pioneer on this field [26, 27].

As with all perturbation theories, a small parameter is needed to control the approximations made in the process. In general the perturbation theories work well for low magnetic fields and disorder distributions with short range scatterers where the mean free path l and the Fermi wave vector k_F are large, so that $(k_F l)^{-1}$ is a small parameter. But in the regime of strong magnetic fields with long range disorder, where we expect to see the quantum Hall effect, it is difficult to control the perturbation theory, as the bare states are highly degenerate. For example, the standard self-consistent Born approximation which works well at low fields leads to unphysical results at high fields.

To give a concrete example for such a perturbation theory and its limits let us calculate the density of states for a zero mean Gaussian distributed disorder potential using the self consistent Born approximation in the limit of high magnetic fields [28]. Let \hat{G}_0 be the free and \hat{G} the full retarded Green's function defined by

$$\lim_{\eta \rightarrow 0} \hat{G}_0(E - \hat{\mathcal{H}}_0 + i\eta) = \hat{1}, \quad \lim_{\eta \rightarrow 0} \hat{G}(E - \hat{\mathcal{H}} + i\eta) = \hat{1}. \quad (1.34)$$

The two Green's functions obey the Dyson equation $\hat{G} = \hat{G}_0 + \hat{G}_0 \hat{V} \hat{G}$. To simplify the following discussion let us introduce the Feynman diagrams

$$\hat{G}_0 = \bullet \text{---} \bullet, \quad \hat{V} = \bullet \text{---} \bullet. \quad (1.35)$$

The Dyson equation can be expanded as

$$\hat{G} = \bullet \text{---} \bullet + \bullet \text{---} \hat{V} \bullet + \bullet \text{---} \hat{V} \hat{V} \bullet + \bullet \text{---} \hat{V} \hat{V} \hat{V} \bullet + \bullet \text{---} \hat{V} \hat{V} \hat{V} \hat{V} \bullet + \dots \quad (1.36)$$

Let us now introduce $\hat{g} = \langle \hat{G} \rangle = \bullet \text{---} \bullet$ as the disorder average. As we suppose the disorder to be zero mean Gaussian distributed, odd moments are zero and we can use Wick's theorem to do the average. We denote the average graphically by joining the curly lines, representing the disorder, in all possible pairings.

$$g = \langle \hat{G} \rangle = \bullet \text{---} \bullet + \bullet \text{---} \text{---} \bullet + \bullet \text{---} \text{---} \text{---} \bullet + \bullet \text{---} \text{---} \text{---} \text{---} \bullet + \bullet \text{---} \text{---} \text{---} \text{---} \text{---} \bullet + \dots \quad (1.37)$$

The self consistent Born approximation consists now in neglecting all diagrams with crossings. In order to sum up the remaining diagrams, we define a self-energy $\hat{\Sigma}$ as the sum of all remaining irreducible diagrams without the outermost \hat{G}_0 -lines.

$$\hat{\Sigma} = \text{---} \text{---} + \text{---} \text{---} \text{---} + \text{---} \text{---} \text{---} \text{---} + \text{---} \text{---} \text{---} \text{---} \text{---} + \dots = \text{---} \text{---} = \langle \hat{V} \hat{g} \hat{V} \rangle \quad (1.38)$$

Looking at what remains of \hat{g} after the Born approximation and at $\hat{\Sigma}$ we realize that they are identical up to the outermost arc and therefore the last equation holds. At

the same time, \hat{g} can be expressed as $\hat{g} = \hat{G}_0 + \hat{G}_0 \hat{V} \hat{G}_0 + \dots$, a geometric series which leads to a Dyson equation for \hat{g}

$$\hat{g} = \hat{G}_0 + \hat{G}_0 \hat{\Sigma} \hat{g}. \quad (1.39)$$

Let us project this Dyson equation into the basis built by the states defined in equation (1.8) labeled by the quantum number $\alpha = n, k$ where n is the Landau level index and k labels the guiding center coordinates. As we suppose the disorder to be isotropic, \hat{g} will be diagonal in this basis and depend only on the Landau level index n :

$$g_n = \frac{1}{E - \epsilon_n - \Sigma_n}. \quad (1.40)$$

The density of states is given by the imaginary part of the retarded Green's function \hat{g} : To calculate it, we decompose the self-energy into its real and imaginary parts, $\Sigma_n = \Delta_n + i\Gamma_n$ leading to

$$\rho(E) = \lim_{\eta \rightarrow 0} \lim_{L_x, L_y \rightarrow \infty} \frac{1}{\pi L_x L_y} \text{Tr}\{\text{Im}(\hat{g}(E + i\eta))\} \quad (1.41)$$

$$= \frac{1}{2\pi l_B^2} \sum_n \frac{1}{\pi} \frac{\Gamma_n(E)}{(E - \epsilon_n - \Delta_n(E))^2 + \Gamma_n^2(E)}. \quad (1.42)$$

Projecting equation (1.38) into the Landau Basis leads to

$$\Sigma_n = \sum_{n', k'} \langle |V_{nk, n'k'}|^2 \rangle g_{n'}. \quad (1.43)$$

For strong magnetic fields the original Landau levels are well separated and the disorder potential does not couple them, which means that V is diagonal in n .

$$\Sigma_n(E) = \sum_{k'} \langle |V_{nk, nk'}|^2 \rangle g_n = \frac{a_n}{E - \epsilon_n - \Sigma_n} \text{ with } a_n = \sum_{k'} \langle |V_{nk, nk'}|^2 \rangle \quad (1.44)$$

$$\iff \Sigma_n(E) = \frac{1}{2} (E - \epsilon_n) \pm \sqrt{(E - \epsilon_n)^2 - 4a_n} \quad (1.45)$$

The density of states is only different from zero in the regions where Σ_n has an imaginary part. This is the case for $\epsilon_n - 2\sqrt{a_n} < E < \epsilon_n + 2\sqrt{a_n}$, where

$$\Delta_n(E) = \frac{1}{2}(E - \epsilon_n), \quad \Gamma_n(E) = \frac{1}{2}\sqrt{4a_n - (E - \epsilon_n)^2}. \quad (1.46)$$

Plugging this into equation (1.42), we get the self consistent Born density of states

$$\rho(E) = \frac{1}{2\pi l_B^2} \sum_n \frac{\sqrt{4a_n - (E - \epsilon_n)^2}}{2\pi a_n} \Theta(4a_n - (E - \epsilon_n)^2). \quad (1.47)$$

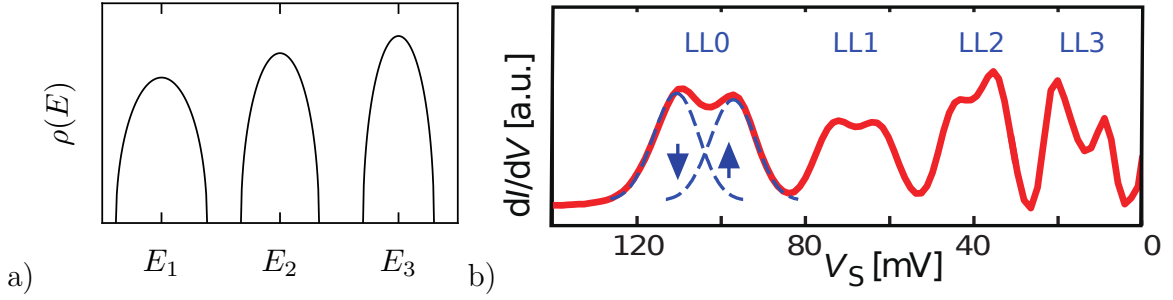


Figure 1.6.: a) The density of states in self consistent Born approximation. As an artefact of this approximation, the density of states goes to zero with infinite slope at $E = E_n \pm 2\sqrt{a_n}$.
b) Density of states obtained as spatial average of STM measurements[29]. The Landau levels appear as double peaks due to the electron spin. The blue curves are Gaussian fits.

This density of states consists of semi-ellipses (see figure 1.6): There are gaps where the density of states is exactly zero and these gaps are reached with infinite slope. This behavior seems unphysical: The energy of an electron is essentially given by its Landau level energy plus the average over the potential energy of the area over which the cyclotron motion of the electron is spread. In a random potential, extreme energy fluctuations are rare, but they occur and therefore the spectrum should never be exactly zero. Comparison with experimental data shows that the shape of the self consistent Born density of states is wrong. Even though, the width of the semi-ellipses predicts correctly the narrowing of the experimental measured peaks with increasing Landau level index. Physically, the narrowing of the peaks in the density of states is easily understood. In the same way as for a classical particle the radius of its cyclotron motion increases with increasing energy, the wave function spreads over a large area for a quantum mechanical particle in higher Landau levels. Therefore, the disorder landscape is averaged over a larger area, the averages for different states differ less and less from each other and the peaks in the density of states become larger.

In reference [30] it is shown that, if the correlation length of the potential of disorder is much longer than the magnetic length, the contribution of crossing diagrams which are neglected in the self-consistent Born approach, is as big as the contribution of the non crossing diagrams. This clearly invalidates the self-consistent Born approximation in the high field limit. To give the order of magnitude, the magnetic length is $l_B = 8\text{nm}$ for a magnetic field of $B = 10\text{T}$ and the correlation length is typical between $a = 20\text{nm}$ and $a = 100\text{nm}$. The self consistent Born approximation shows even worse problems, when transport properties are studied.

The authors of [31] show that the Gaussian line shape of the density of states can

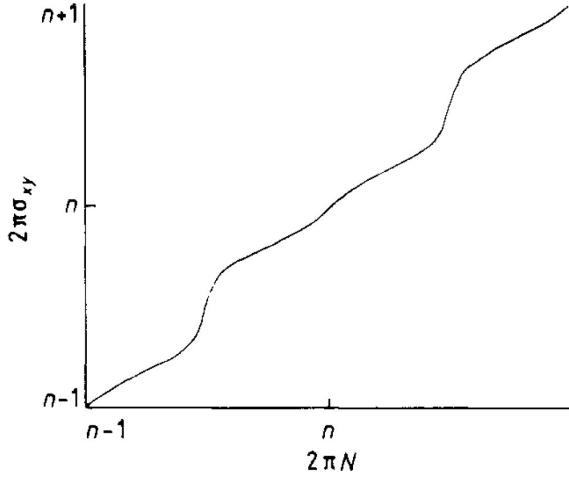


Figure 1.7: Hall conductivity in the limit of infinitely high Landau levels [34]. This Hall conductivity does not feature plateaus in consistency with the absence of localized states in the self-consistent Born approximation.

be recovered by summing up all diagrams which is possible in the limit of smooth disorder $l_B/a \rightarrow 0$ if the correlations of the disorder potential are supposed to be distance independent. Another way, also in the limit of smooth disorder, is the cumulant expansion of [32, 33], which yields a gaussian lineshape, too.

In reference [34] the limit of infinitely high Landau levels is studied at high magnetic fields. This regime is experimentally not achievable, but in this limit the self-consistent Born approximation becomes exact. With the Born approximation the localized states are lost. As one sees in figure 1.7, this Hall conductivity does not feature plateaus. This is an evidence that localized states are needed to get plateaus.

1.8. The Gradient Expansion of the Disorder Potential

As we have seen in the last section, a perturbation expansion directly in the strength of the disorder potential is difficult, as the free Hamiltonian is highly degenerate. The idea of the gradient expansion is to decompose the potential into a local constant term and higher gradient terms. The local constant term lifts the degeneracy and a non-degenerate perturbation expansion in the gradient terms is possible. Examples for this method are [35] and the more systematic vortex Green's function method [8–10] presented in chapter 4.2. In the vortex Green's function method the electron position is, inspired by the classical motion, decomposed into a guiding center coordinate and a relative coordinate. The degeneracy is lifted by the local potential at the guiding center positions and the Gaussian density of states is trivially recovered [36]. The small parameter in the expansion is $l_B^2/(a^2 + 2l_B^2)$, where a is the correlation length of the disorder potential. The gradient expansion theory converges rapidly for smooth disorder where $a \gg l_B$.

1.9. The "Classical" Percolation Model

The "classical" percolation model is based on the physical discussions in section 1.4: Under high magnetic fields the classical motion and the quantum mechanical wave functions follow equipotential lines. The equipotential lines are geometric objects, which can be studied with the methods of percolation theory. Percolation theory addresses the question of the spatial extension ξ of the equipotential lines. Does an equipotential line of a certain energy "percolate" through the system *i. e.* in finite systems connects one extremity of the sample to the other? In an infinite system an object percolates, if its localization length ξ diverges. The divergence occurs with an critical exponent ν when the critical energy E_c is approached. What are the values of ν and E_c ? How is the circumference of an equipotential line connected to its spatial extension? These geometrical properties of the equipotential lines must then be translated to properties of the wave functions and connected to transport quantities.

The model is called "classical", even if the percolating object is a wave function, as long as there are no quantum tunneling effects. This is valid at high enough temperatures for smooth disorder. As we will see in chapter 4, the energy connected to quantum tunneling is $E_{\text{tunnel}} \propto (l_B^2/a^2)\sqrt{\langle V^2 \rangle}$, where a is the correlation length of the disorder potential and $\sqrt{\langle V^2 \rangle}$ its typical amplitude. The two of them are highly sample dependent. If for example $a = 40\text{nm}$, $l_B(B = 10\text{T}) = 8\text{nm}$ and $\sqrt{\langle V^2 \rangle} = 2\text{meV}$, the tunnel effect is negligible for temperatures higher than $E_{\text{tunnel}}/k_B \approx 1\text{K}$.

As concrete examples for the application of the percolation model I point to chapter 2. The work of Simon and Halperin [2] presented in detail in section 2.1 and my own work are based on the percolation model.

1.10. The Chalker-Coddington Model

The Chalker-Coddington model [14, 37] is a quantum network model based on percolation ideas. It allows to investigate the influence of tunneling over saddle points on the localization-delocalization quantum phase transition, which has been spared out in the classical percolation model. Tunneling affects the shape of the transition between plateaus. The Chalker-Coddington model works at low (zero) temperature.

In the Chalker-Coddington model, the potential landscape is replaced by a regular network of saddle points, connected via links along which the probability amplitude can propagate. While traveling along a link, the absolute value of the probability amplitude does not change, but it acquires a phase. The saddle points are described by their scattering matrices. Often, the scattering matrix for a purely quadratic saddle point is used, which has been calculated analytically by Fertig and Halperin [38] and will be the subject of chapter 4.

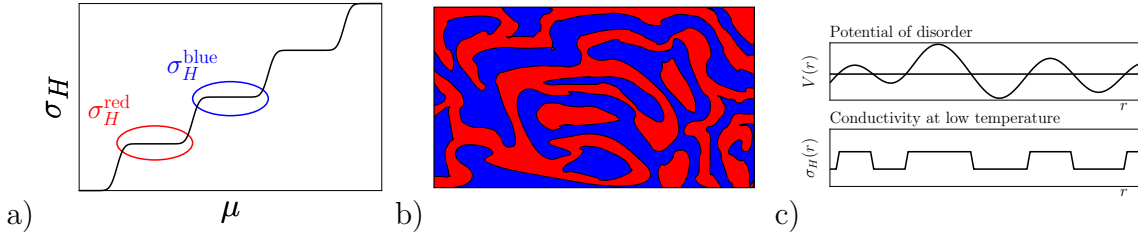


Figure 1.8.: The Hall conductivity depends on the local chemical potential a), therefore it fluctuates spatially with the potential of disorder b). c) Sketch of the dependence of the local Hall conductivity on the potential of disorder.

As in the classical percolation model the first goals are to calculate the localization length ξ and its critical exponent ν . There does not yet exist consensus on the values of this quantities [39]. The method gives also access to other quantities as for example the energy level statistics and the statistics of the conductance. (As the studied systems are coherent, there is no self averaging. The conductance fluctuates strongly from sample to sample and it is not enough to give the mean value.)

The Chalker-Coddington model has initiated a lot of experimental work. Often the temperature scaling of the plateau-to-plateau transition is measured, e.g. in [40–42], either as the half width ΔB of the peaks in the longitudinal resistance which vanishes as $\Delta B \propto T^\kappa$ when zero temperature is reached or as the slope of the Hall resistance at the values of the plateau transitions B_c which diverges as $dR_{xy}/dB|_{B_c} \propto T^{-\kappa}$ for vanishing temperature. The exponent κ is related to the localization length critical exponent ν via $\kappa = p/(2\nu)$, where p is the critical exponent of the phase coherence length $L_\phi \propto T^{-p/2}$.

1.11. The Two Phase Model

The two phase model of Dykhne and Ruzin [43] is a phenomenological theory, which allows, starting from the assumption that the sample consists of a random mixture of two phases with different Hall conductivities, to derive a relationship between longitudinal and Hall conductance and to calculate the peak height of the longitudinal conductivity. I present this theory here, as it can be seen as the low temperature version of what I do in chapter 2. However, the regime they treat is somehow pathological, as they need on the one hand low temperature to make the transitions from one Landau level to the next sharp, but use at the other hand a local conductivity approach, which neglects tunneling and quantum coherence effects. The model of Dykhne and Ruzin applies also to the fractional quantum Hall effect, but I will only have a look at the integer quantum Hall effect.

The first important assumption used in the two phase model is that the conductivity $\hat{\sigma}$ is a purely local quantity and therefore Ohm's law holds in its local version

$\mathbf{j}(\mathbf{r}) = \hat{\sigma}(\mathbf{r})\mathbf{E}(\mathbf{r})$. The second assumption is that the conductivity takes exactly two different values in the sample. The Hall conductivity depends on the chemical potential as schematically depicted in figure 1.8. Close to a plateau transition a small change in the chemical potential lets the Hall conductivity jump between two different values. The chemical potential is a local quantity in the sense that it is the sum of the global chemical potential of the sample and the local value of the potential of disorder. The fluctuations in the disorder potential lead then to fluctuations in the local Hall conductivity. The system is supposed to have also a small longitudinal conductivity due to scattering at short range defects or phonons. The local conductivity tensor takes the form:

$$\hat{\sigma}(\mathbf{r}) = \begin{pmatrix} \sigma_L(\mathbf{r}) & -\sigma_H(\mathbf{r}) \\ \sigma_H(\mathbf{r}) & \sigma_L(\mathbf{r}) \end{pmatrix}, \text{ with } \sigma_L(\mathbf{r}) = \begin{cases} \sigma_L^{(1)} \\ \sigma_L^{(2)} \end{cases}, \quad \sigma_H(\mathbf{r}) = \begin{cases} \sigma_H^{(1)} \\ \sigma_H^{(2)} \end{cases}. \quad (1.48)$$

The goal is now to calculate an effective conductivity $\hat{\sigma}^e$ which is defined as

$$\langle \mathbf{j} \rangle = \hat{\sigma}^e \langle \mathbf{E} \rangle, \quad (1.49)$$

where $\langle \mathbf{j} \rangle$ and $\langle \mathbf{E} \rangle$ are the spatially averaged current density and the spatial averaged electric field. It is not possible to calculate the components of the effective conductivity tensor separately. But with a mathematical trick, Dykhne and Ruzin arrive at an expression which connects the Hall and the longitudinal effective conductivity:

$$(\sigma_H^e - \sigma_H^0)^2 + (\sigma_L^e)^2 = (\sigma_L^0)^2, \quad (1.50)$$

where, in the limit $\sigma_L(\mathbf{r}) \rightarrow 0$ (It is possible to give the general expressions, but they are lengthy.):

$$\sigma_H^0 = \frac{\sigma_H^{(2)} + \sigma_H^{(1)}}{2} \text{ and } \sigma_L^0 = \frac{|\sigma_L^{(2)} - \sigma_L^{(1)}|}{2}. \quad (1.51)$$

As $\sigma_H^{(1)}$ and $\sigma_H^{(2)}$ are the conductivities of two adjacent plateaus, their difference is $\frac{e^2}{h}$ and therefore the peak value of the longitudinal conductivity is predicted to be

$$\sigma_L^{peak} = \sigma_H^0 = \frac{e^2}{2h}. \quad (1.52)$$

It is remarkable, that this model predicts a finite value of the effective longitudinal conductivity σ_L^e even for vanishing local longitudinal conductivity $\sigma_L(\mathbf{r}) \rightarrow 0$, while models based on percolation theory predict a power law scaling of effective longitudinal conductivity with the local longitudinal conductivity $\sigma_L^e \propto \sigma_L^{1-\kappa}$ (see section 2.1 and 2.8) as saddle points are bottle-necks to the current. In the two phase model the local conductivity is non-differentiable and therefore saddle points do not exist.

1.12. Summary

This first chapter was an introduction to various aspects of the quantum Hall effect. After the description of the phenomenology, some historical remarks and a side note on the physical realization of two dimensional electron gases, an intuitive explanation of the quantum Hall effect was given: Constraining electrons to a two dimensional plan under a strong perpendicular magnetic field in presence of a disorder potential leads to an energy spectrum of broadened Landau levels containing mainly localized states. Only at the centers of the Landau levels there are delocalized states. As localized states do not contribute to global transport, they lead to the plateaus in the Hall conductivity and to extremely small longitudinal conductance values, while the delocalized states lead to the risers between the plateau and the peaks in the longitudinal conductance.

Afterwards, I gave an overview over some more sophisticated theories and their limitations. This part showed that the explanation of the quantum Hall effect is far from trivial and that many pieces of the puzzle are still to be found.

On the background of this introductory chapter, I will in the following chapters present my two pieces of the jigsaw puzzle: A transport theory for the high temperature regime of the quantum Hall effect and a determination of the transmission coefficient for tunneling over saddle points in ordinary two dimensional electron gases and in graphene based on the scattering of semi-coherent state wave packets.

2. Diagrammatic Approach for the Classical Percolation Regime of Quantum Hall Transitions

This chapter deals with transport in the high-temperature regime of the quantum Hall effect, where the thermal energy is higher than the typical fluctuations v_0 of the disorder potential ($k_B T \gg v_0$). We will calculate the conductance of systems like the one depicted in figure 2.1: A two dimensional electron gas under a strong perpendicular magnetic field and a smooth disorder potential, which fluctuates randomly in space. The research presented here has been published in [44] and [45].

We use a local conductivity approach, *i. e.* we suppose Ohm's law to be valid in its local form:

$$\mathbf{j}(\mathbf{r}) = \hat{\sigma}(\mathbf{r})\mathbf{E}(\mathbf{r}), \quad (2.1)$$

with \mathbf{j} the local current density, $\hat{\sigma}(\mathbf{r})$ the local conductivity tensor and \mathbf{E} the local electric field. The local conductivity model is justified if the temperature is high enough, that phase-breaking processes, such as electron-phonon scattering, occur on length scales that are shorter than the typical variations of the disorder potential. The determination of the local conductivity tensor $\hat{\sigma}$, presented in section 2.5, needs quantum mechanics. But once $\hat{\sigma}$ is known, the problem is a purely classical one and our task is to solve the continuity equation $\nabla \cdot \mathbf{j} = 0$ from classical electrodynamics. The random spatial fluctuations of the disorder potential, on which we have a closer look in section 2.4, lead to spatially fluctuating Hall components of the conductivity tensor. In an experiment, the local current density and the local electric field are not easily accessible. Therefore, we use an effective conductivity approach, presented

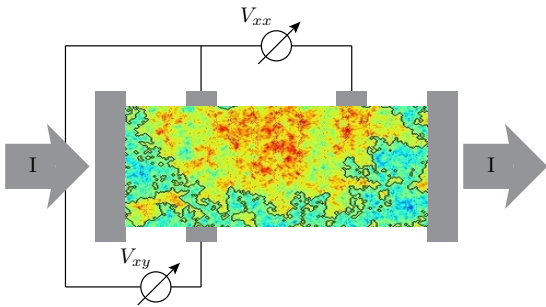


Figure 2.1: Sketch of the studied system: A disorder potential created by charge inhomogeneities leads to a spatially fluctuating local Hall conductivity represented by the color map. Our goal is to calculate the global conductance from the local conductivity.

in section 2.2, to calculate the effective conductivity $\hat{\sigma}_e$ defined as

$$\langle \mathbf{j} \rangle = \hat{\sigma}_e \langle \mathbf{E} \rangle, \quad (2.2)$$

where the brackets $\langle \dots \rangle$ denote a spatial average. The effective conductivity depends on the value of the Ohmic component of the conductivity tensor σ_0 . If the Ohmic component is large in comparison to the typical amplitude $\sqrt{\langle \delta\sigma^2 \rangle}$ of conductance fluctuations, the effective conductivity can be calculated perturbatively in $\sqrt{\langle \delta\sigma^2 \rangle}/\sigma_0$. Section 2.3 presents this perturbation theory in general and section 2.5 for the specific form of the conductivity tensor in the quantum Hall regime. However, quantum Hall samples are typically in the opposite regime of strong conductivity fluctuations and small σ_0 . The fluctuations of the Hall conductivity are of the order of $\sqrt{\langle \delta\sigma^2 \rangle} \sim 2e^2/\hbar$ in the spin degenerate case, while the local ohmic conductivity σ_0 is smaller than the effective longitudinal conductivity which is usually smaller than the conductance quantum e^2/h . Fits of experimental data with our theory show, that $\sigma_0 \ll \sigma_L < \sigma_H$ (see section 3.5.2). With the extrapolation technique described in 2.8, we are able to calculate the effective conductivity for the whole range from large to small σ_0 . In the limit $\sigma_0 \rightarrow 0$ the effective longitudinal conductivity σ_L^e vanishes with a critical exponent κ in the form of $\sigma_L^e = C \langle \delta\sigma^2 \rangle^{\frac{\kappa}{2}} \sigma_0^{1-\kappa}$. The value of the critical exponent has been conjectured by Simon and Halperin [2] and by Isichenko *et al.* [3] to be $\kappa = 10/13$. I will present their arguments in section 2.1. Our microscopic calculations confirm their conjecture.

2.1. Percolation Arguments for the Critical Exponent

In this section, I will explain the heuristic arguments which allowed Simon and Halperin [2] and Isichenko *et al.* [3] to conjecture the critical exponent κ . Isichenko *et al.* do not study a conductivity model, but the advection-diffusion equation in the stationary state $\nabla \cdot [n\mathbf{v}(x)] - D_0 \nabla^2 n = 0$, where n is a density, \mathbf{v} a velocity field and D_0 a diffusion coefficient. This equation could for example describe the distribution of sugar in a cup of coffee stirred with a teaspoon [46]. n would stand for the sugar concentration, \mathbf{v} would be the velocity field created by the teaspoon in the coffee and D_0 would be the molecular diffusion coefficient of sugar in coffee. The advection term $\nabla \cdot [n\mathbf{v}(x)]$ describes the passive motion of sugar molecules with the coffee, while the term $D_0 \nabla^2 n$ describes the diffusion. Alternatively, the advection-diffusion equation could describe the heat transport in the coffee. Then, n would be the local temperature, D_0 the thermal conductivity, the first summand would stand for heat transport by convection and the second summand for heat transport by heat conduction. The averaged version of the advection-diffusion equation reads $\nabla(\hat{D}_e \nabla N) = 0$, where N is the averaged density and \hat{D}_e the effective diffusivity. By identifying N with the electric potential and \hat{D}_e with the effective conductivity tensor, we see that this equation is equivalent to the continuity equation $\nabla \mathbf{j} = \nabla(\hat{\sigma}_e \nabla \phi) = 0$

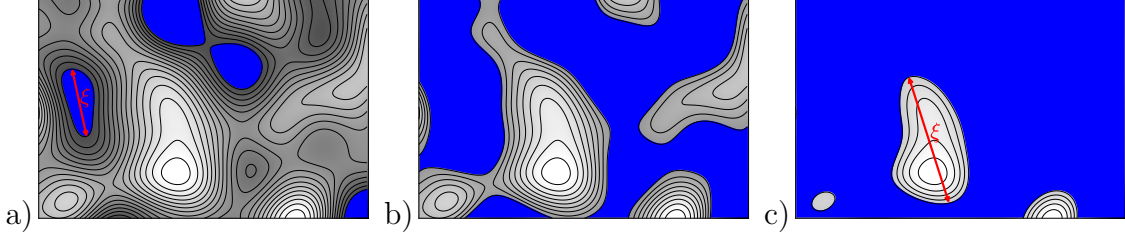


Figure 2.2.: a) The see level is below the percolation threshold. The correlation length ξ is given by the size of the largest lake. b) The see level is at the percolation threshold. There is one coastline which percolates the system. The correlation length ξ diverges. c) The see level is above the percolation threshold, the correlation length is given by the size of the largest island.

for the current density.

Simon and Halperin consider the critical exponent for the resistivity, not for the conductivity. But as the studied system is two dimensional and $\rho_H \gg \rho_L$

$$\sigma_L = \frac{\rho_L}{\rho_L^2 + \rho_H^2} \approx \frac{\rho_L}{\rho_H^2}, \quad (2.3)$$

i. e. conductivity and resistivity are proportional and will therefore have the same critical exponent.

The local resistivity tensor is supposed to have the form

$$\hat{\rho}(\mathbf{r}) = \begin{pmatrix} \rho_0 & \rho_H \\ -\rho_H & \rho_0 \end{pmatrix} + \begin{pmatrix} 0 & \delta\rho_H(\mathbf{r}) \\ -\delta\rho_H(\mathbf{r}) & 0 \end{pmatrix}, \quad (2.4)$$

where the diagonal part ρ_0 describes phenomenologically dissipative processes, such as scattering with phonons and short range impurities, ρ_H is the mean value of the Hall resistivity and $\delta\rho_H(\mathbf{r})$ the fluctuating, position dependent part with $\langle \delta\rho_H(\mathbf{r}) \rangle = 0$ and $\langle \delta\rho_H(\mathbf{r})\delta\rho_H(\mathbf{r}') \rangle = \lambda^2 g(|\mathbf{r} - \mathbf{r}'|)$.

The first important point is that in the regime of vanishing dissipation $\rho_0 \rightarrow 0$ the current is confined to lines of constant $\delta\rho_H(\mathbf{r})$. From the Maxwell equation $\nabla \times \mathbf{E} = 0$ with $\mathbf{E} = \hat{\rho}\mathbf{j}$ and current conservation $\nabla \cdot \mathbf{j} = 0$, we get the transport equation which describes our system.

$$-(\nabla\delta\rho_H) \cdot \mathbf{j} + \rho_0(\partial_x j_y - \partial_y j_x) = 0. \quad (2.5)$$

For small ρ_0 , we have $(\nabla\delta\rho_H) \cdot \mathbf{j} \approx 0$: The current is perpendicular to the gradient of the off-diagonal resistivity, *i. e.* the lines, on which current flows, are level lines $\delta\rho_H(\mathbf{r}) = \text{const.}$ This allows us to formulate a percolation problem in the sense of [47]: Are there, and at which energies, level lines percolating the whole system? This problem can be illustrated (see figure 2.2) by identifying the current flow lines with the shore lines produced by successively floating a hilly terrain $z = \delta\rho_H(\mathbf{r})$. For

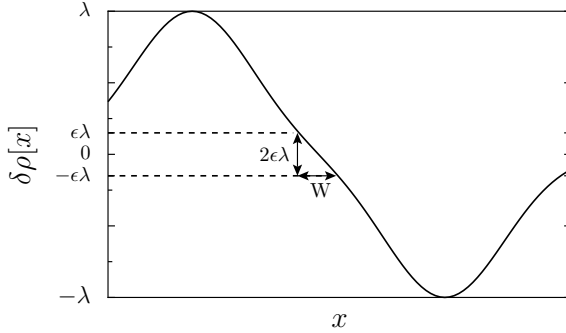


Figure 2.3: The quotient of the cut-off $\lambda\epsilon$ and the typical channel width W is proportional to typical slope of the conductance landscape $\lambda\epsilon/W \propto \lambda/a$.

low water levels, there will be mainly dry land with some lakes in it. For high water levels, there will be an ocean with some islands. At the transition point between dry land and ocean, there will be at least one coast line percolating the system. The Hall conductance fluctuations $\delta\rho_H(\mathbf{r})$ being defined symmetrically distributed about zero, the percolating contour line is at $\delta\rho_H(\mathbf{r}) = 0$.

As we are interested in the case where a small but finite value of ρ_0 leads to a finite width of the conducting channels, we choose a small cut-off ϵ and define all points $|\delta\rho_H(\mathbf{r})|/\lambda < \epsilon$ as belonging to the current carrying channels and all other points to be insulating.

Defining a as the typical length scale of the fluctuations in $\delta\rho_H$ and recalling that λ is the typical amplitude of the fluctuations in $\delta\rho_H$, the variations of $\delta\rho_H$ in one conductance channel are proportional to $\lambda\epsilon$ and the typical slope of the off-diagonal conductance landscape is λ/a . This allows us to connect the typical channel width W to the cut-off ϵ (see figure 2.3):

$$W \propto \epsilon a \quad (2.6)$$

In our percolation problem, the percolation length ξ is defined as the size (diameter) of the largest insulating island. ξ gives the typical distance between saddle points. Close to the percolation threshold ($\epsilon \rightarrow 0$), the correlation length ξ diverges as:

$$\xi \propto a\epsilon^{-\nu}. \quad (2.7)$$

The channel length s is the distance between two saddle points, following the conducting channel which snakes around the insulating island with diameter ξ .

$$s \propto a \left(\frac{\xi}{a} \right)^D \propto a\epsilon^{-\nu D}, \quad (2.8)$$

where D is the fractal dimension of the path.

The system is homogeneous on length scales larger than ξ , so it is enough to study a square of side length ξ . Since there is typically only one conducting path in such a square, the macroscopic longitudinal resistance of the square R_L is proportional

to the resistance of the conducting channel R_s . As resistance equals by definition resistivity times length divided by the cross section, we have

$$R_L \propto R_s \propto \frac{\tilde{\rho}s}{W}. \quad (2.9)$$

Studying the transport equation close to a saddle point will give us a second estimation of the typical channel width W . At a saddle point $\nabla\delta\rho_H = 0$ and close to a saddle point the expansion $\rho_H \approx xy \frac{\partial^2 \rho_H}{\partial_x \partial_y} \approx xy \frac{\lambda}{as}$ holds. Plugging this expression for ρ_{xy} into the transport equation (2.5) yields

$$-\tilde{y}j_x - \tilde{x}j_y + (\partial_{\tilde{x}}j_y - \partial_{\tilde{y}}j_x) = 0 \quad (2.10)$$

$$\text{with } \tilde{x} = \sqrt{\frac{\lambda}{\rho_0 as}}x, \quad \tilde{y} = \sqrt{\frac{\lambda}{\rho_0 as}}y. \quad (2.11)$$

This tells us, that $\mathbf{j} = \mathbf{j}(\tilde{x}, \tilde{y})$: Changes in the current profile occur on a typical length scale $\sqrt{\rho_0 as/\lambda}$, which is proportional to the channel width

$$W \propto \sqrt{\frac{\rho_0 sa}{\lambda}} \propto a \sqrt{\frac{\rho_0 \epsilon^{-\nu D}}{\lambda}}. \quad (2.12)$$

From the two estimations for the channel width, we get

$$\epsilon \propto \lambda^{-\frac{1}{2+\nu D}} \rho_0^{\frac{1}{2+\nu D}}. \quad (2.13)$$

With the definition

$$\kappa = 1 - \frac{1}{2 + \nu D} \quad (2.14)$$

the final result reads

$$R_L \propto \frac{\tilde{\rho}s}{W} \propto W \frac{\lambda}{a} \propto \epsilon \lambda \propto \lambda^\kappa \rho_0^{1-\kappa}. \quad (2.15)$$

For the case that the disorder has only one length scale, it is known that $\nu = 4/3$ [46] and it is believed that $D = 7/4$ [46], leading to the conjecture

$$\kappa = \frac{10}{13}. \quad (2.16)$$

This is a conjecture not a proof. First, not all of the above listed arguments are completely convincing. Second, the determination of the fractal dimension D depends on the assumption that its value for continuum percolation problems is identical to its value for site percolation problems. Third, Simon and Halperin [2] point out that D would change, if the current flow would not follow all the tiny wiggles of the conductivity landscape but readjust to cut off death ends.

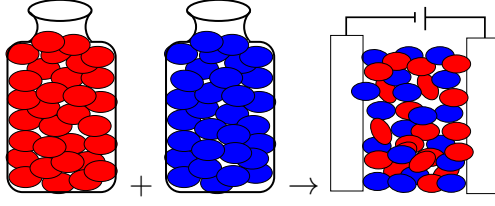


Figure 2.4: If grains of two different media with conductivity $\sigma^{(1)}$ and $\sigma^{(2)}$ are mixed, what is the effective conductivity σ_e of the mixture?

2.2. The Effective Medium Approach

If two granular media with different conductivities $\sigma^{(1)}$ and $\sigma^{(2)}$ are mixed in a certain fraction, as depicted in figure 2.4, what will be the effective conductivity of the mixture defined by equation (2.2)? This kind of question was a subject of active research at the beginning of the last century. As the method we use to study transport in the quantum Hall regime is closely related to the calculation of effective quantities for mixtures of granular media, let us start with the textbook method [48] to tackle this question. It has been explicitly applied to conductivity in [49] to study the critical behavior of resistivity close to ferromagnetic phase transitions.

Current-density, conductivity and the electric field are decomposed in an average part and a spatially fluctuating contribution:

$$\mathbf{j} = \mathbf{j}_0 + \delta\mathbf{j}(\mathbf{r}), \quad \sigma = \sigma_0 + \delta\sigma(\mathbf{r}), \quad \mathbf{E} = \mathbf{E}_0 + \delta\mathbf{E}(\mathbf{r}). \quad (2.17)$$

The mean value for the current density is:

$$\mathbf{j}_0 = \langle (\sigma_0 + \delta\sigma(\mathbf{r}))(\mathbf{E}_0 + \delta\mathbf{E}(\mathbf{r})) \rangle = \sigma_0\mathbf{E}_0 + \langle \delta\sigma(\mathbf{r})\delta\mathbf{E}(\mathbf{r}) \rangle \quad (2.18)$$

as by definition $\langle \delta\sigma(\mathbf{r}) \rangle = 0$, $\langle \delta\mathbf{E}(\mathbf{r}) \rangle = 0$ if the mean value is taken over the entire volume of the sample. The spatially fluctuating part of the current density is given by:

$$\delta\mathbf{j}(\mathbf{r}) = \delta\sigma(\mathbf{r})\mathbf{E}_0 + \sigma_0\delta\mathbf{E}(\mathbf{r}). \quad (2.19)$$

As $\nabla \cdot (\mathbf{j}_0 + \delta\mathbf{j}) = 0$ by the continuity equation and as the divergence of the constant vector \mathbf{j}_0 is zero, also

$$0 = \nabla \cdot \delta\mathbf{j} = \sigma_0 \nabla \cdot \delta\mathbf{E} + \mathbf{E}_0 \cdot \nabla \delta\sigma(\mathbf{r}). \quad (2.20)$$

The variations of σ occur on a macroscopic length scale, the size of the grains, while the fluctuations of the electric field $\mathbf{E}(\mathbf{r})$ occur on microscopic length scales. We average equation (2.20) over a region where $\delta\sigma(\mathbf{r})$ is constant. To distinguish this average over a small region, from the average over the whole volume, we denote it by a dash

$$\sigma_0 \nabla \cdot \overline{\delta\mathbf{E}} = -\mathbf{E}_0 \nabla \overline{\delta\sigma(\mathbf{r})}. \quad (2.21)$$

Supposing the fluctuations of the electric field to be isotropic on the length scale of the fluctuations of the conductivity leads to $\nabla \delta \mathbf{E} = 3\partial \delta E_x / \partial x = 3\partial \delta E_y / \partial y = 3\partial \delta E_z / \partial z$. Let, without loss of generality, the mean electric field \mathbf{E}_0 point in x-direction yielding

$$3\sigma_0 \frac{\partial \delta E_x}{\partial x} = -E_{0x} \frac{\partial \delta \sigma(\mathbf{r})}{\partial x}. \quad (2.22)$$

Integration leads to

$$3\sigma_0 \delta E_x = -E_{0x} \delta \sigma(\mathbf{r}). \quad (2.23)$$

As the direction of the electric field was chosen arbitrarily, this equation holds also as vector equation.

$$\delta \mathbf{E} = -\frac{\mathbf{E}_0}{3\sigma_0} \delta \sigma(\mathbf{r}). \quad (2.24)$$

This result allows us to calculate the average in equation (2.18):

$$\langle \delta \sigma(\mathbf{r}) \delta \mathbf{E}(\mathbf{r}) \rangle = \langle \delta \sigma(\mathbf{r}) \overline{\delta \mathbf{E}(\mathbf{r})} \rangle = -\frac{\mathbf{E}_0}{3\sigma_0} \langle [\delta \sigma(\mathbf{r})]^2 \rangle \quad (2.25)$$

and leads to the effective conductivity

$$\sigma_e = \sigma_0 - \frac{\langle [\delta \sigma(\mathbf{r})]^2 \rangle}{3\sigma_0}. \quad (2.26)$$

This means for example for a 50-50 random mixture where $\delta \sigma = (\sigma^{(1)} - \sigma^{(2)})/2$, the effective conductivity is $\sigma_e = \sigma_0 - (\sigma^{(1)} - \sigma^{(2)})^2 / (12\sigma_0)$, which holds as long as $|\sigma^{(1)} - \sigma^{(2)}| \ll \sigma_0$.

The effective medium approach presented so far has two drawbacks. First, for the derivation the granularity of the media is explicitly needed, and second, it would be tedious to calculate higher order corrections of the effective conductivity with this method. We want to study a system at high temperature, where the conductivity fluctuations are continuous. Also, we want to leave the regime of weak fluctuations, where first order perturbation theory is sufficient. Therefore, we use a Green's function version of the effective medium approach, developed by Stroud [1], which can handle continuous fluctuations and where high order correction terms are easily generated. A similar formalism was developed in [50]. As field of application for their formalism, the authors of both references had polycrystalline materials in mind. The effective conductivity under an applied magnetic field is one subject amongst others in [1] and the core subject of [50]. But, as the quantum Hall effect was not yet discovered when those papers were written, they concentrated on the three dimensional case. The conductivity fluctuations they study do not occur in one medium, but are a consequence of the medium being polycrystalline.

We study a sample with d dimensional volume V , bounded by a surface S . Due to disorder, its conductivity tensor $\hat{\sigma}(\mathbf{r})$ is spatially varying. Locally, the current density is $\mathbf{j}(\mathbf{r}) = \hat{\sigma}(\mathbf{r})\mathbf{E}(\mathbf{r})$. As in most cases only the current, the integral over the current density, is experimentally accessible, it is enough to know the average current density $\langle \mathbf{j} \rangle$. Let us imagine, that a constant electric field \mathbf{E}_0 is applied at the boundary of our sample. Then the average current density is connected to this constant field by an effective position independent conductivity tensor $\hat{\sigma}_e$:

$$\langle \mathbf{J} \rangle = \langle \hat{\sigma}(\mathbf{r})\mathbf{E}(\mathbf{r}) \rangle \equiv \hat{\sigma}_e \mathbf{E}_0 = \hat{\sigma}_e \langle \mathbf{E} \rangle. \quad (2.27)$$

The effective conductivity is, up to a geometric factor, the conductance. We decompose $\hat{\sigma}(\mathbf{r})$ in a constant and in a position dependent part

$$\hat{\sigma}(\mathbf{r}) = \hat{\sigma}_0 + \delta\hat{\sigma}(\mathbf{r}). \quad (2.28)$$

At this stage, the decomposition is arbitrary. Later, it will be convenient to choose $\hat{\sigma}_0$ as the average conductivity. Expressing the electric field by its potential $\mathbf{E}(\mathbf{r}) = -\nabla\Phi(\mathbf{r})$ and plugging the constitutional equation $\mathbf{J} = \hat{\sigma}(\mathbf{r})\mathbf{E}(\mathbf{r})$ into the continuity equation $\nabla \cdot \mathbf{J} = 0$, we get

$$\nabla \cdot [\hat{\sigma}(\mathbf{r})\nabla\Phi(\mathbf{r})] = 0, \quad (2.29)$$

which leads with (2.28) to the boundary value problem

$$\nabla \cdot [\hat{\sigma}_0 \nabla\Phi(\mathbf{r})] = -\nabla \cdot [\delta\hat{\sigma}(\mathbf{r})\nabla\Phi(\mathbf{r})] \text{ in } V \quad (2.30)$$

$$\Phi(\mathbf{r}) = \Phi_0(\mathbf{r}) \equiv -\mathbf{E}_0 \cdot \mathbf{r} \text{ on } S. \quad (2.31)$$

We solve this boundary value problem formally with the Green's function $G(\mathbf{r}, \mathbf{r}')$ defined by

$$\nabla \cdot \hat{\sigma}_0 \cdot \nabla G(\mathbf{r}, \mathbf{r}') = -\delta(\mathbf{r} - \mathbf{r}') \text{ in } V, \quad (2.32)$$

$$G(\mathbf{r}, \mathbf{r}') = 0, \text{ for } \mathbf{r}' \text{ on } S. \quad (2.33)$$

Now, we can express the potential $\Phi(\mathbf{r})$ as

$$\Phi(\mathbf{r}) = \Phi_0(\mathbf{r}) + \int_V d^d r' G(\mathbf{r}, \mathbf{r}') \nabla' \cdot \delta\hat{\sigma}(\mathbf{r}') \cdot \nabla' \Phi(\mathbf{r}') \quad (2.34)$$

with the shorthand notation $\nabla' = \nabla_{\mathbf{r}'}$. Integration by parts using $\nabla' G(\mathbf{r}, \mathbf{r}') = -\nabla G(\mathbf{r}, \mathbf{r}')$ and taking the gradient on both sides leads to

$$\begin{aligned} \mathbf{E}(\mathbf{r}) &= \mathbf{E}_0 + \int_V d^d r' \nabla \cdot (\nabla G(\mathbf{r}, \mathbf{r}') \cdot \delta\hat{\sigma}(\mathbf{r}') \cdot \mathbf{E}(\mathbf{r}')) \\ &= \mathbf{E}_0 + \int_V d^d r' \hat{\mathcal{G}}_0(\mathbf{r}, \mathbf{r}') \cdot \delta\hat{\sigma}(\mathbf{r}') \cdot \mathbf{E}(\mathbf{r}'), \end{aligned} \quad (2.35)$$

where $^1 \left[\hat{\mathcal{G}}_0 \right]_{ij} = \frac{\partial}{\partial r_i} \frac{\partial}{\partial r_j} G(\mathbf{r}, \mathbf{r}')$. Multiplication of (2.35) by $\delta\hat{\sigma}$ from the left hand side and introduction of the tensor $\hat{\chi}$ defined by $\delta\hat{\sigma}(\mathbf{r})\mathbf{E}(\mathbf{r}) = \hat{\chi}(\mathbf{r})\mathbf{E}_0$ leads to

$$\hat{\chi}(\mathbf{r})\mathbf{E}_0 = \delta\hat{\sigma}(\mathbf{r})\mathbf{E}_0 + \delta\hat{\sigma}(\mathbf{r}) \int_V d^d r' \hat{\mathcal{G}}_0(\mathbf{r}, \mathbf{r}') \hat{\chi}(\mathbf{r}')\mathbf{E}_0. \quad (2.36)$$

As equation (2.36) is valid for all possible directions of \mathbf{E}_0 , the following self-consistent matrix equation also holds:

$$\hat{\chi}(\mathbf{r}) = \delta\hat{\sigma}(\mathbf{r}) + \delta\hat{\sigma}(\mathbf{r}) \int_V d^d r' \hat{\mathcal{G}}_0(\mathbf{r}, \mathbf{r}') \hat{\chi}(\mathbf{r}'). \quad (2.37)$$

Spatial averaging of the current $\mathbf{j}(\mathbf{r}) = [\hat{\sigma}_0 + \hat{\chi}(\mathbf{r})]\mathbf{E}_0$ over conductivity fluctuations $\delta\hat{\sigma}(\mathbf{r})$ leads therefore to the effective conductivity

$$\hat{\sigma}_e = \hat{\sigma}_0 + \langle \hat{\chi} \rangle. \quad (2.38)$$

In the limit of an infinite sample $V \rightarrow \infty$ the Green's function which solves ² the boundary value problem (2.32) is

$$G(\mathbf{r}, \mathbf{r}') = \int \frac{d^d p}{(2\pi)^d} \frac{e^{i\mathbf{p} \cdot (\mathbf{r} - \mathbf{r}')}}{\mathbf{p} \hat{\sigma}_0 \mathbf{p} + 0^+} \quad (2.39)$$

where 0^+ is a small positive quantity which ensures $G \rightarrow 0$ for $|\mathbf{r}| \rightarrow \infty$ as asked by the boundary condition ³ (2.33).

2.3. Systematic Expansion at Strong Dissipation

The tensor $\hat{\chi}$ is given by the self-consistent equation (2.37). Iteration of this equation leads to a development in powers of $\delta\sigma/\sigma_0$, as the free Green's function $\hat{\mathcal{G}}_0$

1. Sign error in equation (2.10) of reference [1].
2. $\nabla \cdot \hat{\sigma}_0 \cdot \nabla G(\mathbf{r}) = \nabla \cdot \hat{\sigma}_0 \cdot \nabla \int \frac{d^d p}{(2\pi)^d} \frac{e^{i\mathbf{p} \cdot \mathbf{r}}}{\mathbf{p} \hat{\sigma}_0 \mathbf{p} + i0^+} = \nabla \cdot \hat{\sigma}_0 \cdot \int \frac{d^d p}{(2\pi)^d} \frac{i\mathbf{p} e^{i\mathbf{p} \cdot \mathbf{r}}}{\mathbf{p} \hat{\sigma}_0 \mathbf{p} + i0^+} = \int \frac{d^d p}{(2\pi)^d} \frac{-\mathbf{p} \cdot \hat{\sigma}_0 \cdot \mathbf{p} e^{i\mathbf{p} \cdot \mathbf{r}}}{\mathbf{p} \hat{\sigma}_0 \mathbf{p} + i0^+} = - \int \frac{d^d p}{(2\pi)^d} e^{i\mathbf{p} \cdot \mathbf{r}} = -\delta(\mathbf{r})$.
3. Without loss of generality, let us choose $\mathbf{r} = (r_1, 0, \dots, 0)$ and take the limit $r_1 \rightarrow \infty$. As conductivity tensors are anti-symmetric with positive diagonal elements: $\lim_{r_1 \rightarrow \infty} G(\mathbf{r}) = \lim_{r_1 \rightarrow \infty} \prod_{n=2}^d \int \frac{dp_n}{2\pi} \int \frac{dp_1}{2\pi} \frac{e^{ip_1 r_1}}{\mathbf{p} \hat{\sigma}_0 \mathbf{p} + 0^+} = \lim_{r_1 \rightarrow \infty} \prod_{n=2}^d \int \frac{dp_n}{2\pi} \int \frac{dp_1}{2\pi} \frac{e^{ip_1 r_1}}{p_1^2 (\sigma_0)_{1,1} + \sum_{\alpha=2}^d p_\alpha^2 (\sigma_0)_{\alpha\alpha} + 0^+}$. The denominator has singular points at $p_1 = \pm i \left(\sqrt{\sum_{\alpha=2}^d p_\alpha^2 (\sigma_0)_{\alpha\alpha}} + 0^+ \right)$ and the integral can be done with the residue theorem: $\lim_{r_1 \rightarrow \infty} G(\mathbf{r}) = \lim_{r_1 \rightarrow \infty} \prod_{n=2}^d \int \frac{dp_n}{2\pi} \frac{e^{-\left(\sqrt{\sum_{\alpha=2}^d p_\alpha^2 (\sigma_0)_{\alpha\alpha}} + 0^+ \right) r_1}}{2 \sum_{\alpha=2}^d p_\alpha^2 (\sigma_0)_{\alpha\alpha} + 0^+}$. After the change of variables $p'_n = p_n r_1$, we see that the boundary condition (2.33) is fulfilled: $\lim_{r_1 \rightarrow \infty} G(\mathbf{r}) = \lim_{r_1 \rightarrow \infty} e^{-0^+ r_1} \prod_{n=2}^d \int \frac{dp'_n}{2\pi} \frac{e^{-\left(\sqrt{\sum_{\alpha=2}^d p_\alpha'^2 (\sigma_0)_{\alpha\alpha}} \right)}}{2 \sum_{\alpha=2}^d p_\alpha'^2 (\sigma_0)_{\alpha\alpha} + 0^+} = 0$.

is proportional to $1/\sigma_0$:

$$\begin{aligned}\hat{\chi}(\mathbf{r}) = & \delta\hat{\sigma}(\mathbf{r}) + \delta\hat{\sigma}(\mathbf{r}) \int_V d^d r_1 \hat{\mathcal{G}}_0(\mathbf{r}, \mathbf{r}_1) \delta\hat{\sigma}(\mathbf{r}_1) \\ & + \delta\hat{\sigma}(\mathbf{r}) \int_V d^d r_1 \int_V d^d r_2 \hat{\mathcal{G}}_0(\mathbf{r}, \mathbf{r}_1) \delta\hat{\sigma}(\mathbf{r}_1) \hat{\mathcal{G}}_0(\mathbf{r}_1, \mathbf{r}_2) \delta\hat{\sigma}(\mathbf{r}_2) + \dots\end{aligned}\quad (2.40)$$

To simplify the notation, we introduce the Feynman-Diagrams

$$\hat{\mathcal{G}}_0(\mathbf{r} - \mathbf{r}_1) = \underset{\mathbf{r}}{\bullet} \text{---} \underset{\mathbf{r}_1}{\bullet} \quad \text{and} \quad \delta\hat{\sigma}(\mathbf{r}) = \underset{\mathbf{r}}{\bullet} \text{---} \quad (2.41)$$

With the convention to integrate over the \mathbf{r}_n , the expansion (2.40) can be graphically represented by

$$\hat{\chi}(\mathbf{r}) = \underset{\mathbf{r}}{\bullet} \text{---} + \underset{\mathbf{r}}{\bullet} \text{---} \underset{\mathbf{r}_1}{\bullet} + \underset{\mathbf{r}}{\bullet} \text{---} \underset{\mathbf{r}_1}{\bullet} \text{---} \underset{\mathbf{r}_2}{\bullet} + \underset{\mathbf{r}}{\bullet} \text{---} \underset{\mathbf{r}_1}{\bullet} \text{---} \underset{\mathbf{r}_2}{\bullet} \text{---} \underset{\mathbf{r}_3}{\bullet} + \dots\quad (2.42)$$

Even though our final goal is the conductivity tensor in the quantum Hall regime, let us first study a purely resistive and isotropic medium to illustrate the method. In this case, the conductivity tensor is diagonal and $\hat{\sigma}_0 = \sigma_0 \mathbb{1}$, $\delta\hat{\sigma}(\mathbf{r}) = \delta\sigma(\mathbf{r}) \mathbb{1}$. We choose σ_0 to be the average conductivity, so that $\langle \delta\sigma(\mathbf{r}) \rangle = 0$. In the limit of strong dissipation compared to the typical fluctuations of conductivity ($\sigma_0 \gg \sqrt{\langle \delta\sigma^2 \rangle}$), we can truncate equation (2.40) after the second order and get for the effective conductivity $\hat{\sigma}_e = \sigma_{xx} \mathbb{1}$ with

$$\begin{aligned}\sigma_{xx} = & \sigma_0 - \frac{1}{\sigma_0} \int d^d r \int \frac{d^d p}{(2\pi)^d} \frac{p_x^2 e^{i\mathbf{p}\cdot\mathbf{r}}}{\mathbf{p}^2 + 0^+} \langle \delta\sigma(\mathbf{r}) \delta\sigma(\mathbf{0}) \rangle \\ = & \sigma_0 - \frac{1}{\sigma_0} \int d^d r \frac{\delta(\mathbf{r})}{d} \langle \delta\sigma(\mathbf{r}) \delta\sigma(\mathbf{0}) \rangle = \sigma_0 - \frac{\langle \delta\sigma^2 \rangle}{d\sigma_0}.\end{aligned}\quad (2.43)$$

We recover thus equation (2.26).

The Green's function formulation of the effective medium problem is immediately appealing, because arbitrary orders of the strong-dissipation expansion can be generated in a compact fashion (equation (2.42)). In the diagonal case where $\delta\hat{\sigma}(\mathbf{r}) = \delta\sigma(\mathbf{r}) \mathbb{1}$, the fluctuating part of the conductivity commutes with the free Green's function $\hat{\mathcal{G}}_0$, and we can extract the Green's functions from the averages.

$$\begin{aligned}\langle \hat{\chi}(\mathbf{r}) \rangle = & \langle \delta\sigma(\mathbf{r}) \rangle \mathbb{1} + \int d^2 \mathbf{r}_1 \langle \delta\sigma(\mathbf{r}) \delta\sigma(\mathbf{r}_1) \rangle \hat{\mathcal{G}}_0(\mathbf{r}, \mathbf{r}_1) \\ & + \int d^2 \mathbf{r}_1 \int d^2 \mathbf{r}_2 \langle \delta\sigma(\mathbf{r}) \delta\sigma(\mathbf{r}_1) \delta\sigma(\mathbf{r}_2) \rangle \hat{\mathcal{G}}_0(\mathbf{r}, \mathbf{r}_1) \hat{\mathcal{G}}_0(\mathbf{r}_1, \mathbf{r}_2) + \dots\end{aligned}\quad (2.44)$$

If the sample is self averaging, we can replace the spatial average by an ensemble average. If in addition the fluctuations of the conductivity follow a Gaussian distribution, these averages can be calculated by contracting the different $\delta\hat{\sigma}(\mathbf{r})$ using Wick's theorem. In section 2.4, I will argue, why the conductivity fluctuations in a quantum Hall sample are often well described by a Gaussian distribution. In our graphical representation, we denote these contractions by joining the curly lines and get for example:

$$\begin{aligned} \langle \{ \quad \} \rangle &= \text{diagram with two curly lines connected by a wavy line} \\ \langle \{ \quad \} \{ \quad \} \rangle &= \text{diagram with two pairs of curly lines connected by two wavy lines} + \text{diagram with two pairs of curly lines connected by two wavy lines in a different topology} + \text{diagram with two pairs of curly lines connected by two wavy lines in a third topology} \end{aligned} \quad (2.45)$$

Odd moments of Gaussian distributions are zero and therefore the odd orders of the development of $\hat{\chi}$ do not contribute. A second simplification comes from the fact that all particle reducible diagrams (diagrams that can be split in two parts by cutting a single line of $\hat{\mathcal{G}}_0$) are identically zero. Taking the volume integrals is equivalent to studying the Fourier transformed diagrams at zero momentum. Particle reducible diagrams contain a factor $[\hat{\mathcal{G}}_0]_{ij}(\mathbf{p} = 0) = 0$ and are therefore zero.

2.4. Form of the Potential Correlations

Already in the last section, and for all following calculations, the disorder potential is chosen to be Gaussian distributed with Gaussian shaped pair correlator. In this section, I give some arguments for this choice beside the obvious one, that it is very convenient for analytical calculations.

First, a Gaussian-type random potential reflects the physical reality of a potential created by a large number of weak, randomly distributed scattering sources [51]. As we will see in the next paragraph, this can on theoretical grounds be understood from a functional form of the central limit theorem. Second, even for samples where the impurity density is too low to class the disorder potential automatically in the category of “created by a large number of weak scattering sources”, the experimental findings suggest a Gaussian distribution. As an example recall figure 1.6b which shows the density of states obtained by a scanning tunneling microscope measurement [29]. The energy of an electron being essentially given by its Landau level energy plus the average over the potential energy of the area over which the cyclotron motion of the electron is spread, the shape of the density of states reflects the shape of the potential distribution. Finally, one of our main goals is to calculate a percolation critical exponent. It is generally believed, that the exact form of the potential is not relevant for this kind of calculations [52].

Let us see how the Gaussian character of the potential correlations arises as a consequence of a functional form of the central limit theorem: Let $u(\mathbf{r} - \mathbf{r}_i)$ be the potential in the plane of the electron gas at position \mathbf{r} created by the donor atom

2. The Classical Percolation Regime of Quantum Hall Transitions

at position (\mathbf{r}_i, z) and let $P_{\mathbf{u}}(\mathbf{r}_i) = 1/L^2$ be the probability distribution for finding an impurity at position \mathbf{r}_i , where L^2 is the surface of our sample. We choose L^2 to be large enough to ignore boundary effects, but finite so that N impurities lead to a finite total potential. The total potential $V(\mathbf{r})$, we are interested in, is given by the sum over the potential created by all impurities. To simplify calculations, we chose the origin of energy in a way, that the mean value of the total potential is zero, leading to

$$V(\mathbf{r}) = \sum_{i=1}^N u(\mathbf{r} - \mathbf{r}_i) - N\langle u \rangle. \quad (2.46)$$

The probability density P_V for $V(\mathbf{r})$ is given by the functional integral:

$$\begin{aligned} P[V(\mathbf{x})] &= \prod_{i=1}^N \int \frac{d^2 r_i}{L^2} \delta \left(V(\mathbf{x}) - \sum_j^N [u(\mathbf{x} - \mathbf{r}_j) - \langle u \rangle] \right) \\ &= \prod_{i=1}^N \int \frac{d^2 r_i}{L^2} \int \mathcal{D}\lambda \, e^{i \int d^2 r \lambda(\mathbf{r}) (V(\mathbf{x} - \mathbf{r}) - \sum_j^N [u(\mathbf{x} - \mathbf{r} - \mathbf{r}_j) - \langle u \rangle])} \\ &= \int \mathcal{D}\lambda \, e^{i \int d^2 r \lambda(\mathbf{r}) V(\mathbf{x} - \mathbf{r})} \left[\int \frac{d^2 r'}{L^2} e^{-i \int d^2 r \lambda(\mathbf{r}) [u(\mathbf{x} - \mathbf{r} - \mathbf{r}') - \langle u \rangle]} \right]^N \\ &= \int \mathcal{D}\lambda \, e^{i \int d^2 r \lambda(\mathbf{r}) V(\mathbf{x} - \mathbf{r}) + N \log \left[\int \frac{d^2 r'}{L^2} e^{-i \int d^2 r \lambda(\mathbf{r}) [u(\mathbf{x} - \mathbf{r} - \mathbf{r}') - \langle u \rangle]} \right]}. \end{aligned} \quad (2.47)$$

Using the saddle point method, we neglect terms which are higher than quadratic order in λ leading to a Gaussian distribution. The error estimation for this step follows bellow.

$$\begin{aligned} P[V(\mathbf{x})] &= \int \mathcal{D}\lambda \, e^{i \int d^2 r \lambda(\mathbf{r}) V(\mathbf{x} - \mathbf{r}) - \frac{1}{2} N \int \frac{d^2 r'}{L^2} \int d^2 r_1 \int d^2 r_2 \lambda(\mathbf{r}_1) \lambda(\mathbf{r}_2) u(\mathbf{x} - \mathbf{r}_1 - \mathbf{r}') u(\mathbf{x} - \mathbf{r}_2 - \mathbf{r}')} \\ &= \frac{1}{\sqrt{\det[c(\mathbf{r}_1 - \mathbf{r}_2)]}} e^{\frac{1}{2} \int d^2 r_1 \int d^2 r_2 V(\mathbf{r}_1 - \mathbf{r}') V(\mathbf{r}_2 - \mathbf{r}') c^{-1}(\mathbf{r}_1 - \mathbf{r}_2)}, \end{aligned} \quad (2.48)$$

$$\text{with } c(\mathbf{r}_1 - \mathbf{r}_2) = N \int \frac{d^2 r'}{L^2} u(\mathbf{r}_1 - \mathbf{r}') u(\mathbf{r}_2 - \mathbf{r}'). \quad (2.49)$$

The potential u , created by the ionized donor atoms, is a screened coulomb potential. In samples where the distance d between the donor atoms and the plane of the electron gas is large compared to the screening length $\xi_s = \sqrt{\xi_0^2 + 2l_B^2}$ (often $10\text{nm} < d < 100\text{nm}$ and $\xi_0 \approx 5\text{nm}$ [53], the term $2l_B^2$ takes into account that the potential has to be averaged over the region over which the wave function is spread)

the screened Coulomb potential can be well approximated by a Gaussian potential:

$$\begin{aligned} u(\mathbf{r}, z=0) &= A \frac{1}{\sqrt{d^2 + (\mathbf{r} - \mathbf{r}')^2}} e^{-\frac{\sqrt{d^2 + (\mathbf{r} - \mathbf{r}')^2}}{\xi_0}} \\ &\approx \frac{A}{d} \frac{1}{1 + \frac{(\mathbf{r} - \mathbf{r}')^2}{d^2}} e^{-\frac{d}{\xi_s}} e^{-\frac{(\mathbf{r} - \mathbf{r}')^2}{2d\xi_0}} \approx B e^{-\frac{(\mathbf{r} - \mathbf{r}')^2}{\xi'^2}} \end{aligned} \quad (2.50)$$

$$\text{with } \xi'^2 = 2d\xi_s = 2d\sqrt{s_0^2 + 2l_B^2} \quad (2.51)$$

If u is a Gaussian, the correlation function c is, as a convolution of two Gaussians, also a Gaussian with correlation length $a = \sqrt{2}\xi'$.

To estimate the error we made in neglecting terms higher than quadratic order in λ , we study the ratio of the third and the second moment of V at coinciding points, where it can be evaluated exactly. At coinciding points, we can treat V as a normal probability variable, and for the n -th cumulant κ_n of V holds, as cumulants are additive,

$$\kappa_n(V) = \kappa_n \left(\sum_{i=1}^N (u(\mathbf{r}_i) - \langle u \rangle) \right) = N \kappa_n(u - \langle u \rangle). \quad (2.52)$$

As V has zero mean value, the second and third cumulants are identical to the second and third moments, and

$$\frac{\langle V^3 \rangle}{\langle V^2 \rangle^{\frac{3}{2}}} = \frac{\kappa_3(V)}{[\kappa_2(V)]^{\frac{3}{2}}} = \frac{N \kappa_3(u - \langle u \rangle)}{N^{\frac{3}{2}} [\kappa_2(u - \langle u \rangle)]^{\frac{3}{2}}}. \quad (2.53)$$

For u given by equation (2.50) and impurity density $n = N/L^2$, we can calculate these cumulants and take the thermodynamic limit

$$nL^2 \kappa_3(u - \langle u \rangle) \xrightarrow{L \rightarrow \infty} \frac{\pi}{3} B^3 n \xi'^2 \quad (2.54)$$

$$nL^2 \kappa_2(u - \langle u \rangle) \xrightarrow{L \rightarrow \infty} \frac{\pi}{2} B^2 n \xi'^2, \quad (2.55)$$

leading to the final result

$$\frac{\langle V^3 \rangle}{\langle V^2 \rangle^{\frac{3}{2}}} \approx \frac{1}{3} \sqrt{\frac{2}{\pi n \xi'^2}} \approx \frac{1}{3} \sqrt{\frac{4}{\pi n a^2}}. \quad (2.56)$$

The potential fluctuations are in good approximation Gaussian correlated, if the impurity density in units of the correlation length of the potential is large. This can be achieved in high density, high mobility samples. In the sample we study in the next chapter $d = 10\text{nm}$ leading with $\xi_0 \approx 5\text{nm}$ [53] at 2T to $\xi' \approx 20\text{nm}$. If we suppose the impurity density to equal the carrier density, $n = 4 \cdot 10^{11}\text{cm}^{-2}$ and $\langle V^3 \rangle / \langle V^2 \rangle^{\frac{3}{2}} \approx 0.2$ which is reasonably small.

2.5. Application to the Quantum Hall Effect

In this section, we come back to our initial problem and apply the above developed formalism to the quantum Hall effect. The conductivity tensor in this system has, after decomposition in a spatially constant and in a spatially fluctuating part, the form

$$\hat{\sigma}(\mathbf{r}) = \begin{pmatrix} \sigma_0 & -\sigma_H \\ \sigma_H & \sigma_0 \end{pmatrix} + \begin{pmatrix} 0 & -\delta\sigma(\mathbf{r}) \\ \delta\sigma(\mathbf{r}) & 0 \end{pmatrix} \quad (2.57)$$

if we assume that only the off-diagonal elements fluctuate. As $\sigma_0 \ll \sigma_H$, the neglect of fluctuations in the diagonal component is justified.

The diagonal part describes phenomenologically all dissipative processes, especially scattering with phonons. We suppose it to be space independent. This does not exclude a dependence on temperature, the magnetic field, *etc.* (see section 3.1).

To get the off-diagonal part of the conductivity tensor, we use linear response theory, *i. e.* we suppose that the conductivity which connects the current density in response to the external electric field \mathbf{E}_0 is the same as the conductivity which connects the equilibrium current density to gradients of the disorder potential $(-\nabla V(\mathbf{r}))$.

Let us first have a look at the local equilibrium current density for the case of the linear potential we studied in chapter 1. We read from equation (1.28) that every filled state carries a current density proportional to the drift velocity:

$$\mathbf{j}_m(\mathbf{r}) = e\mathbf{v}_d = ec \frac{\mathbf{E} \times \mathbf{u}_z}{B}. \quad (2.58)$$

The local equilibrium current density is the sum of the contributions of all filled Landau levels. Due to the disorder potential, the density of filled states is position dependent $n_e = n_e(\mathbf{r})$ and

$$\mathbf{j}^{\text{eq}}(\mathbf{r}) = n_e(\mathbf{r})\mathbf{j}_m(\mathbf{r}) = n_e(\mathbf{r})ec \frac{\mathbf{E} \times \mathbf{B}}{B^2}. \quad (2.59)$$

We read the Hall conductivity from the equilibrium current density:

$$\sigma_H(\mathbf{r}) = \frac{|e|cn_e(\mathbf{r})}{B} = \frac{e^2}{h} \frac{n_e(\mathbf{r})}{2\pi l_B} = \frac{e^2}{h} \nu(\mathbf{r}). \quad (2.60)$$

The position dependent filling factor $\nu(\mathbf{r})$ can be expressed as a sum over Fermi-functions with the local energy. In the limit of $l_B \rightarrow 0$ the local energy is $E_m(\mathbf{r}) = E_m + V(\mathbf{r})$ (see equation (1.22)). This leads to the final expression

$$\sigma_H(\mathbf{r}) = \frac{e^2}{h} \sum_m n_F(E_m + V(\mathbf{r}) - \mu), \quad (2.61)$$

where n_F is the Fermi-distribution. This derivation of the current density is strictly spoken only valid in the case of a disorder potential with purely linear position

dependance. But the final result is in the limit $l_B \ll \xi$ valid for arbitrary disorder configurations. It can be derived more rigorously using a gradient expansion of the local potential controlled by the magnetic length l_B . This is done in reference [9] with the vortex Green's function method (see section 4.2) and in reference [35] with a Green's function formalism where the gauge is chosen in a way that the vector potential is perpendicular to the local gradient of the potential. As discussed in section 2.4, we choose a Gaussian distribution for the smooth potential of disorder $V(\mathbf{r})$:

$$\langle V(\mathbf{r})V(\mathbf{r}') \rangle = v_0^2 e^{-\frac{|\mathbf{r}-\mathbf{r}'|}{a^2}} \quad (2.62)$$

which is thus characterized by the energy scale v_0 and the length scale a . In the regime $k_B T \gg \sqrt{\langle V^2 \rangle}$ we can linearize equation (2.61) and get

$$\sigma_H(\mathbf{r}) = \sigma_H + \delta\sigma_H(\mathbf{r}) \approx \frac{e^2}{h} \sum_m n_F(E_m - \mu) + V(\mathbf{r}) \frac{e^2}{h} \sum_m n'_F(E_m - \mu). \quad (2.63)$$

Therefore, the correlations between conductivity fluctuations are

$$\langle \delta\sigma(\mathbf{r})\delta\sigma(\mathbf{r}') \rangle = k_0^2(T) e^{-\frac{|\mathbf{r}-\mathbf{r}'|}{a^2}} \quad (2.64)$$

$$\text{with } k_0(T) = v_0 \frac{e^2}{h} \sum_m n'_F(E_m - \mu). \quad (2.65)$$

In the case of the regime of the quantum Hall effect, the conductivity fluctuations are no longer diagonal, but have the form $\delta\hat{\sigma}(\mathbf{r}) = \delta\sigma(\mathbf{r})\hat{\epsilon}$ with $\hat{\epsilon} = \begin{pmatrix} 0 & -1 \\ 1 & 0 \end{pmatrix}$. We can still regroup the scalar factors $\delta\sigma$ and calculate the average by contracting them. The difference to the diagonal case is that for each $\delta\hat{\sigma}$ a factor $\hat{\epsilon}$ stays in the matrix product of the Green's functions,

$$\begin{aligned} \langle \hat{\chi}(\mathbf{r}) \rangle &= \langle \delta\hat{\sigma}(\mathbf{r}) \rangle + \int d^2r_1 \langle \delta\hat{\sigma}(\mathbf{r})\delta\sigma(\mathbf{r}_1) \rangle \hat{\epsilon} \hat{\mathcal{G}}_0(\mathbf{r}, \mathbf{r}_1) \hat{\epsilon} \\ &+ \int d^2r_1 \int d^2r_2 \langle \delta\hat{\sigma}(\mathbf{r})\delta\sigma(\mathbf{r}_1)\delta\sigma(\mathbf{r}_2) \rangle \\ &\times \hat{\epsilon} \hat{\mathcal{G}}_0(\mathbf{r}, \mathbf{r}_1) \hat{\epsilon} \hat{\mathcal{G}}_0(\mathbf{r}_1, \mathbf{r}_2) \hat{\epsilon} + \dots \end{aligned} \quad (2.66)$$

Up to the new rule, to add a matrix $\hat{\epsilon}$ for every dot, the diagrammatic remains unchanged and in graphical representation

$$\langle \hat{\chi}(\mathbf{r}) \rangle = \text{diagram 1} + \text{diagram 2} + \text{diagram 3} + \dots \quad (2.67)$$

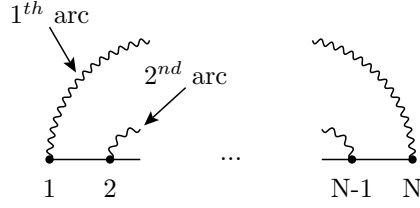


Figure 2.5: Numeration of points and arcs.

For all diagrams the off-diagonal elements are zero and the two diagonal elements are identical. Physically, this is due to isotropy, mathematically we will show it in section 2.7. Therefore the effective conductivity has the form

$$\hat{\sigma}_e = \begin{pmatrix} 0 & -\sigma_H \\ \sigma_H & 0 \end{pmatrix} + \sigma_0 \left[1 + \sum_{n=1}^{\infty} a_n \frac{\langle \delta\sigma^2 \rangle^n}{\sigma_0^{2n}} \right] \begin{pmatrix} 1 & 0 \\ 0 & 1 \end{pmatrix} = \begin{pmatrix} \sigma_L^e & -\sigma_H \\ \sigma_H & \sigma_L^e \end{pmatrix} \quad (2.68)$$

where the dimensionless coefficient a_n collects all diagrams of order n in perturbation theory in $\langle \delta\sigma^2 \rangle / \sigma_0^2$. In the next two sections, we will calculate the diagrams up to the sixth order. As in the quantum Hall regime $\sigma_0 \ll \sqrt{\langle \delta\sigma^2 \rangle}$, simple truncation of this series at a given order does not work. But in section 2.8, I will show how one can get insight in the interesting regime of small dissipation by extrapolation techniques.

2.6. Creation of the Diagrams

The averaging process consists in summing all possible contractions of $\delta\hat{\sigma}$ at one given order.

$$\begin{aligned} \langle \hat{\chi}^{(n)} \rangle &= \int d^2r_1 \dots d^2r_n \langle \delta\sigma(\mathbf{r}_0) \delta\sigma(\mathbf{r}_1) \dots \delta\sigma(\mathbf{r}_n) \rangle \\ &\quad \times \hat{e} \hat{\mathcal{G}}_0(\mathbf{r} - \mathbf{r}_1) \epsilon \hat{\mathcal{G}}_0(\mathbf{r}_1 - \mathbf{r}_2) \dots \epsilon \hat{\mathcal{G}}_0(\mathbf{r}_{n-1} - \mathbf{r}_n) \hat{e}. \end{aligned} \quad (2.69)$$

This means in the diagrammatic language that every possible way of connecting two curly lines gives one diagram. For the lower orders these diagrams can be drawn by hand as we have already seen in equation (2.45). As the number of possible diagrams increases rapidly with the order, the diagrams have to be created systematically. To do this, we study the structure of the diagrams. A diagram of order N consists of $N/2$ arcs, which connect N points on a straight line. We numerate these points and arcs to be able to refer to them more easily (see figure 2.5). The first arc starts from point one and can end on any point whose number is bigger than one. Every following arc starts from the smallest not yet connected point and can end on any point which is not yet taken. Every diagram is unambiguously given by the suit of the start and end points of its arcs: (end 1st arc, begin 2nd arc, end 2nd arc, ..., begin N^{th} arc, end N^{th} arc). This gives us a method to write a **Python**-Script which creates all diagrams in the following way:

First, it creates all permutations p of $(2,3,\dots,n)$.

Second, it make sure that the $(n+1)$ th-arc starts after the n -th arc. The elements of the suite of start and end points are referred by $(p[0], p[1], \dots, p[n-2])$. Only permutations for which $p[4] > p[2]$, $p[6] > p[4]$, \dots , $p[n-3] > p[n-5]$ holds are kept.

Third, it makes sure that every arc begins before it ends by discarding all permutations for which the following does not hold: $p[3] > p[2]$, $p[5] > p[4]$, \dots , $p[n-2] > p[n-3]$

The calculation of the diagrams is more easily done in momentum space. All diagrams consist of the following three elements:

$$\hat{\mathcal{G}}_0(\mathbf{p}) = -\frac{1}{\sigma_0} \begin{pmatrix} \cos^2(\theta) & \cos(\theta)\sin(\theta) \\ \cos(\theta)\sin(\theta) & \sin^2(\theta) \end{pmatrix} = -\frac{1}{\sigma_0(p_x^2 + p_y^2)} \begin{pmatrix} p_x^2 & p_x p_y \\ p_x p_y & p_y^2 \end{pmatrix} \quad (2.70)$$

$$\hat{\epsilon} = \begin{pmatrix} 0 & -1 \\ 1 & 0 \end{pmatrix} \quad (2.71)$$

$$K(\mathbf{p}) = \pi \xi^2 k_0^2 e^{-\frac{\xi^2 p^2}{4}} = \pi \xi^2 k_0^2 e^{-\frac{\xi^2}{4}(p_x^2 + p_y^2)}. \quad (2.72)$$

Re-translating the diagrams into equations is done in two steps. First, to each line the corresponding momentum has to be attributed. The first, second ... n -th arc carries the momentum $\mathbf{p}_1, \mathbf{p}_2 \dots \mathbf{p}_n$. Every straight line carries a momentum equal to the sum of the momenta carried by the arc passing over this line. In this way, the sum of momenta at each vertex is zero. Second, every arc stands for a factor K with the corresponding momentum as argument and every straight line stands for a matrix $\hat{\mathcal{G}}_0$ also with the corresponding momentum as its argument. The $\hat{\mathcal{G}}_0$ have to be multiplied from the right to the left with an $\hat{\epsilon}$ matrix at the beginning, between every $\hat{\mathcal{G}}_0$ -matrix and at the end. The whole expression has to be integrated over all momenta. For example the second order diagram with one crossing is:

$$\text{Diagram} = \iint \frac{d^2 p_1}{(2\pi)^2} \frac{d^2 p_2}{(2\pi)^2} K(\mathbf{p}_1) K(\mathbf{p}_2) \hat{\epsilon} \hat{\mathcal{G}}_0(\mathbf{p}_1) \hat{\epsilon} \hat{\mathcal{G}}_0(\mathbf{p}_1 + \mathbf{p}_2) \hat{\epsilon} \hat{\mathcal{G}}_0(\mathbf{p}_2) \hat{\epsilon}. \quad (2.73)$$

2.7. Evaluation of the Diagrams

The second order diagram in equation (2.67) can be calculated by hand:

$$\begin{aligned} \text{Diagram} &= \int \frac{d^2 p}{(2\pi)^2} K(\mathbf{p}) \hat{\epsilon} \hat{\mathcal{G}}_0(\mathbf{p}) \hat{\epsilon} \\ &= \frac{k_0^2}{\pi \sigma_0} \iint d^2 p \, p e^{-p^2} d\theta \begin{pmatrix} \sin^2(\theta) & -\cos(\theta)\sin(\theta) \\ -\cos(\theta)\sin(\theta) & \cos^2(\theta) \end{pmatrix} = \frac{k_0^2}{2\sigma_0} \begin{pmatrix} 1 & 0 \\ 0 & 1 \end{pmatrix} \end{aligned} \quad (2.74)$$

Before calculating the higher order diagrams, we remember, that all particle reducible diagrams are zero. Although the conductivity is a matrix, we have to evaluate only one element as every diagram \hat{D} is a diagonal matrix with identical diagonal elements,

2. The Classical Percolation Regime of Quantum Hall Transitions

i. e. $\hat{D} = D\mathbb{1}$. To prove this, let us study the effect of two different changes of variables, the rotation by π of every momentum and the interchange of the x and the y components of every momentum on the diagrams. The diagrams have the general form

$$\hat{D} = \left(\prod_j \int \frac{dp_x^j dp_y^j}{(2\pi)^2} K(\mathbf{p}^j) \right) \underbrace{\hat{\mathcal{G}}_0 \hat{\mathcal{G}}_0 \hat{\mathcal{G}}_0 \hat{\mathcal{G}}_0 \dots \hat{\mathcal{G}}_0 \hat{\mathcal{G}}_0 \hat{\mathcal{G}}_0 \hat{\mathcal{G}}_0}_{\text{odd number of } \hat{\mathcal{G}}_0\text{-matrices}}. \quad (2.75)$$

First change of variables: For all j $p_x^j \rightarrow p_y^j$, $p_y^j \rightarrow -p_x^j$. The functional determinant for this change of variables is one. The $K(\mathbf{p}^j)$ remain unchanged. For the free Green's function the variable change can be expressed by multiplication with $\hat{\epsilon}$ -matrices: $\hat{\mathcal{G}}_0 \rightarrow -\hat{\epsilon} \hat{\mathcal{G}}_0 \hat{\epsilon}$.

$$\begin{aligned} \hat{D} &= - \left(\prod_j \int \frac{dp_x^j dp_y^j}{(2\pi)^2} K(\mathbf{p}^j) \right) \hat{\epsilon} \hat{\mathcal{G}}_0 \hat{\epsilon} \hat{\mathcal{G}}_0 \hat{\epsilon} \hat{\mathcal{G}}_0 \hat{\epsilon} \hat{\mathcal{G}}_0 \hat{\epsilon} \hat{\mathcal{G}}_0 \hat{\epsilon} \dots \hat{\epsilon} \hat{\mathcal{G}}_0 \hat{\epsilon} \hat{\mathcal{G}}_0 \hat{\epsilon} \hat{\mathcal{G}}_0 \hat{\epsilon} \hat{\mathcal{G}}_0 \hat{\epsilon} \hat{\mathcal{G}}_0 \hat{\epsilon} \\ &= - \left(\prod_j \int \frac{dp_x^j dp_y^j}{(2\pi)^2} K(\mathbf{p}^j) \right) \hat{\mathcal{G}}_0 \hat{\mathcal{G}}_0 \hat{\mathcal{G}}_0 \hat{\mathcal{G}}_0 \dots \hat{\mathcal{G}}_0 \hat{\mathcal{G}}_0 \hat{\mathcal{G}}_0 \hat{\mathcal{G}}_0 = -\hat{\epsilon} \hat{D} \hat{\epsilon}. \end{aligned} \quad (2.76)$$

Second change of variables: For all j $p_x^j \rightarrow p_y^j$, $p_y^j \rightarrow p_x^j$. As for the first change of variables, the functional determinant is one and the $K(\mathbf{p}^j)$ remain unchanged. For the free Green's function the variable change can be expressed by multiplication with $\hat{\eta}$ -matrices: $\hat{\mathcal{G}}_0 \rightarrow \hat{\eta} \hat{\mathcal{G}}_0 \hat{\eta}$, where $\hat{\eta}$ is defined as $\hat{\eta} = \begin{pmatrix} 0 & 1 \\ 1 & 0 \end{pmatrix}$.

$$\hat{D} = \left(\prod_j \int \frac{dp_x^j dp_y^j}{(2\pi)^2} K(\mathbf{p}^j) \right) \hat{\epsilon} \hat{\eta} \hat{\mathcal{G}}_0 \hat{\eta} \hat{\epsilon} \hat{\mathcal{G}}_0 \hat{\eta} \hat{\epsilon} \hat{\mathcal{G}}_0 \hat{\eta} \hat{\epsilon} \hat{\mathcal{G}}_0 \hat{\eta} \hat{\epsilon} \dots \hat{\eta} \hat{\epsilon} \hat{\mathcal{G}}_0 \hat{\eta} \hat{\epsilon} \hat{\mathcal{G}}_0 \hat{\eta} \hat{\epsilon} \hat{\mathcal{G}}_0 \hat{\eta} \hat{\epsilon} \quad (2.77)$$

with $\hat{\eta} \hat{\epsilon} \hat{\eta} = -\hat{\epsilon}$ and $\hat{\eta} \hat{\eta} = -\hat{\epsilon} \hat{\eta}$

$$\hat{D} = \left(\prod_j \int \frac{dp_x^j dp_y^j}{(2\pi)^2} K(\mathbf{p}^j) \right) \hat{\eta} \hat{\epsilon} \hat{\mathcal{G}}_0 \hat{\epsilon} \hat{\mathcal{G}}_0 \hat{\epsilon} \hat{\mathcal{G}}_0 \hat{\epsilon} \dots \hat{\epsilon} \hat{\mathcal{G}}_0 \hat{\epsilon} \hat{\mathcal{G}}_0 \hat{\epsilon} \hat{\mathcal{G}}_0 \hat{\eta} = \hat{\eta} \hat{D} \hat{\eta}. \quad (2.78)$$

The two changes of variables yield the equality $\hat{D} = -\hat{\epsilon} \hat{D} \hat{\epsilon} = \hat{\eta} \hat{D} \hat{\eta}$ or written component wise

$$\begin{pmatrix} D_{xx} & D_{xy} \\ D_{yx} & D_{yy} \end{pmatrix} = \begin{pmatrix} D_{yy} & -D_{yx} \\ -D_{xy} & D_{xx} \end{pmatrix} = \begin{pmatrix} D_{yy} & D_{yx} \\ D_{xy} & D_{xx} \end{pmatrix}, \quad (2.79)$$

which can only be fulfilled if $\hat{D} = D\mathbb{1}$.

We calculate the fourth and sixth-order diagrams using the computer algebra program *Mathematica*. To save computation time and working memory, we proceed

in the following steps:

First, the expressions for the diagrams are created in Cartesian coordinates. The factor $\xi^2/4$ in the function K is absorbed in a change of variables. We get rid of the denominator in the expression for $\hat{\mathcal{G}}_0$ by rewriting them with the Feynman trick:

$$\frac{1}{x} = \int_0^\infty dt e^{-tx}. \quad (2.80)$$

The integrals over the auxiliary variables t will only be done after the integrals over the momenta.

Second, the integrals over the x and y components are done one after the other. Instead of using the built-in integration routine, which is too time-consuming, we remark that every integral has the form

$$\int dx e^{-x^2+b_1x+b_0} \sum_{n=0} a_n x^n. \quad (2.81)$$

It is enough to evaluate this integral once in its general form. Afterwards, the corresponding coefficients are extracted from the expressions to integrate and plugged into the general expression.

Third, the result has to be simplified after the integration over the last momentum. The built-in simplification routines are slow and do not arrive at a satisfying level of simplification. The results of the integrations have the form of continued fractions. The different parts of the expression are written into a table. This table allows to write the fractions systematically, starting from the bottom, on common numerators. Fourth, the integrals over the auxiliary variable t have to be done. In most cases the built-in integration and simplification routines work fine. But for some expressions terms containing logarithms have to be simplified by hand e.g. replace $\ln(8 + 16t)$ by $(3\ln(2) + \ln(1 + 2t))$.

The results for the fourth and sixth order diagrams are given in table 2.1.

The diagrams of eighth, tenth and twelfth order are calculated numerically. Again we use a `python` script to create the diagrams, to discard the particle reducible ones and to write the corresponding functions down in `C`-code. We pass to hyper spherical coordinates⁴ with the dimension corresponding to the order of the diagrams. The integral over the radius is always the same and can be done analytically which has the advantage of avoiding integrals over infinite intervals.

Afterwards, the angular integrals are done using the **Vegas** Monte Carlo integration routine from the **GNU Scientific Library**. In a plain Monte-Carlo integration the sample points are drawn from an evenly distributed probability distribution. With a constant number of sampling points, the integral could be evaluated much

4. $p_{1x} = r \cos(\phi_1)$, $p_{1y} = r \sin(\phi_1) \cos(\phi_2)$, $p_{2x} = r \sin(\phi_1) \sin(\phi_2) \cos(\phi_3)$, ... , $p_{nx} = r \sin(\phi_1) \cdots \sin(\phi_{n-2}) \cos(\phi_{n-1})$, $p_{ny} = r \sin(\phi_1) \cdots \sin(\phi_{n-2}) \sin(\phi_{n-1})$. Volume element: $dV = r^{n-1} \sin^{n-2}(\phi_1) \sin^{n-3}(\phi_2) \cdots \sin(\phi_{n-2}) dr d\phi_2 d\phi_3 \cdots d\phi_{n-1}$

2. The Classical Percolation Regime of Quantum Hall Transitions

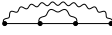
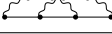




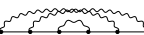
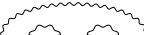
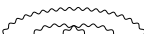
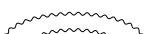
Diagram	Multiplicity	Analytical Value	Decimal Value
fourth order			
	1	$-\frac{1}{4} \log(2)$	-0.173287
	1	$\frac{1}{8}(1 - \log(4))$	-0.048287
sixth order			
	1	$\frac{1}{96} (3 - \pi^2 + 3 \log[3](-3 + \log[9]) + 12 \text{Li}_2 [\frac{2}{3}])$	0.005040
	2	$\frac{1}{32} \log [\frac{27}{16}]$	0.016352
	1	$\frac{1}{16} (2 \log[2]^2 - 3 \log[3] + \log[8] + \text{Li}_2 [\frac{1}{4}])$	0.000760
	2	$\frac{1}{384} (2 + 100 \log[2] - 63 \log[3])$	0.005474
	1	$\frac{1}{8} \log [\frac{32}{27}]$	0.021237
	1	$\frac{1}{8} \log [\frac{27}{16}]$	0.065406
	1	$-\frac{1}{48} - \frac{\log[2]}{6} + \frac{9 \log[3]}{64}$	0.018135
	1	$\frac{3}{16} \log [\frac{4}{3}]$	0.053940

Table 2.1.: Multiplicity and analytical values of the diagonal elements of the non-zero fourth and sixth order diagrams. Li_2 is the dilogarithm defined by $\text{Li}_2(z) = \int_z^0 dt \frac{\log(1-t)}{t}$.

Order	Method	Coefficient a_n
1	Analytical	$\frac{1}{2}$
2	Analytical	$\frac{1}{8} - \frac{1}{2} \log(2)$
3	Analytical	0.2034560502
4	Numerical	-0.265 ± 0.001
5	Numerical	0.405 ± 0.001
6	Numerical	-0.694 ± 0.001

Table 2.2: Coefficients a_n of the perturbative series (2.68) up to sixth loop order.

more accurately, if the function evaluations were concentrated to regions where the integrand is largest in magnitude (importance sampling). But this needs knowledge of the integrand behavior prior to integration. The Vegas algorithm is an iterative algorithm which uses information generated during a Monte Carlo integration to adapt the probability distribution used in subsequent integrations [54, 55].

As we are only interested in the sum of the diagrams and integration is time consuming, it is impracticable to integrate all diagrams one by one. Instead, we sum the diagrams before integration. Table 2.2 gives an overview of all calculated coefficients.

Some high order diagrams can even be evaluated analytically. With them, we can test the numerical integration and confirm the built-in error estimation. The analytically evaluated diagrams and their numerical and analytical values are given in table 2.3. For the analytical calculation, we remark that these diagrams are only

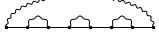
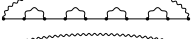
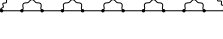
diagram	analytical value	numerical value
	$\frac{-44 \log[2] + 27 \log[3]}{32} = -0.0261233$	-0.026071
	$\frac{162 \log[3] + 125 \log[5] - 32 \log[131072]}{192} = 0.01084$	0.010879
	$\frac{-6496 \log[2] - 486 \log[3] + 3125 \log[5]}{1536} = -0.004632$	-0.004630

Table 2.3.: Comparison of analytical and numerical values of certain diagrams.

composed of bare propagators and of the first order self-energy

$$\hat{\Sigma}_1(\mathbf{p}) = \frac{\mathbf{p}}{\mathbf{p}} \cdot \text{diagram} \cdot \frac{\mathbf{p}}{\mathbf{p}} = \frac{\langle \delta \sigma^2 \rangle}{\sigma_0} \frac{1}{(p_x^2 + p_y^2)^2} \begin{pmatrix} a & b \\ b & c \end{pmatrix}, \quad (2.82)$$

$$\text{with } a = \frac{1}{2}(p_y^2 - p_x^2) \left[e^{-p_x^2 - p_y^2} - 1 \right] + p_x^2 p_y^2 + p_y^4,$$

$$b = -p_x p_y [e^{-p_x^2 - p_y^2} - 1 + p_x^2 + p_y^2],$$

$$c = \frac{1}{2}(p_x^2 - p_y^2) \left[e^{-p_x^2 - p_y^2} - 1 \right] + p_x^2 p_y^2 + p_x^4.$$

For $\hat{\Sigma}_1$ the off diagonal elements are not zero, because it has a finite in and outgoing momentum. Using this, already integrated building block, reduces the number of integrals we have to do. The eighth-order diagram e.g. is:

$$\text{diagram} = \int \frac{d^2 p}{(2\pi)^2} K(\mathbf{p}) \times \hat{\epsilon} \hat{\mathcal{G}}_0(\mathbf{p}) \Sigma(\mathbf{p}) \hat{\mathcal{G}}_0(\mathbf{p}) \Sigma(\mathbf{p}) \hat{\mathcal{G}}_0(\mathbf{p}) \Sigma(\mathbf{p}) \hat{\mathcal{G}}_0(\mathbf{p}) \hat{\epsilon}. \quad (2.83)$$

2.8. Extrapolation to the Regime of Small Dissipation

Knowing the first coefficients of the perturbation series, we can very well describe the regime where the conductivity is governed by phonons, *i. e.* $\sigma_0 \gg \sqrt{\langle \delta \hat{\sigma}^2 \rangle}$. But what happens in the opposite regime of small dissipation and how does the effective conductivity behave on the crossover between the two regimes? To answer this question, we use here an extrapolation technique. In view of the diagrammatic representation, it would perhaps seem more natural to use a self consistent Born approximation. This idea is explored in appendix A, but it does not lead to the desired result, as the convergence is too slow.

The effective longitudinal conductivity σ_L^e vanishes [2] in the limit $\sigma_0 \rightarrow 0$. For small values of σ_0 , the current density is orthogonal to the gradient of the potential *i. e.* parallel to the level lines. This can be seen from the Maxwell equation $\nabla \times \mathbf{E} = 0$

2. The Classical Percolation Regime of Quantum Hall Transitions

which yields in the limit $\sigma_0 \rightarrow 0$ using current conservation $\nabla \cdot \mathbf{j} = 0$ and expressing the electric field as $\mathbf{E} = \hat{\sigma}^{-1} \mathbf{j}$ with $\hat{\sigma}$ given by equation (2.57)

$$\frac{1}{\sigma_H^2} (\nabla \sigma_H) \cdot \mathbf{j} = 0 \Leftrightarrow (\nabla V(\mathbf{r})) \cdot \mathbf{j} = 0, \quad (2.84)$$

where the last equivalence holds because of equation (2.61). For vanishing longitudinal conductance, all current filaments are parallel to the equipotential lines. Therefore, most of them circuit summits or basins of the potential and are localized. To have an effective conductivity different from zero, some current filaments have to reach from one end of the sample to the other. The current filaments percolate the system only at one energy. But at this energy they have to pass saddle points, where the gradient of the potential is zero. Conductance over saddle points is only possible via electron-phonon processes encoded in σ_0 and the smaller σ_0 the smaller the effective conductivity. From this considerations we expect, that the effective conductivity behaves as

$$\sigma_L^e = C \langle \delta \sigma^2 \rangle^{\frac{\kappa}{2}} \sigma_0^{1-\kappa} \quad (2.85)$$

for small σ_0 . With this assumption in mind, we extrapolate the series established above for $\sigma_0 \gg \sqrt{\langle \delta \sigma^2 \rangle}$ to $\sigma_0 \rightarrow 0$ and determine the critical exponent κ . For the extrapolation we use two methods, series expansion of the logarithmic derivative with Padé approximants and a four point fit.

Padé approximants are a particular type of rational fraction approximations to the value of a function for which only limited information is available [56]. The basic idea is similar to Taylor expansion. While in a Taylor expansion, the unknown function is approximated by a polynomial, the Padé approximant consists of a fraction of two polynomials. More concretely:

$$\text{Padé}[L/M] = \frac{P_L(x)}{Q_M(x)} \quad (2.86)$$

is a $[L/M]$ Padé approximant to a function $f(x)$ if

$$f(x) - \frac{P_L(x)}{Q_M(x)} = O(x^{L+M+1}), \quad (2.87)$$

$P_L(x)$ and $Q_M(x)$ are polynomials with degrees $\deg(P_L) \leq L$, $\deg(Q_M) \leq M$ and $Q_M(0) = 1$, where O is the Landauer O . For uniqueness P_L and Q_M must not have common factors. For non-polynomial functions, Padé approximants have often a larger convergence radius and converge faster than the corresponding Taylor expansion.

Series expansion of the logarithmic derivative with Padé approximants (the so called Dlog Padé approximants) is a standard method to calculate critical exponents [57].

Order	b_2	b_4	b_6	b_8	b_{10}	b_{12}
Coefficient	-1	$\log(4)$	-2.135	3.698	-6.919	13.823

Table 2.4.: Coefficients b_n for the the small- x series expansion (2.89) of the function $f(x)$ defined in equation (2.88).

As indicated by the name of the method, we have to start with the dimensionless logarithmic derivative of the function to extrapolate:

$$f(x) := \sigma_0 \frac{d \log[\sigma_L^e(\sigma_0)]}{d\sigma_0} \bigg|_{\sigma_0/\sqrt{\langle \delta\sigma^2 \rangle}=1/x} \quad (2.88)$$

Starting from the expansion of σ_L^e given in equation (2.68), we expand $f(x)$ at small x in a power series to order N in the number of arcs of the diagrams respectively to order $2N$ in powers of x

$$f_N(x) = 1 + \sum_{n=1}^{2N} b_n x^n. \quad (2.89)$$

All odd terms in this expansion are zero, because σ_L^e is an odd function of σ_0 . The even coefficients are given in table 2.4. From the coefficients of the power series, we calculate the $[N/N]$ Padé approximant of $f(x)$:

$$\text{Padé}[N/N](f) = \frac{\sum_{n=0}^N p_n x^n}{1 + \sum_{n=1}^N q_n x^n}. \quad (2.90)$$

Again the numerator and the denominator polynomial are even functions of x . This means $\text{Padé}[(2n-1)/(2n-1)](f) = \text{Padé}[(2n)/(2n)](f)$ and we always have to calculate two orders more to get new information.

Plugging the expected behavior of the conductivity at small dissipation (equation (2.85)), into the definition of $f(x)$ (equation (2.88)), we get $f(x) \rightarrow 1 - \kappa$ for $x \rightarrow \infty$. The critical exponent κ is thus obtained by extrapolating the Padé approximant (2.90) to infinity, which simply reads

$$1 - \kappa = \lim_{x \rightarrow \infty} f(x) \approx \lim_{x \rightarrow \infty} \text{Padé}[N/N](f(x)) = \frac{p_N}{q_N} \quad (2.91)$$

at the order N . To get the corrections of the effective conductivity at order N , we have to replace $f(x)$ by $\text{Padé}[N/N](f(x))$ in equation (2.88) and solve the resulting differential equation. The solution is

$$\sigma_L^e(\sigma_0) \approx C \sigma_0 e^{\int_0^x dx \frac{\langle \delta\sigma^2 \rangle}{\sigma_0^2} \frac{\sum_{n=0}^N p_n x^n}{1 + \sum_{n=1}^N q_n x^n}} = C \sigma_0 \prod_n^N \left(1 + c_n \frac{\langle \delta\sigma^2 \rangle}{\sigma_0^2} \right)^{d_n}, \quad (2.92)$$

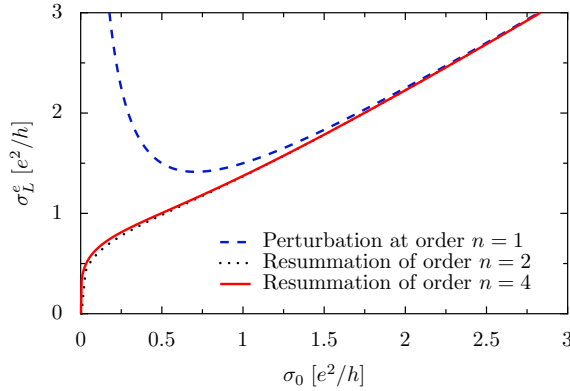


Figure 2.6: Scaling function of the longitudinal conductance from the percolating ($\sigma_0 \rightarrow 0$) to the dissipative regime ($\sigma_0 \rightarrow \infty$). The first order bare perturbation theory (controlled only at large dissipation) is shown in comparison to the resummations of the $n = 2$ and $n = 4$ orders, showing good convergence for all values of σ_0 .

where C is the integration constant and the c_n , d_n are dimensionless numbers determined from the coefficients of the Padé expansion. The last equation holds, if all roots of the denominator polynomial of the integral have multiplicity one.

At second order, the critical exponent is $\kappa = 0.72 \pm 0.09$ and the effective conductivity reads

$$\sigma_L^e(\sigma_0) = C\sigma_0 \left[1 + \frac{1}{\kappa} \frac{\langle \delta\sigma^2 \rangle}{\sigma_0^2} \right]^{\kappa/2}. \quad (2.93)$$

To obtain the error bar on κ , equation (2.93) has been expanded to third order in $\langle \delta\sigma^2 \rangle / \sigma_0^2$ with κ arbitrary, and the resulting third order coefficient has been compared with the exact a_3 value. Equation (2.93) describes the full crossover between the regime of strong dissipation $\langle \delta\sigma^2 \rangle \ll \sigma_0^2$, which is already well described by first order perturbation theory to the non-perturbative limit of vanishing dissipation $\sigma_0 \rightarrow 0$ where percolation effects dominate, see figure 2.6.

In order to obtain a better estimate for the exponent, we push the calculation of the effective conductivity to fourth order where it is given by $\kappa = 0.779 \pm 0.006$, and the resulting formula for the effective conductivity takes the form:

$$\sigma_L^e(\sigma_0) = \sigma_0 \left(1 + A \frac{\langle \delta\sigma^2 \rangle}{\sigma_0^2} \right)^B \left(1 + C \frac{\langle \delta\sigma^2 \rangle}{\sigma_0^2} \right)^D \quad (2.94)$$

One part of the error bar on κ is again obtained by expanding equation (2.94) to fifth order with arbitrary κ and comparing the resulting coefficient to a_5 . The second part is due to the error bar of the coefficients which have been evaluated numerically.

In principle, the calculation of the sixth order corrections should allow an even more precise estimation of the critical exponent κ , but in that case the Padé approximant features a spurious pole [58], that invalidates the method. The general form of the Padé approximant (2.92) gives a hint why the Padé method becomes unstable at high orders.

$$\sigma_L^e(\sigma_0) \propto \langle \delta\sigma^2 \rangle^{\kappa/2} \sigma_0^{1-\kappa} \left[1 + E \frac{\sigma_0^2}{\langle \delta\sigma^2 \rangle} + \dots \right]. \quad (2.95)$$

Order	Method	Exponent $1 - \kappa$
2	Padé	0.28 ± 0.09
4	Padé	0.221 ± 0.006
4	n-Fit	0.233 ± 0.002
∞	Conjecture	$3/13 \simeq 0.2308$

Table 2.5: Critical exponent $1 - \kappa$. The indicated error bounds have been estimated with the next coefficient of the series. They clearly underestimate the true error. But they indicate the order of magnitude and that the four point fit method gives the best result.

The sub-leading exponent κ' is not independent of the leading exponent κ , but is automatically given by $\kappa' \simeq 3 - \kappa$, which is unlikely to correspond with good precision to the right value. Probably this lack of flexibility is the source of the spurious pole in the Padé approximant. To circumvent this problem authors [59] have used a generalized n-Fit method. For the case of the fourth order conductivity, we try the following additive form:

$$\sigma_L^e(\sigma_0) = F\sigma_0 \left(1 + G \frac{\langle \delta \sigma^2 \rangle}{\sigma_0^2}\right)^H + (1 - F)c_0 \left(1 + G \frac{\langle \delta \sigma^2 \rangle}{\sigma_0^2}\right)^I. \quad (2.96)$$

The critical exponent is here given by $\kappa = \min[2H, 2I]$. The sub-leading exponent is independent of the leading critical exponent and reads $\kappa' = \max[2H, 2I]$. To obtain the numerical coefficients of equation. (2.96), it is expanded about $x = \sqrt{\langle \delta \sigma^2 \rangle}/\sigma_0 = 0$ and the first four coefficients of the resulting series are identified with the first four coefficients of Table 2.4. The fifth coefficient is again used for the error estimation. We find $\kappa = 0.767 \pm 0.002$, in excellent agreement with the conjectured value $\kappa = 10/13 \simeq 0.7692$.

2.9. Summary

In this sometimes quite technical chapter, we have developed a transport theory for the high temperature regime of the quantum Hall effect based on an effective medium approach. It allows us to describe the entire crossover from the percolating to the dissipative regime. We were able to determine the critical exponent for the longitudinal effective conductivity accurately in a fully microscopic theory.

3. Classical Percolating Transport: Theory and Experiment

In the previous chapter, we derived an expression for the effective conductivity as a function of the local Ohmic conductivity σ_0 , that applies in the classical percolation regime of the quantum Hall effect. In this chapter, we will express the effective conductivity as a function of the experimental accessible quantities temperature and magnetic field. This allows us to compare our theoretical results to recent experimental data obtained by Benjamin Piot *et al.* [5] at the “Laboratoire National des Champs Magnétiques Intenses (LNCMI)” in Grenoble and to the experiment by V. Renard *et al.* (partially published in [6]).

3.1. Estimation of the Local Ohmic Conductivity from Phonon Scattering

The first element we need, in order to calculate the temperature and magnetic field dependence of the effective conductivity, is the temperature and magnetic field behavior of the Ohmic conductivity σ_0 describing transport at short length scales. As σ_0 encodes mainly electron-phonon processes, we estimate it with the Drude formula

$$\sigma_0 = \frac{ne^2\tau_{ph}/m^*}{1 + (\omega_c\tau_{ph})^2} \quad (3.1)$$

using the electron-phonon scattering time τ_{ph} . The following estimation for the electron-phonon scattering rate in the regime of the quantum Hall effect follows [4]. This derivation is close to the standard textbook version of electron-phonon scattering which can for example be found in [60]. But instead of a homogeneous three dimensional electron density, the high field two dimensional density given by Landau states is used. The electron-phonon interaction Hamiltonian is given by [60]

$$\hat{\mathcal{V}}_{\text{el-ph}} = \int d^3r \, \rho_{\text{el}}(\mathbf{r}) \sum_j e\mathbf{u}_j \cdot \nabla_{\mathbf{r}} V_{\text{ion}}(\mathbf{r} - \mathbf{R}_j^0). \quad (3.2)$$

It states that the electron gas characterized by its density ρ_{el} interacts with ions, which are displaced from their equilibrium position \mathbf{R}_j^0 by \mathbf{u}_j via the electrostatic

3. Classical Percolating Transport: Theory and Experiment

potential V_{ion} created by the ions. For simplicity, only one three dimensional acoustic phonon mode is studied and we have [60]

$$\mathbf{u}_j = \sqrt{\frac{\hbar}{2MN}} \sum_{\mathbf{p}} \frac{\mathbf{e}_{\mathbf{p}}}{\sqrt{\omega_{\mathbf{p}}}} (\hat{a}_{\mathbf{p}} + \hat{a}_{-\mathbf{p}}^\dagger) e^{i\mathbf{p} \cdot \mathbf{R}_j^0}, \quad (3.3)$$

where N is the number of ions, M the ionic mass, $\omega_{\mathbf{p}} = c_L |\mathbf{p}|$ the phonon frequency, c_L the speed of sound, $\mathbf{e}_{\mathbf{p}}$ the polarization vector and $\hat{a}_{\mathbf{p}}, \hat{a}_{\mathbf{p}}^\dagger$ bosonic annihilation/creation operators for phonons in mode \mathbf{p} . We use the Fourier representation in the volume \mathcal{V} for the gradient of the ion potential

$$\nabla_{\mathbf{r}} V_{\text{ion}}(\mathbf{r} - \mathbf{R}_j^0) = \frac{1}{\mathcal{V}} \sum_{\mathbf{g}} i\mathbf{g} V_{\mathbf{g}}^{\text{ion}} e^{i\mathbf{g} \cdot (\mathbf{r} - \mathbf{R}_j^0)}. \quad (3.4)$$

As discussed in section 1.4, the electron motion in a smooth disorder potential under a strong magnetic field is well described by the semi-classical picture of electrons moving on equipotential lines. As electron-phonon interaction is a local process, we neglect curvature effects, introduce a local coordinate system x, y where the x -direction is given by a tangent to the equipotential line and the y -direction is normal to it and approximate the disorder potential locally by¹ $V(x, y) = (v_0/a)y$. This leads to a locally linearized Hamiltonian of the form of equation (1.18). For simplicity, we consider only the lowest Landau level and recall its eigenstates $\phi_{k_x}(x, y)$ and eigenenergies E_{k_x} :

$$\phi_{n=0, k_x}(x, y) = \frac{1}{\sqrt{\sqrt{\pi} l_B L}} e^{ik_x x - \frac{(y-y_0)^2}{2l_B^2}} \quad (3.5)$$

$$\epsilon_{k_x} = E_{n=0, k_x} = \frac{1}{2} \hbar \omega_c + k_x l_B^2 \frac{v_0}{a} + \frac{l_B^2}{2\hbar \omega_c} \frac{v_0^2}{a^2} \quad (3.6)$$

The electron density can be calculated as the product of field operators $\rho_{\text{el}}(\mathbf{r}) = \hat{\Psi}^\dagger(\mathbf{r}) \hat{\Psi}(\mathbf{r})$. In the Landau basis, taking only the lowest Landau level into account, the field operator reads $\sum_k \phi_{n=0, k_x}(x, y) \hat{c}_{k_x}$ where \hat{c}_{k_x} is a fermionic annihilation operator, leading to the two dimensional electron density

$$\rho_{\text{el}}(x, y) = \frac{1}{\sqrt{\pi} l_B L} \sum_{q_x, k_x} e^{-iq_x x} e^{-\frac{(y-y_0)^2}{2l_B^2}} \hat{c}_{k_x+q_x}^\dagger \hat{c}_{k_x} \quad (3.7)$$

$$= \frac{1}{L^2} \sum_{\mathbf{q}, k_x} e^{-i(q_x x + q_y y)} e^{iq_y y_0} e^{-\frac{q_y^2 l_B^2}{4}} \hat{c}_{k_x+q_x}^\dagger \hat{c}_{k_x}, \quad (3.8)$$

1. To be consistent with the notation in section 2.1 the typical amplitude of the potential fluctuations is denoted by v_0 , the correlation length by a . With respect to the notation in reference [4] this means $\lambda \rightarrow a$ and $u_0 \rightarrow v_0$.

where in the second step the Gaussian has been expressed by its Fourier representation $e^{-(y-y_0)^2/(2l_B^2)} = (\sqrt{\pi}l_B/L) \sum_{q_y} e^{-iq_y(y-y_0)} e^{-(q_y^2 l_B^2)/4}$. With these expressions, the electron-phonon interaction Hamiltonian becomes using $\int dx \int dy e^{i[(q_x-g_x)x+(q_y-g_y)y]} = L^2 \delta_{q_x, g_x} \delta_{q_y, g_y}$ and $\sum_j e^{i(\mathbf{p}-\mathbf{g}) \cdot \mathbf{R}_j^0} = \mathcal{V} \delta_{\mathbf{p}, \mathbf{g}}$:

$$\hat{\mathcal{V}}_{\text{el-ph}} = ie \sqrt{\frac{\hbar}{2MNc_L}} \sum_{\mathbf{q}, k_x} \sqrt{q} V_{\mathbf{q}}^{\text{ion}} e^{iq_y y_0} e^{-\frac{q_y^2 l_B^2}{4}} \hat{c}_{k_x+q_x}^\dagger \hat{c}_{k_x} (\hat{a}_{\mathbf{q}} + \hat{a}_{-\mathbf{q}}^\dagger). \quad (3.9)$$

Knowing the interaction Hamiltonian, we can calculate the lifetime τ_{k_x} for an electron with relative energy ϵ_k above the Fermi energy with Fermi's golden rule.² The electron will be scattered from the initial state $|k_x\rangle_{\text{el}}$ into the state $|k_x + q_x\rangle_{\text{el}}$. This can happen in two ways, either by emitting a phonon into the phonon mode $|-\mathbf{q}\rangle_{\text{ph}}$ or by absorption of a phonon from the phonon mode $|\mathbf{q}\rangle_{\text{ph}}$:

$$\begin{aligned} \frac{1}{\tau_{k_x}} &= \frac{e^2 \pi}{MNc_L} \sum_{\mathbf{q}} q (V_{\mathbf{q}}^{\text{ion}})^2 e^{-\frac{q_y^2 l_B^2}{2}} [1 - n_F(k_x + q_x)] \\ &\quad \times [n_B(\mathbf{q}) \delta(\epsilon_{k_x+q_x} - \epsilon_{k_x} - \hbar\omega_{\mathbf{q}}) + (n_B(-\mathbf{q}) + 1) \delta(\epsilon_{k_x+q_x} - \epsilon_{k_x} + \hbar\omega_{\mathbf{q}})], \end{aligned} \quad (3.10)$$

where n_F is the electron and n_B the phonon distribution function. For the ionic potential a screened Coulomb potential is used $V_{\mathbf{q}}^{\text{ion}} = e(\epsilon_r \epsilon_0 a_0^3)^{-1} (k_0^2 + q^2)^{-1}$, where a_0 is the lattice constant, k_0 the inverse screening length, ϵ_0 the vacuum permittivity and ϵ_r the relative permittivity. Due to the Gaussian factor in the sum, high q -values do not contribute to the sum and as long as $q \ll k_0$, the potential depends only weakly on momentum $V_{\mathbf{q}}^{\text{ion}} \approx V_0^{\text{ion}}$, which allows us to take it out of the sum.

To evaluate the sum, we replace it by an integral $\sum_{\mathbf{q}} = \mathcal{V} \int d^3q / (2\pi)^3$. The integral over the q_x component collapses with the δ -functions giving a prefactor $a/(l_B^2 v_0)$ and the relationship $q_x^2 = q^2 (\hbar^2 c_L^2 a^2) / (l_B^2 v_0^2)$. In order to get a finite scattering rate, $\hbar^2 c_L^2 a^2 / (l_B^2 v_0^2)$ has to be smaller than one, as $q_x^2 \leq q^2$. Assuming $q_x \ll q$ (to be checked later), one can use $q^2 \approx q_y^2 + q_z^2$. After setting $\hbar\omega_{\mathbf{q}} / (k_B T) \approx \hbar c_L \sqrt{q_y^2 + q_z^2} / (k_B T) = x$ and passing to polar coordinates, we get for the scattering rate

$$\begin{aligned} \frac{1}{\tau_k} &= \frac{e^2 (V_0^{\text{ion}})^2 k_B^3 T^3 a}{8\pi^2 \rho \hbar^3 c_L^4 v_0 l_B^2} \int_0^\infty dx \int_0^{2\pi} d\theta x^2 e^{-\frac{\alpha^2 x^2 \cos^2(\theta)}{2}} \frac{e^{\frac{\epsilon_k}{k_B T}} \left[e^{\frac{\epsilon_k}{k_B T}} + 1 \right] (e^x + 1)}{\left[e^{\frac{\epsilon_k}{k_B T} + x} + 1 \right] \left[e^{\frac{\epsilon_k}{k_B T} - x} + 1 \right] (e^x - 1)} \\ &= \frac{e^2 (V_0^{\text{ion}})^2 k_B^3 T^3 a}{4\pi \rho \hbar^3 c_L^4 v_0 l_B^2} \int_0^\infty dx x^2 e^{-\frac{\alpha^2 x^2}{4}} I_0 \left(\frac{x^2 \alpha^2}{2} \right) \frac{e^{\frac{\epsilon_k}{k_B T}} \left[e^{\frac{\epsilon_k}{k_B T}} + 1 \right] (e^x + 1)}{\left[e^{\frac{\epsilon_k}{k_B T} + x} + 1 \right] \left[e^{\frac{\epsilon_k}{k_B T} - x} + 1 \right] (e^x - 1)}, \end{aligned} \quad (3.11)$$

2. Fermi's golden rule states for the lifetime τ_i of an initial state i with energy E_i that can decay in final states f with energies E_f : $\frac{1}{\tau_i} = \frac{2\pi}{\hbar} \sum_f |\langle f | \hat{\mathcal{V}}_{\text{el-ph}} | i \rangle|^2 \delta(E_f - E_i)$.

with the density $\rho = MN/\mathcal{V}$, $\alpha = k_B T l_B / (\hbar c_L)$ and $I_n(z)$ the modified Bessel function of the first kind. If $\alpha \geq 1$ the Gaussian function provides a strong cut-off for the x values and we can estimate the integral by developing the rest of the integrand about $x = 0$, leading to:

$$\frac{1}{\tau_k} = \frac{e^2 (V_0^{\text{ion}})^2 k_B^3 T^3 a}{2\pi \rho \hbar^3 c_L^4 v_0 l_B^2} \frac{e^{\frac{\epsilon_k}{k_B T}}}{\left[e^{\frac{\epsilon_k}{k_B T}} + 1 \right]} \int_0^\infty dx \, x e^{-\frac{\alpha^2 x^2}{4}} = \frac{e^2 (V_0^{\text{ion}})^2 k_B T a}{\pi \rho \hbar^3 c_L^2 v_0 l_B^4} \frac{1}{\left[e^{-\frac{\epsilon_k}{k_B T}} + 1 \right]}. \quad (3.12)$$

As we consider energies close to the percolation threshold, the exponential factors depend only very slowly on temperature, so that they can be neglected, leading to a linear temperature dependence of the scattering rate. It depends inversely on the fourth power of the magnetic length, thus quadratically on the magnetic field. We thus find with the Drude formula

$$\sigma_0 = \frac{n e^2 \tau_{ph} / m^*}{1 + (\omega_c \tau_{ph})^2} \approx \frac{n e^2}{m^* \omega_c^2 \tau_{ph}} = \frac{n m^* a e^4 (V_0^{\text{ion}})^2 k_B T}{2\pi \rho \hbar^3 c_L^2 v_0}. \quad (3.13)$$

assuming $\omega_c \tau_{ph} \gg 1$ (to be checked later). The local longitudinal conductivity depends linearly on temperature and is independent of the magnetic field.

In this derivation some approximations have been made. Let us check for what sample parameters they are justified.

In order to neglect the momentum dependence of the ionic potential, the momentum has to be small in comparison to the inverse screening length. The screening length is not well known, but in [53] it is estimated to be $k_0 \approx 2 \cdot 10^8 \text{m}^{-1}$ for GaAs. The Gaussian function cuts momentum as soon as it is of the order of $1/l_B$. For B between 1T and 10T, $1/l_B < 1.2 \cdot 10^8 \text{m}^{-1}$, so smaller than k_0 and this approximation should be safe. For GaAs $a_0 = 5.7 \cdot 10^{-10} \text{m}$ [19] and $\epsilon_r = 13.18$ [19], so that we can estimate $V_0^{\text{ion}} \approx 185 \text{V}$.

Because of the Dirac-Delta-functions, the scattering rate has only a finite value if $\hbar^2 c_L^2 a^2 / (l_B^4 v_0^2) < 1$. The speed of sound in GaAs is about $4 \cdot 10^3 \text{m/s}$ [19]. For the GaAs sample we use, we estimate $v_0 = k_B \cdot 3 \text{K} \approx 4 \cdot 10^{-23} \text{J}$ from the experimental data in section 3.5.2. With this values, the correlation length of the potential has to be smaller than $a < (1/B) \cdot 6 \cdot 10^{-8} \text{kg m C}^{-1} \text{s}^{-1}$. If we estimate a as $a \approx 2\sqrt{d} \sqrt{\xi_0^2 + 2l_B^2}$ (see 2.4) where ξ_0 is the screening length and d the distance between the donor atoms and the electron gas, the correlation length becomes too long for magnetic field values higher than 2T. If the scattering rate vanishes in first order perturbation theory, multi-phonon processes gain importance. To capture them, one has to go beyond the first order perturbation theory performed here, but it may not change the results dramatically.

The condition $\alpha > 1$ is fulfilled for temperatures higher than 5K for the B-field range from 1T to 5T. For lower temperatures, the magnetic field should not be too

high. For the experimental data studied in the following α is larger than one. As a side note, for $\alpha \ll 1$ and ϵ_k small, Zhao and Feng [4] predict the scattering rate to be proportional to T^3 . Therefore, the inverse linear dependence of the coherence length on temperature [61] observed at very low temperatures cannot be explained by electron-phonon scattering.

The approximation $\omega_c^2 \tau_{ph}^2 \gg 1$ is convenient, as it allows to describe the temperature dependence of σ_0 with only one fit-parameter in the form $\sigma_0 \approx AT$. But it is not essential because one could always use $\sigma_0 \approx A_1 T / (1 + A_2 T^2)$. With the density of GaAs $\rho = 5360 \text{ kg/m}^3$ [19], we find for $T = 1 \text{ K}$ and $B = 1 \text{ T}$ an acceptable value of $\omega_c^2 \tau_{ph}^2 \approx 34$, but at higher temperatures and magnetic fields, we reach the opposite regime as for example $\omega_c^2 \tau_{ph}^2 \approx 0.003$ for $B = 5 \text{ T}$ and $T = 40 \text{ K}$.

Finally and perhaps most importantly, the Drude theory can only be used to calculate the conductance locally, if electrons undergo a large number of scattering processes while they cover the correlation length of the potential, *i. e.* if the sample is in the diffusive regime at short length scales, where $v_d \tau_{ph} \ll a$. The drift velocity can be estimated as $v_d = |\nabla V| / (|e|B) \approx v_0 / (a|e|B)$. At high temperatures, this condition is easily fulfilled, for $T = 40 \text{ K}$ and $B = 1 \text{ T}$ for example $v_d \tau_{ph} / a \approx 0.01$. The ratio between scattering length and correlation length increases with decreasing temperature and for $T = 1 \text{ K}$ and $B = 1 \text{ T}$, we have only $v_d \tau_{ph} / a \approx 0.4$. But at least for temperatures higher than 5 K , the Drude formula can be used.

A large number of the used approximations is at the brink of validity. However, some parameters, especially k_0 , v_0 and a are not well known. As I have no better estimation for the moment, I use in the following the assumption that the local longitudinal conductivity depends linearly on temperature and is independent of the magnetic field. A change in the temperature dependence of σ_0 could explain the deviations of the experimental values from the theoretical predicted curve form occurring in sample *NRC1649* at high temperatures (see figure 3.4). It would be worthwhile to extend the calculation of this section beyond first order perturbation theory.

3.2. Reexpressing the Effective Longitudinal Conductivity with the Poisson Summation Formula

In the previous chapter, we found for the effective longitudinal conductivity (equations (2.85) and (2.65))

$$\sigma_L^e = C \sigma_0^{1-\kappa} \left| \frac{e^2}{h} \sqrt{\langle V^2 \rangle} \sum_{m=0}^{\infty} n'_F(E_m - \mu) \right|^{\kappa}. \quad (3.14)$$

3. Classical Percolating Transport: Theory and Experiment

The infinite sum over the Landau levels is at high temperatures difficult to handle, as it converges slowly and the lowest order terms are not necessarily the most important ones. In the high temperature limit, there exists a more convenient form, where high order terms are exponentially suppressed. In a first step the sum is rewritten with a variation of the Poisson sum formula³ [62]

$$\sum_{n=0}^{\infty} f(n) = \sum_{l=-\infty}^{\infty} \int_0^{\infty} f(t) e^{-2\pi i l t} dt \quad (3.15)$$

and becomes

$$\begin{aligned} \frac{d}{d\mu} \sum_{m=0}^{\infty} n_F(E_m - \mu) &= \frac{-1}{4k_B T} \sum_{m=0}^{\infty} \frac{1}{\cosh^2 \left(\frac{\hbar\omega_c(m+\frac{1}{2})-\mu}{2k_B T} \right)} \\ &= \frac{-1}{4k_B T} \sum_{l=-\infty}^{\infty} \int_0^{\infty} dt \, e^{i2\pi l t} \frac{1}{\cosh^2 \left(\frac{\hbar\omega_c(t+\frac{1}{2})-\mu}{2k_B T} \right)}. \end{aligned} \quad (3.16)$$

After the change of variables $x = \frac{1}{k_B T} [\hbar\omega_c t + \frac{\hbar\omega_c}{2} - \mu]$

$$\frac{d}{d\mu} \sum_{m=0}^{\infty} n_F(E_m - \mu) = \frac{-1}{4\hbar\omega_c} \sum_{l=-\infty}^{\infty} (-1)^l e^{i2\pi l (\frac{\mu}{\hbar\omega_c})} \int_{\frac{\hbar\omega_c}{2k_B T} - \frac{\mu}{k_B T}}^{\infty} dx \, \frac{e^{i2\pi l \frac{k_B T}{\hbar\omega_c} x}}{\cosh^2 \left(\frac{x}{2} \right)}, \quad (3.17)$$

the limit $\mu/(k_B T) \rightarrow \infty$ can be taken, which limits the usability of the formula to the regime $\mu \gg k_B T$ and yields

$$\frac{d}{d\mu} \sum_{m=0}^{\infty} n_F(E_m - \mu) = \frac{-1}{4\hbar\omega_c} \sum_{l=-\infty}^{\infty} (-1)^l e^{i2\pi l (\frac{\mu}{\hbar\omega_c})} \int_{-\infty}^{\infty} dx \, \frac{e^{i2\pi l \frac{k_B T}{\hbar\omega_c} x}}{\cosh^2 \left(\frac{x}{2} \right)}. \quad (3.18)$$

The integral is nothing but the Fourier transform $\int_{-\infty}^{\infty} dx \, \frac{e^{ikx}}{[\cosh(\frac{x}{2})]^2} = \frac{4\pi k}{\sinh(\pi k)}$ [63]:

$$\frac{d}{d\mu} \sum_{m=0}^{\infty} n_F(E_m - \mu) = \frac{-1}{\hbar\omega_c} \sum_{l=-\infty}^{\infty} (-1)^l e^{i2\pi l (\frac{\mu}{\hbar\omega_c})} \frac{2\pi^2 l \frac{k_B T}{\hbar\omega_c}}{\sinh \left(2\pi^2 l \frac{k_B T}{\hbar\omega_c} \right)}. \quad (3.19)$$

Using $\lim_{x \rightarrow 0} \frac{x}{\sinh(x)} = 1$, the $l = 0$ term can be extracted

$$\frac{d}{d\mu} \sum_{m=0}^{\infty} n_F(E_m - \mu) = \frac{-1}{\hbar\omega_c} \left[1 + \sum_{l=1}^{\infty} (-1)^l \cos \left(\frac{2\pi l \mu}{\hbar\omega_c} \right) \frac{4\pi^2 l \frac{k_B T}{\hbar\omega_c}}{\sinh \left(2\pi^2 l \frac{k_B T}{\hbar\omega_c} \right)} \right]. \quad (3.20)$$

3. Proof for our function: Multiply the representation of the Dirac-comb $\sum_{n=-\infty}^{\infty} \delta(x - n) = \sum_{k=-\infty}^{\infty} e^{2\pi i k x}$ by $n'_F(x)$ and integrate over x from zero to infinity. Interchange sum and integral using monotone convergence on the left hand side and Lebesgue dominated convergence ($|n'_F(x) e^{2\pi i k x}| \leq n'_F(x)$) on the right-hand side.

With this form of the sum over the derivatives of the Fermi functions, equation (3.14) reads

$$\sigma_L^e = C\sigma_0^{1-\kappa} \left[\frac{e^2}{h} \frac{\sqrt{\langle V^2 \rangle}}{\hbar\omega_c} \right]^\kappa \left[1 + \sum_{l=1}^{\infty} (-1)^l \cos \left(\frac{2\pi l \mu}{\hbar\omega_c} \right) \frac{4\pi^2 l \frac{k_B T}{\hbar\omega_c}}{\sinh \left(2\pi^2 l \frac{k_B T}{\hbar\omega_c} \right)} \right]^\kappa. \quad (3.21)$$

3.3. High Temperature Magnetic Field Dependence

At high temperatures $k_B T \gg \hbar\omega_c/4$, the infinite sum in equation (3.21) can be neglected, leading to a formula which gives via the cyclotron frequency the magnetic field dependence of the longitudinal conductivity

$$\sigma_L^e = C\sigma_0^{1-\kappa} \left[\frac{e^2}{h} \frac{\sqrt{\langle V^2 \rangle}}{\hbar\omega_c} \right]^\kappa \propto B^{-\kappa} \quad (3.22)$$

owing to the fact that σ_0 is independent of the magnetic field at high field amplitudes. This formula has been derived from a local conductivity tensor assuming that the guiding centers drift along equipotential lines and is therefore only valid for high enough magnetic fields. For low magnetic fields, where the motion of the guiding centers is rather a random walk, the longitudinal conductivity can be described by the Drude formula

$$\sigma_L^{Drude} = \frac{ne^2\tau/m^*}{1 + (\omega_c\tau)^2} \quad (3.23)$$

and we expect to see a crossover between these two regimes in experimental data. Fogler *et al.* [64] have estimated the magnetic field B_c where the classical Drude description breaks down as

$$B_c = \frac{\sqrt{m^*E}}{ed} \left(\frac{v_0}{E} \right)^{\frac{2}{3}}, \quad (3.24)$$

where E is the energy of the electrons which can be estimated as the Fermi energy and d is the correlation length of the bare potential which is, in difference to a , not yet corrected with the average over the spread of the wave function. The estimation of the critical magnetic field B_c is based on a comparison of the cyclotron radius with the correlations length of the potential and on a comparison of the cyclotron energy with the drift energy taking into account that the bare potential has to be averaged over one cyclotron orbit.

Reference [6] contains an experimental high temperature magneto-resistance study. They find at a temperature of 40K and magnetic fields $B > 5\text{T}$ for the longitudinal

effective resistivity $\rho_L^e \propto B^\alpha$ with $\alpha = [0.9, 1.1]$. For the effective conductivity, this gives

$$\sigma_L^e = \frac{\rho_L^e}{(\rho_L^e)^2 + \rho_H^2} \approx \frac{\rho_L^e}{\rho_H^2} \propto \frac{B^\alpha}{B^2} \propto B^{\alpha-2}, \quad (3.25)$$

as $\rho_H \gg \rho_L^e$ in the experimental range considered. Thus $\kappa = 2 - \alpha = [0.9, 1.1]$ which leads to a critical exponent slightly larger than the one predicted in the last chapter. However, the extraction of the critical exponent from the magnetic field dependence is difficult, as in practice only a small window of magnetic field strength is usable. The magnetic field has to be high enough to be in the high field regime, but small enough that $k_B T \gg \hbar \omega_c / 4$ holds.

The authors of [6] compare their result to the theoretical predictions of [65] who study the interplay of a long-range correlated random potential and short range scattering on antidots⁴. They claim that their results are also applicable to unstructured two dimensional electron gases. There, the role of the antidots is played by what we encode in σ_0 . The authors of [65] find $\alpha = 10/13$ in the strict limit $B \rightarrow \infty$. On a first glance, this seems to be in contradiction with our result $\kappa \approx 10/13$. The relation $\kappa = 2 - \alpha$ was derived for the experimental accessible region where $\sigma_H \ll \sigma_L$. But as $\sigma_L^e \propto B^{-\kappa}$, $\sigma_H \propto B^{-1}$ and $\kappa < 1$, the longitudinal conductance will overtake the Hall conductance at high enough magnetic fields leading to $\sigma_L^e \propto 1/\rho_L^e$ and $\alpha = \kappa$ in this limit. So the result of [65] is consistent with our result, but cannot be used to describe experiments at moderate magnetic fields.

3.4. Temperature Dependence of the Peak Conductivity

Expression (3.21) can also be used to describe the temperature dependence of the effective longitudinal conductivity at constant magnetic field, but only if the chemical potential μ is known. We recall from chapter 1.5 that the transition from one plateau to the next in the Hall conductivity and the peaks in the longitudinal conductivity occur, when the extended states in the middle of a Landau band are filled. As the centers of the disorder broadened Landau bands are at the energies of the Landau levels $E_n = \hbar \omega_c (n + 1/2)$, the chemical potential in the plateau transition regions is given by

$$\mu = \hbar \omega_c \left(n + \frac{1}{2} \right) \quad (3.26)$$

4. Antidots are small potential hills which can be formed in a two dimensional electron gas by lithographic etching.

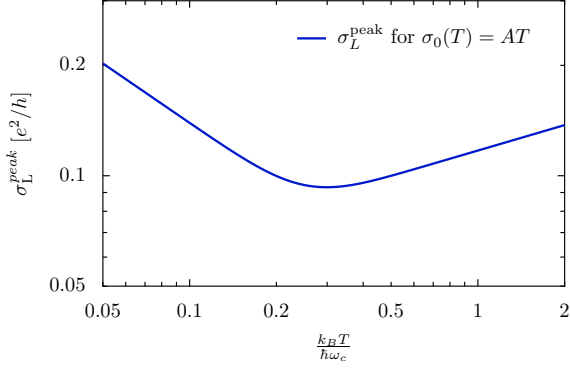


Figure 3.1: Temperature dependence of the effective peak longitudinal conductivity from equation (3.27) in logarithmic scale. A crossover occurs at $k_B T^* = \hbar \omega_c / 4$ between a low- T power law $[\sigma_L^{peak} \propto T^{1-2\kappa}]$ and a high- T power law $[\sigma_L^{peak} \propto T^{1-\kappa}]$.

leading to

$$\sigma_L^{peak}(T) = C[\sigma_0(T)]^{1-\kappa} \left[\frac{e^2}{h} \frac{\sqrt{\langle V^2 \rangle}}{\hbar \omega_c} \right]^\kappa \left[1 + \sum_{l=1}^{\infty} \frac{4\pi^2 l \frac{k_B T}{\hbar \omega_c}}{\sinh \left(2\pi^2 l \frac{k_B T}{\hbar \omega_c} \right)} \right]^\kappa. \quad (3.27)$$

In section 3.1, we have seen that the local phonon contribution to the Ohmic conductivity depends linearly on temperature $\sigma_0(T) = AT$. Figure 3.1 shows a plot of the resulting longitudinal conductivity. Inspecting this plot and the last factor in equation (3.27), we notice two temperature regimes. For $k_B T > \hbar \omega_c / 4$, the infinite sum does not contribute, the temperature dependence of the effective longitudinal conductance is uniquely given by the temperature dependence of σ_0 leading to the high temperature power law $\sigma_L^{peak} \propto T^{1-\kappa}$. For $k_B T < \hbar \omega_c / 4$, the infinite sum is bigger than one and the effective longitudinal conductance follows the power law $\sigma_L^{peak} \propto T^{1-2\kappa}$, as can be inferred from the alternative equation (3.14).

This low temperature power law valid on the conductivity peaks differs from the power law $\sigma_L^e \propto T^{-10/13} e^{-\Delta/T}$ with the cyclotron gap Δ valid on the plateaus of σ_H between two Landau levels found by [66, 67].

The experimental literature measuring conductivity versus temperature mostly concentrates on temperatures much smaller than the regime we studied. V. Renard provided us with the data used to study the magnetic field dependence of the effective longitudinal resistivity, which allow to extract some data points for the temperature dependence of the longitudinal effective conductivity at the peak values. I point to section 3.5.2 for a comparison with this data and with more detailed data of a recent experiment that was motivated by our present calculation.

3.5. Experimental Data

In this section I will compare the theoretical results to experimental data obtained by B. Piot *et al.* [5] at the LNCMI in Grenoble and by V. Renard *et al.* (partially

	No.	Aspect ratio L_x/L_y	Density $[cm^{-2}]$	Mobility at 1.2K $[cm^2/Vs]$
Sample 1	NU573	6	$4 \cdot 10^{11}$	$3.3 \cdot 10^5$
Sample 2	NRC1649	3	$7 \cdot 10^{11}$	$8 \cdot 10^4$
Sample 3	Renard218	—	$1.9 \cdot 10^{11}$	$4.3 \cdot 10^5$

Table 3.1.: Characteristics of the samples used for the presented measurements.

published in [6]).

The experiment is a standard, lock-in amplified, four point Hall measurement: The sample is cooled down to temperatures between 1K and 50K. Coils provide a variable magnetic field in z -direction. A current of the order of 20nA is injected along the long side of the Hall bar. To this end, the Hall bar is connected in series with a resistance of 100M Ω and a low frequency voltage (~ 10 Hz, 2V) is applied. With the four lateral contacts, the longitudinal and the Hall voltage is measured. The small voltage signal is amplified with a preamplifier and a lock-in amplifier, which is the reason to apply a modulated current.

The samples are delta-doped GaAs Hall bars with the densities and mobilities given in table 3.1. The mobilities have been purposely chosen in the hope that they are high enough that one can assume the potential to be smooth, but low enough that spin-splitting can be neglected.

From the measured voltages the longitudinal R_{xx} and transverse R_{xy} resistances are calculated and we get the effective conductivity by the following formula:

$$\sigma_{xx} \left[\frac{e^2}{h} \right] = \frac{\rho_{xx}}{\rho_{xx}^2 + \rho_{xy}^2} \frac{h}{e^2} = \frac{R_{xx} \frac{L_y}{L_x}}{\left(R_{xx} \frac{L_y}{L_x} \right)^2 + (R_{xy})^2} \frac{h}{e^2} \quad (3.28)$$

where L_x and L_y are the dimensions of the two dimensional electron gas which are of the order of half a millimeter.

3.5.1. Longitudinal Magneto-Conductance

Figure 3.2 shows the longitudinal magneto-conductance of the two samples measured by B. Piot *et al.* [5] at 47K and 50K respectively. The crossover between the low field Drude behavior and the high field regime is clearly visible. To illustrate it further, the low field part has been fitted with the Drude formula given in equation (3.23) and presented as blue curves. The end of validity of the Drude formula lies between one and two Tesla. The estimation of Fogler *et al.* [64] (equation (3.24)) predicts the break down already at $B_c = 0.5$ T if we use $d = 1 \cdot 10^{-8}$ m, $v_0 = k_B \cdot 3$ K and take for E the chemical potential at the transition between the Hall conductance plateaus eight and

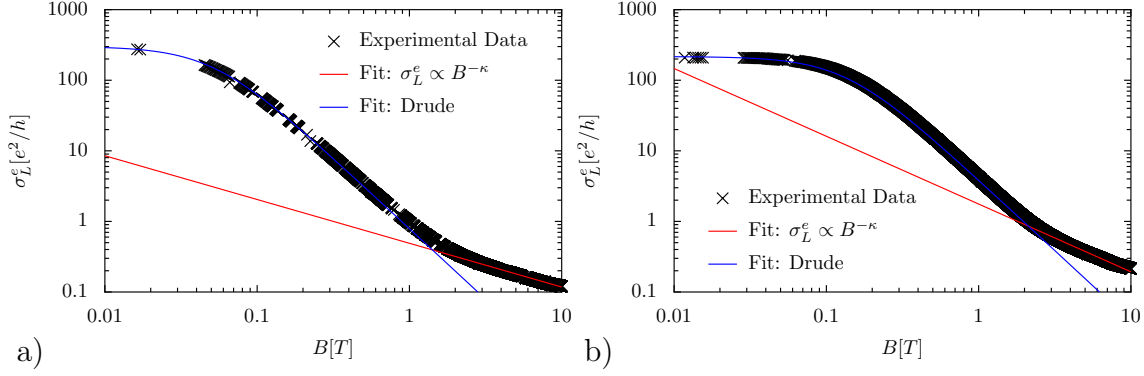


Figure 3.2.: Effective longitudinal magneto-conductivity for sample 1 and sample 2. Fit with the Drude formula (equation (3.23)), valid at low magnetic fields and with the formula given in equation (3.22), valid in the regime of the quantum Hall effect. a) sample 1, $T = 47K$, $\tau = 7.43 \cdot 10^{-12}s$, $\kappa = 0.62$, b) sample 2, $T = 50K$, $\tau = 2.85 \cdot 10^{-12}s$, $\kappa = 0.96$, (data by B. Piot et al. [5])

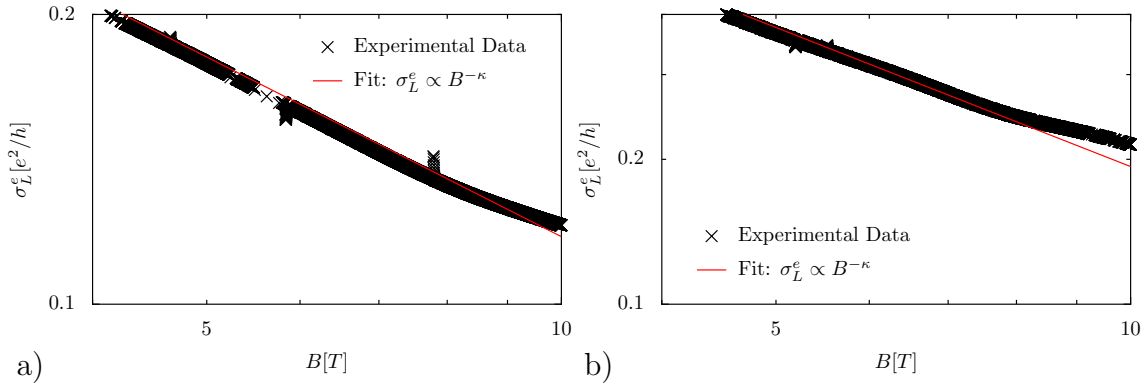


Figure 3.3.: Zoom into the high field part of the effective longitudinal conductivity plots shown in figure 3.2. Deviations from the $\sigma_L^e \propto B^{-\kappa}$ law are clearly visible for magnetic field values higher than 8T, as $k_B T$ becomes comparable to $\hbar \omega_c / 4$. a) sample 1, $T = 47K$, $\kappa = 0.62$, b) sample 2, $T = 50K$, $\kappa = 0.96$, (data by B. Piot et al. [5])

ten occurring at 1.7T in the first sample, so that $E = \mu = \hbar\omega_c(4 + 1/2) \approx 2 \cdot 10^{-21} J$. However, equation (3.24) is only an estimation and we do not know precisely what values for d and v_0 should be taken. If we use for example $v_0 = k_B \cdot 10K$, the critical field reaches one Tesla.

The zoom into the high field part presented in figure 3.3 shows that there is a second crossover. Equation (3.22) predicts a power law behavior of the magneto-conductance in the high magnetic field high temperature range. But it is only valid if the inequality $\hbar\omega_c \ll k_B T/4$ holds. Otherwise, we have to go back to equation (3.21) and use more terms in the sum. If we ask e.g. the $l = 1$ term to be smaller than 0.1 using the effective mass of electrons in GaAs, we can use equation (3.22) at $T = 47K$ up to magnetic fields of 8.6T. We try to extract κ from the interval $2.7T < B < 8.7T$ and get $\kappa = 0.62 \pm 0.05$ for the first sample and $\kappa = 0.96 \pm 0.05$ for the second sample. However, the magnetic field interval is too small for an accurate determination of the critical exponent κ . The longitudinal conductivity for very high magnetic fields $B > 8.7T$ eludes a simple analytical treatment. First, for the application of equation (3.21) the chemical potential μ would have to be determined self consistently. Second, the spin is clearly split and its role is more complicated than a global factor two. If one takes the Zeeman effect into account, the reexpression of the sum over Landau levels with the Poisson sum formula is still possible:

$$\begin{aligned} & \sum_{\sigma=\pm 1} \frac{d}{d\mu} \sum_{m=0}^{\infty} n_F(E_m - \mu + \sigma E_z) \\ &= \frac{-1}{\hbar\omega_c} \left[2 + \sum_{l=1}^{\infty} (-1)^l 4 \cos\left(\frac{2\pi l \mu}{\hbar\omega_c}\right) \cos\left(\frac{2\pi l E_z}{\hbar\omega_c}\right) \frac{2\pi^2 l \frac{k_B T}{\hbar\omega_c}}{\sinh\left(2\pi^2 l \frac{k_B T}{\hbar\omega_c}\right)} \right]. \end{aligned} \quad (3.29)$$

At first glance, only a constant phase $\cos(2\pi l E_z/(\hbar\omega_c)) = \cos(gm^*/(2m))$ has to be added. But there are exchange interaction effects between the two spin species [20] which have to be taken into account with an effective g-factor. As the effective g_{eff} factor is expected to vary in the considered magnetic field range from its bulk value $g = 0.43$ [19] up to the order of ten [21], the analysis of the data is impossible as long as no independent information about the field dependence of g_{eff} is available.

3.5.2. Temperature Dependence of the Peak Conductivity

As discussed in section 3.4, the longitudinal effective conductivity is most conveniently evaluated at the plateau transition values. At low temperatures, the longitudinal effective conductivity as a function of the magnetic field features clear maxima and the effective conductivity is taken at the peak positions, varying slightly the magnetic field. At higher temperature, the maxima are washed out (see figure 3.4a). Therefore, the measurement is then done at constant B-fields. The peaks to be studied have to be chosen at high enough magnetic fields in order to be in the

quantum Hall regime, but at the same time at low enough fields that the two spin species are not yet split. On figure 3.4a, we see that the conductivity peak marked with a green arrow is already split at $T = 1.2\text{K}$, therefore, we can only use it at higher temperatures, so that the green points in figure 3.4b start accordingly only at 2.5K . The figures 3.4b-d show double logarithmic plots of the effective longitudinal peak conductivity for the three samples. The measurements in all three samples feature two different regimes: a high temperature regime with positive slope and a low temperature regime with negative slope. To compare the experimental data with our theoretical predictions and to extract the critical exponents, they are fitted with

$$\sigma_L^{peak}(T) = AT^{1-\kappa} \left| 1 + \sum_{l=0}^{l=12} \frac{4\pi^2 l \frac{k_B T}{\hbar \omega_c}}{\sinh\left(2\pi^2 l \frac{k_B T}{\hbar \omega_c}\right)} \right|^\kappa. \quad (3.30)$$

There are only two fit parameters: κ and A . Their values are given in table 3.2. The cyclotron frequency ω_c is not a fit parameter but is calculated using the literature value of the effective electron mass in GaAs [19]: $m^* = 0.067m_e$. The value of the cyclotron frequency ω_c determines the position of the minimum of the curve and it is remarkable that it appears at the right positions for all samples. For the sample NU573, shown on figure 3.4b, measured points and fit curve are in excellent agreement. This analysis confirms also that there is a linear temperature dependence of σ_0 on the whole temperature range. For the peak at the $10 \rightarrow 8$ transition (blue), the values of the critical exponent κ is in good agreement with the theoretical prediction. The agreement diminishes with increasing magnetic field value of the peak position. One explanation could be that spin splitting effects, despite the precautions taken to avoid them, play an increasing role.

In the sample NRC1649 the fitted curves deviate clearly from the measurements for high temperatures. To rule out the possibility that the poor agreement is a consequence of (3.30) being only valid in the limit of vanishing σ_0 , we also tried a fit with

$$\sigma_{xx} \approx (A_1 \cdot T) \left[1 + \frac{A_2}{\kappa} \frac{\left\{ 1 + \sum_{l=0}^{l=12} \frac{4\pi^2 l \frac{k_B T}{\hbar \omega_c}}{\sinh\left(2\pi^2 l \frac{k_B T}{\hbar \omega_c}\right)} \right\}^2}{(A_0 + A_1 T)^2} \right]^{\frac{\kappa}{2}}. \quad (3.31)$$

This is the equation one obtains from the second order interpolation between the percolation and the dissipative regime (see equation (2.93)). But the resulting curves and the fitted values for κ stay the same. Inspection of A_1 and A_2 show that $A_2 \gg A_1$ and therefore the summand one in the parentheses in equation (3.31) is negligible and we recover equation (3.30). A second, perhaps more likely explanation for the deviations is that the approximation $(\omega_c \tau_{ph})^2 \gg 1$ used for the derivation of the linear temperature dependence of σ_0 is not valid. We redo the fits with $\sigma_0 \propto A_1 * (T/(1 + A_2 T^2))^{1-\kappa}$. The resulting plots are shown in figure 3.5 and the

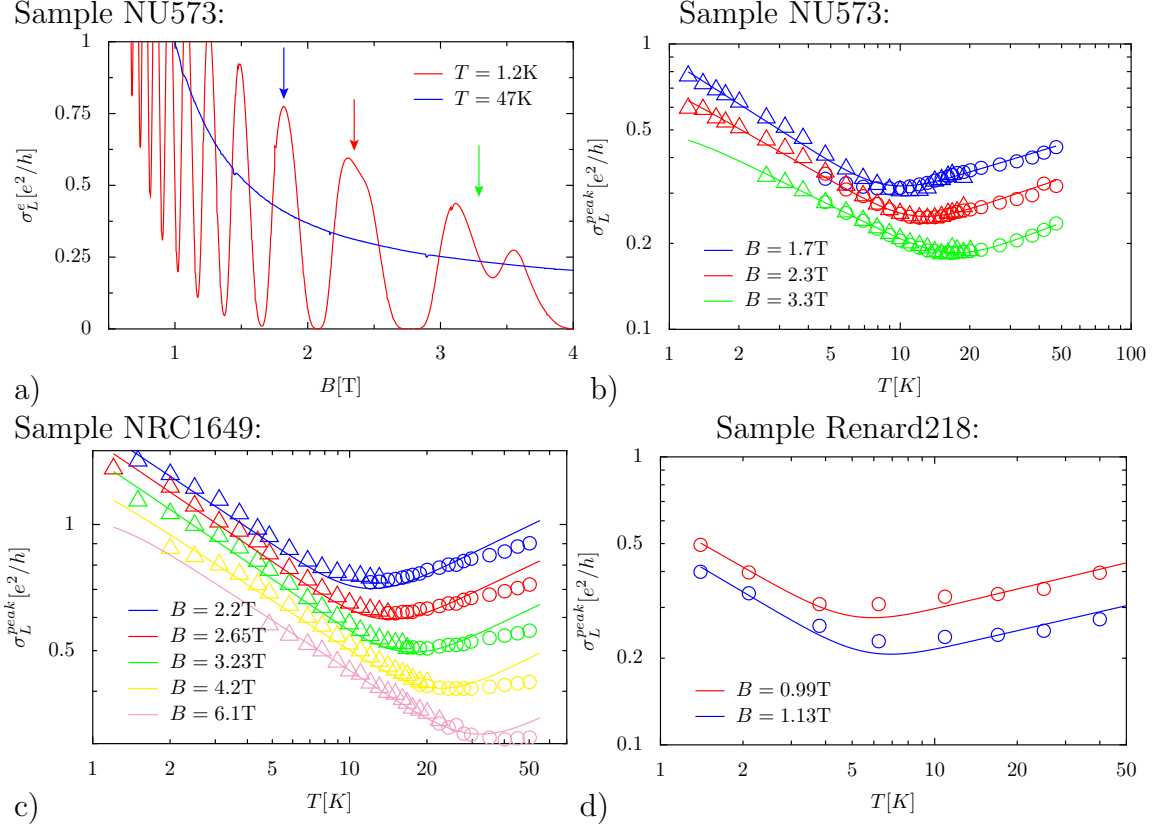


Figure 3.4.: a) Longitudinal effective conductivity as a function of the magnetic field. At low temperature ($T = 1.2K$), there are clearly distinguishable resistance peaks. At higher temperature ($T = 47K$), these peaks are washed out. Therefore, the measurement is then done at constant B -fields. The arrows indicate the conductivity peaks studied for the sample NU573 (data by B. Piot et al. [5]).

b) Temperature dependence of the longitudinal effective conductivity at the indicated magnetic field values corresponding to the integer quantum Hall transitions $10 \rightarrow 8$ (blue), $8 \rightarrow 6$ (red), $6 \rightarrow 4$ (green) for sample NU573 (Data B. Piot et al. [5]). Triangles design values measured at the conductance peaks, circles values at the indicated B fields (see text). The lines are the fit curves with equation (3.30) and the fit parameters given in table 3.2.

c) as b), but for sample NRC1649 (data by B. Piot et al. [5])

d) as b), but for sample Renard218 (data by V. Renard et al., partially published in [6])

Sample	$B[T]$	$\omega_c[K]$	$A[\frac{h}{e^2}K^{\kappa-1}]$	κ
NU573	1.7 ± 0.1	34 ± 2	0.16 ± 0.01	0.76 ± 0.01
NU573	2.3 ± 0.1	46 ± 2	0.115 ± 0.002	0.729 ± 0.005
NU573	3.3 ± 0.1	64 ± 2	0.071 ± 0.002	0.697 ± 0.006
NRC1649	2.2 ± 0.1	43 ± 1	0.34 ± 0.03	0.695 ± 0.005
NRC1649	2.65 ± 0.05	53 ± 1	0.260 ± 0.004	0.723 ± 0.004
NRC1649	3.23 ± 0.05	65 ± 2	0.198 ± 0.003	0.709 ± 0.004
NRC1649	4.2 ± 0.1	83.2	0.153 ± 0.005	0.723 ± 0.006
NRC1649	6.1 ± 0.3	122 ± 4	0.101 ± 0.003	0.698 ± 0.005
Renard218	0.99	19.9	0.175 ± 0.004	0.77 ± 0.01
Renard218	1.13	22.7	0.129 ± 0.003	0.78 ± 0.01

Table 3.2.: Values of the fit parameters for the data shown in figure 3.4. The error bars on the B -field values indicate the scatter of the positions of the conductivity peaks at low temperature. This leads to a uncertainty in the cyclotron frequency and in the conductivities at higher temperatures. The error bars on A and κ were determined by error propagation of these effects. For the sample Renard218 the raw data were not available and the error bars indicated for A and κ reflect only the incertitude of the fit.

fit-parameters in table 3.3. The additional fit parameter allows a better adaptation to the measured points. However, now the fit-curves will decrease for temperatures higher than $\approx 40K$, a trend which is not visible in the measured data points. All exponents found from the second sample are slightly lower than the theoretically predicted exponent.

The third measurement by V. Renard *et al.*, whose initial purpose was not to determine the temperature dependence at the peak values suffers from a lack of data points. The extracted values of the critical exponent are in good agreement with the theoretical prediction.

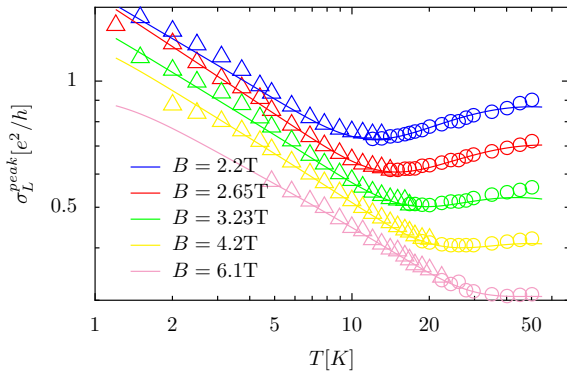


Figure 3.5: Temperature dependence of the effective longitudinal conductivity for sample NRC1649 (data by B. Piot *et al.* [5]), fitted supposing for temperature dependence of the Ohmic longitudinal conductivity to be $\sigma_0 \propto A_1 * (T/(1+A_2T^2))^{1-\kappa}$.

Sample	$B[T]$	$A_1[\frac{h}{e^2}K^{\kappa-1}]$	$A_2[10^{-4}s^{-2}]$	κ
NRC1649	2.2 ± 0.1	0.31 ± 0.01	4 ± 1	0.68 ± 0.01
NRC1649	2.65 ± 0.05	0.26 ± 0.01	3.2 ± 0.3	0.701 ± 0.004
NRC1649	3.23 ± 0.05	0.20 ± 0.01	5.2 ± 0.7	0.686 ± 0.003
NRC1649	4.2 ± 0.1	0.15 ± 0.01	4 ± 0.1	0.688 ± 0.001
NRC1649	6.1 ± 0.3	0.100 ± 0.005	3 ± 1	0.698 ± 0.005

Table 3.3.: Values of the fit parameters for the data of sample NRC1649 shown in figure 3.5 fitted supposing the temperature dependence of the Ohmic longitudinal conductivity to be $\sigma_0 \propto A_1 * (T/(1 + A_2 T^2))^{1-\kappa}$.

3.6. Outlook towards Lower Temperatures

In section 3.4, we predicted that the peak longitudinal conductivity scales with $T^{1-2\kappa}$ in the temperature range $v_0 \ll k_B T \ll \hbar\omega_c/4$ which was confirmed by experimental data. What will happen for even lower temperatures? The approach to linearize the conductivity fluctuations (see section 2.5) is then no longer justified. Taking naively the limit of zero temperature in the expression we used so far for the local Hall conductivity yields

$$\sigma_H = \frac{e^2}{h} \sum_m n_F(E_m + V(\mathbf{r}) - \mu) \xrightarrow{T \rightarrow 0} \frac{e^2}{h} [\nu + \Theta(-V(\mathbf{r}) + \mu)]. \quad (3.32)$$

The conductivity jumps between two discrete values. This is exactly the two phase model investigated by [43] that I have presented in section 1.11. The two phase model predicts the height of the conductivity peaks to be in the limit of zero temperature $\sigma_L^{\text{peak}} = e^2/(2h)$ per spin species thus $\sigma_L^{\text{peak}} = e^2/h$ for spin unresolved conductance peaks. This result is exact within the assumptions of the model. However, the saturation of the conductivity has not been observed experimentally. Instead, for low enough temperatures, the peak conductivity decreases again. Figure 3.6 shows an example of such a measurement. Going back to the derivation of the local Hall conductivity in [9], it turns out that a more accurate expression is

$$\sigma_H(\mathbf{r}) = \frac{e^2}{h} \int d^2R \sum_m |\Psi_{m,\mathbf{R}}(\mathbf{r})|^2 n_F(E_m + V(\mathbf{r}) - \mu) \quad (3.33)$$

where $\Psi_{m,\mathbf{R}}(\mathbf{r})$ is a vortex wave function. We will have a closer look on vortex wave functions in the next chapter. For the moment it is enough to now, that these functions are localized on the scale of the magnetic length l_B . The Fermi function varies on the length scale $ak_B T/v_0$ which is for high temperatures much larger than l_B . So, the wave function contribution acts as a delta function, leading to the expression used so far for the Hall conductivity. With decreasing temperature the Fermi function becomes

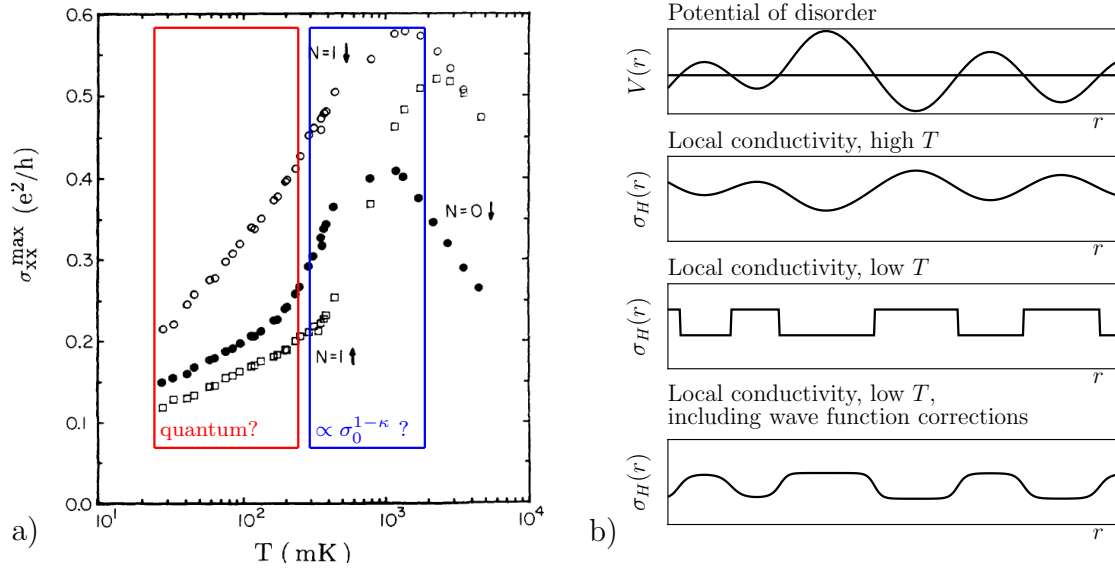


Figure 3.6.: a) Peak longitudinal conductivity at low temperatures [68].
 b) Sketch of the relation between disorder fluctuations and local conductivity. In the high temperature limit, the local Hall conductivity is proportional to the disorder potential. In the naive zero temperature limit the conductivity jumps between the values between $\sigma_H = \frac{e^2}{h}\nu$ and $\sigma_H = \frac{e^2}{h}(\nu + 1)$. The inclusion of the wave function contribution leads to smoother transitions between these two values.

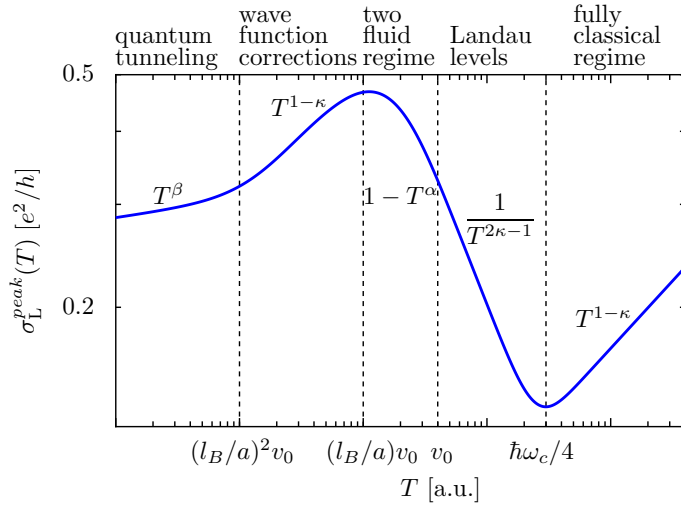


Figure 3.7: Summary of the different power-laws for the temperature dependence of the effective longitudinal conductivity [45].

a sharper step function, varying on a length scale shorter than the wave function contribution $|\Psi_{m,\mathbf{R}}(\mathbf{r})|^2$ which dominates then the spatial width of the transition. As the wave function is localized in the transverse direction on the scale of the magnetic length, the width of the transition between $\sigma_H = (e^2/h)\nu$ and $\sigma_H = (e^2/h)(\nu+1)$ is at low temperatures given by l_B . Consequently the conductivity fluctuations $\sqrt{\langle \delta\sigma_H^2(\mathbf{r}) \rangle}$ are dominated by l_B and independent of temperature at low temperatures. So we expect to find in the temperature interval $(l_B/a)^2 v_0 \ll k_B T \ll (l_B/a) v_0$, as in the very high temperature regime, an effective longitudinal conductivity which is dominated by the phonon contribution:

$$\sigma_L^e \propto \sigma_0^{1-\kappa}. \quad (3.34)$$

This explains qualitatively the drop of the longitudinal effective conductivity at temperatures lower than 1K which can be seen in figure 3.6. At even lower temperatures, yet another regime enters. There, the local conductivity approach breaks down, and quantum corrections have to be taken into account. The saturation predicted in the two phase model could be observable in very clean samples, where the window $(l_B/a) v_0 \ll k_B T \ll v_0$ is large enough. The schematic in figure 3.7 summarizes again the different power-laws for the temperature dependence of the effective longitudinal conductivity: In the fully classical regime, the conductivity scales as $T^{1-\kappa}$. With the formation of Landau levels, the exponent becomes negative and σ_L^e scales as $T^{1-2\kappa}$. In the two fluid regime, the conductivity saturates to the value $e^2/(2h)$ per spin species. Wave function corrections lead in the interval $(l_B/a)^2 v_0 \ll k_B T \ll (l_B/a) v_0$ again to a scaling with $T^{1-\kappa}$ before for even lower temperatures the local conductivity model breaks down. In the next chapter, we will study one ingredient needed in the quantum regime: tunneling over saddle points.

3.7. Summary

We have derived theoretically the temperature and magnetic field dependencies of the effective longitudinal conductivity in the classical limit of the quantum Hall regime. They are in good agreement with experimental data and allow the determination of the classical percolation critical exponent κ .

Our theory cannot describe the temperature regime where the thermal energy is comparable to the typical fluctuations of the disorder potential. But we predict that for even lower temperatures the effective longitudinal conductivity will again follow a simple scaling law.

4. Transmission Coefficient through a Saddle Point Electrostatic Potential in the Quantum Hall Regime

After the semi-classical high temperature regime we studied in the last chapters, let us now turn to a purely quantum mechanical problem, the tunneling through saddle points. A quadratic saddle point is simple enough to allow an analytical treatment but on the same time complicated enough to show non-trivial behavior. In experiments, saddle points play a role on both the macroscopic and the microscopic length scale. A lot of experiments performed in two dimensional electron gases use quantum point contacts formed by metallic split gates. For example, in reference [69] interference experiments with electrons are done and quantum point contacts are used as beam splitters. On the microscopic level, the saddle points of the disorder potential form bottle-necks for transport and it is at the saddle points where a semi-classical description fails first at low temperature. The transmission probability of saddle points is a key ingredient of percolation network models [14, 37].

The saddle point problem is described by the Hamiltonian

$$\hat{\mathcal{H}} = \hat{\mathcal{H}}_0 + V(r) \text{ with } V(r) = by^2 - ax^2 + V_0 \quad (4.1)$$

where $\hat{\mathcal{H}}_0$ is given by equation (1.2), a and b are real positive coefficients and V_0 is the electrostatic potential value at the saddle point. Figure 4.1 shows a sketch of a saddle point electrostatic potential with some classical trajectories. At high magnetic fields the classical trajectories follow equipotential lines and a particle with energy lower than the saddle point entering from the left hand side at the position marked with “in” will be reflected by the saddle point, *i. e.* stay at its left hand side and will leave the picture at the position marked with “refl”. Quantum mechanically, there is a certain probability that particles will be transmitted through the saddle point and leave the picture at the position marked with “trans”. It is this transmission probability that we want to calculate in this chapter.

For ordinary two dimensional electron gases, Fertig and Halperin [7] (see section 4.1) have solved the saddle point tunneling problem exactly. They calculate the transmission probability from the quotient of scattering (*i. e.* plane wave like) wave

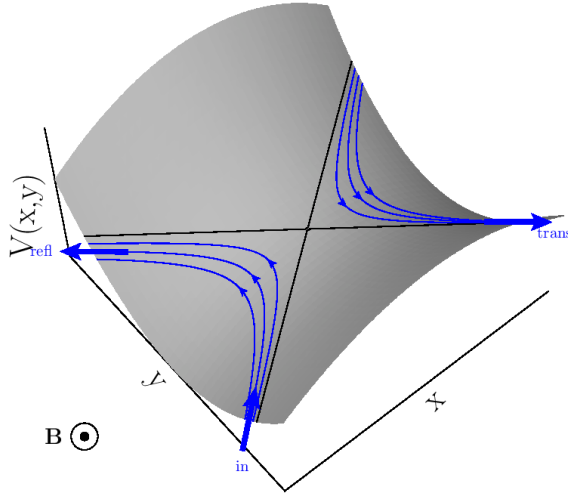


Figure 4.1: Sketch of a saddle point with some classical trajectories at energies lower than the saddle point energy following equipotential lines. If a particle entering at the position marked with “in” follows its classical trajectory to leave at the position marked with “refl”, we speak of reflection. If it is transmitted through the saddle point and leaves the picture at the with “trans” marked position, we speak of transmission.

functions. We develop a different method and extract the transmission probability from vortex Green’s functions [8–10], that I will shortly introduce in section 4.2. Our vortex Green’s function method is a scattering theory with wave packets. The advantage of the vortex Green’s function formalism is that, at least when neglecting Landau level mixing, it can also be applied to graphene, where exact analytical solutions are absent so far. I will present some of the peculiarities of graphene and describe how the vortex Green’s functions have to be adapted to graphene [70] in section 4.4 so that we can calculate the transmission probability through a saddle point for a scalar potential in graphene in section 4.5. The research presented in this chapter has been published in [71], where the main focus lies on the application to graphene.

4.1. The Exact Solution to the Saddle Point Tunneling Problem by Fertig and Halperin [7]

Fertig and Halperin diagonalise the Hamiltonian (4.1) exactly. One part of the difficulty of the saddle point problem is that it is a two dimensional problem depending on the two spatial coordinates x and y and their conjugated momenta. After a series of Bogoliubov transformations, Fertig and Halperin pass from the initial variables x and y to a new set of variables X and s with conjugated momenta P and p , which can be separated. The Hamiltonian can be written as a sum

$$\hat{\mathcal{H}} = \hat{\mathcal{H}}_1(\hat{X}, \hat{P}) + \hat{\mathcal{H}}_2(\hat{s}, \hat{p}) \quad (4.2)$$

of two independent and commuting Hamiltonians $[\hat{\mathcal{H}}_1, \hat{\mathcal{H}}_2] = 0$ depending only on X, P or s, p respectively. The eigenfunctions $\Psi(X, s)$ can be written as a product $\Psi(X, s) = \psi(s)\phi(X)$ of functions depending on X or s . The Hamiltonian $\hat{\mathcal{H}}_2$ turns

out to be a harmonic oscillator with eigennergies $E_n = E_2(n + 1/2)$ where

$$E_2 = \hbar\omega_c \sqrt{\sqrt{\frac{(bl_B^2 + al_B^2)^2}{\hbar^2\omega_c^2} + \frac{1}{4}} + \frac{bl_B^2 - al_B^2}{\hbar\omega_c} + \frac{1}{2} + \frac{bl_B^2 - al_B^2}{\hbar\omega_c}} \quad (4.3)$$

and can be completely eliminated from the problem, leading to a one dimensional tunneling problem, with exactly known scattering eigenstates with eigennergies

$$\epsilon = \frac{E - (n + \frac{1}{2}) E_2 - V_0}{E_1} \quad (4.4)$$

$$\text{with } E_1 = \frac{\hbar\omega_c}{2} \sqrt{\sqrt{\frac{(bl_B^2 + al_B^2)^2}{\hbar^2\omega_c^2} + \frac{1}{4}} + \frac{bl_B^2 - al_B^2}{\hbar\omega_c} - \frac{1}{2} - \frac{bl_B^2 - al_B^2}{\hbar\omega_c}}. \quad (4.5)$$

All these steps are exact and work at arbitrary magnetic fields. The price to pay is that s and X have no general simple physical interpretation. However, in the limit $\omega_c \rightarrow \infty$, the oscillator levels of the Hamiltonian $\hat{\mathcal{H}}_2$ can be identified with the Landau levels, s describes the cyclotron motion and X a guiding center coordinate. At finite magnetic fields, the initial spatial coordinate x is a linear combination of X and s and the spatial coordinate y is a linear combination of P and p . The eigenstates of the one dimensional tunneling problem are composed of two terms, one denoted by ψ_{in} , describing a motion towards the saddle point and one denoted by ψ_{out} describing a motion away from the saddle point. As X is proportional to the initial variable x we can state, that large negative values of X describe a position at the left hand side of the saddle point and large positive values of X describe a position at the right hand side of the saddle point. A linear combination of eigenstates is constructed in a way that the ψ_{in} component vanishes for large positive values of X in order to reproduce the situation sketched in figure 4.1: Particles enter only from the left hand side, but can leave at the right or the left hand side. The transmission coefficient may then be written as

$$T_{1D} = \lim_{X \rightarrow \infty} \frac{|\psi_{out}(X)|^2}{|\psi_{in}(-X)|^2}. \quad (4.6)$$

Once the transmission probability for the one dimensional problem is found the analytical expression for the transmission probability for the whole system is also known:

$$T^{FH} = \frac{1}{1 + e^{-\pi\epsilon}}. \quad (4.7)$$

This result is exact and valid for arbitrary magnetic fields.

4.2. The Vortex Green's Function Formalism

This section gives a short introduction to the vortex Green's function formalism developed by Florens and Champel in [8–10].

As we have seen in section 1.3, the spectrum of the free Hamiltonian (1.2) describing a two dimensional electron gas under a strong magnetic field is highly degenerate, which leads to a wide choice of eigenstate bases. If an additional potential $V(\mathbf{r})$, which lifts the degeneracy, is added, the choice of a basis reflecting the symmetries of the potential simplifies calculations. For the case of a general disorder potential, without global symmetries, the vortex states basis turns out to be convenient. As we have seen in section 1.4 the classical motion of charged particle in a magnetic field can be decomposed into a fast cyclotron motion around a guiding center and a slow drift motion of the guiding center. It is often instructive to separate motions which occur on different time scales. One well known example for such a separation is the Born-Oppenheimer approximation in molecular physics. The approximation consists in writing molecular wave functions as a product of a function describing the slow motion of the cores and a function describing the electron shell, which evolves much faster. Vortex wave functions reflect the classical motion and allow a similar separation of guiding center and cyclotron motion. In difference to the example from molecular physics, this is possible without any approximation. The first quantum number of a vortex wave function is the guiding center coordinate \mathbf{R} , reminiscent of the slow drift motion. Self-interference in closed cyclotron orbits leads to the energy quantification in Landau levels. The second quantum number, the Landau level index m , is therefore a consequence of the fast cyclotron motion. The amplitude of a vortex wave function is centered on a circle around the guiding center. The lateral spread of the vortex wave function is given by the magnetic length l_B . In the symmetrical gauge, $\mathbf{A} = (1/2)\mathbf{B} \times \mathbf{r}$, where \mathbf{r} is an in plane vector (x y) and the vortex wave functions are given by

$$\Psi_{m,\mathbf{R}}(\mathbf{r}) = \langle \mathbf{r} | m, \mathbf{R} \rangle = \frac{1}{\sqrt{2\pi l_B^2 m!}} \left(\frac{z - Z}{\sqrt{2} l_B} \right)^m e^{-\frac{|z|^2 + |Z|^2 - 2Zz^*}{4l_B^2}}, \quad (4.8)$$

with $z = x + iy$ and $Z = X + iY$. Figure 4.2 shows some vortex wave functions.

The scalar product of two vortex functions is

$$\langle m_1, \mathbf{R}_1 | m_2, \mathbf{R}_2 \rangle = \delta_{m_1, m_2} \langle \mathbf{R}_1 | \mathbf{R}_2 \rangle = \delta_{m_1, m_2} e^{-\frac{(\mathbf{R}_1 - \mathbf{R}_2)^2 - 2i\mathbf{u}_z \cdot (\mathbf{R}_1 \times \mathbf{R}_2)}{4l_B^2}} \quad (4.9)$$

with \mathbf{u}_z an unitary vector pointing in the direction of the magnetic field and $\langle \mathbf{R}_1 | \mathbf{R}_2 \rangle = \langle m\mathbf{R}_1 | m\mathbf{R}_2 \rangle$. This tells us that vortex states are orthogonal with respect to the quantum number m , but have coherent state character with respect to the continuous quantum number \mathbf{R} . The wave functions being non-orthogonal makes a perturbation

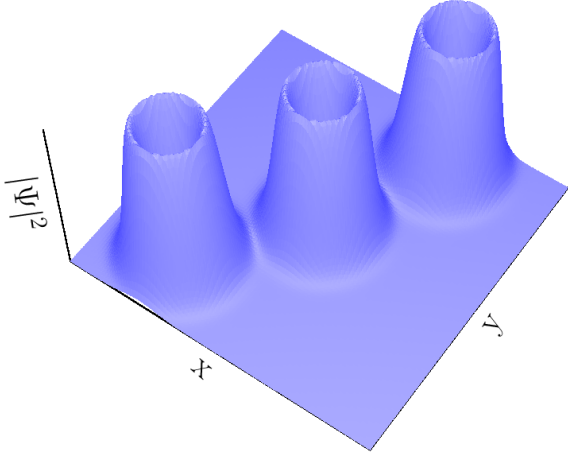


Figure 4.2: Squared amplitude of some vortex wave functions.

theory in wave functions difficult. But they obey the completeness relation

$$\int \frac{d^2\mathbf{R}}{2\pi l_B^2} \sum_{m=0}^{\infty} |m, \mathbf{R}\rangle \langle m, \mathbf{R}| = 1, \quad (4.10)$$

which assures that the expansion of an analytical function in vortex states is unique. So vortex states can be used as basis states in a Green's function formalism.

The projection of the definition of the retarded Green's function

$$(E - \hat{\mathcal{H}}_0 + \hat{V} + i\eta)\hat{G} = \hat{\mathbb{1}} \quad (4.11)$$

with η a small positive quantity into the vortex basis $|\mathbf{R}, m\rangle$ yields

$$\begin{aligned} (\hbar\omega - E_{m_1} + i\eta)G_{m_1, m_2}(\mathbf{R}_1, \mathbf{R}_2) &= \delta_{m_1, m_2} \langle \mathbf{R}_1 | \mathbf{R}_2 \rangle \\ &+ \int \frac{d^2\mathbf{R}_3}{2\pi l_B^2} \sum_{m_3=0}^{\infty} G_{m_1, m_3}(\mathbf{R}_1, \mathbf{R}_3) V_{m_3, m_2}(\mathbf{R}_3, \mathbf{R}_2) \end{aligned} \quad (4.12)$$

where $G_{m_1, m_2}(\mathbf{R}_1, \mathbf{R}_2) = \langle m_1, \mathbf{R}_1 | \hat{G} | m_2, \mathbf{R}_2 \rangle$, $V_{m_1, m_2}(\mathbf{R}_1, \mathbf{R}_2) = \langle m_1, \mathbf{R}_1 | \hat{V} | m_2, \mathbf{R}_2 \rangle$. Let us introduce new functions by extracting the overlap of two vortices from the Green's function and from the potential

$$G_{m_1, m_2}(\mathbf{R}_1, \mathbf{R}_2) = \langle \mathbf{R}_1 | \mathbf{R}_2 \rangle g_{m_1, m_2}(\mathbf{R}_1, \mathbf{R}_2) \text{ and} \quad (4.13)$$

$$V_{m_1, m_2}(\mathbf{R}_1, \mathbf{R}_2) = \langle \mathbf{R}_1 | \mathbf{R}_2 \rangle v_{m_1, m_2}(\mathbf{R}_1, \mathbf{R}_2). \quad (4.14)$$

With them equation (4.12) reads

$$\begin{aligned} (\hbar\omega - E_{m_1} + i\eta)g_{m_1, m_2}(\mathbf{R}_1, \mathbf{R}_2) &= \delta_{m_1, m_2} \\ &+ \int \frac{d^2\mathbf{R}_3}{2\pi l_B^2} \sum_{m_3=0}^{\infty} g_{m_1, m_3}(\mathbf{R}_1, \mathbf{R}_3) v_{m_3, m_2}(\mathbf{R}_3, \mathbf{R}_2) \frac{\langle \mathbf{R}_1 | \mathbf{R}_3 \rangle \langle \mathbf{R}_3 | \mathbf{R}_2 \rangle}{\langle \mathbf{R}_1 | \mathbf{R}_2 \rangle}, \end{aligned} \quad (4.15)$$

4. Transmission Coefficient through a Saddle Point

where after introducing the center-of-mass coordinate $\mathbf{c}_{12} = (\mathbf{R}_1 + \mathbf{R}_2)/2$ and the relative coordinate $\mathbf{d}_{12} = (\mathbf{R}_2 - \mathbf{R}_1)/2$

$$\frac{\langle \mathbf{R}_1 | \mathbf{R}_3 \rangle \langle \mathbf{R}_3 | \mathbf{R}_2 \rangle}{\langle \mathbf{R}_1 | \mathbf{R}_2 \rangle} = e^{-\frac{[\mathbf{R}_3 - (\mathbf{c}_{12} + i\mathbf{d}_{12} \times \mathbf{u}_z)]^2}{2l_B^2}}. \quad (4.16)$$

Supposing the potential $V(x, y)$ to be an analytic function, the matrix element $v_{m_1, m_2}(\mathbf{R}_1, \mathbf{R}_2)$ can be expanded in a series in powers of the magnetic length l_B about the point $\mathbf{R}_{12} = \mathbf{c}_{12} + i\mathbf{d}_{12} \times \mathbf{u}_z$

$$v_{m_1, m_2}(\mathbf{R}_1, \mathbf{R}_2) = \sum_{j=0}^{+\infty} \left(\frac{l_B}{\sqrt{2}} \right)^j v_{m_1, m_2}^{(j)}(\mathbf{R}_1, \mathbf{R}_2) \quad (4.17)$$

$$\begin{aligned} \text{with } v_{m_1, m_2}^{(j)}(\mathbf{R}_1, \mathbf{R}_2) &= \sum_{k=0}^j \frac{(m_1 + k)!}{\sqrt{m_1! m_2!}} \frac{\delta_{m_1+k, m_2+j-k}}{k!(j-k)!} (\partial_X + i\partial_Y)^k \\ &\quad \times (\partial_X - i\partial_Y)^{(j-k)} V(\mathbf{R})|_{\mathbf{R}=\mathbf{R}_{12}}. \end{aligned} \quad (4.18)$$

Instead of projecting equation (4.11) directly into the vortex basis, we could have multiplied it with \hat{G} from the left hand and with \hat{G}^{-1} from the right hand side to obtain $\hat{G}(E - \hat{\mathcal{H}}_0 + \hat{V} + i\eta) = \hat{\mathbb{1}}$. Applying the differential operator $(\partial_{X_1} - i\partial_{Y_2})$ to equation (4.15) and the differential operator $(\partial_{X_2} + i\partial_{Y_2})$ on the equation analogous to equation (4.15) when $\hat{G}(E - \hat{\mathcal{H}}_0 + \hat{V} + i\eta) = \hat{\mathbb{1}}$ is the starting point, one gets the set of differential equations

$$\partial_{X_1} g_{m_1, m_2}(\mathbf{R}_1, \mathbf{R}_2) = i\partial_{Y_1} g_{m_1, m_2}(\mathbf{R}_1, \mathbf{R}_2) \quad (4.19)$$

$$\partial_{X_2} g_{m_1, m_2}(\mathbf{R}_1, \mathbf{R}_2) = -i\partial_{Y_2} g_{m_1, m_2}(\mathbf{R}_1, \mathbf{R}_2). \quad (4.20)$$

This system of differential equations tells us the dependence of the Green's function g on its two spatial variables:

$$g_{m_1, m_2}(\mathbf{R}_1, \mathbf{R}_2) = g_{m_1, m_2}(\mathbf{c}_{12} + i\mathbf{d}_{12} \times \mathbf{u}_z). \quad (4.21)$$

Knowing the general dependence of the Green's functions on their two spatial coordinates, it is enough to study them at coinciding points $\mathbf{R}_1 = \mathbf{R}_2 = \mathbf{R}$. Introducing this simplification into equation (4.15), the integral over \mathbf{R}_3 can be performed analytically, after expanding the matrix elements of $v_{m_1, m_3}(\mathbf{R}, \mathbf{R}_3)$ and $g_{m_3, m_1}(\mathbf{R}_3, \mathbf{R})$ about the point \mathbf{R} , yielding

$$\begin{aligned} (\hbar\omega_c - E_{m_1} + i\eta)g_{m_1, m_2}(\mathbf{R}) &= \delta_{m_1, m_2} + \sum_{m_3=0}^{+\infty} \sum_{k=0}^{+\infty} \left(\frac{l_B}{\sqrt{2}} \right)^{2\kappa} \\ &\quad \times \frac{1}{k!} (\partial_X - i\partial_Y)^k v_{m_1, m_3}(\mathbf{R}) (\partial_X + i\partial_Y)^k g_{m_3, m_2}(\mathbf{R}). \end{aligned} \quad (4.22)$$

With the convention that ∂^g acts only on the Green's function and ∂^v acts only on the matrix element of the potential, we can write equation (4.22) in compacter form

$$(\hbar\omega_c - E_m + i\eta)g_{m_1;m_2}(\mathbf{R}) = \delta_{m_1,m_2} + \sum_{m_3=0}^{+\infty} e^{\frac{l_B^2}{2}(\partial_X^v - i\partial_Y^v)(\partial_X^g + i\partial_Y^g)} v_{m_1,m_3}(\mathbf{R})g_{m_3,m_2}(\mathbf{R}) \quad (4.23)$$

In the limit of vanishing Landau level mixing, *i. e.* $\omega_c \rightarrow \infty$ with l_B finite, the vortex Green's function becomes purely diagonal with $g_{m_1;m_2}(\mathbf{R}) = \delta_{m_1,m_2}g_{m_1}(\mathbf{R})$ and equation (4.23) becomes

$$(\hbar\omega - E_m + i\eta)g_m(\mathbf{R}) = 1 + e^{\frac{l_B^2}{2}(\partial_X^v - i\partial_Y^v)(\partial_X^g + i\partial_Y^g)} v_m(\mathbf{R})g_m(\mathbf{R}). \quad (4.24)$$

Equation (4.24) has the disadvantage of coupling the X and the Y component of Green's function and potential matrix element in a non-trivial way. Even for a one dimensional potential $V = V(X)$ this equation would stay a differential equation of infinite order. The two spatial variables X and Y can be decoupled by introducing the new functions \tilde{g}_m and \tilde{v}_m by applying the convolution operator

$$\hat{A}[f(\mathbf{R})] = e^{-\frac{l_B^2}{4}\Delta_{\mathbf{R}}} = - \int \frac{d\mathbf{u}}{\pi l_B^2} f(\mathbf{u}) e^{\frac{(\mathbf{R}-\mathbf{u})^2}{l_B^2}} \quad (4.25)$$

to the function \tilde{g} and \tilde{v} . After this change of functions, equation (4.24) takes the form

$$(\hbar\omega - E_m + i\eta)\tilde{g}_m(\mathbf{R}) = 1 + e^{i\frac{l_B^2}{2}(\partial_X^v \partial_Y^g - \partial_Y^v \partial_X^g)} \tilde{v}_m(\mathbf{R})\tilde{g}_m(\mathbf{R}) \quad (4.26)$$

which becomes trivial for one dimensional potentials.

The form of the equations (4.24) and (4.26) and the transformation between them are deeply related to the theory of phase space quantization. Besides the use of operators in Hilbert space and the path integral formalism, phase space quantization provides a third approach to quantum mechanics, which is especially well suited to describe the semi-classical limit. In the phase space quantization theory, two concepts play an important role: phase space distribution functions, such as the Wigner- or the Husimi-distribution and for each of these distribution functions a noncommutative operator called star product. A star product is composed of a power series of differential operators acting on the phase space variables which are usually position x and momentum p . The star product connected to the Wigner-function is called the Moyal star product [72] and can be represented as $\star_M = \exp[(i\hbar/2)(\overleftarrow{\partial}_x \overrightarrow{\partial}_p - \overleftarrow{\partial}_p \overrightarrow{\partial}_x)]$, where the arrows indicate if the differential operators act to the right hand or to the left hand side. The star product connected to the Husimi-function is called the Voros star product [73] and reads $\star_V = \exp[(\hbar/2)(\overleftarrow{\partial}_x - i\overrightarrow{\partial}_p)(\overrightarrow{\partial}_x + i\overrightarrow{\partial}_p)]$. The dynamics

of static phase space functions is described by $H \star y = Ey$ [72], the time independent version of the Moyal-equation, where y is a phase space distribution function, H the Hamilton function and \star the star product corresponding to the distribution function. The operators from Hilbert space quantum mechanics corresponding to the phase space variables position and momentum have the commutator relation $[\hat{x}, \hat{p}] = i\hbar$. The X and the Y coordinate of the guiding centers have a similar relationship $[\hat{X}, \hat{Y}] = il_B^2$ [17]. Therefore, in a two dimensional electron gas under a strong magnetic field, the phase space is the real space. Replacing position and momentum by the guiding center coordinates and the reduced Planck constant by the square of the magnetic length, we can identify the differential operator $\exp[(l_B^2/2)(\partial_X^v - i\partial_Y^v)(\partial_X^g + i\partial_Y^g)]$ from equation (4.24) with the Voros star product and the differential operator $\exp[i(l_B^2/2)(\partial_X^v \partial_Y^g - \partial_Y^v \partial_X^g)]$ of equation (4.26) with the Moyal star product. The equations (4.23) and (4.26) are nothing but the defining equations of the Green's functions to the operator $(H_0 \star + V \star - E)$. The operator \hat{A} in equation (4.25) has also an analog in phase space quantization theory. It is the operator which transforms Husimi distributions into Wigner distributions.

An analogous calculation with $\hat{G}(E - \hat{\mathcal{H}}_0 + \hat{V} + i\eta) = \hat{1}$ as starting point yields

$$(\hbar\omega - E_m + i\eta)\tilde{g}_m(\mathbf{R}) = 1 + e^{-i\frac{l_B^2}{2}(\partial_X^v \partial_Y^g - \partial_Y^v \partial_X^g)}\tilde{v}_m(\mathbf{R})\tilde{g}_m(\mathbf{R}). \quad (4.27)$$

If one limits oneself to quadratic order in the potential, the Green's function \tilde{g}_m can be calculated analytically. The potential matrix element for a potential expanded up to quadratic order about the point \mathbf{R}_0 reads

$$\tilde{v}_m(\mathbf{R}) = V(\mathbf{R}_0) + \frac{l_B^2}{2} \left(m + \frac{1}{2} \right) \Delta_{\mathbf{R}} V|_{\mathbf{R}=\mathbf{R}_0}. \quad (4.28)$$

If we insert this expansion into the equations (4.26) and (4.27), the sum of those two equations yields the partial differential equation

$$\begin{aligned} \frac{l_B^4}{8} [(\partial_Y^2 V)\partial_X^2 + (\partial_X^2 V)\partial_Y^2 - 2(\partial_X \partial_Y V)\partial_X \partial_Y] \tilde{g}_m(\mathbf{R}) \\ + [\hbar\omega - E_m - \tilde{v}_m(\mathbf{R}) + i\eta] \tilde{g}_m(\mathbf{R}) = 1 \end{aligned} \quad (4.29)$$

and the difference the constraint

$$(\partial_X V)\partial_Y \tilde{g}_m(\mathbf{R}) - (\partial_Y V)\partial_X \tilde{g}_m(\mathbf{R}) = 0, \quad (4.30)$$

which tells us that $\tilde{g}_m(\mathbf{R})$ has the same equipotential lines as $V(\mathbf{R})$. Thus we use $E(\mathbf{R}) = V(\mathbf{R}) - V(\mathbf{R}_0)$ to write the Green's function as a functional $\tilde{g}_m(\mathbf{R}) = f_m[E(\mathbf{R})]$ and substitute it into equation (4.29) which then becomes an ordinary differential equation

$$\left[(\gamma E + \eta) \frac{d^2}{dE^2} + \gamma \frac{d}{dE} \right] f_m(E) + [\tilde{E}_m - E + i\eta] f_m(E) = 1 \quad (4.31)$$

with

$$\tilde{E}_m = \hbar\omega - E_m - \tilde{v}_m(0), \quad (4.32)$$

$$\gamma = \frac{l_B^4}{4} [\partial_X^2 V \partial_Y^2 V - (\partial_X \partial_Y V)^2]_{\mathbf{R}=\mathbf{R}_0}, \quad (4.33)$$

$$\eta = \frac{l_B^4}{8} [\partial_X^2 V (\partial_Y V)^2 + \partial_Y^2 (\partial_X V)^2 - 2\partial_X V \partial_Y V \partial_X \partial_Y V]_{\mathbf{R}=\mathbf{R}_0}. \quad (4.34)$$

The solution to this differential equation is

$$\tilde{g}_m(\mathbf{R}) = \int_{-\infty}^{\infty} dt h_m^{R,A}(\mathbf{R}_0, t) e^{-i[V(\mathbf{R}) - V(\mathbf{R}_0)]\tau(t)}, \quad (4.35)$$

with

$$h_m(\mathbf{R}_0, t) = \frac{-i\theta(t)}{\cos(\sqrt{\gamma}t)} e^{-i(\eta/\gamma)\tau(t) + i(\tilde{E}_m + \eta/\gamma + i\delta)t}, \quad \tau(t) = \frac{1}{\sqrt{\gamma}} \tan(\sqrt{\gamma}t). \quad (4.36)$$

In the next section we will use this solution to treat the saddle point potential, which is purely quadratic. But this formula is also useful for more complex potentials. If one is interested in local quantities and can choose appropriate expansion points \mathbf{R}_0 , a quadratic approximation will often be sufficient, especially as it is unlikely that the gradient and all three second order derivatives of the potential vanish simultaneously.

4.3. Tunneling over Saddle Points in an Ordinary Two Dimensional Electron Gas

In this section, we calculate the transmission coefficient over a saddle point in the absence of Landau level mixing using asymptotic forms of retarded vortex Greens functions. For this, we have to remember the significance of vortex Green's functions: The Green's function $G_m(\mathbf{R}_1, \mathbf{R}_2, \omega)$ tells us the probability amplitude that a vortex with energy $\hbar\omega$ propagates from the position \mathbf{R}_1 to the position \mathbf{R}_2 . We will do a scattering theory with vortices instead of ordinary wave packets. Let us have a look at figure 4.3, to clarify the notion of reflection and transmission and how they are represented in terms of Green's functions. We choose the saddle point position as the origin of our coordinate system. The classical trajectory for a vortex with energy lower than the saddle point arriving from the left hand side of the saddle point will lead it back to the left hand side. If a vortex with energy lower than the saddle point follows its classical path, we call it reflected, if it arrives at the opposite side of the saddle point, transmitted. The classical trajectory for a vortex with energy higher than the saddle point leads to the right hand side. But we use the convention to call all vortices arriving from the left hand side and staying on the left hand

4. Transmission Coefficient through a Saddle Point

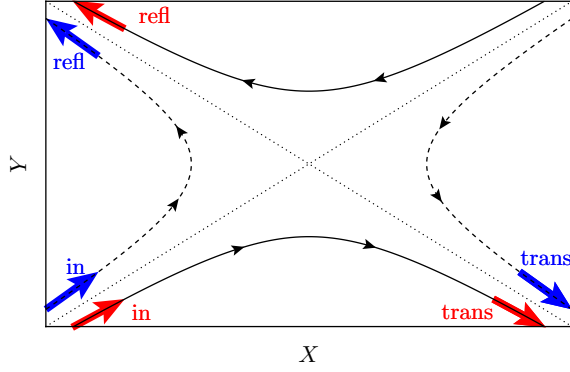


Figure 4.3: Schematic to identify the Green's functions for reflection and transmission. Solid (dashed) lines correspond to an equipotential line $V > 0$ ($V < 0$). Dotted lines denote the asymptotes of the potential in equation (4.1).

side “reflected” and all vortices incoming from the left hand side and outgoing at the right hand side “transmitted”, regardless of their energy. Expressed with the vortex coordinates \mathbf{R}_1 and \mathbf{R}_2 this means that the sign function of the product of X -coordinates $\text{sgn}(X_1 X_2)$ is positive for vortex Green's function describing reflection and negative for vortex Green's functions describing transmission. Far away from the saddle point the Green's functions can be written as products of asymptotic wave functions Ψ^{in} , Ψ^{trans} and Ψ^{refl} . If we denote the transmission amplitude by t , the reflection amplitude by r and the corresponding probabilities by capital letters T and R , we have for the Green's function describing transmission

$$G^{\text{trans}} \propto \Psi^{\text{in}} \Psi^{\text{trans}*} = |\Psi^{\text{in}}|^2 t. \quad (4.37)$$

As the scattering state $|\Psi^{\text{in}}|^2$ is not normalizable, we cannot directly extract the Transmission coefficient from G^{trans} . But as we also know the Green's function describing reflection

$$G^{\text{refl}} \propto \Psi^{\text{in}} \Psi^{\text{refl}*} = |\Psi^{\text{in}}|^2 r, \quad (4.38)$$

we can form the quotient of these two expressions

$$\frac{T}{R} = \left| \frac{t}{r} \right|^2 = \left| \frac{G^{\text{trans}}}{G^{\text{refl}}} \right|^2 \quad (4.39)$$

and with the general relationship $T + R = 1$, we find

$$T = \frac{1}{1 + \left| \frac{G^{\text{refl}}}{G^{\text{trans}}} \right|^2}. \quad (4.40)$$

So, in order to obtain the transmission coefficient, we have to calculate the asymptotic form of the high magnetic field vortex Green's functions $G_m(\mathbf{R}_1, \mathbf{R}_2)$ for the saddle point potential given in equation (4.1), starting from the general solution for the

tilde vortex Green's functions \tilde{g}_m we derived in the last section. The different Green's functions are connected by

$$G_m(\mathbf{R}_1, \mathbf{R}_2, \omega) = \langle \mathbf{R}_1 | \mathbf{R}_2 \rangle g_m(\mathbf{R}_{12}) = \langle \mathbf{R}_1 | \mathbf{R}_2 \rangle e^{\frac{l_B^2}{4} \Delta \mathbf{R}_{12}} \tilde{g}_m(\mathbf{R}_{12}) \quad (4.41)$$

$$\text{with } \mathbf{R}_{12} = \frac{1}{2} [\mathbf{R}_1 + \mathbf{R}_2 + i(\mathbf{R}_2 - \mathbf{R}_1) \times \mathbf{u}_z]. \quad (4.42)$$

We choose the saddle point for both, the coordinate origin and the reference point for the expansion of the potential, so that $\mathbf{R}_0 = 0$ and $V(\mathbf{R}_0) = 0$. The curvature

$$\gamma = \frac{l_B^4}{4} [\partial_X^2 V \partial_Y^2 V - (\partial_X \partial_Y V)^2]_{\mathbf{R}=0} = -l_B^4 ab \quad (4.43)$$

is negative, its roots are complex so that the trigonometric functions in the expression (4.35) of the Green's function $\tilde{g}_m^{R,A}$ have to be replaced by their hyperbolic counterparts $\cos(i\sqrt{|\gamma|t}) = \cosh(\sqrt{|\gamma|t})$ and $\tan(i\sqrt{|\gamma|t}) = i \tanh(\sqrt{|\gamma|t})$. The parameter η can be reexpressed by the product of the curvature and the potential

$$\eta(\mathbf{R}_{12}) = -l_B^4 ab [bY_{12}^2 - aX_{12}^2] = \gamma V(\mathbf{R}_{12}), \quad (4.44)$$

and the tilde Green's function \tilde{g}_m reads for the saddle point

$$\tilde{g}_m(\mathbf{R}_{12}) = \int_0^\infty dt h_m(0, t) e^{-iV(\mathbf{R}_{12})\tau(t)}, \quad (4.45)$$

$$h_m(0, t) = \frac{-ie^{i(\tilde{E}_m + i\eta)t}}{\cosh(\sqrt{|\gamma|t})}. \quad (4.46)$$

To transform the tilde Green's function back, we have to apply to it the differential operator \hat{A} defined in equation (4.25) and get

$$\begin{aligned} g_m(\mathbf{R}_{12}) &= \hat{A}[\tilde{g}_m(\mathbf{R}_{12})] = \int_0^\infty dt h_m(\mathbf{0}, t) \int \frac{d\mathbf{u}^2}{\pi l_B^2} e^{-i(bu_y^2 - au_x^2)\tau(t)} e^{-\frac{(\mathbf{R}_{12} - \mathbf{u})^2}{l_B^2}} \\ &= \int_0^\infty dt h_m(\mathbf{0}, t) \frac{e^{-\frac{\tau(t)(iV(\mathbf{R}_{12}) - \gamma(\mathbf{R}_{12}^2/l_B^2))\tau(t)}{(1+i\zeta+|\gamma|\tau^2)}}}{\sqrt{1+i\zeta+|\gamma|\tau^2}} \end{aligned} \quad (4.47)$$

with

$$\zeta = \frac{l_B^2}{2} \Delta_{\mathbf{r}} V(\mathbf{r}) = l_B^2 (b - a). \quad (4.48)$$

In order to solve the integral over t , we first make the change of variable

$$s = d \frac{1 - |\gamma|\tau^2(t)}{1 + |\gamma|\tau^2(t)} \text{ with } d = \frac{|X_1 Y_2 - X_2 Y_1|}{l_B^2} \quad (4.49)$$

4. Transmission Coefficient through a Saddle Point

which leads to

$$g_m(\mathbf{R}_{12}) = \int_d^0 ds \frac{ide^{-\frac{\sqrt{(d-s)(d+s)}V(\mathbf{R}_{12})+i(d-s)\mathbf{R}_{12}^2/l_B^2\sqrt{|\gamma|}}{\sqrt{(d-s)(d+s)\zeta-2id\sqrt{|\gamma|}}} + \frac{i(\tilde{E}_m+i\eta)\text{arctanh}\left(\sqrt{\frac{d-s}{d+s}}\right)}{\sqrt{|\gamma|}}}}{\sqrt{2(d-s)s(d+s)}(i\sqrt{d^2-s^2}\sqrt{|\gamma|\zeta}+2d|\gamma|)}. \quad (4.50)$$

To calculate the transmission coefficient, it is sufficient to know the asymptotic form of the Green's function $G_m(\mathbf{R}_1, \mathbf{R}_2)$, where the vortex positions \mathbf{R}_1 and \mathbf{R}_2 are asymptotically far away from the saddle point located at the origin. So we will later take the limits $|X_1| \rightarrow \infty$ and $|X_2| \rightarrow \infty$, while $V(X_1, X_2) = V(X_2, Y_2) = \text{const.}$ and we can already simplify the local Green's function $g_m(\mathbf{R}_{12})$, by expanding it about the limit $d \rightarrow \infty$. In the pre-factor it is enough to keep the term proportional to $1/\sqrt{d}$. In the exponent, which contains terms proportional to $X_1 X_2$, we have to keep terms up to linear order. The part of the exponential function containing the hyperbolic area tangent function can be simplified with $\text{arctanh}(\sqrt{(d-s)/(d+s)}) = 1/2 \ln(2d/s) + O(1/d)^2$ to $(2d/s)^{i(\tilde{E}_m+i\eta)/(2\sqrt{|\gamma|})}$, so that we get

$$\lim_{d \rightarrow \infty} g_m(\mathbf{R}_{12}) = g_m^\infty(\mathbf{R}_{12}) = \frac{-i(2d)^{-\frac{1}{2} + \frac{i(\tilde{E}_m+i\eta)}{2\sqrt{|\gamma|}}}}{\sqrt{i\zeta\sqrt{|\gamma|} + 2|\gamma|}} e^{-\frac{V(\mathbf{R}_{12})+i\sqrt{|\gamma|}\mathbf{R}_{12}^2/l_B^2}}{\zeta-2i\sqrt{|\gamma|}}} \int_0^\infty ds s^{-\frac{1}{2} - \frac{i(\tilde{E}_m+i\eta)}{2\sqrt{|\gamma|}}} e^{-s \frac{i\mathbf{R}_{12}^2\sqrt{|\gamma|}}{dl_B^2(\zeta-2i\sqrt{|\gamma|})}}. \quad (4.51)$$

The integral over s can be expressed in terms of the gamma function, defined as

$$\Gamma(z) = x^z \int_0^\infty e^{-xt} t^{z-1} dt, \quad (4.52)$$

if we set $t = s$, $x = i\mathbf{R}_{12}^2\sqrt{|\gamma|}/[dl_B^2(\zeta - 2i\sqrt{|\gamma|})]$ and $z = 1/2 - i(\tilde{E}_m + i\delta)/(2\sqrt{|\gamma|})$. We are looking for asymptotic Green's functions, where the vortices are close to the asymptotes of the saddle point potential $V(\mathbf{R})$. The asymptotes are given by the equations $Y_1 = \sqrt{a/b}X_1$ and $X_2 = -\sqrt{b/a}Y_2$. If we use these relationships in the term replacing x , it simplifies to

$$x = \frac{i\mathbf{R}_{12}^2\sqrt{|\gamma|}}{dl_B^2(\zeta - 2i\sqrt{|\gamma|})} = \frac{i\text{sgn}(X_1 X_2)}{2} \quad (4.53)$$

and with $\ln[i] = i\pi/2$

$$x^{-z} = e^{-z \ln[x]} = 2^{\frac{1}{2} - i\frac{(\tilde{E}_m+i\delta)}{2\sqrt{|\gamma|}}} e^{-\frac{\pi \text{sgn}(X_1 X_2)}{4}} \left(i + \frac{\tilde{E}_m+i\delta}{\sqrt{|\gamma|}}\right), \quad (4.54)$$

so that

$$g_m^\infty(\mathbf{R}_{12}) = \frac{-id^{-\frac{1}{2} + \frac{i(\tilde{E}_m + i\eta)}{2\sqrt{|\gamma|}}}}{\sqrt{i\zeta\sqrt{|\gamma|} + 2|\gamma|}} e^{-\frac{V(\mathbf{R}_{12}) + i\sqrt{|\gamma|}\mathbf{R}_{12}^2/l_B^2}{\zeta - 2i\sqrt{|\gamma|}}} \times \Gamma\left(\frac{1}{2} - i\frac{(\tilde{E}_m + i\delta)}{2\sqrt{|\gamma|}}\right) e^{-\frac{\pi \text{sgn}(X_1 X_2)}{4}\left(i + \frac{\tilde{E}_m + i\delta}{\sqrt{|\gamma|}}\right)}. \quad (4.55)$$

To get the asymptotic two point Green's function $G_m^\infty(\mathbf{R}_1, \mathbf{R}_2)$, we only have to multiply the asymptotic local Green's function with the overlap $\langle \mathbf{R}_1 | \mathbf{R}_2 \rangle$ and get after replacing \mathbf{R}_{12} by its definition (4.42):

$$G_m^\infty(\mathbf{R}_1, \mathbf{R}_2) = \frac{-id^{-\frac{1}{2} + \frac{i(\tilde{E}_m + i\eta)}{2\sqrt{|\gamma|}}}}{\sqrt{i\zeta\sqrt{|\gamma|} + 2|\gamma|}} e^{i\frac{(\sqrt{a}X_1 - \sqrt{b}Y_1)(\sqrt{b}X_1 + \sqrt{a}Y_1) + (\sqrt{a}X_2 + \sqrt{b}Y_2)(\sqrt{b}X_2 - \sqrt{a}Y_2)}{2(a+b)l_B^2}} \times \Gamma\left(\frac{1}{2} - i\frac{(\tilde{E}_m + i\delta)}{2\sqrt{|\gamma|}}\right) e^{-\text{sgn}(X_1 X_2)\left(\frac{i}{4} + \frac{\tilde{E}_m + i\delta}{4\sqrt{|\gamma|}}\right)} e^{-\frac{(\sqrt{a}X_1 + \sqrt{b}Y_1)^2 + (\sqrt{a}X_2 - \sqrt{b}Y_2)^2}{2(a+b)l_B^2}}. \quad (4.56)$$

For the case of a transmitted vortex $\text{sgn}(X_1 X_2) = -1$, for the case of a reflected vortex $\text{sgn}(X_1 X_2) = +1$, so that

$$\frac{T}{R} = \left| \frac{G_m^\infty(\mathbf{R}_1, \mathbf{R}_2)|_{\text{sgn}(X_1 X_2)=-1}}{G_m^\infty(\mathbf{R}_1, \mathbf{R}_2)|_{\text{sgn}(X_1 X_2)=+1}} \right|^2 = \left| e^{+i\frac{\pi}{2} + \frac{\pi}{2}\frac{\tilde{E}_m}{\sqrt{|\gamma|}}} \right|^2 = e^{\pi\frac{\tilde{E}_m}{\sqrt{|\gamma|}}} \quad (4.57)$$

and finally the transmission probability reads

$$T_m^{\text{vortex}} = \frac{1}{1 + e^{-\pi\frac{\tilde{E}_m}{\sqrt{|\gamma|}}}} = \frac{1}{1 + e^{-\pi\frac{\hbar\omega - (\hbar\omega_c + \zeta)(m + \frac{1}{2})}{\sqrt{|\gamma|}}}} = \frac{1}{1 + e^{-\pi\frac{\hbar\omega - (\hbar\omega_c + l_B^2(a-b))(m + \frac{1}{2})}{l_B^2\sqrt{ab}}}}. \quad (4.58)$$

For symmetric saddle points where $a = b$, the standard Landau level energy $E_n = \hbar\omega_c(n + 1/2)$ is compared to the energy scale $l_B^2\sqrt{ab}$ of the saddle point in the exponential part of the expression of the transmission probability. For asymmetric saddle points, the cyclotron pulsation is modified by the term $l_B^2(a - b)$. In reference [74] the transmission probability has been connected via the Landauer-Büttiker formula to the conductance, which reads at zero temperature

$$\mathcal{G}(\mu) = \frac{2e^2}{h} \sum_{m=0}^{+\infty} T_m(\mu), \quad (4.59)$$

where the global factor two accounts for the spin degeneracy. The conductance is thus a step function. The difference between a symmetric and an asymmetric saddle

point will only lie in the length of the steps and will, as the modification is small, be difficult to perceive experimentally.

Let us compare our result obtained with vortex Green's function to the exact result of Fertig and Halperin. Our result was obtained in the limit of $\omega_c \rightarrow \infty$, so we have to take the limit $\omega_c \rightarrow \infty$ in expression (4.4) and get for the transmission coefficient

$$\lim_{\omega_c \rightarrow \infty} T^{FH} = \frac{1}{1 + e^{-\pi \frac{\hbar\omega - (\hbar\omega_c + 2l_B^2(a-b))(m+\frac{1}{2})}{l_B^2 \sqrt{ab}}}}. \quad (4.60)$$

For symmetrical saddle points, our result coincides with the exact result. The exact result, too, predicts a modification of the cyclotron frequency in the case of an asymmetric saddle point. However, this correction is by a factor 2 larger than the one obtained with vortex Green's functions. This deviation is a consequence of the fact that Landau level mixing has been completely neglected. It could be avoided by including the first order corrections for Landau Level mixing.

4.4. Vortex Green's Functions for Graphene

Graphene is an allotrope of carbon where the carbon atoms are arranged in a planar honeycomb lattice. This material, only discovered in 2004, has excited a lot of interest in the last years as it has some unusual properties. First, there is the electron spectrum to mention. In a large number of materials, the low energy electron spectrum is well approximated by the quadratic spectrum of free electrons $E(\mathbf{k}) = \hbar^2 k^2 / (2m)$, if the electron mass m is replaced by the effective mass m^* . This is not the case for graphene [75], where the electron spectrum in the low energy limit is given by $E_+ = \hbar v_F |\mathbf{k}|$ with v_F the Fermi velocity. Second, in graphene, the Fermi-velocity is independent of the electron mass, while in the usual case $v_F = k_F / m$. Third, the hole spectrum is given by $E_- = -\hbar v_F |\mathbf{k}|$ and there is no band gap between the electron and the hole spectrum. From these three properties it follows, that one should not use scalar wave functions to describe graphene, but spinors, vectors with electron- and hole-like elements. The evolution of the spinors is not given by the Schrödinger equation, but by the Dirac equation for massless particles. Graphene is composed of two sub-lattices leading to two valleys in the quasi-particle spectrum. We assume that the two valleys of graphene do not interact and it is enough to take the degeneracy of the two valleys with a factor two into account. Spin degeneracy leads to an additional factor two.

The free Dirac Hamiltonian for a two dimensional graphene sheet in the (x, y) -plane under a strong magnetic field in z -direction is given by

$$\hat{\mathcal{H}}_0 = v_F \begin{pmatrix} 0 & \Pi_x - \Pi_y \\ \Pi_x + \Pi_y & 0 \end{pmatrix} \quad (4.61)$$

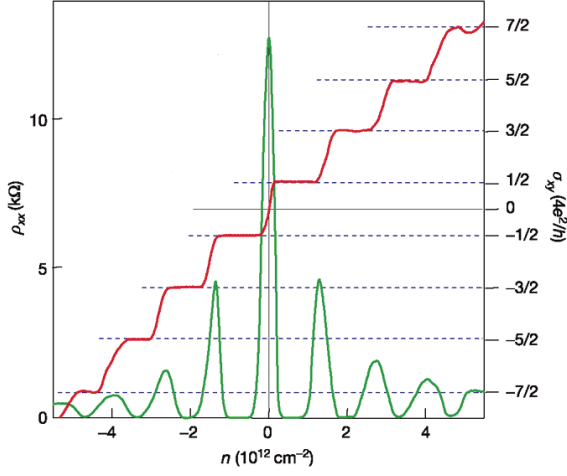


Figure 4.4: Longitudinal and Hall conductivity in graphene as a function of the charge-carrier density at $T = 4K$ and $B = 14T$, showing the anomalous quantum Hall effect in graphene: The plateaus in the Hall conductivity occur at half-integer multiples of the conductance quantum $4e^2/h$. Adapted from [76].

where the canonical momentum $\Pi = -i\hbar\nabla_r - e\mathbf{A}(\mathbf{r})/c$ is defined as in the ordinary case. The corresponding eigenenergies are

$$E_{m,\lambda} = \lambda\sqrt{m}\hbar\Omega_c, \quad (4.62)$$

where the Landau level index m is a non-negative integer, λ is a band index, which is equal to ± 1 if $m \geq 1$ and 0 if $m = 0$ and the equivalent of the cyclotron frequency in graphene is a function of the Fermi-velocity and the magnetic length

$$\Omega_c = \sqrt{2}\frac{v_F}{l_B}. \quad (4.63)$$

In difference to ordinary two dimensional electron gases, there is no zero point energy ($E_{0,0} = 0$) and the Landau level energy increases only as the square root of, not linearly in, the Landau level index. This leads to the anomalous quantum Hall effect: The conductance is quantized in half integer multiples of the conductance quantum ($4e^2/h$ if spin and valley are degenerated) instead of the quantization in integer multiples which is observed for ordinary two dimensional electron gases. Figure 4.4 shows an experimental curve of the conductance. Remarkable is the Landau level which occurs at zero energy.

One possible set of eigenstates for the graphene Dirac Hamiltonian are the graphene vortex states

$$\tilde{\Psi}_{m,\mathbf{R},\lambda}(\mathbf{r}) = \frac{1}{\sqrt{1+|\lambda|}} \begin{pmatrix} \lambda\Psi_{m-1,\mathbf{R}}(\mathbf{r}) \\ i\Psi_{m,\mathbf{R}}(\mathbf{r}) \end{pmatrix}, \quad (4.64)$$

or in Dirac notation

$$|m, \mathbf{R}, \lambda\rangle = \frac{1}{\sqrt{1+|\lambda|}} \begin{pmatrix} \lambda|m-1, \mathbf{R}\rangle \\ i|m, \mathbf{R}\rangle \end{pmatrix}, \quad (4.65)$$

4. Transmission Coefficient through a Saddle Point

composed of the vortex states for ordinary two dimensional electron gases defined in equation (4.8). As the initial vortex states, these vortex states are non-orthogonal with respect to the continuous quantum number \mathbf{R} , but orthogonal with respect to the discrete quantum numbers

$$\langle n_1, \mathbf{R}_1, \lambda_1 | n_2, \mathbf{R}_2, \lambda_2 \rangle = \delta_{n_1, n_2} \langle \mathbf{R}_1 | \mathbf{R}_2 \rangle \delta_{\lambda_1, \lambda_2}, \quad (4.66)$$

where the overlap $\langle \mathbf{R}_1 | \mathbf{R}_2 \rangle$ remains as given in equation (4.9). The graphene vortex states obey the completeness relation

$$\int \frac{d^2 R}{2\pi l_B^2} \sum_{m=0}^{+\infty} \sum_{\lambda} |m, \mathbf{R}, \lambda\rangle \langle m, \mathbf{R}, \lambda| = \mathbb{1}. \quad (4.67)$$

The disorder potential is, like the Hamiltonian, a two by two matrix. Using the Pauli matrices σ_p , $p \in \{x, y, z\}$, and $\sigma_s = \mathbb{1}$ as a basis for the space of quadratic matrices, it can be represented as

$$V(\mathbf{r}) = \sum_{p=s,x,y,z} \sigma_p V_p(\mathbf{r}). \quad (4.68)$$

The different parts of the potential have different physical origins [70]. The diagonal V_s term is called the scalar potential and describes the electrostatic potential and the random disorder potential created by charged impurities. The diagonal but antisymmetric V_z term is called the random mass potential and is usually due to the underlying substrate in single-layer graphene or to the second layer in bilayer graphene. It is energetically favorable for graphene to be not entirely flat, but to form ripples. These spatial distortions of the graphene sheet are described by the off-diagonal contributions V_x and V_y .

The vortex Green's function formalism allows to treat all three types of potentials. But in the following, we will assume the scalar potential to be at most quadratic and the other potentials to be flat, *i. e.* at most linear, in order to simulate quantum point contact experiments.

The graphene vortex Green's function formalism works exactly analogously to the case of an ordinary two dimensional electron gas: The two point graphene vortex Green's functions $G_{m_1, m_2, \lambda_1, \lambda_2}(\mathbf{R}_1, \mathbf{R}_2)$ and the potential matrix elements are defined by projection of the definition of the retarded Green's function $(E - \hat{\mathcal{H}}_0 + \hat{V} + i\eta)\hat{G} = \hat{\mathbb{1}}$ with $\hat{\mathcal{H}}_0$ the Dirac Hamiltonian (4.61) on the vortex states. After extraction of the overlap term a local graphene vortex Green's function $g_{m_1, m_2, \lambda_1, \lambda_2}(\mathbf{R})$ that is entirely defined by its behavior at coinciding points can be found. In the limit of $\omega_c \rightarrow \infty$, the Green's function becomes diagonal in the m -space. The transformation with the exponential differential operator \hat{A} (defined in equation (4.25)) leads again to a modified Green's function $\tilde{g}_{m, \lambda_1, \lambda_2}$ which can be exactly calculated, if the disorder

potential is at most quadratic. The general solution for a flat mass potential and a quadratic scalar potential reads

$$\tilde{g}_{m;\lambda_1;\lambda_2}(\mathbf{R}) = \int_0^\infty dt \frac{-ie^{i(\eta_m^+(\mathbf{R})/\gamma_m^+(\mathbf{R}))[t-\tau_m^+(t)]+it(\hbar\omega+i\eta)}}{\cos(\sqrt{\gamma_m^+(\mathbf{R})t})} h_{m,\lambda_1,\lambda_2}(t) \quad (4.69)$$

$$\text{with } h_{m,\lambda_1,\lambda_2}(t) = \sum_{\epsilon=\pm} \frac{e^{-it\xi_{m,\epsilon}(\mathbf{R})}}{2} [(1 + \epsilon\lambda_1\alpha_m(\mathbf{R}))\delta_{\lambda_1,\lambda_2} + \epsilon\beta_m(\mathbf{R})\delta_{-\lambda_1,\lambda_2}], \quad (4.70)$$

where the effective energy is given by

$$\xi_{m;\pm}(\mathbf{R}) = \tilde{v}_m^+(\mathbf{R}) \pm \sqrt{E_m^2 + [\tilde{v}_m^-(\mathbf{R})]^2}, \quad (4.71)$$

the effective potentials \tilde{v}_m^+ and \tilde{v}_m^- are given by

$$\tilde{v}_m^+(\mathbf{R}) = V_s(\mathbf{R}) + m \frac{l_B^2}{2} \Delta_{\mathbf{R}} V_s(\mathbf{R}) \quad (4.72)$$

$$\tilde{v}_m^-(\mathbf{R}) = -V_z + \frac{l_B^2}{4} \Delta_{\mathbf{R}} V_s(\mathbf{R}) \quad (4.73)$$

the geometric parameters γ_m^+ and η_m^+ by

$$\gamma_m^+(\mathbf{R}) = \frac{l_B^4}{4} [(\partial_X^2 \tilde{v}_m^+)(\partial_Y^2 \tilde{v}_m) - (\partial_X \partial_Y \tilde{v}_m)^2]_{\mathbf{R}}, \quad (4.74)$$

$$\eta_m^+(\mathbf{R}) = \frac{l_B^4}{8} [(\partial_X^2 \tilde{v}_m^+)(\partial_Y \tilde{v}_m^+)^2 + (\partial_Y^2 \tilde{v}_m^+)(\partial_X \tilde{v}_m^+)^2 - 2(\partial_X \partial_Y \tilde{v}_m^+)(\partial_X \tilde{v}_m^+)(\partial_Y \tilde{v}_m^+)] \quad (4.75)$$

$$\text{and } \alpha_m(\mathbf{R}) = \frac{E_m}{\sqrt{E_m^2 + [\tilde{v}_m^-(\mathbf{R})]^2}}, \quad \beta_m(\mathbf{R}) = \frac{\tilde{v}_m^-(\mathbf{R})}{E_m^2 + [\tilde{v}_m^-(\mathbf{R})]^2}. \quad (4.76)$$

4.5. Transmission Coefficients through a Saddle Point Electrostatic Potential for Graphene

Knowing the vortex Green's function for a quadratic scalar potential, we can calculate the transmission coefficient through a saddle point in the scalar potential in absence of a mass potential for graphene in the same way as we calculated the transmission coefficient in an ordinary two dimensional electron gas. Again, we have to calculate the two point Green's function $G_{m,\lambda_1,\lambda_2}(\mathbf{R}_1, \mathbf{R}_2)$ from the Green's function $\tilde{g}_{m,\lambda_1,\lambda_2}(\mathbf{R})$ with which it is connected by

$$G_{m,\lambda_1,\lambda_2}(\mathbf{R}_1, \mathbf{R}_2, \omega) = \langle \mathbf{R}_1 | \mathbf{R}_2 \rangle g_{m,\lambda_1,\lambda_2}(\mathbf{R}) = \langle \mathbf{R}_1 | \mathbf{R}_2 \rangle e^{\frac{l_B^2}{4} \Delta_{\mathbf{R}}} \tilde{g}_{m,\lambda_1,\lambda_2}(\mathbf{R}). \quad (4.77)$$

4. Transmission Coefficient through a Saddle Point

For the purely quadratic saddle point, the geometric parameters γ_m^+ and η_m^+ simplify to $\gamma_m^+ = \gamma = -l_B^4 ab$, $\eta_m^+ = \eta(\mathbf{R}) = \gamma V(\mathbf{R})$ as in the ordinary electron gas and with $\zeta = l_B^2(b - a)$, this leads to the Green's function

$$\tilde{g}_{m;\lambda_1;\lambda_2}(\mathbf{R}) = \int_0^\infty dt \frac{-ie^{it(\hbar\omega + i\eta) - i\tau(t)V(\mathbf{R})}}{\cosh(\sqrt{|\gamma|}t)} h_{m,\lambda_1,\lambda_2}(t) \quad (4.78)$$

$$\text{with } h_{m,\lambda_1,\lambda_2}(t) = \sum_{\epsilon=\pm} \frac{e^{-it\xi_{m,\epsilon}(\mathbf{R})}}{2} [(1 + \epsilon\lambda_1\alpha_m)\delta_{\lambda_1,\lambda_2} + \epsilon\beta_m\delta_{-\lambda_1,\lambda_2}], \quad (4.79)$$

$$\alpha_m = \frac{\sqrt{m}\hbar\Omega_c}{\sqrt{m(\hbar\Omega_c)^2 + \zeta^2/4}}, \quad \beta_m = \frac{\zeta/2}{\sqrt{n(\hbar\omega_c)^2 + \zeta^2/4}}. \quad (4.80)$$

The position dependent part has the same form as before, and the convolution with the operator \hat{A} leads to

$$\begin{aligned} g_{m,\lambda_1,\lambda_2} &= \int \frac{d\mathbf{u}^2}{\pi l_B^2} \tilde{g}_{m,\lambda_1,\lambda_2}(\mathbf{u}) e^{-\frac{\mathbf{u}-\mathbf{R}}{l_B^2}} \\ &= \int_0^\infty dt \frac{-ie^{it\hbar\omega + i\eta}}{\cosh(\sqrt{|\gamma|}t)} h_{m,\lambda_1,\lambda_2}(t) e^{\frac{-i\tau(t)V(\mathbf{R}) + \gamma\tau^2(t)((\mathbf{R}^2/l_B^2))}{1 + i\zeta\tau(t) - \gamma\tau^2(t)}}. \end{aligned} \quad (4.81)$$

Let us now have a closer look at the function

$$h_{m,\lambda_1,\lambda_2} = \begin{pmatrix} 1 + \alpha_m & \beta_m \\ \beta_m & 1 - \alpha_m \end{pmatrix} \frac{e^{-itE_{m,+}}}{2} + \begin{pmatrix} 1 - \alpha_m & \beta_m \\ \beta_m & 1 + \alpha_m \end{pmatrix} \frac{e^{-itE_{m,-}}}{2}. \quad (4.82)$$

For $m \geq 1$ and $\zeta \neq 0$ it is not diagonal in the λ space. It is more convenient to use quantum numbers that are not mixed by the saddle point. The matrix

$$T = \begin{pmatrix} \frac{\alpha_m + 1}{\beta_m} & 1 \\ \frac{\alpha_m - 1}{\beta_m} & 1 \end{pmatrix} \quad (4.83)$$

diagonalizes $h_{m,\lambda_1,\lambda_2}$ and lets us pass from λ to ϵ space

$$Th_{m,\lambda_1,\lambda_2}T^{-1} = \begin{pmatrix} e^{-itE_{m,+}} & 0 \\ 0 & e^{-itE_{m,-}} \end{pmatrix} = e^{-itE_{m,\epsilon}} = h_{m,\epsilon} \quad (4.84)$$

where the function h and with it the entire Green's function is diagonal. From now on we use the quantum number ϵ , which labels the electron-like and the hole-like energy band. We use the same substitution

$$s = \frac{d(1 - |\gamma|\tau^2(t))}{1 + |\gamma|\tau^2(t)} \text{ with } d = \frac{|X_1Y_2 - X_2Y_1|}{l_B^2} \quad (4.85)$$

as in the case of an ordinary two dimensional electron gas and arrive with analogous steps at the asymptotic form of the two point Green's function

$$G_{m;\epsilon}^\infty(\mathbf{R}_1, \mathbf{R}_2) = e^{-\frac{(\sqrt{a}X_1 - \sqrt{b}Y_1)^2 + (\sqrt{a}X_2 + \sqrt{b}Y_2)^2}{2l_B^2(a+b)}} e^{i\frac{(\sqrt{a}X_1 - \sqrt{b}Y_1)(\sqrt{b}X_1 + \sqrt{a}Y_1) + (\sqrt{a}X_2 + \sqrt{b}Y_2)(\sqrt{b}X_2 - \sqrt{a}Y_2)}{2l_B^2(a+b)}} \\ - \frac{id^{-1/2+i(E-E_{n,\epsilon})/(2\sqrt{|\gamma|})}}{\sqrt{2|\gamma| + i\zeta\sqrt{|\gamma|}}} e^{-\sigma\frac{\pi}{4}\left(\frac{E-E_{n,\epsilon}}{\sqrt{|\gamma|}} + i\right)} \Gamma\left(\frac{1}{2} - i\frac{E-E_{n,\epsilon}}{2\sqrt{|\gamma|}}\right). \quad (4.86)$$

For the electron-like energy band with band index $\epsilon = 1$, the extraction of the transmission coefficient works exactly as in the case of the ordinary two dimensional electron gas and

$$\frac{T_{m,+}}{R_{m,+}} = \left| \frac{G_{m,+}^\infty(\mathbf{R}_1, \mathbf{R}_2)_{\text{sgn}(X_1 X_2)=-1}}{G_{m,+}^\infty(\mathbf{R}_1, \mathbf{R}_2)_{\text{sgn}(X_1 X_2)=1}} \right|^2 = \left| e^{\frac{\pi}{2}\left(i + \frac{\hbar\omega E_{m,+}}{\sqrt{|\gamma|}}\right)} \right|^2 = e^{\pi\frac{\hbar\omega - E_{m,+}}{\sqrt{|\gamma|}}}. \quad (4.87)$$

In the valence band, the vortices carry a positive charge. To make later calculations of conductance easier, we want to study the transmission of negative charges and therefore we have to interchange the Green's function for reflection and transmission.

$$\frac{T_{m,-}}{R_{m,-}} = \left| \frac{G_{m,+}^\infty(\mathbf{R}_1, \mathbf{R}_2)_{\text{sgn}(X_1 X_2)=1}}{G_{m,+}^\infty(\mathbf{R}_1, \mathbf{R}_2)_{\text{sgn}(X_1 X_2)=-1}} \right|^2 = \left| e^{-\frac{\pi}{2}\left(i + \frac{\hbar\omega E_{m,-}}{\sqrt{|\gamma|}}\right)} \right|^2 = e^{-\pi\frac{\hbar\omega - E_{m,-}}{\sqrt{|\gamma|}}}. \quad (4.88)$$

The transmission coefficient is thus

$$T_{n,\epsilon}(E) = \left[1 + \exp\left(-\epsilon\pi\frac{E - E_{n,\epsilon}}{l_B^2\sqrt{ab}}\right) \right]^{-1}. \quad (4.89)$$

The transmission coefficient of the lowest Landau level is special, as it is composed to equal parts from the electron and the hole-like contribution, leading to

$$T_0(E) = \frac{1}{2}[T_0^+(E) + T_0^-(E)] = \frac{1}{2}. \quad (4.90)$$

From the transmission coefficients, we can calculate the zero temperature conductance at the chemical potential μ with the Landauer-Büttiker formula [74]

$$\mathcal{G}(\mu) = \frac{4e^2}{h} \left[T_0(\mu) + \sum_{n=1}^{+\infty} \sum_{\epsilon=\pm} T_{n,\epsilon}(\mu) \right], \quad (4.91)$$

where we have accounted for the spin and valley degeneracies in graphene with the overall prefactor 4. The function is shown in figure 4.5. The first observation is the

4. Transmission Coefficient through a Saddle Point

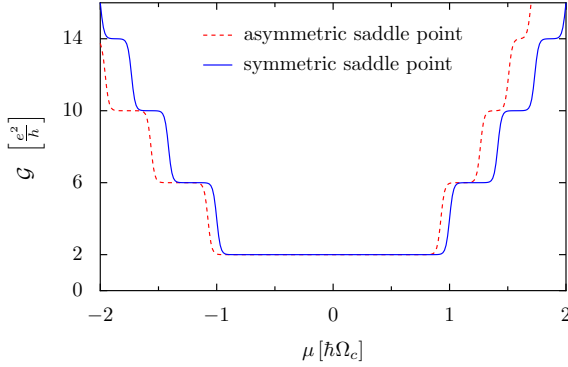


Figure 4.5: Zero-temperature conductance for a saddle point electrostatic potential with $l_B^2 a = l_B^2 b = 0.05\Omega_c$ (symmetric case) and $l_B^2 a = 4l_B^2 b = 0.1\Omega_c$ (asymmetric case). Asymmetries of the electrostatic saddle point potential reflect in asymmetries between the electron and hole sectors for the conductance.

half-integer quantization in terms of the conductance quantum (here $4e^2/h$) with plateau values $(n + 1/2)4e^2/h$, reminiscent of the half-integer quantization of the Hall conductance. At positive energies, current is carried by electrons, at negative energies by holes. The conductance curve for a symmetric saddle point potential, where $a = b$ and thus $\zeta = 0$, represented with a blue solid line, is symmetric for positive and negative energies and has therefore particle hole symmetry. For an asymmetric saddle point, where $a \neq b$ and $\zeta \neq 0$, particle hole symmetry is broken. The red dashed conductance curve for the asymmetric saddle points is not symmetric in energy. The plateau width is, in our example, larger for negative than for positive energies. Although, we know from the case of the ordinary two dimensional electron gas, that one cannot rely quantitatively on the corrections for asymmetric saddle points, we expect that it is qualitatively correct. In difference to the case of an ordinary two dimensional electron gas, the effect of an asymmetric saddle point in graphene should be experimentally observable. For an ordinary two dimensional electron gas, an asymmetric saddle point only leads to a small modification of the plateau width, which would, as an absolute value, be difficult to measure. In graphene, however, one can compare the conductance at positive and at negative energies and the asymmetry should be clearly visible.

4.6. Summary

We have developed a scattering theory of semi-coherent state wave packets based on vortex Green's functions to calculate the transmission coefficients through saddle points. It is applicable to ordinary two dimensional electron gases and to graphene under high magnetic fields.

In the case of the ordinary two dimensional electron gas, we recover for symmetric saddle points the exact result of Fertig and Halperin [7]. For asymmetric saddle points our result differs quantitatively from the exact one, because we have neglected Landau level mixing.

The result for graphene is especially interesting as there exists no exact solution.

While in an ordinary two dimensional electron gas an asymmetry in the saddle point leads only to a redefinition of the cyclotron frequency, it causes an asymmetric energy dependence of the conductance of graphene.

Part II.

Conductance and Differential Current Cross-Correlations in Three-Terminal Normal Conductor-Superconductor-Normal Conductor Hybrid Structures

5. Introduction to Normal Conductor-Superconductor Hybrid Structures

This second part of my thesis deals with three-terminal normal conductor-superconductor hybrid structures. I will concentrate on symmetric structures with one central superconducting electrode and two lateral normal conducting electrodes abbreviated as NSN-systems. In this introductory chapter, I want to motivate, why it is interesting to study these structures and give a short overview over the rich physics connected with them. In the next chapters, I will describe the model I study and present my results.

In section 5.1, I present the nontrivial charge transfer processes which occur at interfaces between normal metals and superconductors. There are propositions to use a three-terminal normal conductor-superconductor hybrid structure as a source of entangled electrons. With entangled electrons one could perform Einstein-Podolsky-Rosen experiments to test the foundations of quantum mechanics or do quantum cryptography. Although these ideas are difficult to implement, they have inspired the research on normal conductor-superconductor hybrid structures and I give a short introduction to this topic in section 5.2. So far NSN-structures have mainly been studied over their conductance, which will be subject of section 5.3. In the last section before the summary of this introductory chapter, we will see, why it is interesting to study, besides conductance, also noise and current cross-correlations.

5.1. Charge Transfer Processes at Interfaces between Normal Conductors and Superconductors

In a superconductor, there are no single electron states for energies smaller than the gap. Therefore, an electron with an energy smaller than the gap arriving from the normal conducting side at a normal conductor-superconductor (NS) interface cannot be transmitted as a single electron. But there are alternative charge transfer processes, which avoid the forbidden single particle transmission: namely local Andreev reflection (AR) and in structures with multiple normal conducting electrodes additionally elastic cotunneling (EC) and crossed Andreev reflection (CAR). The

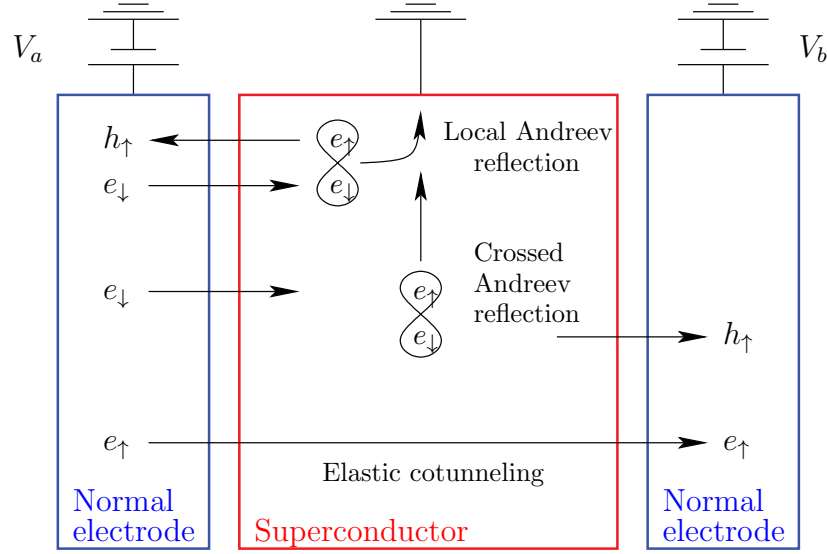


Figure 5.1.: Charge transfer processes at interfaces between normal and superconducting electrodes [77].

three processes are sketched in figure 5.1.

In a local Andreev reflection process, an electron arrives from the normal conducting side and an electron-hole pair is created at the interface. The hole is reflected into the normal metal and the electron forms a Cooper pair with the incoming electron inside the superconductor. The inverse process is also possible: a hole arrives at the interface and recombines with one electron of a Cooper pair. The second electron of the Cooper pair changes over to the normal conductor. In an Andreev reflection process a charge of twice the electron charge is transferred. This process was discovered independently by Saint-James [78, 79] and by Andreev [80], when solving the Bogoliubov-de Gennes equations close to a normal conductor-superconductor interface. Saint-James was interested in the spectrum of a slab of normal metal deposited on the superconductor. He found that the level spacing in a normal metal next to a superconductor is divided by two in comparison to an isolated normal metal. In an isolated normal metal, discrete energy levels are a consequence of the electrons being reflected at the borders of the metal. In a normal metal next to a superconductor, an electron is not directly reflected but transformed into a hole, the hole traverses the normal metal, is reflected at the outer border of the normal metal, returns to the interface with the superconductor and is re-transformed into an electron. This process doubles the way the particles have to traverse and reduces consequently the distance between energy levels by two.

Andreev studied heat conduction over normal metal superconductor interfaces. With the “over-the-barrier reflection of quasi-particles” he found, he was able to explain the reduction of the thermal conductance at normal metal-superconductor interfaces.

It took almost twenty years, until Blonder, Tinkham and Klapwijk used the Bogoliubov-de Gennes equations to study conductance. They included also semi-transparent interfaces, modeled by a δ -potential into their study. We will use a generalization of their method to calculate scattering matrices of normal conductor-superconductor hybrid structures in the next chapter.

If there are two normal electrodes connected to the superconductor within a distance comparable to the coherence length of the superconductor, a variant of this Andreev reflection can occur. Owing to the incidence of an electron, again an electron-hole pair is formed, but the reflection of the hole takes place in an electrode different from the one in which the electron has arrived. One can interpret this process also the other way round: a Cooper pair arrives from the superconducting side and splits up into two electrons which continue in different electrodes. This process is called crossed Andreev reflection (CAR). It is always in concurrence to the process where electrons (or holes) traverse the superconductor by the tunnel effect. In analogy to a similar process in quantum dots, this process is called elastic cotunneling (EC). These non-local processes have been discovered by Byers and Flatté [81] while theoretically investigating how one could detect gap anisotropies by two point scanning tunneling microscopy in order to distinguish s-wave and d-wave superconductors.

With the theoretical method used in this thesis, one can decompose the conductance into its AR, CAR and EC contribution and calculate them separately (see section 6.3). I will discuss experimental observations of EC and CAR processes in section 5.3. Theorists have envisioned devices where the CAR process could be used to create entangled electrons separated in space. This is the subject of the next section.

5.2. Einstein-Podolsky-Rosen Experiments with Electrons

Quantum mechanics is a powerful theory and the accuracy of its predictions has been experimentally verified over and over again. But it contradicts often our intuition and can lead to philosophical questions. In their famous paper [82] Einstein, Podolsky and Rosen, skeptical of quantum mechanics, started the discussion whether quantum mechanics is a complete local realistic theory and found that it is either not local realistic or not complete. Let us have a look at what this means by studying the Bohm variant [83] of the Einstein-Podolski-Rosen (EPR) experiment: A quantum system consisting of two electrons carrying each spin one-half is prepared in a singlet-state (or EPR-state) of total spin zero. If $|\uparrow_i\rangle_\alpha$ and $|\downarrow_i\rangle_\alpha$ describe the spin eigenfunctions of the i -th electron ($i \in \{1, 2\}$) with respect to the axes α , the EPR-state is given by

$$|EPR\rangle = \frac{1}{2}(|\uparrow_1\rangle_\alpha |\downarrow_2\rangle_\alpha - |\downarrow_1\rangle_\alpha |\uparrow_2\rangle_\alpha). \quad (5.1)$$

The next step is to separate the two electrons without destroying their spin entanglement. Afterwards, the spins of the two electrons are measured in two independent, spacelike separated measurements along, let us say, either the z or the x -axes. Spacelike separated events are events that occur at a distance so long and at time difference so short that the ratio between them is larger than the speed of light. According to Einstein's relativity theory, spacelike separated events cannot influence each other. Quantum mechanics predicts that the result of the measurement of the spin of one electron is plus one-half in fifty percent of the measurements and minus one-half in the other fifty percent of the measurements. This is the case for all axes. If one measures the spin of the two separated electrons along the same but arbitrarily chosen axes, their spins will always be opposite to each other. Here enters the paradox, the z and the x -component of the spin are non-commuting variables. They can, according to Heisenberg's uncertainty principle, not be measured simultaneously with arbitrary precision and a quantum mechanical state cannot have at the same time a well defined spin in z -direction and a well defined spin in x -direction. So, how are the two electrons able to have always opposite spin? The first possibility would be, that the x and the z -component of the spin are fixed already before the measurement is done. In this case, quantum mechanics could be a strictly local theory, but it would be incomplete: Even though the x and the z -component are fixed, they are not described by quantum mechanical states. There have to be hidden parameters. The second possibility would be that the spin is only chosen in the moment it is measured. The two measurements, even though spacelike separated, are not independent. This would make quantum mechanics a non-local theory. Bell formulates in [84] an inequality later know as the Bell inequality, which allows to distinguish between quantum theory and a hidden variable theory. He proposes to measure correlations between the result of the measurement of the spin of electron one in direction \mathbf{a} and of the spin of electron two in direction \mathbf{b} denoted by $P(\mathbf{a}, \mathbf{b})$. The inequality is most often used in a variant of Clauser, Horne, Shimony and Holt [85] which states that for a hidden variable theory

$$S = P(\mathbf{a}', \mathbf{b}) + P(\mathbf{a}', \mathbf{b}') + |P(\mathbf{a}, \mathbf{b}) - P(\mathbf{a}, \mathbf{b}')| \leq 2, \quad (5.2)$$

where \mathbf{a} and \mathbf{a}' are the measurement axes for the first electron, \mathbf{b} and \mathbf{b}' the axes for the second electron and \mathbf{a}' and \mathbf{b} are chosen in a way that $P(\mathbf{a}', \mathbf{b}) = 1 - \delta$ with $0 \leq \delta \leq 1$. Quantum mechanics, however, predicts that values of $S = 2\sqrt{2} > 2$ could be achieved by a an appropriate choice of the measurement axes.

Violations of Bell type inequalities have been measured with photons, where polarization replaces the spin, as entangled photons are much easier to produce, guide and detect. Let me name here only two examples. Aspect and his coworkers take care to measure spacelike separated photons and in their third experiment [86] the axes along which the polarization is measured is only chosen after the creation of the photon pair, to rule out the possibility that the way the source emits its photons is influenced by the choice of the axes along which the spins are later measured.

While in the experiment of Aspect *et al.* [86] the two measurements are already performed at a macroscopic distance of 13m, in reference [87] the two detectors are separated by 18km. It is not easy to determine when a quantum measurement is finished and there are theories saying that one should displace a macroscopic mass after doing a quantum measurement to make sure it is finished. With this large distance it is possible to perform the measurement and move a mass while the two detectors are spacelike separated.

There are few experiments using other quantum systems than photons for an EPR-experiment. In [88] the quantum system is given by two Josephson phase qubits entangled by a resonator. EPR-experiments with electrons have not been performed, yet. There are several difficulties to overcome: The creation of the entangled electron pairs, the transport of the electrons which is more difficult to control in solid state devices, as the electrons do not propagate in vacuum but in a Fermi sea and the detection of entanglement in a stream of electrons, as it is difficult to send electron pairs one by one.

Let us, after this quite lengthy side note on EPR experiments in general, now come back to the versions including NSN-structures. Recher, Sukhorukov and Loss [89] on the one hand and Lesovik, Martin and Blatter [90] on the other hand have proposed two different three-terminal NSN-devices as a source of electrons either entangled in spin or in energy. The idea is that a Cooper pair could in a CAR process split up into two electrons which are separated into two different electrodes. These two electrons would have opposite spins and, if energy is measured from the chemical potential of the superconductor, opposite energies. The CAR process is always in competition with AR and EC processes, which do not lead to entangled electrons. Deutscher and Feinberg [91] proposed to use spin polarized ferromagnets instead of normal metals for the leads to suppress EC. But of course, this configuration would not allow to measure entanglement, as it follows directly from the spin polarization into which lead the spin-up and the spin-down electron will propagate.

In the proposition of Recher *et al.* [89], the normal electrodes are connected to the superconductor via two quantum dots which are in the Coulomb blockade regime. The Coulomb repulsion prevents that more than one electron enters the same dot and consequently impedes AR processes. The two normal conducting electrodes are kept on the same chemical potential to prevent EC processes. If the superconductor is at a higher chemical potential than the two normal electrodes, Cooper pairs split up and tunnel coherently into the two different leads.

In the proposition by Lesovik *et al.* [90], CAR processes are identified by filtering the electrons either in energy to measure spin entanglement or in spin to measure energy entanglement. The idea of energy filtering is further developed in reference [92] where a Bell like inequality is proposed in terms of current cross-correlations. Current cross-correlations would be much easier to measure than particle coincidences needed for the original Bell inequality. One kind of possible energy filters is a Fabry-perot interferometer. In chapter 7, I calculate concretely conductance and current cross-

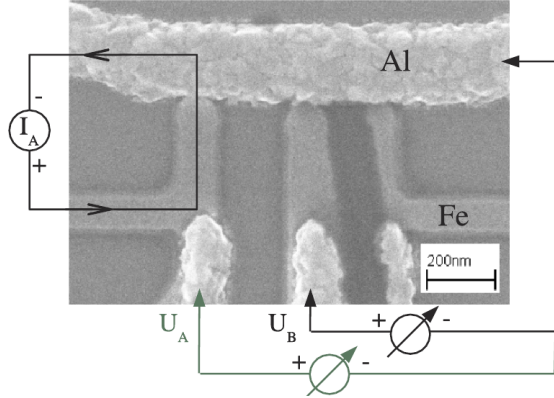


Figure 5.2: Scanning electron image of a sample used in the experiment of Beckmann *et al.* [94] to measure non-local conductance for parallel or anti-parallel spin-polarized electrodes.

correlations for a model system containing two Fabry-Perot interferometers. The idea of energy entanglement has been studied in more detail in [93].

The above described propositions of EPR-experiments in NSN-structures are for the moment out of the range of experiments. But before dreaming of entanglement tests, one should get a more in-depth understanding of the elementary processes in NSN-devices and their influence on conductivity and current cross-correlations. In section 5.3 we will have a look at which experiments in NSN-devices have already been performed. Noise measurements are the next point on the agenda of experimentalists after conductance measurements and we will have a look at what we can learn from current cross-correlations in section 5.4.

5.3. Conductance in Three-Terminal Normal Metal-Superconductor-Normal Metal Devices

The first quantity that has been measured in order to characterize NSN-devices is the conductance and the non-local conductance. There are two ways of measuring non-local conductance. Either a modulated voltage is applied between one normal conducting electrode and the superconductor and the resulting current between the superconductor and the second normal conducting electrode is measured and amplified with a lock-in amplifier, or a modulated current is injected and voltage is measured.

Beckmann *et al.* [94] have implemented the idea of Deutscher and Feinberg [91] to use spin-polarized ferromagnetic electrodes to distinguish between CAR and EC contributions to the non-local conductance. Their sample consists of an aluminum bar, superconducting at temperatures below $T_c \approx 1.15\text{K}$, contacted with iron wires. The prolate form of the iron wires leads to a magnetic shape anisotropy which confines the magnetization to point always along the wire, either towards or away from the superconducting electrode. A current is induced between one iron electrode

and the superconducting aluminum bar (in figure 5.2 marked with I_A) and the non-local voltage (in figure 5.2 marked with U_B) is measured on a second electrode. The observed non-local resistance $R = U_B/I_A$ is slightly different depending on whether the magnetizations in the iron wires are parallel or anti-parallel aligned. This difference is explained as being the consequence of favoring either the EC or the CAR component. If the conductance is measured at higher temperatures, where aluminum is no longer in the superconducting state, spin accumulation effects lead also to a difference between parallel and anti-parallel magnetization. However, the length scale on which the difference in the non-local resistance decreases if the distance between the two iron-wires is increased, is given by the superconducting coherence length if the aluminum bar is in the superconducting state and by the much longer spin-diffusion length if the aluminum bar is in the normal conducting state. This is evidence for the scenario that the different contributions of EC and CAR processes are the reason for the difference in the non-local conductance. On the theoretical side the non-local conductance of spin-polarized multi-probe structures in the tunneling limit has been studied by Falci *et al.* [95] and the decay of the non-local conductance with the coherence length has been predicted. The interfaces in the experiment of Beckmann *et al.* are of medium to high transparency. This regime has been covered by Mélin and Feinberg [96] using a microscopic Green's function formalism which is able to deal with arbitrary interface transparencies. While in the tunneling regime CAR contributes with a positive sign and EC with a negative sign to the non-local conductance, for high interface transparencies and low to intermediate spin polarizations, both processes lead to a negative non-local conductance. Only for high spin polarization the CAR contribution becomes again positive.

Russo *et al.* [97] have studied in the same way, *i. e.* injecting current and measuring non-local voltage, NSN-structures with non-magnetic normal electrodes connected via tunnel barriers to a superconductor. They find that the non-local voltage changes its sign as a function of the amplitude of the injected current. They attribute the positive non-local voltage, which occurs at low current amplitudes, to EC processes and the negative non-local voltages, that occurs at higher current amplitudes, to CAR processes. Again, the signal decreases with increasing width of the superconductor. That there are bias regions where the CAR contribution dominates and bias regions where the EC contributions dominates, was surprising in the light of the non-interacting theories existing in those days [96, 98, 99], which had predicted that the CAR and the EC contribution would cancel each other in the tunneling limit. Yeyati *et al.* [100] were able to explain the result of the experiment of Russo *et al.* within a model including interaction effects. The fact that CAR dominates at low energies can be understood with the simplified picture, that in a CAR process two electrons have to enter the superconductor at the same time, which makes them pay an additional charging energy in comparison to the EC process, where only one electron passes through the superconductor in a virtual state. In figure 5.3 we see the good qualitative agreement between theory and experiment.

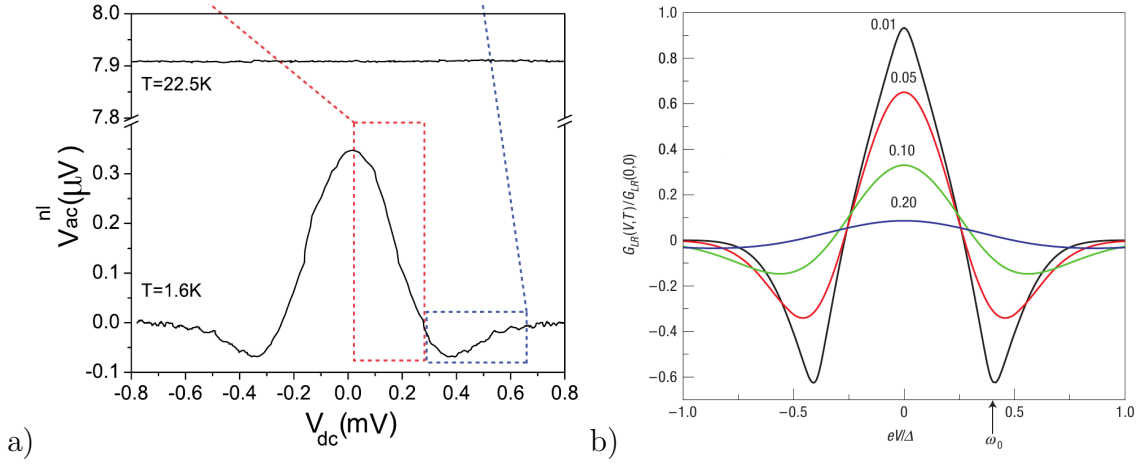


Figure 5.3.: a) Non-local voltage as a function of the injected current ($V_{dc} \propto I$) [97]. The positive non-local voltage observed at low V_{dc} marked with a red box is contributed to EC, the negative signal observed at higher bias marked with a blue box is contributed to CAR. b) Non-local conductance calculated in a model including interaction [100] at different temperatures.

Cadden-Zimansky *et al.* [101, 102] did experiments similar to the two experiments discussed above, but with highly transparent instead of tunnel interfaces. In their sample, one superconducting electrode is contacted by several normal conducting/ferromagnetic electrodes. Using different electrode pairs for their measurement, they can get information about the distance dependence very easily. They find that the observation of CAR and EC processes is further complicated by a third process, charge imbalance: The injection of quasi-particles into the superconductor leads to a non-equilibrium distribution of quasi-particles and Cooper pairs near the NS-interfaces. For the non-local conductance, Cadden-Zimansky *et al.* find a positive signal below the gap which diverges and changes sign when the gap is reached. These results have been theoretically explained by Mélin *et al.* [103] using a model with a self-consistently calculated gap.

Brauer *et al.* [104] found additional oscillations in the non-local conductance in the tunneling regime. To date, there is no theory which explains this experiment. The sample for this experiment has been nano-fabricated by shadow mask evaporation, which leads to additional layers of material where they have not been intended. Parts of the normal metal electrodes are covered by aluminum, so that one could ask if the sample is not rather an SNSNS-device instead of an NSN-device.

The experiments of [105–108] implement the idea to gain control over the conducting process by inserting a quantum dot in the Coulomb blockade regime between the superconducting and the normal metal electrodes (see figure 5.4). The quantum dots are formed in a nanowire contacting the two normal and the superconducting electrodes. The quantum dots can be individually tuned by underlying gates. As an

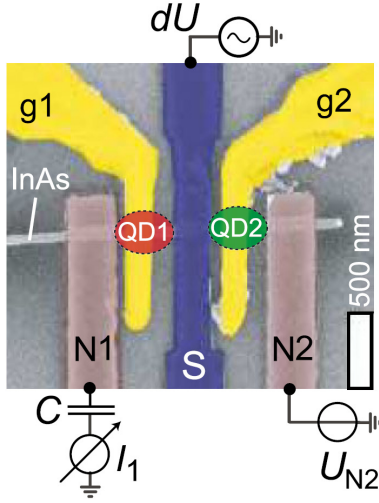


Figure 5.4: False color scanning electron microscope image [105] of a device where a central superconducting electrode is connected to two normal metal electrodes over two quantum dots. The quantum dots are formed in a nanotube contacting the three electrodes. The quantum dots can be individually tuned by the gates $g1$ and $g2$.

example let us have a closer look at one of the experiment of Hofstetter *et al.* [105]. There, the non-local differential conductance over the quantum dot QD1 is measured as a function of the voltage U_{N2} applied to the normal electrode N2 (see figure 5.4). The normal electrode N1 and the superconductor are approximately at the same potential. A small ac-voltage U is applied to the superconductor and the current I_1 on the normal electrode N1 is measured to get the differential conductance $G1 = dI_1/dU$. In figure 5.5a, the deviation $\Delta G_1(U_{N2}) = G_1(-1\text{mV}) - G_1(U_{N2})$ of the non-local conductance from the non-local conductance at 1mV is shown in the situation where the quantum dot QD2 is completely open and the quantum dot QD1 is tuned to have its resonance at slightly negative voltages. With the schematics shown in figure 5.5b-e, we can understand the features of ΔG_1 . Shown are the filled single electron states in the leads (grey), the region where QD1 is transmitting (blue) and the oscillations of the occupation due to the voltage oscillations (red). In figure 5.5b U_{N2} is more negative than the gap. As this configuration is the point of reference for G_1 , ΔG_1 is by definition zero. If the voltage oscillations occur at the energy where the quantum dot QD1 is conducting (figure 5.5c), the rate of EC processes changes. If U_{N2} increases (the number of filled states decreases), EC processes become less likely and ΔG_1 features a dip. If the voltage oscillation occur at minus the energy of the resonance of QD1, the rate with which Cooper pairs split in CAR processes changes. As CAR processes become more likely if U_{N2} increases (the number of filled states decreases) this leads to the peak in ΔG_1 . If U_{N2} is further increased (figure 5.5e) CAR processes are still possible, but their rate does not change and so $\Delta G_1 = 0$.

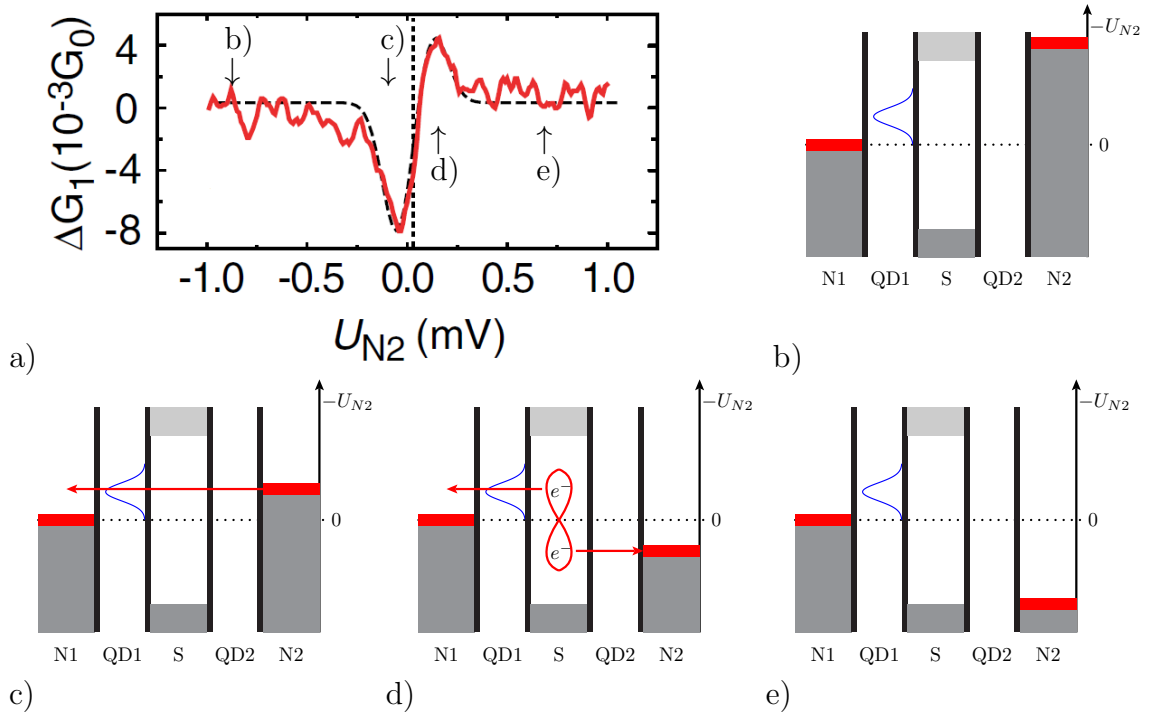


Figure 5.5.: a) Non-local differential conductance [105] of the device shown in figure 5.4. b)-e) Schematics for the interpretation of the non-local conductance curve shown in a), see text.

5.4. Noise and Current Cross-Correlations

Other quantities one can measure in a circuit besides current are noise and current cross-correlations. In macroscopic systems, noise is seen as something annoying, limiting the achievable accuracy of measurements. In mesoscopic systems there are three kinds of noise: $1/f$ -noise, thermal noise and partition noise, where the latter is not a nuisance but carries information about the system, not obtainable in conductance measurements.

The $1/f$ -noise got its name from its inverse proportionality on frequency. A general theory of $1/f$ -noise does not yet exist, but it is supposed that in metals mobile defects are at its origin [109]. $1/f$ -noise limits the accuracy of low frequency measurements.

Thermal noise is a consequence of fluctuations of the thermal occupations of states. For fermionic systems thermal noise vanishes at zero temperature. Thermal noise exists also in equilibrium systems and is via the fluctuation-dissipation theorem connected to the conductance of the system. Therefore, measurements of thermal noise in an equilibrium system give the same information as conductance measurements [110].

Partition noise has its origin in the quantization of charge. It occurs only in out-of-equilibrium systems, e.g. samples where a finite voltage is applied. It carries, for example, information on the statistics of the particles and on the effective charge.

Before motivating why it is interesting to study current cross-correlations, let us define them for a NSN-system: Let \hat{I}_a be the quantum mechanical operator for the current in the normal lead N_a and \hat{I}_b the operator for the current in the normal lead N_b . If we denote quantum mechanical expectation values by brackets $\langle \dots \rangle$ the average current in lead N_a is given by $\langle \hat{I}_a \rangle$, the deviations from the mean by $\Delta \hat{I}_a = \hat{I}_a - \langle \hat{I}_a \rangle$, the current noise by

$$S_{aa}(\tau) = \langle \Delta \hat{I}_a(t) \Delta \hat{I}_a(t + \tau) + \Delta \hat{I}_a(t + \tau) \Delta \hat{I}_a(t) \rangle \quad (5.3)$$

and the current cross-correlations are given by

$$S_{ab}(\tau) = \langle \Delta \hat{I}_a(t) \Delta \hat{I}_b(t + \tau) + \Delta \hat{I}_b(t + \tau) \Delta \hat{I}_a(t) \rangle. \quad (5.4)$$

In my thesis, I study the spectral function of the current fluctuations which is the Fourier transform of equation (5.4) exclusively at zero frequency. This is sufficient, as thermal and partition noise are supposed to be white noise and as $1/f$ -noise is not included in our model.

As we have seen in the last section, it is not easy to distinguish the different contributions to the current. In local conductance measurements the AR component dominates everything and in non-local conductance measurements, the CAR and the EC component are in competition to each other. Bignon *et al.* [98] propose to measure current cross-correlations instead of (non-local) conductance to get access

to the CAR and EC amplitudes. They calculate the current cross-correlations in the tunneling limit and find

$$S_{ab}^{tunnel} = 2e \frac{2e^2}{h} \left[(V_A + V_B) \coth \left(\frac{eV_A + eV_b}{2k_B T} \right) A^{CAR} - (V_a - V_b) \coth \left(\frac{eV_A - eV_b}{2k_B T} \right) A^{EC} \right] \quad (5.5)$$

where A^{CAR} is the amplitude of the CAR and A^{EC} the amplitude of the EC contribution. In the current cross-correlation, the AR component is absent and one can easily distinguish between CAR and EC contributions by choosing the voltages in a way that either $V_a + V_b = 0$ or $V_a - V_b = 0$. I will discuss the decomposition of the current cross-correlations in the different components beyond the tunneling limit in section 6.3.

In purely fermionic systems, current cross-correlations are always negative [12, 111] due to the Fermi-Dirac statistics. However, they can become positive if some kind of interaction is present [112]. The BCS-interaction in a superconductor is such an interaction that can lead to positive current cross-correlations. From equation (5.5) or from the intuitive picture that in a CAR process one Cooper pair splits up into two electrons, while for an EC process no direct interactions with the condensate in the superconductor is needed, one could conclude that CAR processes lead to positive, EC processes to negative current cross-correlations. Even though this conclusion is oversimplified, as we will see in section 6.3, we can say that positive current cross-correlations are always an evidence that something non-trivial is going on. Finally, measurements of current cross-correlations are an important element for the Bell-inequality tests we have seen in section 5.2.

Noise and current cross-correlation measurements are difficult to implement. To date, there exist only a few experiments measuring noise in normal metal- superconductor hybrid structures.

Wei *et al.* [113] have measured the non-local conductance and the voltage cross-correlations in a NSN structure in the tunneling limit. They find the cross-correlations to be always positive, independently of the induced currents I_A and I_B . This is not yet understood theoretically, as existing theories predict negative voltage cross-correlations for asymmetric bias and positive voltage cross-correlations for symmetric bias. But in the experiment of Wei *et al.* already the non-local conductance has an unexpected sign: It is negative for low values of induced currents, which would imply a dominance of CAR, while the experiments and theories we have seen above found always a dominance of the EC effect in the non-local conductance in the low energy tunneling regime.

In the preprint [108], Das *et al.* report positive current cross-correlations in a system where the superconductor is connected via quantum dots in the Coulomb blockade regime to the normal conductors. The positive current cross-correlations occur when

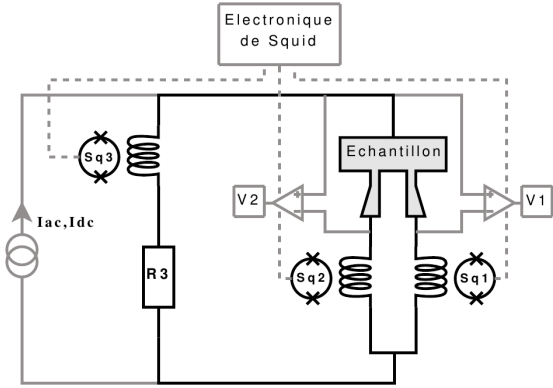


Figure 5.6: Schematic of a circuit for the measurement of current cross-correlations [114].

the quantum dots are at resonance. This makes the interpretation more difficult, as in a quantum dot at resonance the number of electrons on the dot is not well defined and local Andreev reflection is not suppressed.

Kaviraj *et al.* [115] measured noise and current cross-correlations in a three-terminal SNS-structure. The results are less interesting for us, as we want to study NSN-structures. But their measurement device, depicted in figure 5.6, merits to be mentioned, as it allows to measure directly current cross-correlations instead of voltage cross-correlations. Even though the circuit is polarized in current, the sample is effectively voltage biased due to the resistance R_3 in parallel to the sample. The currents flowing via the different arms of the sample are measured via the magnetic field created by them with SQUIDS.¹ To extract the current cross-correlations the SQUID signals of two different SQUIDS are analyzed with a spectral analyzer.

Torrès and Martin have theoretically studied a superconductor connected to a normal electrode which splits up in two electrodes in a beam splitter [116, 117]. They find that current cross-correlations can be both positive or negative depending on the transmission of the beam splitter, the interface transparency between normal and superconductor and the applied voltage. The largest positive current cross-correlations occur for intermediate transmission of the beam splitter, low transparency of the NS-interface and low bias voltage. The positive correlations always disappear for bias voltages higher than the superconducting gap.

Mélin, Benjamin and Martin have studied the geometry where two normal metal electrodes are independently connected to the superconductor using on the one hand scattering theory, where the scattering matrix is calculated in the BTK-approach [11] (see section 6.2), and on the other hand a microscopic Green's function approach based on a tight binding Hamiltonian. Both approaches allow to go beyond the tunneling limit studied by Bignon *et al.* [98] and reveal positive current cross-correlations at high interface transparencies.

1. A SQUID consists of a superconducting ring interrupted by two Josephson-junctions. The Josephson effect leads to a current in the superconducting ring which is extremely sensible on the magnetic flux passing through the ring.

During my master's thesis, I contributed to the article by Freyn, Flöser and Mélin [118], where we have studied the case of a symmetrically biased NSN-structure at arbitrary bias in more detail. We have obtained analytical expressions for current, noise and current cross-correlations in the limit of small bias voltages within scattering theory and we have analyzed the different contributions to the current cross-correlations within the microscopic Green's function approach. We were able to show that positive current cross-correlations do not automatically imply CAR processes.

5.5. Summary

Three-terminal normal conductor-superconductor-normal conductor (NSN) hybrid structures feature transport processes absent in two terminal structures. Of special interest is the process called crossed Andreev reflection (CAR) where a Cooper pair in the superconductor splits up and the resulting electrons are transmitted into two different normal conducting electrodes. This process is the basis for propositions to build a source of entangled electrons. CAR and the competing process elastic cotunneling EC have been observed in several non-local conductance experiments. The study of noise and current cross-correlations could give further insight into the physics of three-terminal NSN-structures. As noise measurements are difficult to implement, experiments on noise and current cross-correlations were only started recently.

In my thesis I continue the work of Sylvie Duhot [119] and of my master's thesis. Like Sylvie Duhot, I study NSN-structures, where additional scattering barriers have been inserted into the normal conducting leads. While Sylvie Duhot concentrated on the non-local conductance of metallic structures, I calculate in addition current cross-correlations and extend my studies to ballistic systems. To gain deeper insight into the microscopic processes leading to negative or positive current cross-correlations, I analyze the different contributions to the current cross-correlations in the framework of scattering theory similar to the analysis in the language of Green's functions of [118].

6. Three-Terminal Normal Metal-Superconductor-Normal Metal Hybrid Structures

This chapter starts with the descriptions of the models that will be studied. The approach by Blonder, Tinkham and Klapwijk [11] (see section 6.2) will allow us to calculate the elements of the scattering matrices of the studied systems. In an NSN-system, the current contains an AR, CAR and EC contribution. Inspired by the decomposition of the current, I will propose a similar decomposition of the current cross-correlations in section 6.3, which will make the following discussion easier. Positive cross-correlations are often equated with CAR. In section 6.4, we will see that current cross-correlations can be positive in absence of CAR processes at high interface transparency. The phenomenon of reflectionless tunneling is a motivation to study symmetric NSN-devices with additional barriers in the normal conducting electrodes (NNSNN-devices), which is the main subject of this chapter. Therefore, reflectionless tunneling will be presented in section 6.5. In section 6.6 metallic NNSNN-systems are studied. There, multidimensional behavior is simulated within a one-dimensional model by mode averaging. The main result of this section is that effects similar to reflectionless tunneling enhance strongly the local AR process, but have little effect on the non-local components EC and CAR as long as the modes in the normal section on the right and on the left hand side of the superconductor are averaged independently.

6.1. The Model

We study one dimensional models of normal metal-superconductor hybrid structures. We are mainly interested in the two symmetric three-terminal normal-superconductor-normal metal hybrid structures depicted in figure 6.1a and c. We will refer to the former one as NSN-structure, to the latter one as NNSNN-structure. To understand the difference between the two of them, it is instructive to study the NNS-structure depicted in figure 6.1b. The central superconducting electrode is grounded, the normal terminals can be biased with voltages V_a and V_b . The length R of the superconducting electrode in the NSN and NNSNN-structure is comparable to the superconducting coherence length, which makes the observation

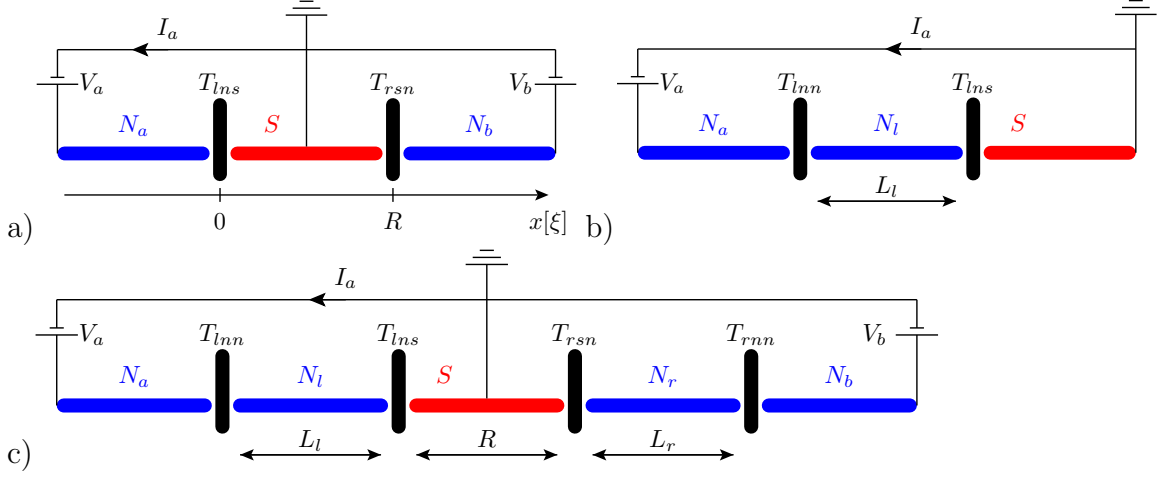


Figure 6.1.: Schematics of the studied models.

of interesting non-local effects possible. The interfaces between the normal metal and the superconducting electrodes are modeled by barriers with transparencies T_{lns} and T_{rsn} . In the NNSN structure there are additional barriers at a distance L_l (respectively L_r) from the normal metal superconductor interface with transparency T_{lnn} (respectively T_{rnn}).

For energies lower than the superconducting gap Δ , the NSN and the NNSN-system can be described by a 4×4 scattering matrix $s_{ij}^{\alpha\beta}$ where Latin indices run over the normal electrodes a and b and Greek indices over electrons e and holes h . For energies lower than the superconducting gap, there are no single electron or hole states in the bulk of the superconducting electrode. Consequently, there is no scattering of electrons or holes in or out of the reservoir in the superconducting electrode and the superconducting electrode does not appear in the scattering matrix. However, the used scattering theory supposes implicitly that the superconductor is a reservoir of Cooper pairs. So it is essential that the superconducting electrode is grounded. The transformation of quasi-particles into Cooper pairs is taken into account by the correlation length ξ with which the electron and hole functions are damped in the superconductor.

The elements of the scattering matrix are evaluated from the BTK approach [11] (see section 6.2). To calculate the current and current cross-correlations, we use the

formulas derived by Anantram and Datta in [12]:

$$I_i = \frac{|e|}{h} \sum_{k \in \{a,b\}} \sum_{\alpha, \beta \in \{e,h\}} \text{sgn}(\alpha) \int dE \left[\delta_{ik} \delta_{\alpha\beta} - |s_{ik}^{\alpha\beta}|^2 \right] f_{k\beta}(E) \quad (6.1)$$

$$S_{ij} = \frac{2e^2}{h} \sum_{k,l \in \{a,b\}} \sum_{\alpha, \beta, \gamma, \delta \in \{e,h\}} \text{sgn}(\alpha) \text{sgn}(\beta) \int dE A_{k\gamma, l\delta}(i\alpha, E) A_{l\delta, k\gamma}(i\alpha, E) f_{k\gamma}(E) [1 - f_{l\delta}(E)] \quad (6.2)$$

with $A_{k\gamma, l\delta}(i\alpha, E) = \delta_{ik} \delta_{il} \delta_{\alpha\gamma} \delta_{\alpha\delta} - s_{ik}^{\alpha\gamma\dagger} s_{il}^{\alpha\delta}$, $\text{sgn}(\alpha = e) = 1$, $\text{sgn}(\alpha = h) = -1$ and $f_{i\alpha}$ the occupancy factors for the electron and hole states in electrode i , given by the Fermi function where the chemical potentials are the applied voltages. In the zero temperature limit to which I limit my studies, the Fermi functions read:

$$f_{ie}(E) = \left[1 + \exp \left(\frac{E - |e|V_i}{k_B T} \right) \right]^{-1} \xrightarrow{T \rightarrow 0} \theta(-E + |e|V_i) \text{ and} \quad (6.3)$$

$$f_{ih}(E) = \left[1 + \exp \left(\frac{E + |e|V_i}{k_B T} \right) \right]^{-1} \xrightarrow{T \rightarrow 0} \theta(-E - |e|V_i). \quad (6.4)$$

In our one-dimensional model, current and noise are highly sensitive to the distances L_l , R , L_r between the barriers: they oscillate as a function of these distances with a period equal to the Fermi wavelength $\lambda_F \ll L_l, R, L_r$. In a ballistic system, the multiple barriers act like a Fabry-Perot interferometer. We study these interference effects and how one can use them to distinguish AR, EC and CAR contributions in chapter 7. In a higher-dimensional system with more than one transmission mode, the oscillations in the different modes are independent and thus they are averaged out. Multi-dimensional behaviour can be simulated qualitatively with a one-dimensional system by averaging all quantities over one oscillation period:

$$\overline{X}(L_l, R, L_r) = \frac{1}{\lambda_F^3} \int_{L_l - \lambda_F/2}^{L_l + \lambda_F/2} dl_l \int_{R - \lambda_F/2}^{R + \lambda_F/2} dr \int_{L_r - \lambda_F/2}^{L_r + \lambda_F/2} dl_r X(l_l, r, l_r). \quad (6.5)$$

This procedure is appropriate to describe qualitatively metallic systems. This chapter is dedicated to these averaged quantities, while we study a ballistic system in the next chapter.

6.2. Calculation of the Scattering Matrix with the approach of Blonder, Tinkham and Klapwijk

The elements $s_{ij}^{\alpha\beta}$ of the scattering matrix are calculated within the approach of Blonder, Tinkham and Klapwijk (BTK)[11]: The one dimensional model of a

normal-metal-superconductor hybrid structure is described by the Bogoliubov-de Gennes equations [120], i.e by an effective Hamiltonian of the form

$$\hat{\mathcal{H}} = \begin{pmatrix} -\frac{\hbar^2 \nabla^2}{2m} - \mu(x) + V(x) & \Delta(x) \\ \Delta(x) & \frac{\hbar^2 \nabla^2}{2m} + \mu(x) - V(x) \end{pmatrix}. \quad (6.6)$$

In the BTK model, the chemical potential $\mu(x)$ is set to the applied voltages, the potential $V(x)$ is zero except for δ -peaks at the interfaces and the superconducting gap $\Delta(x)$ is supposed to be zero in the normal conducting regions and constant in the superconducting regions. In a more realistic model, the gap would have to be determined self-consistently. The approximation of a constant gap leads to a simpler, easier to understand model and allows an analytical treatment for simple cases. For the example of the NSN-structure depicted in figure 6.1a, the potential is given by $V(x) = Z_{lns} \hbar v_F \delta(x) + Z_{rsn} \hbar v_F \delta(R - x)$, where the BTK parameter Z_i is connected to the interface transparency T_i by $T_i = (1 + Z_i^2)^{-1}$. Solutions to this Hamiltonian are two-component wave functions, where the upper component describes electrons and the lower component holes. The solutions in the normal conducting regions are superpositions of right and left moving plane waves with wave vectors close to the Fermi wave vector $\hbar k_F = \sqrt{2m\mu}$. The wave vector for electrons reads $\hbar q^+ = \sqrt{2m\sqrt{\mu + E}}$, the one for holes $\hbar q^- = \sqrt{2m\sqrt{\mu - E}}$. In the superconducting regions the amplitudes of the wave functions have to be modified with the coherence factors u and v which read for energies smaller than the gap ($E < \Delta$):

$$u_E = \frac{1}{\sqrt{2}} \sqrt{1 + \frac{i\sqrt{\Delta^2 - E^2}}{E^2}}, \quad v_E = \frac{1}{\sqrt{2}} \sqrt{1 - \frac{i\sqrt{\Delta^2 - E^2}}{E^2}}. \quad (6.7)$$

In the superconductor, there are two kinds of quasi-particles: electron-like quasi-particles proportional to $(u_E \ v_E)^T$ with wave vector $\hbar k^+ = \sqrt{2m\sqrt{\mu + i\sqrt{\Delta^2 - E^2}}}$ and hole-like quasi-particles proportional to $(v_E \ u_E)^T$ with wave vector $\hbar k^- = \sqrt{2m\sqrt{\mu - i\sqrt{\Delta^2 - E^2}}}$. As we are also interested in the energy dependence of the quantities we calculate, we keep, except if stated otherwise, the full expressions for the wave vectors and do not use the Andreev approximation $q^+ = q^- = k_F$, $k^+ = k_F + i\xi$ and $k^- = k_F - i\xi$ used in the original BTK-paper [11].

As a concrete example, let us have a look at the NSN-system depicted in figure 6.1a. For an electron incoming from electrode N_a , the wave functions in the sections N_a , S and N_b respectively take the form:

$$\begin{aligned} \psi_{N_a}(x) &= \begin{pmatrix} 1 \\ 0 \end{pmatrix} \left(1 e^{iq^+x} + s_{aa}^{ee} e^{-iq^+x} \right) + \begin{pmatrix} 0 \\ 1 \end{pmatrix} \left(s_{aa}^{he} e^{iq^-x} + 0 e^{-iq^-x} \right), \\ \psi_S(x) &= \begin{pmatrix} u_E \\ v_E \end{pmatrix} \left(c_1 e^{ik^+x} + c_2 e^{-ik^+(x-R)} \right) \end{aligned} \quad (6.8)$$

$$+ \begin{pmatrix} v_E \\ u_E \end{pmatrix} \left(c_2 e^{-ik^-x} + c_3 e^{ik^-(x-R)} \right), \quad (6.9)$$

$$\begin{aligned} \psi_{N_b}(x) = & \begin{pmatrix} 1 \\ 0 \end{pmatrix} \left(s_{b,a}^{e,e} e^{iq^+(x-R)} + 0 e^{-iq^+(x-R)} \right) \\ & + \begin{pmatrix} 0 \\ 1 \end{pmatrix} \left(0 e^{iq^-(x-R)} + s_{b,a}^{h,e} e^{-iq^-(x-R)} \right). \end{aligned} \quad (6.10)$$

Using the continuity of the wave functions at the interfaces [$\psi_{N_a}(0) = \psi_S(0)$, *etc.*] and the boundary condition for the derivatives [$\psi'_S(0) - \psi'_{N_a}(0) = Z\hbar v_F \psi_{N_a}(0)$, *etc.*] we get a system of 8 equations. From this system of equations, we can eliminate the coefficients c_i , $i \in \{1, 2, 3, 4\}$ and calculate the scattering matrix elements $s_{a,a}^{e,e}$, $s_{a,a}^{h,e}$, $s_{b,a}^{h,e}$ and $s_{b,a}^{e,e}$. The remaining elements of the scattering matrix can be obtained from the other possible scattering processes *i. e.* a hole incoming from electrode N_a , an electron/hole incoming from electrode N_b . These systems of equations can be written in a compact form with the matrix of coefficients M , which reads for the NSN-case:

$$M = \begin{pmatrix} 1 & 0 & 0 & 0 & -u_E & -e_p u_E & -v_E & -e_m v_E \\ 0 & 1 & 0 & 0 & -v_E & -e_p v_E & -u_E & -e_m u_E \\ 0 & 0 & 1 & 0 & -e_p u_E & -u_E & -e_m v_E & -v_E \\ 0 & 0 & 0 & 1 & -e_p v_E & -v_E & -e_m u_E & -u_E \\ i\frac{q^+}{k_F} - 2Z_{lns} & 0 & 0 & 0 & i\frac{k^+}{k_F} u_E & -i\frac{k^+}{k_F} e_p u_E & -i\frac{k^-}{k_F} v_E & i\frac{k^-}{k_F} e_m v_E \\ 0 & -i\frac{q^-}{k_F} - Z_{lns} & 0 & 0 & i\frac{k^+}{k_F} v_E & -i\frac{k^+}{k_F} e_p v_E & -i\frac{k^-}{k_F} u_E & i\frac{k^-}{k_F} e_m u_E \\ 0 & 0 & i\frac{q^+}{k_F} - 2Z_{rsn} & 0 & -i\frac{k^+}{k_F} e_p u_E & i\frac{k^+}{k_F} u_E & i\frac{k^-}{k_F} e_m v_E & -i\frac{k^-}{k_F} v_E \\ 0 & 0 & 0 & -i\frac{q^-}{k_F} - 2Z_{rsn} & -i\frac{k^+}{k_F} e_p v_E & i\frac{k^+}{k_F} v_E & i\frac{k^-}{k_F} e_m u_E & -i\frac{k^-}{k_F} u_E \end{pmatrix}. \quad (6.11)$$

The equations are for an electron incoming from the left-hand side

$$\begin{aligned} & (s_{aa}^{ee} \ s_{aa}^{he} \ s_{ba}^{ee} \ s_{ba}^{he} \ c_1 \ c_2 \ c_3 \ c_4) \cdot M^T \\ & = \begin{pmatrix} -1 & 0 & 0 & 0 & i\frac{q^+}{k_F} + 2Z_{lns} & 0 & 0 & 0 \end{pmatrix}, \end{aligned} \quad (6.12)$$

for an hole incoming from the left-hand side

$$\begin{aligned} & (s_{aa}^{eh} \ s_{aa}^{hh} \ s_{ba}^{eh} \ s_{ba}^{hh} \ c_1 \ c_2 \ c_3 \ c_4) \cdot M^T \\ & = \begin{pmatrix} 0 & -1 & 0 & 0 & 0 & -i\frac{q^+}{k_F} + 2k_F Z_{rsn} & 0 & 0 \end{pmatrix}, \end{aligned} \quad (6.13)$$

for an electron incoming from the right-hand side

$$\begin{aligned} & (s_{ab}^{ee} \ s_{ab}^{he} \ s_{bb}^{ee} \ s_{bb}^{he} \ c_1 \ c_2 \ c_3 \ c_4) \cdot M^T \\ & = \begin{pmatrix} 0 & 0 & -1 & 0 & 0 & 0 & i\frac{q^-}{k_F} + 2Z_{rsn} & 0 \end{pmatrix} \end{aligned} \quad (6.14)$$

and for a hole incoming from the right-hand side

$$\begin{aligned} & (s_{ab}^{eh} \ s_{ab}^{hh} \ s_{bb}^{eh} \ s_{bb}^{hh} \ c_1 \ c_2 \ c_3 \ c_4) \cdot M^T \\ & = \begin{pmatrix} 0 & 0 & 0 & -1 & 0 & 0 & 0 & -i\frac{q^-}{k_F} + 2Z_{rsn} \end{pmatrix}. \end{aligned} \quad (6.15)$$

coherence length	ξ	1
gap	Δ	$1 \cdot 10^{-4}$
Fermi wave length	k_F	$1 \cdot 10^3$
reduced Planck constant	\hbar	1
effective mass	m	$1 \cdot 10^7$
Fermi energy	μ	$5 \cdot 10^{-2}$

Table 6.1: Parameter values for the numerical calculations.

In the still relatively simple NSN cases and in the limit of zero energy, the system of equations giving the scattering matrix elements can be solved analytically (see [118]). We will use an analytically calculated scattering matrix for the NNS-system when discussing the phenomenon of reflectionless tunneling in section 6.5. But as we are also interested in the energy dependence of the scattering matrix and in the more complicated NNSNN-case, we solve the equations numerically in most of the cases.

The generalization to the NNSNN-case is straightforward. We only have to insert

$$\begin{aligned} \psi_{N_l}(x) = & \begin{pmatrix} 1 \\ 0 \end{pmatrix} \left(c_5 e^{iq^+x} + c_6 e^{-iq^+(x-L_l)} \right) \\ & + \begin{pmatrix} 0 \\ 1 \end{pmatrix} \left(c_7 e^{iq^-x} + c_8 e^{-iq^-(x-L_l)} \right) \end{aligned} \quad (6.16)$$

between the N_a and the S section, and

$$\begin{aligned} \psi_{N_r}(x) = & \begin{pmatrix} 1 \\ 0 \end{pmatrix} \left(c_9 e^{iq^+(x-L_l-R)} + c_{10} e^{-iq^+(x-L_l-R-L_r)} \right) \\ & + \begin{pmatrix} 0 \\ 1 \end{pmatrix} \left(c_{11} e^{iq^-(x-L_l-R)} + c_{12} e^{-iq^-(x-L_l-R-L_r)} \right) \end{aligned} \quad (6.17)$$

between the S and the N_b section. We obtain a system of 64 equations. It can again, after elimination of the c_i , be used to calculate numerically the 16 coefficients of the scattering matrix.

In our problem, the energy scale is given by the superconducting gap Δ and the length scale by the coherence length $\xi = \hbar^2 k_F / (m\Delta)$. Table 6.1 summarizes the parameters used in the numerical calculations. The amplitudes of the non-local processes CAR and EC decrease exponentially with the length R of the superconducting electrode. To get large CAR and EC signals, I use if not indicated otherwise, $R = 0.25\xi$ which is smaller than the length $R \approx \xi$ routinely obtained in experiments. In most cases, larger R -values lead only to a reduced amplitude, but not to a qualitative change of the curve. One exception is the ballistic system studied in chapter 7. The lengths L_l and L_r have no influence on the scattering matrix at low energies. However, if we want to study finite energy effects, a good choice is $L_l \approx L_r \approx 10\xi$. To solve the linear systems of equations for the scattering matrix, routines from the

libraries LAPACK and BLAS are used. The numerical integrations, necessary to calculate the mode averages, are done with integration routines from the GNU Scientific Library.

6.3. Components of the Differential Conductance and the Differential Current Cross-Correlations

As we have seen in section 5.1, an electron arriving from one of the normal metal reservoirs at the interface to the superconductor can have four different destinies: It can be reflected as an electron (normal reflection (NR)), reflected as a hole (Andreev reflection (AR)), transmitted as an electron (elastic cotunneling (EC)) or transmitted as a hole (crossed Andreev reflection (CAR)). The same holds for holes. The corresponding elements of the scattering matrix are for normal reflection: s_{aa}^{ee} , s_{aa}^{hh} , s_{bb}^{ee} , s_{bb}^{hh} , local Andreev reflection: s_{aa}^{eh} , s_{aa}^{he} , s_{bb}^{eh} , s_{bb}^{he} , elastic cotunneling: s_{ab}^{ee} , s_{ab}^{hh} , s_{ba}^{ee} , s_{ba}^{hh} , and crossed Andreev reflection: s_{ab}^{eh} , s_{ab}^{he} , s_{ba}^{eh} , s_{ba}^{he} .

The current in electrode N_a given by equation (6.1) can naturally be divided into AR, CAR and EC contributions (to calculate this expression the unitarity of the scattering matrix has been used):

$$\begin{aligned}
 I_a = \frac{|e|}{h} \int dE & \left[\underbrace{(|s_{aa}^{eh}(E)|^2 + |s_{aa}^{he}(E)|^2) (f_{ae}(E) - f_{ah}(E))}_{\text{local Andreev reflection}} \right. \\
 & + \underbrace{|s_{ab}^{ee}(E)|^2 (f_{ae}(E) - f_{be}(E)) + |s_{ab}^{hh}(E)|^2 (f_{bh}(E) - f_{ah}(E))}_{\text{elastic cotunneling}} \\
 & \left. + \underbrace{|s_{ab}^{eh}(E)|^2 (f_{ae}(E) - f_{bh}(E)) + |s_{ab}^{he}(E)|^2 (f_{be}(E) - f_{ah}(E))}_{\text{crossed Andreev reflection}} \right]. \quad (6.18)
 \end{aligned}$$

In the following, we do not study current, but the differential conductance. We study the non local conductance, where $V_a = 0$ and the current I_a is differentiated with respect to V_b and the symmetric case where $V_a = V_b = V$ and the current I_a is differentiated with respect to V . In the zero temperature limit, only the non-local processes crossed Andreev reflection and elastic cotunneling contribute to the non-local conductance:

$$\begin{aligned}
 \left. \frac{\partial I_a}{\partial V_b} \right|_{V_a=0} &= \underbrace{-\frac{e^2}{h} [|s_{ab}^{ee}(|e|V_b)|^2 + |s_{ab}^{hh}(-|e|V_b)|^2]}_{\text{elastic cotunneling}} + \underbrace{\frac{e^2}{h} [|s_{ab}^{eh}(-|e|V_b)|^2 + |s_{ab}^{he}(|e|V_b)|^2]}_{\text{crossed Andreev reflection}}, \quad (6.19)
 \end{aligned}$$

while the symmetric case contains local Andreev reflection and crossed Andreev

reflection:

$$\begin{aligned}
 \left. \frac{\partial I_a}{\partial V} \right|_{V_a=V_b=V} &= \frac{e^2}{h} \underbrace{[(|s_{aa}^{eh}(|e|V)|^2 + |s_{aa}^{he}(|e|V)|^2) + (|s_{aa}^{eh}(-|e|V)|^2 + |s_{aa}^{he}(-|e|V)|^2)]}_{\text{local Andreev reflection}} \\
 &+ \frac{e^2}{h} \underbrace{[(|s_{ab}^{eh}(|e|V)|^2 + |s_{ab}^{he}(|e|V)|^2) + (|s_{ab}^{eh}(-|e|V)|^2 + |s_{ab}^{he}(-|e|V)|^2)]}_{\text{crossed Andreev reflection}}
 \end{aligned} \tag{6.20}$$

We now want to carry out a similar analysis for the current cross-correlations. We study only the zero temperature limit, where $f_{k\gamma}(E)[1 - f_{l\delta}(E)]$ is zero if $k = l$ and $\gamma = \delta$ and the current cross-correlations are:

$$\begin{aligned}
 S_{ab}(T=0) &= \frac{2e^2}{h} \sum_{k,l \in \{a,b\}} \sum_{\alpha,\beta,\gamma,\delta \in \{e,h\}} \text{sgn}(\alpha)\text{sgn}(\beta) \\
 &\times \int dE s_{ak}^{\alpha\gamma\dagger}(E) s_{al}^{\alpha\delta}(E) s_{bl}^{\beta\delta\dagger}(E) s_{bk}^{\beta\gamma}(E) f_{k\gamma}(E) [1 - f_{l\delta}(E)]
 \end{aligned} \tag{6.21}$$

Every summand in S_{ab} contains the product of four elements of the scattering matrix. As pointed out in [121, 122], in difference to the situation for the current, it is impossible to combine those matrix elements to absolute squares. Let us now try to classify the contributions of the noise as we did above for the current. We find that no summand consists of only one kind of elements of the scattering matrix. Every element consists of two local elements (NR or AR) and two non-local elements (CAR or EC). Either the two local elements and the two non-local elements are members of the same category, that gives the components EC-NR, CAR-NR, EC-AR, CAR-AR, or all four matrix elements belong to different categories and we will call these summands MIXED. Sometimes, it is useful to divide MIXED further as a function of its voltage dependence (see appendix B). As the formulas for the current cross correlations are lengthy, I relegate them into appendix B.

For the interpretation of current cross-correlations, the global sign plays an important role. The differential current cross-correlations carry for positive applied bias voltages the same sign as the current cross-correlations. For negative applied voltages current cross-correlations and differential current cross-correlations have opposite signs. To avoid confusion, I show only figures of differential current cross-correlations calculated for positive bias voltages (and thus negative energies $E = -|e|V$). Due to the electron-hole symmetry of our model, differential current cross-correlations calculated for negative bias voltages are up to a global sign identical to the ones calculated at positive bias voltage. For small bias voltages, current cross-correlations depend linearly on voltage. Thus, current cross-correlations and differential current cross-correlations show the same qualitative behavior if studied as a function of the interface transparency or the distance between barriers.

Scattering matrix classification	Green's function classification
CAR-NR	CAR
EC-AR	AR-AR
MIXED1, MIXED2	PRIME
EC-NR	EC
CAR-AR	AR-AR
MIXED3, MIXED4	MIXED

Table 6.2: Correspondences between the categories in the language of Green's functions from [118] and in the language of scattering matrix elements.

In reference [118], we carried out a similar analysis of current cross-correlations in terms of Green's functions. The elements of the scattering-matrix are connected to the retarded Green's functions of the tight binding model studied there via

$$s_{ij}^{\alpha\beta} = i\delta_{ij} + 2\pi t_i t_j \sqrt{\rho_i^\alpha} \sqrt{\rho_j^\beta} G_{ij\alpha\beta}^R \quad (6.22)$$

where t_i is the transmission coefficient of the barrier i , ρ_i^α the density of electron or hole states of electrode i and $G_{ij\alpha\beta}^R$ the Green's function connecting the first site in the superconductor next to the electrode j to the first site in the superconductor next to the electrode i .

Table 6.2 shows the correspondences between the categories in the language of Green's functions and in the language of scattering matrix elements.

Bignon *et al.* [98] have studied current cross-correlations in the tunneling limit (see also section 5.4). They find that noise measurements in the tunneling limit can give access to the CAR and EC contribution of the current. We have just seen that at least two processes are involved in every component of noise. The contributions of noise they calculate fall into the categories EC-NR and CAR-NR. In the tunneling limit the NR amplitude is approximately one, so that the current cross-correlations containing products of NR and EC/CAR amplitudes are very similar to the EC and CAR current contributions.

6.4. Positive Cross-Correlations without CAR

In fermionic systems without superconducting electrodes, current cross-correlations are, as a consequence of the Fermi-Dirac statistics, always negative [12, 111]. In superconductors, the coupling of electrons into Cooper pairs makes positive cross-correlations possible. If a CAR process is interpreted as the splitting of a Cooper pair into two electrons leaving the superconductor in different electrodes, positive cross-correlations are the logical consequence. However, the CAR process is not the only one, which can lead to positive cross-correlations. Let us investigate in more detail the influence of the different processes on the current cross-correlations in a NSN-system.

6. Three-Terminal NSN-Hybrid Structures

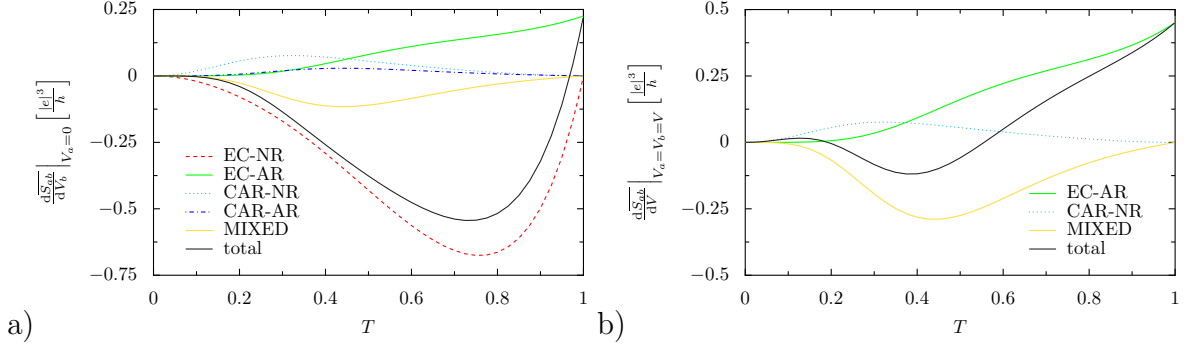


Figure 6.2.: Averaged differential cross-correlations for a NSN-system with $R = 0.25\xi$ as a function of the transparency of the interfaces $T = T_{ins} = T_{rsn}$. The positive cross-correlations at high interface transparency are due to the EC-AR process, represented by a green solid line. a) bias $V_b \ll \Delta/|e|$, $V_a = 0$ b) symmetric bias $V_a = V_b \ll \Delta/|e|$.

The black line in figure 6.2 shows the averaged differential current cross-correlations for a) a system biased for non-local conductance measurements ($V_a = 0$) and for b) a symmetrically biased system ($V = V_a = V_b$). The total current cross-correlations have already been published in [118]. But here, we have in addition the different parts which contribute to the total current cross-correlations separately. For high interface transparencies the total cross-correlations are positive for both biases. For the symmetrically biased case, the total cross-correlations are also positive for low interface transparencies. Inspecting the different contributions, we see that positive current cross-correlations at low interface transparencies are indeed a consequence of a large CAR-NR component and therefore a consequence of CAR processes. But the positive current cross-correlations at high interface transparencies have a different origin: a large positive EC-AR contribution.

We can put the contributions to the current cross-correlations into two categories with respect to their sign, which is independent of the interface transparency. EC-NR, CAR-AR, MIXED2 and MIXED4 carry a negative sign, CAR-NR, EC-AR, MIXED1 and MIXED3 a positive sign. Current can either be carried by electrons I^e or by holes I^h . The sign of the different contributions to the current cross-correlations depends on whether only currents of the same carrier type are correlated ($\langle \Delta \hat{I}_a^e \Delta \hat{I}_b^e \rangle + \langle \Delta \hat{I}_a^h \Delta \hat{I}_b^h \rangle + a \leftrightarrow b$) which is the case for EC-NR, CAR-AR, MIXED2 and MIXED4 and leads to a negative sign or whether electron currents are correlated with hole currents ($\langle \Delta \hat{I}_a^e \Delta \hat{I}_b^h \rangle + \langle \Delta \hat{I}_a^h \Delta \hat{I}_b^e \rangle + a \leftrightarrow b$) which is the case for CAR-NR, EC-AR, MIXED1 and MIXED3 and leads to a positive sign. In purely normal conducting systems the electron and hole currents are uncorrelated, only correlations of the same carrier type contribute to the current cross-correlation and lead to a negative sign. The sign of the total current cross-correlations is a consequence of the relative strength of the different parts of the current cross-correlations, which

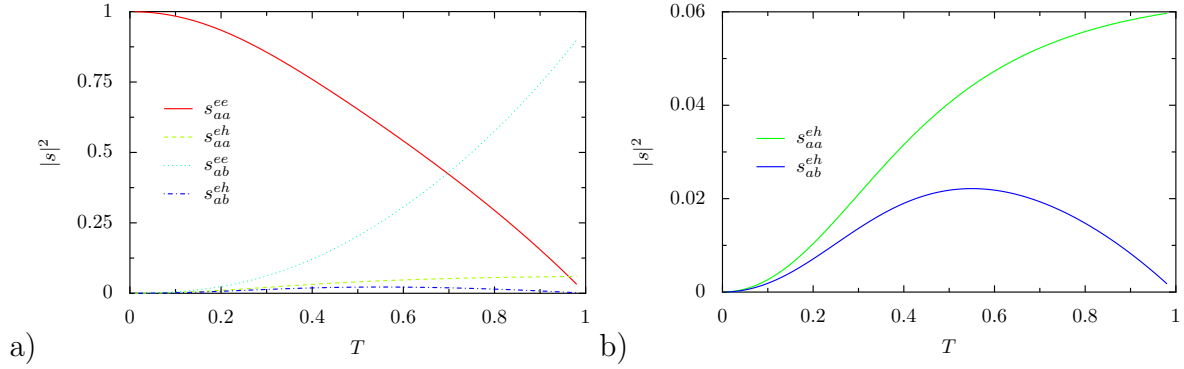


Figure 6.3.: a) Absolute squares of scattering matrix elements for a NSN-system with $R = 0.25\xi$ as a function of the transparency of the interfaces $T = T_{lns} = T_{rsn}$. b) Zoom of a).

depends on the interface transparency.

In order to understand better the dependence on the interface transparency of the different contributions to the current cross-correlations, let us have a look at the absolute squares of the scattering matrix elements for the NSN-system shown in figure 6.3. As the system is symmetric in Na and Nb and in electrons and holes, all scattering matrix elements of one given category (NR, AR, CAR or EC) have the same absolute squares. For an impermeable barrier, the only possible process is normal reflection. Consequently, for $T = T_{lns} = T_{rsn} = 0$, the absolute square of the scattering elements encoding normal reflection are one (red, solid curve on figure 6.3) and all other scattering matrix elements are zero. For the other extreme, in the absence of a barrier where $T = 1$, the scattering processes have to conserve momentum as there is no barrier which could absorb momentum. Normal reflection means that a particle arriving with momentum p at the interface returns with momentum $-p$. A momentum of $2p$ is transferred and the process does not conserve momentum. Crossed Andreev reflection does not conserve momentum either. If, e.g. an electron arrives with momentum p on the left hand side the hole leaving on the right hand side will carry a momentum of $-p$, so that again a momentum transfer of $2p$ takes place. Therefore, the matrix elements for normal reflection and for crossed Andreev reflection vanish in the limit $T \rightarrow 1$.

In the tunneling limit, the processes EC-NR and CAR-NR dominate as they contain a NR amplitude which is large for small T . At high interface transparencies, the process EC-AR dominates, as it is the only one that does neither contain a CAR nor a NR amplitude.

With the "conservation of momentum" argument we can argue that, at least in our model, current cross-correlations due to CAR have to tend to zero at least for very high transparencies. As the total current cross-correlations do not tend to zero in the limit $T \rightarrow 1$, they can not be due to CAR.

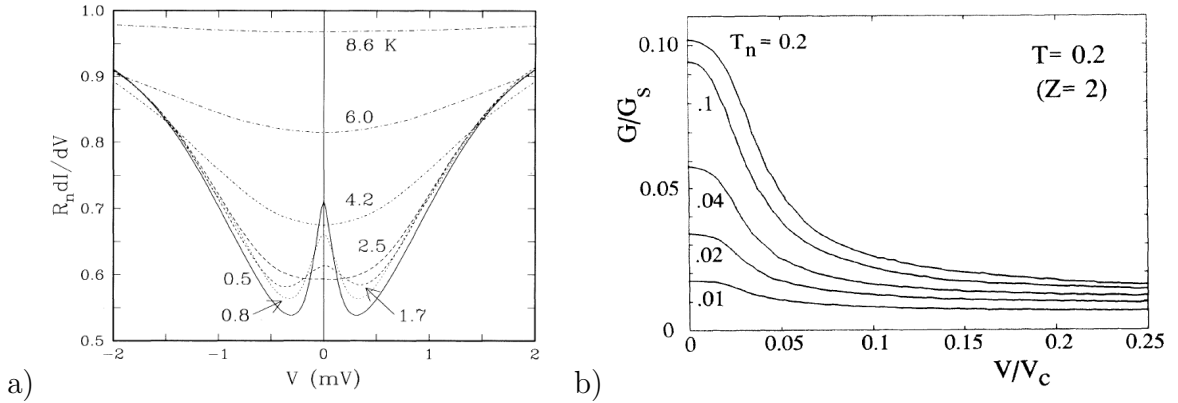


Figure 6.4.: a) Experimental conductance voltage characteristic measured at different temperatures [123]. The excess conductance at low voltage is for the measurements at low temperatures clearly visible.

b) Theoretical conductance voltage characteristic for a superconductor-semiconductor interface by [124]. In agreement with the experiment, the conductance enhancement by reflectionless tunneling occurs only at low voltages.

6.5. Reflectionless Tunneling

The conductance of an NS tunnel junction is influenced by the amount of disorder in the normal conductor. It can be larger for a “dirty” normal conductor containing a large number of non-magnetic impurities, where transport is diffusive, than for a clean normal conductor, where transport is more ballistic. This phenomenon, called reflectionless tunneling has been experimentally observed for the first time by Kastalsky *et al.* [123]. They have measured the conductance in a NS contact, where the normal conducting side had been formed by a doped semi-conductor and have found an increased conductance at low voltages. Figure 6.4a shows one of their measurements with a clear conductance peak at zero voltage for the measurements performed at low temperature. The effect increases if the doping of the semiconductor, *i. e.* the number of impurities is raised. An intuitive explanation for reflectionless tunneling is that electrons and holes are reflected multiple times from the impurities, a process which localizes them close to the NS-interface and increases their chance to pass the tunnel barrier at the interface.

Melsen and Beenakker [13] had the idea to use a normal conductor with an additional tunnel barrier as a simple model of a disordered normal conductor. They studied the resulting NNS-junction with a random matrix approach and found indeed an enhancement of the conductance as a result of the insertion of the second barrier. Random-matrix theory is a mighty theory, but in the form it is used in the first part of [13], it boils down to the average given by equation (6.5). I will therefore explain, how one can obtain the result of Melsen and Beenakker in our language.

In a NNS-structure at energies below the gap, there are no single electron or hole states at the right hand side. Therefore, the transmission of electrons or holes to the right hand side is not possible and the scattering matrix reduces to

$$S = \begin{pmatrix} s_{aa}^{ee} & s_{aa}^{eh} \\ s_{aa}^{he} & s_{aa}^{hh} \end{pmatrix}. \quad (6.23)$$

From equation (6.1) follows for the current in the zero temperature limit

$$I_a = \frac{e}{h} \int dE [|s_{aa}^{he}|^2 + |s_{aa}^{eh}|^2] [\Theta(-E - eV_a) - \Theta(E - eV_a)], \quad (6.24)$$

so that the conductance is given by

$$G_{NNS} = \frac{dI_a}{dV_a} = \frac{e^2}{h} (|s_{aa}^{he}(V_a)| + |s_{aa}^{he}(-V_a)| + |s_{aa}^{eh}V_a| + |s_{aa}^{eh}(-V_a)|). \quad (6.25)$$

In the limit of small energies, the wave vectors in the normal conducting regions become $\lim_{E \rightarrow 0} k^+ = \lim_{E \rightarrow 0} k^- = k_F$, the wave vectors in superconducting region become $\lim_{E \rightarrow 0} q^+ = k_F + i/\xi$ and $\lim_{E \rightarrow 0} q^- = k_F - i/\xi$ with $\xi = \hbar^2 k_F / (m\Delta)$ and the coherence factors simplify to $\lim_{E \rightarrow 0} u_E = u_0 = \sqrt{i\Delta/(2E)}$ and $\lim_{E \rightarrow 0} v_E = \sqrt{-i\Delta/(2E)}$. With this simplifications, we can calculate the scattering matrix analytically and find

$$|s_{aa}^{eh}|^2 = |s_{aa}^{he}|^2 = [(1 + 2Z_{lnn}^2)(1 + 2Z_{lns}^2) + 4Z_{lnn}Z_{lns}((1 - Z_{lnn}Z_{lns})\cos(2k_F L_l) + (Z_{lnn} + Z_{lns})\sin(2k_F L_l))]^{-2}. \quad (6.26)$$

The integration over one period of L_l can also be done analytically

$$\overline{|s_{aa}^{eh}|^2} = \int_{L_l - \frac{\pi}{k_F}}^{L_l - \frac{\pi}{k_F}} dL_l |s_{aa}^{eh}|^2 = \frac{(1 + 2Z_{lnn}^2)(1 + 2Z_{lns}^2)}{(4Z_{lnn}^2 + 4Z_{lnn}^4 + (1 + 2Z_{lns}^2)^2)^{\frac{3}{2}}}. \quad (6.27)$$

If we replace the barrier strengths by the interface transparencies, we get

$$\overline{|s_{aa}^{eh}|^2} = \frac{T_{lnn}^2 T_{lns}^2 (T_{lnn} - 2)(T_{lns} - 2)}{(4(T_{lnn}^2 + T_{lns}^2 - T_{lnn}^2 T_{lns} - T_{lnn} T_{lns}^2) + T_{lnn}^2 T_{lns}^2)^{\frac{3}{2}}}. \quad (6.28)$$

The final result

$$\overline{G}_{NNS} = \frac{4e^2}{h} \overline{|s_{aa}^{eh}|^2} = \frac{4e^2}{h} \frac{T_{lnn}^2 T_{lns}^2 (T_{lnn} - 2)(T_{lns} - 2)}{(4(T_{lnn}^2 + T_{lns}^2 - T_{lnn}^2 T_{lns} - T_{lnn} T_{lns}^2) + T_{lnn}^2 T_{lns}^2)^{\frac{3}{2}}} \quad (6.29)$$

is identical to the one obtained by Melsen and Beenakker [13].

The conductance peak in the experimental curve shown in figure 6.4 disappears for increasing voltage. This was explained with a semi-classical model by [123] (see

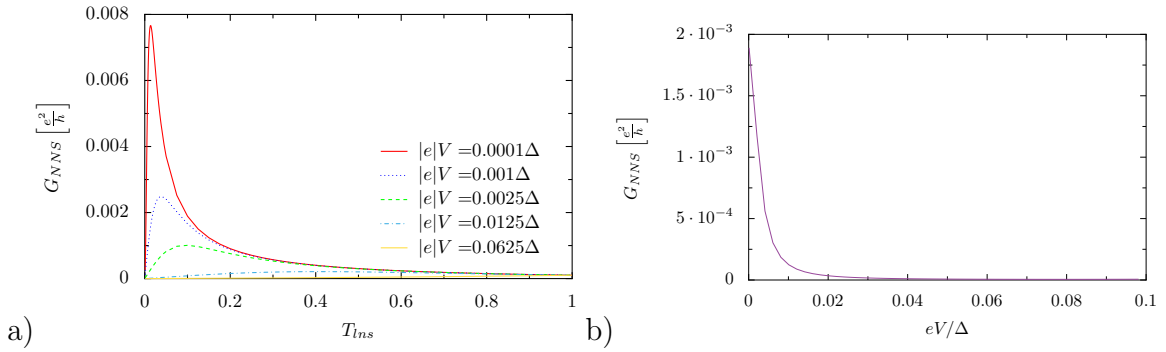


Figure 6.5.: a) Conductance of the NNS-interface as a function of the barrier strength T_{lnn} for different energies. $T_{lns} = 0.01$. b) Conductance of the NNS-interface as a function of the applied voltage. $T_{lnn} = 0.1$, $T_{lns} = 0.01$

figure 6.4b: In an Andreev reflection process the reflected hole traces back the way of the incoming electron. If Andreev reflection occurs at the Fermi energy, the electron and the hole have the same wave vectors and both particle acquire exactly opposite phases on there way leading to constructive interference effects. With increasing voltage bias the energy difference between electrons and holes increases, the wave vectors are no longer the same and the interference effects are reduced.

We can study the voltage dependence of the conductance in an NNS-structure with our method using the energy dependent forms of wave vectors and coherence factors and calculating the scattering matrix numerically. Figure 6.5a shows the conductance of the NNS-interface as a function of the barrier strength T_{lnn} for different energies. The curve for $|e|V = 10^{-4}\Delta$ has the form found analytically in equation 6.29. Higher applied voltages let the conductance peak disappear. Figure 6.5b shows the dependence of the conductance on the applied voltage which is in good qualitative agreement with the experimental result shown in figure 6.4a.

6.6. Multiple Barriers

In the light of the phenomenon of reflectionless tunneling discussed in the preceding section, it is natural to ask if a similar effect could also enhance conductance and current cross-correlations in a three-terminal NSN-structure. Duhot and Mélin [125] have studied the influence of additional barriers on the non-local conductance in three-terminal NSN-structures. They find that two symmetric additional barriers enhance the non-local conductance.

First, we want to get a more in depth understanding of their result by calculating the AR, CAR and EC components of the current separately. Afterwards, we will study the influence of additional barriers on the current cross-correlations.

Figure 6.6 shows the averaged conductivity in the symmetric bias situation

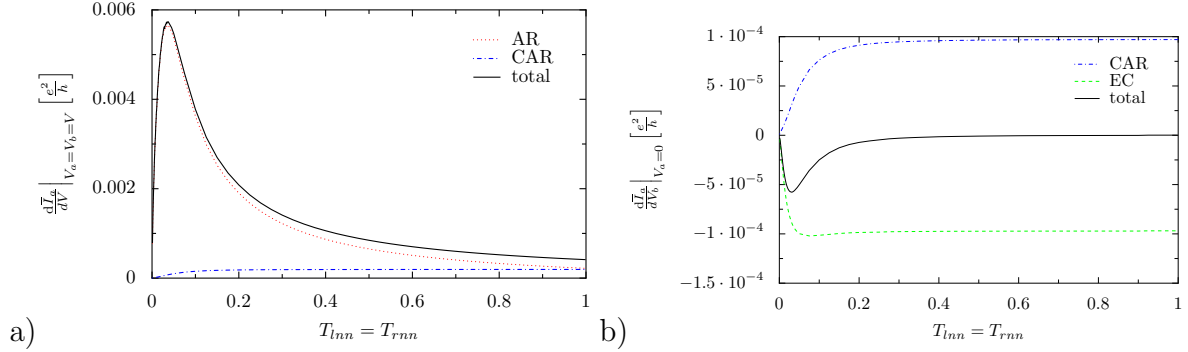


Figure 6.6.: Averaged differential conductance in the limit of zero energy in a) the symmetrical bias situation $V_a = V_b \ll \Delta/|e|$ and b) in the situation of non-local conductance measurements $V_a = 0$, $V_b \ll \Delta/|e|$ for a superconducting electrode much shorter than the coherence length ($R = 0.25\xi$) as a function of the transparencies of the additional barriers $T_{lnn} = T_{rnn}$. The barriers next to the superconductor are in the tunnel regime ($T_{lns} = T_{rsn} = 0.01$).

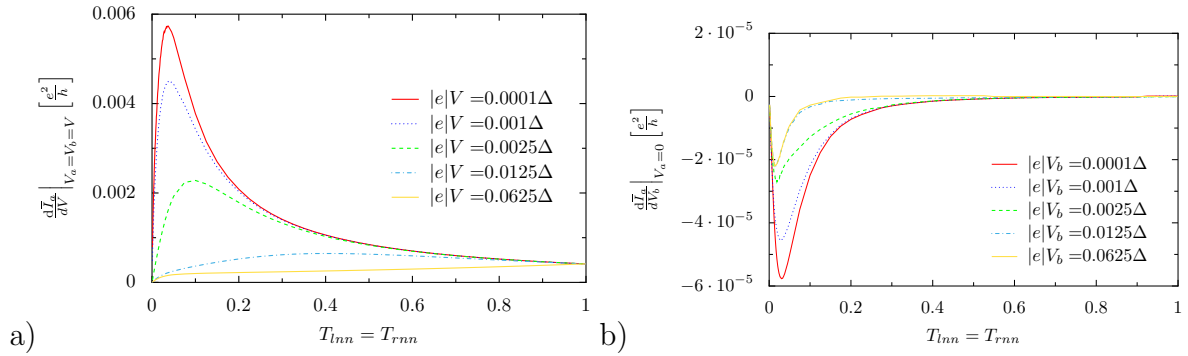


Figure 6.7.: Averaged differential conductance at different energies in a) the symmetrical bias situation $V_a = V_b \ll \Delta/|e|$ and b) in the situation of non-local conductance measurements $V_a = 0$, $V_b \ll \Delta/|e|$ for a superconducting electrode shorter than the coherence length ($R = 0.25\xi$) as a function of the transparencies of the additional barriers $T_{lnn} = T_{rnn}$. The barriers next to the superconductor are in the tunnel regime ($T_{lns} = T_{rsn} = 0.01$).

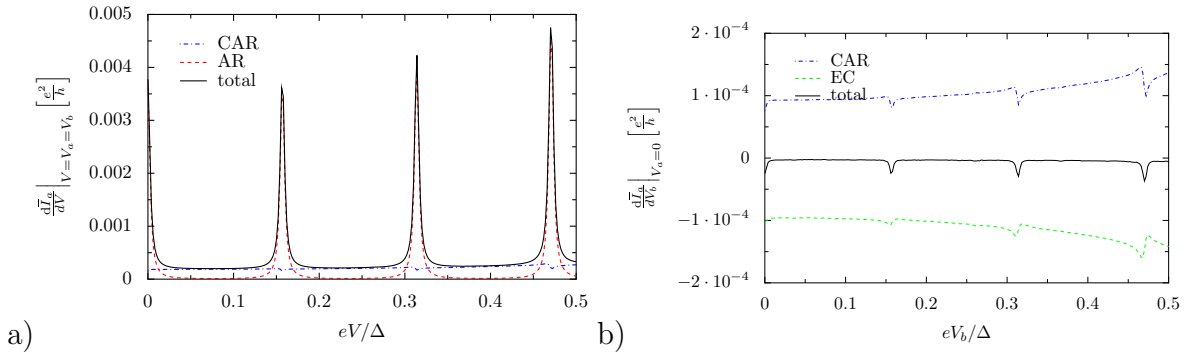


Figure 6.8.: Energy dependence of the averaged differential conductance in a) the symmetrical bias situation $V_a = V_b \ll \Delta/|e|$ and b) in the situation of non-local conductance measurements $V_a = 0$, $V_b \ll \Delta/|e|$ for a superconducting electrode much shorter than the coherence length ($R = 0.25\xi$) as a function of the transparencies of the additional barriers $T_{lnn} = T_{rnn}$. The barriers next to the superconductor are in the tunnel regime ($T_{lns} = T_{rsn} = 0.01$).

$V_a = V_b \ll \Delta/|e|$ and in the situation of non-local conductance measurements $V_a = 0$, $V_b \ll \Delta/|e|$ for a superconducting electrode much shorter than the coherence length ($R = 0.25\xi$). The sum of the AR, CAR and EC components, traced in black, features in both cases an extremum. But, looking at the behavior of their components, we see that they arise by different mechanisms. Let us first have a look at the symmetrically biased case. Without the additional barriers, *i. e.* in the limit $T_{lnn} = T_{rnn} \rightarrow 1$, the contributions of AR and CAR are similar in magnitude. The EC component is completely suppressed, as it is proportional to the difference of the applied voltages. Introduction of two additional barriers increases the AR component by about a factor 30. The shape of the curves is similar to the one of the NNS case which can be recovered exactly by increasing the length of the superconducting electrode far beyond the coherence length. The CAR curve, however, stays almost constant over a long range of values of barrier strength of the additional barriers and vanishes finally when the transparencies go to zero.

In the case of the non-local conductance voltage configuration, the AR component is zero as it is proportional to the local voltage V_a . As in the first case the additional barriers have little influence on the CAR component, except for the fact, that it tends to zero for vanishing transparency. The EC component is over a long range of barrier strength values identical in amplitude, but opposite in sign to the CAR component. For small T -values the EC component features a small extremum, but it is much less pronounced than the maximum of the AR component of the first case. The EC component tends in the limit $T_{lnn} = T_{rnn} \rightarrow 1$ slower to zero than the CAR component which has a minimum in the total conductance as a consequence. That the maximum in the conductance in the symmetrical bias case and in the non-local

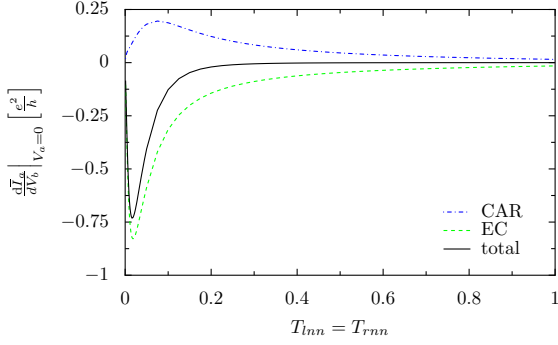


Figure 6.9: Gedankenexperiment with coupled integrals $T_{lns} = T_{rsn} = 0.01$, $R = 0.25\xi$: Now, also the EC and the CAR component are enhanced by reflectionless tunneling.

conductance case have different origins can also be illustrated by studying their energy dependence, depicted in figure 6.7: The enhancement of the AR component of the conductance in the symmetrical biased case disappears completely with increasing bias voltage. The extremum in the non-local conductance decreases slightly with increasing bias voltage, but only up to a certain voltage value, then it saturates.

Why is the AR component enhanced by the additional barriers, but not the EC or CAR components? Reflectionless tunneling is believed to occur because the electrons and holes are localized between the double barrier and have therefore a higher probability to enter the superconductor. There is a double barrier on the right and on the left hand side, so this localization should also happen to the particles involved in EC or CAR processes. The answer is, that in the AR cases the incoming electron and the leaving hole see the same environment. In the EC and CAR processes the incoming particle sees the environment on one side of the superconductor and the leaving particle the environment on the other side. The energy dependence of the conductance enhancement of the AR component, gives us evidence, that reflectionless tunneling can only occur, if the outgoing hole can trace back the way of the incoming electron. At low bias voltages, the electron and the hole have the same energy and the same wave vector, reflectionless tunneling occurs. At higher bias voltage, electrons and holes have different wave vectors and the reflectionless tunneling peak disappears. In our model, reflectionless tunneling reappears once the phase difference between electrons and holes has reached a multiple of π , which is shown in figure 6.8. The height of the resonance peaks increases with increasing energy, because the coherence length in the superconductor is larger at higher energies.

The integrals over the phases between the additional barriers on the left and on the right hand side have, of course, been taken independently. There is no reason to think that the channel mixing, which is emulated by the integrals, on the right and on the left hand side are coupled. To verify this scenario, we couple the two integrals in a gedankenexperiment. We set the distance L_l between the two left hand-side barriers to be equal to the distance L_r between the two right-hand side barriers and do only one integral over $L = L_l = L_r$. The result is shown in figure 6.9. Now, the CAR and the EC component are also enhanced. Still, the effect on the EC

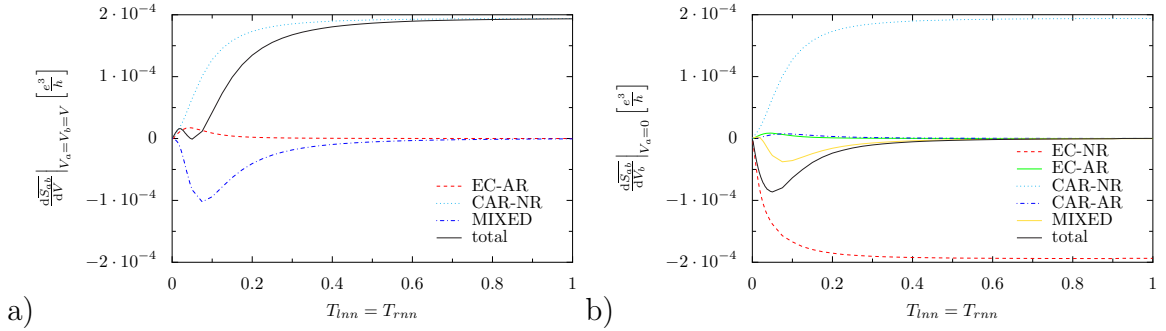


Figure 6.10.: Averaged differential current cross correlations in a) the symmetrical bias situation $V_a = V_b \ll \Delta/|e|$ and b) in the situation of non-local conductance measurements $V_a = 0$, $V_b \ll \Delta/|e|$ for a superconducting electrode shorter than the coherence length ($R = 0.25\xi$) as a function of the transparencies of the additional barriers $T_{lnn} = T_{rnn}$. The barriers next to the superconductor are in the tunnel regime ($T_{lns} = T_{rsn} = 0.01$).

component is larger and EC dominates the non-local conductance.

Let us turn back to independent mode averaging and have a look at the current cross-correlations shown in figure 6.10. In the symmetric bias case the additional barriers do not lead to an enhancement of the signal. The current cross-correlations are dominated by the CAR-NR component, and, as we have seen above, CAR is not influenced by reflectionless tunneling. The EC-AR component is amplified by the additional barriers, because the AR amplitude describing a local process is amplified. This leads to a small shoulder in the total cross-correlations. However, as we are in the tunnel regime and the leading order of CAR-NR is T^2 while the leading order of EC-AR is T^4 , the influence of the EC-AR-component is too small to lead to a global maximum.

In the case $V_a = 0$, $V_b \ll \Delta/|e|$ the additional barriers enhance the signal. But the cross-correlations are dominated by EC-NR and are therefore negative.

6.7. Summary

NSN and NNSNN-devices are described in a simple one-channel model in scattering theory, where the elements of the scattering matrix are calculated by wave function matching in the BTK-approach.

Positive current cross-correlations at high interface transparencies are not consequence of CAR-processes, but of the EC-AR contribution to the current cross-correlations.

In NS-structures in the tunnel regime, the use of a diffusive normal metal-electrode leads by an effect called “reflectionless tunneling” to an enhancement of the conduc-

tance. Inspired by the idea of Melsen and Beenakker to model the diffusive normal metal electrode by a clean normal metal electrode with an additional barrier, one can ask what happens if additional barriers are added to a NSN-structure. Reflectionless tunneling is a consequence of constructive interference occurring only if the involved electrons and holes acquire exactly opposite phases on their way through the system. In phase averaged systems this is only possible, if electrons and holes have the same wave vector and see the same environment. Therefore, in a phase averaged system, additional barriers have little influence on the non-local EC and CAR processes and uniquely the local AR-process is enhanced. Positive cross-correlations in the tunnel regime are due to CAR-NR and cannot be enhanced with additional barriers, if an average over the length has to be done. Thus, it is not to be expected that the use of diffusive normal metals will facilitate the experimental observation of positive current cross-correlation. This negative conclusion is important for experiments.

7. The Ballistic System

Concerning the creation of a source of entangled electrons, there is always the problem of the competition of CAR processes with AR and EC processes. In the propositions for Cooper pair splitters, there are two main strategies to filter between the different processes: The first strategy is to use quantum dots in the Coulomb blockade regime to suppress local Andreev reflection and to use the discrete levels of the quantum dots as energy filters to distinguish between EC and CAR. The second strategy is to use interference effects. For example, a system containing Mach-Zehner interferometers is proposed in [93] and a system containing Fabry-Perot interferometers is proposed in [92]. In this chapter, we want to answer the question whether electronic Fabry-Perot interferometers allow to filter the different processes contributing to the conductance and to the current cross-correlations. To this end, we study in detail a ballistic, one-dimensional NNSNN-system.

The model is to a large extent identical to the one used in the last chapter (see figure 6.1c), but here we do not average over the length of the normal conducting channels. We maintain, however, the average over the central superconducting electrode. One could imagine that the normal conducting channels are formed by single walled carbon nanotubes, where transport is ballistic, while the superconducting central electrode is made from aluminum, where more scattering processes occur.

In the last chapter, we have seen that reflectionless tunneling cannot enhance the non-local process CAR and EC. In the ballistic system studied here, the distances L_l and L_r can be controlled independently. We expect the parts N_l and N_r to act as Fabry-Perot interferometers and hope that constructive interferences for CAR and EC are observable.

This chapter starts with a discussion of the expectations we have from the analogy to optical Fabry-Perot interferometers. The main part consists of the analysis of numerical calculations. The chapter ends with the examination of the challenges connected to an experimental implementation of the studied NNSNN-system.

7.1. Resonances in a Fabry-Perot Interferometer

The NNSNN-system consists in principle of two Fabry-Perot interferometers, one at the left and one at the right hand side of the superconductor. For the final result, we have, of course, to take into account the entire system. But from thinking of the two Fabry-Perot interferometers independently, we can already get a good idea where

we have to expect resonance peaks, and what influence they have on the different components of the conductance and of the current cross-correlations.

In an optical Fabry-Perot interferometer consisting of two parallel mirrors, light is reflected multiple times between the mirrors. Part of the light is transmitted every time the light reaches a mirror. The transmitted intensity results from the interference of light which has undergone a different number of reflections between the two mirrors. The transmission of a Fabry-Perot interferometer is a function of the phase difference between a beam which has been n -times and a beam which has been $(n + 1)$ -times reflected at both interfaces. The same is true for a Fabry-Perot interferometer for electrons. This can also be seen from equation (6.26) giving the matrix elements of the NNS-system before the phase average is carried out. An electron going once back and forth between the two barriers at the left hand side of the NNSNN-system acquires a phase $\phi^e = 2q^+L_l$, a hole acquires a phase $\phi^h = 2q^-L_l$. For low voltages, where $q^+ \approx q^-$, we expect electron and hole resonances for the same resonator lengths. If the voltage is increased, the wave vector $q^+ = \sqrt{2m\hbar^2}\sqrt{\mu - |e|V}$ decreases and the wave vector $q^- = \sqrt{2m\hbar^2}\sqrt{\mu + |e|V}$ increases, shifting the resonance for electrons to higher and the resonance for holes to lower values of L_l . The width of the resonances of a Fabry-Perot interferometer depends on the reflectivity of the interfaces. The smaller the transmission, the more beams having undergone different numbers of reflections interfere with each other and the sharper are the resonance peaks.

Symmetrically applied bias

For a symmetrically applied bias, the differential conductance consists of an AR and a CAR component. If a positive bias is applied to the normal electrode N_a , the current I_a contains an AR contribution, where a hole enters and an electron leaves the superconductor (see figure 7.1a). At low energies, the AR contribution will assume its maximum for values of L_l where electrons and holes are both in resonance. At higher energies, the resonances for electrons and for holes occur at different values of L_l . If the barriers are in the tunnel regime, the resonance peaks are sharp. The resonance peaks for electrons and holes stop to overlap and the AR contribution disappears. If the interface transparency is increased, the resonance peaks broaden. Even if the electron and the hole wave vectors are significantly different, there is an overlap between corresponding resonances leading to a double peak in the AR contribution. AR is a local process, and we expect the AR contribution to the current I_a to be mainly independent of the length L_r .

There are two possibilities for CAR process if the electrodes N_a and N_b are symmetrically positively biased: Either a hole enters the superconductor at the left hand side and an electron leaves the superconductor at the right hand side (see figure 7.1b) or the process occurs the other way round (see figure 7.1c), the hole enters at the right hand side and the electron leaves at the left hand side. In a CAR process, both sides are involved and the position of the resonances will be a function of both L_l and L_r . At low energies, the resonance for the two CAR processes will

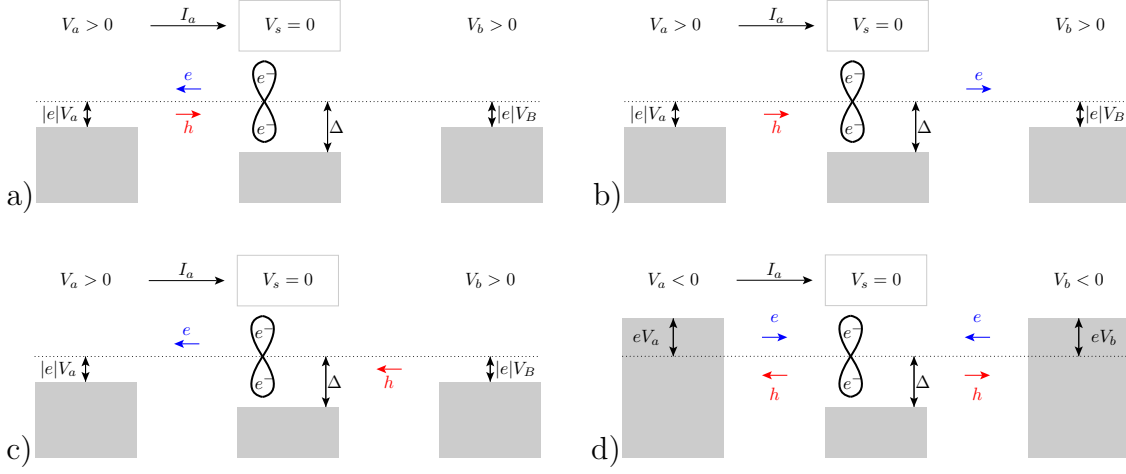


Figure 7.1.: Schematics to identify the contributions to the conductance in the symmetrically biased case. Depicted are the filled states in the three reservoirs, and the current of electrons and holes between the barriers. a) AR contribution for positive bias, b) and c) The two possible CAR contributions for positive bias, d) Summary of the processes for negative bias. If negative voltages are applied, the roles of electrons and holes are interchanged, but the resulting conductance stays unchanged.

be superimposed and occur at length values $L_l = L_r \bmod \pi/k_F$. In a CAR process, the incoming hole and the outgoing electron are spatially separated. It is therefore possible to reach the optimal resonance condition for electrons and for holes even if the two kinds of carriers have different wave vectors. For higher bias values, the conductance maximum due to the CAR process sketched in figure 7.1b will be shifted to lower values of L_l and higher values of L_r . It will be the other way round for the conductance maximum due to the second CAR process. Therefore, we expect the resonance peak to split up into two peaks.

CAR and AR have both a positive contribution to the differential conductance. This can also be seen in figure 7.1: The current I_a is defined to be positive if positive charges enter the superconductor. All electrons on the left leave the superconductor and all holes enter it.

If a negative bias is applied instead of a positive one, electrons and holes will interchange their roles (see figure 7.1d). The resonance positions and the sign of the conductance, however, will not change because $q^+(V) = q^-(-V)$.

Asymmetrically applied bias $V_a = 0$, $V_b > 0$

Now let us shift attention to the bias configuration $V_a = 0$, $V_b > 0$ used to measure non-local conductance. The non-local conductance consists of an EC and a CAR contribution. EC processes involve the same type of charge carriers on both sides of the superconductor. Therefore, the resonances for EC will always occur for diagonal values $L_l = L_r \bmod \pi/k_F$. At positive bias, EC is carried by holes (see figure 7.2a)

7. The Ballistic System

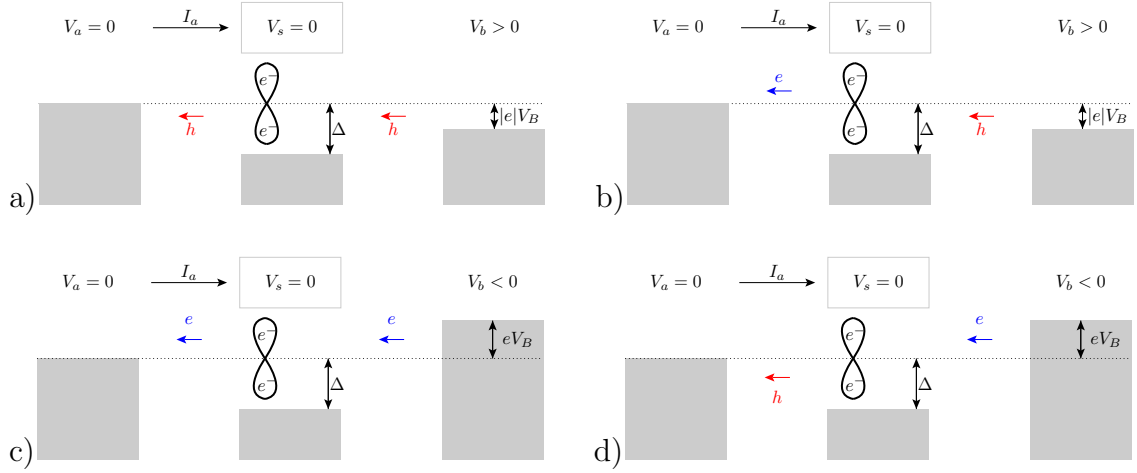


Figure 7.2.: Schematics to identify the contributions to the conductance in the non-local conductance bias configuration. Depicted are the filled states in the three reservoirs, and the current of electrons and holes between the barriers. a) EC contribution carried by holes for positive bias, b) CAR contribution for positive bias, c) EC contribution carried by electrons for negative bias, d) CAR contribution for negative bias. If negative voltages are applied, the roles of electrons and holes are interchanged, but the resulting conductance stays unchanged.

and if the voltage is increased, the resonances in L_l and L_r are simultaneously shifted to lower values. EC leads to a negative differential conductance as the holes move out of the superconductor and the current is defined positive entering the superconductor. From the two kinds of CAR processes possible in the symmetrically biased case, only the second one contributes to the non-local conductance. At low energies the EC and the CAR peak will be superimposed. At higher energies, the CAR peak moves away from the diagonal.

The application of a negative bias interchanges again the roles of electrons and holes, but it does not influence the resonance positions. The only difference between a positive and a negative applied bias is the global sign of the current cross-correlations.

With respect to the central question concerning the idea to use a Fabry-Perot interferometer as a filter for the different processes contributing to the conductance and to the current cross-correlations, we expect that it will be essential to operate the system at energies, where the wave vectors for electrons and holes are significantly different. We are now well prepared to analyze the calculated results, which will turn out to be in qualitative agreement with the scenario discussed in this section. We start with the tunnel regime, investigate then how the contrast diminishes with increasing interface transparency and have finally a closer look at a system with intermediate interface transparencies.

7.2. The Tunnel Regime

Let us now discuss the calculated conductance and the current cross-correlations. In a first step, the barriers between the superconducting and the normal regions are chosen in the tunnel regime ($T_{lrs} = T_{rsn} \approx 0.01$) in order to achieve sharp resonances. The distances L_l and L_r are chosen to be of the order of ten times the coherence length ξ . This distance allows to observe phase differences $\Delta\phi = |\phi^e - \phi^h|$ of the order of 2π between electrons and holes already at energies much smaller than the superconducting gap.

As in the last chapter for the averaged system, we will study four different quantities: The conductance in the symmetrically biased case, the non-local conductance, where the normal electrode in which the current is calculated is on the same potential as the superconductor, and the current cross-correlations in the same two bias configurations. The results are presented in the figures 7.3, 7.4, 7.5 and 7.6. The panels a) and c) show always a three-dimensional plot of the conductance respectively the current cross-correlations as a function of the distances between the barriers L_l and L_r . The three-dimensional plot in panel a) depicts always the situation in the limit of zero energy. The one in panel b) refers to higher energies. The three-dimensional plots are completed by cuts through the resonances. These cuts show the different contributions in different colors and have a higher resolution.

Conductance for a symmetrically biased system

Figure 7.3a shows the differential conductance $dI_a/dV|_{V=V_a=V_b>0}$ in the symmetrically biased case $V_a = V_b$ as a function of the distances L_l and L_r in the limit $V \rightarrow 0$. There are resonance mountain ranges for two values of L_l and there are four peaks which stand out of the mountain ranges. The mountain ranges correspond to a L_r -independent process and will therefore be due to AR. This is confirmed by figure 7.3b showing in a cut along one of the mountain ranges the AR and the CAR component separately. Figure 7.3b shows us also that the mountain peaks are due to CAR. The relative distance of two subsequent resonance peaks in units of k_F is π in L_r and in L_l direction. But the absolute resonance positions are not given by integer multiples of π as it would be the case in a simple optical Fabry-Perot interferometer with two identical mirrors. Figure 7.3c shows the differential conductance at higher voltage (but still much smaller than the gap). As expected from section 7.1, the AR mountain ranges disappear because the electron and hole resonances do not overlap anymore. Every CAR peak splits up into two peaks corresponding to the two CAR contributions.

The observation of the disappearance of AR and the splitting of the CAR peaks is already in itself interesting. As the peaks are uniquely due to CAR processes, the desired filtering is achieved. A NNSNN-system operated with symmetrical bias at energies where AR is suppressed and tuned to a CAR resonance peak, could be a good source of entangled electrons.

Non-local conductance for $V_a = 0$, $V_b > 0$

Figure 7.4 depicts the calculated differential non-local conductance for the bias $V_a = 0$, $V_b > 0$. Panel a) shows the non-local differential conductance $dI_a/dV_b|_{V_a=0}$ as a function of the distances L_l and L_r at very low voltage V_b . There are two resonance peaks on the diagonal, where $L_l = L_r$, and two additional resonance peaks where $L_l = L_r \pm \pi/k_F$. From the considerations in the last section, we expect the EC and the CAR resonances to appear at the same positions. As the peaks are negative, the EC contribution is apparently stronger than the CAR contribution. Figure 7.4b showing a cut through figure 7.4a at constant L_l , where the total current is decomposed into its EC and CAR component, confirms that the peaks in the three-dimensional plot are indeed a superposition of EC and CAR.

When V_b is increased, the EC and the CAR resonance move apart (see figure 7.4c). As expected the EC peaks stay on the diagonals and at $L_l = L_r \pm \pi/k_F$, but their positions are shifted to lower length values. The positive conductance peaks due to CAR appear at the same L_r value as the EC resonance peaks, as both processes are carried by holes on the right hand side. On the left hand side CAR is carried by electrons whose wave vector q^+ decreases with increasing voltage V_b . Consequently, the L_l values of the peak position increase with increasing voltage.

Again, the desired filtering of different processes is obtained. This voltage configuration is interesting as the conductance changes between positive and negative values if L_r is changed.

Differential current cross-correlations

The differential current cross-correlations $dS_{ab}/dV|_{V_a=V_b=V}$ depicted in figure 7.5 and $dS_{ab}/dV_b|_{V_a=0}$ depicted in figure 7.6 behave very similarly to the corresponding differential conductance if one compares the CAR-NR component of the current cross-correlations with the CAR component of the conductance and the EC-NR component with the EC component. The only striking difference is the absence of the mountain range in the noise at low symmetrical bias.

The similarity between current cross-correlations and conductance has already been discussed at the end of section 6.3 in connection to the work of Bignon *et al.* [98]: As the barriers are opaque, the most likely process to occur is normal reflection. Therefore, the elements of the scattering matrix corresponding to normal reflection are close to one and EC-NR is similar to EC and CAR-NR is similar to CAR. Only the AR component of the conductance has no counterpart in the current cross-correlations, because all elements of the current cross-correlations are composed of a local and a non-local process. An AR-NR component does not exist and the AR mountain range is absent in the noise.

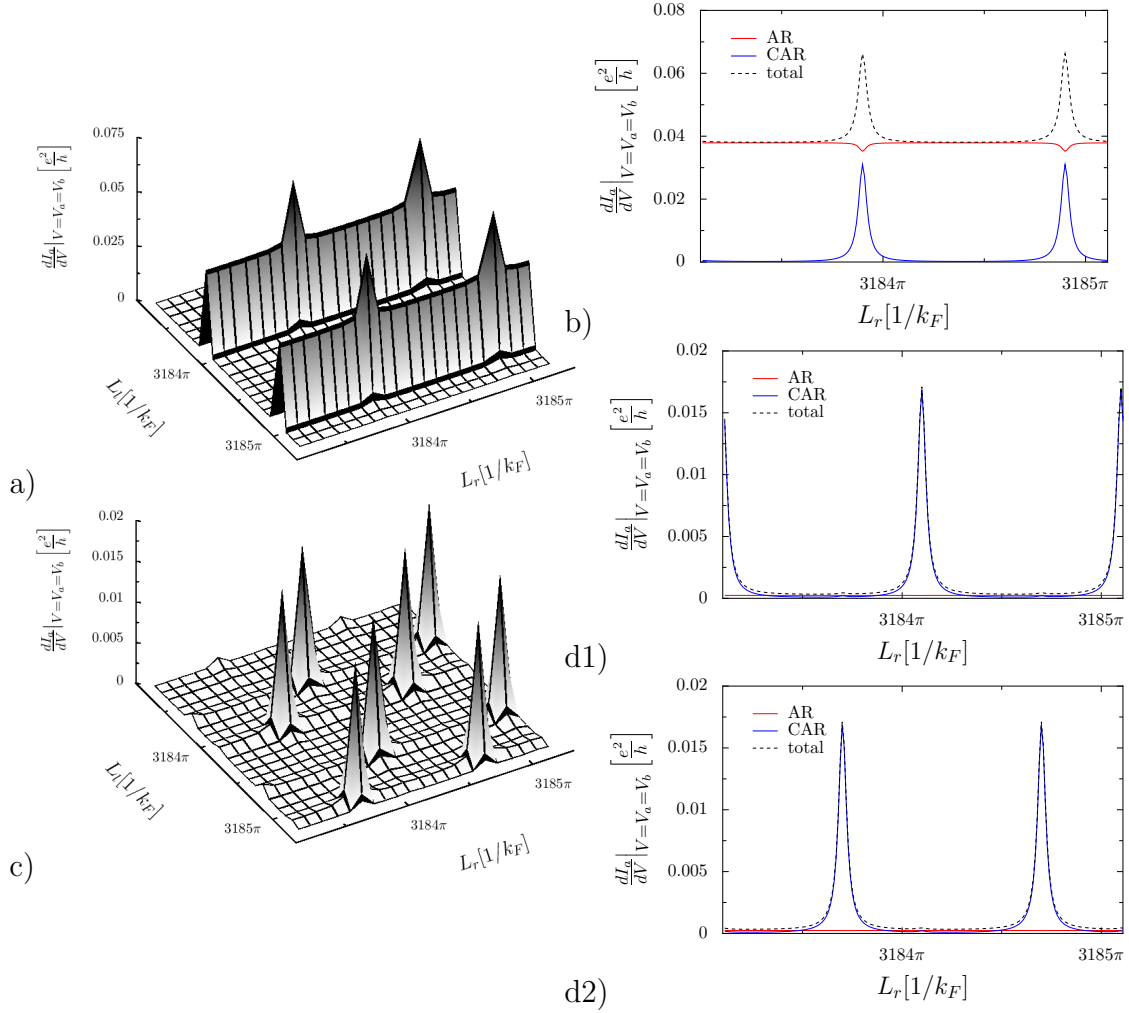


Figure 7.3.: Differential conductance for symmetrically applied bias $V = V_a = V_b$ in the tunneling limit $T_{lrs} = T_{rsn} = 0.01$, $T_{lnn} = T_{rnn} = 0.26$,
 a) as a function of L_r and L_l at low voltage $|e|V = 1 \cdot 10^{-4} \Delta$,
 b) cut through a) along one of the mountain ranges (at $L_l = 3183.9\pi/k_F$) at higher resolution,
 c) as a function of L_r and L_l at higher voltage $|e|V = 6.25 \cdot 10^{-2} \Delta$,
 d1) cut through c) at $L_l = 3183.7\pi/k_F$ at higher resolution,
 d2) cut through c) at $L_l = 3184.1\pi/k_F$ at higher resolution.

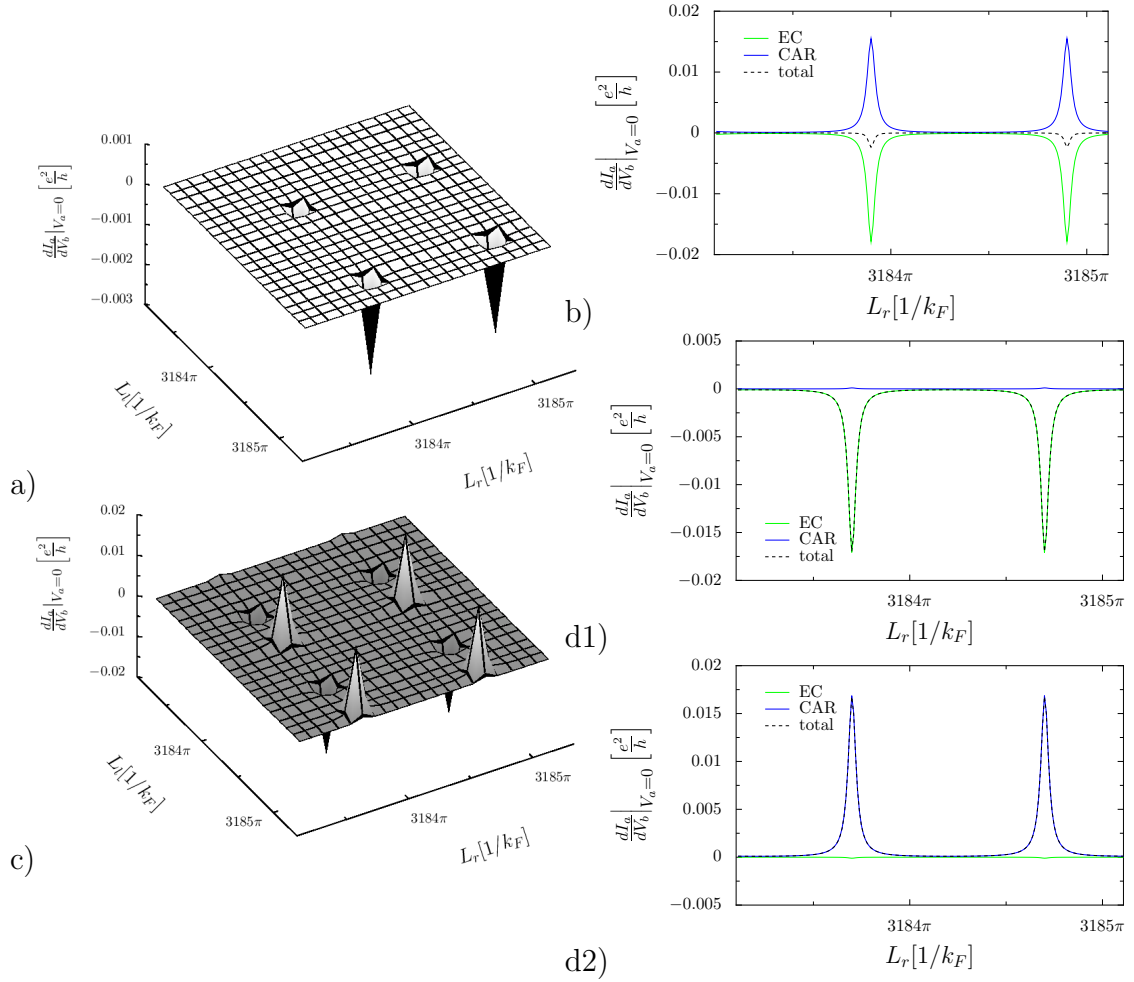


Figure 7.4.: Differential non-local conductance $V_a = 0$ in the tunneling limit $T_{lns} = T_{rsn} = 0.01$, $T_{lnn} = T_{rnn} = 0.26$,
 a) as a function of L_r and L_l at low voltage $|e|V_b = 1 \cdot 10^{-4}\Delta$,
 b) cut through a) at $L_l = 3183.9\pi/k_F$ at higher resolution,
 c) as a function of L_r and L_l at higher voltage $|e|V_b = 6.25 \cdot 10^{-2}\Delta$,
 d1) cut through c) at $L_l = 3183.7\pi/k_F$ at higher resolution,
 d2) cut through c) at $L_l = 3184.1\pi/k_F$ at higher resolution.

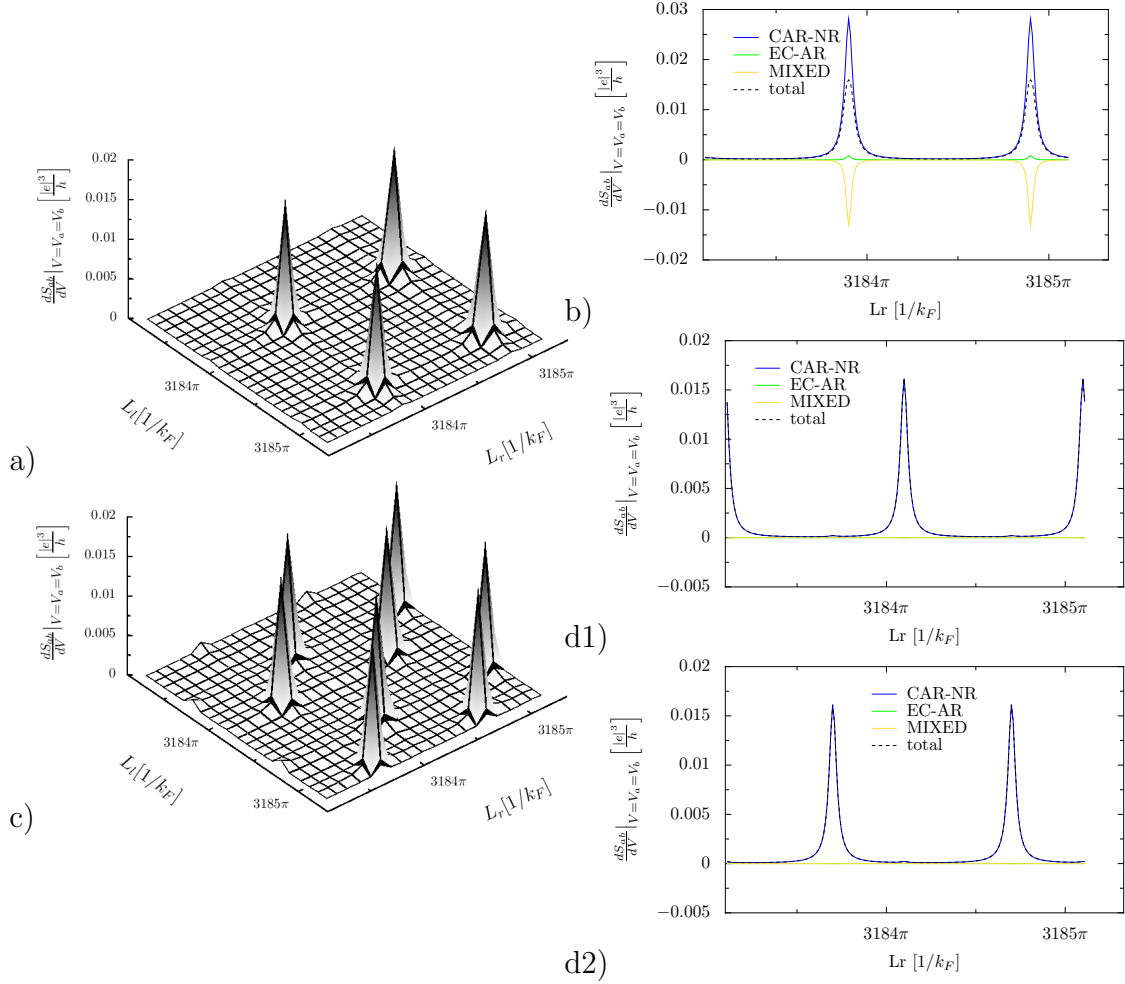


Figure 7.5.: Differential current cross-correlations for $V_a = V_b$ in the tunneling limit $T_{lns} = T_{rsn} = 0.01$, $T_{lnn} = T_{rnn} = 0.26$,
 a) as a function of L_r and L_l at low voltage $|e|V = 1 \cdot 10^{-4} \Delta$,
 b) cut through a) at $L_l = 3183.9\pi/k_F$ at higher resolution,
 c) as a function of L_r and L_l at higher voltage $|e|V = 6.25 \cdot 10^{-2} \Delta$,
 d1) cut through c) at $L_l = 3183.7\pi/k_F$ at higher resolution,
 d2) cut through c) at $L_l = 3184.1\pi/k_F$ at higher resolution.

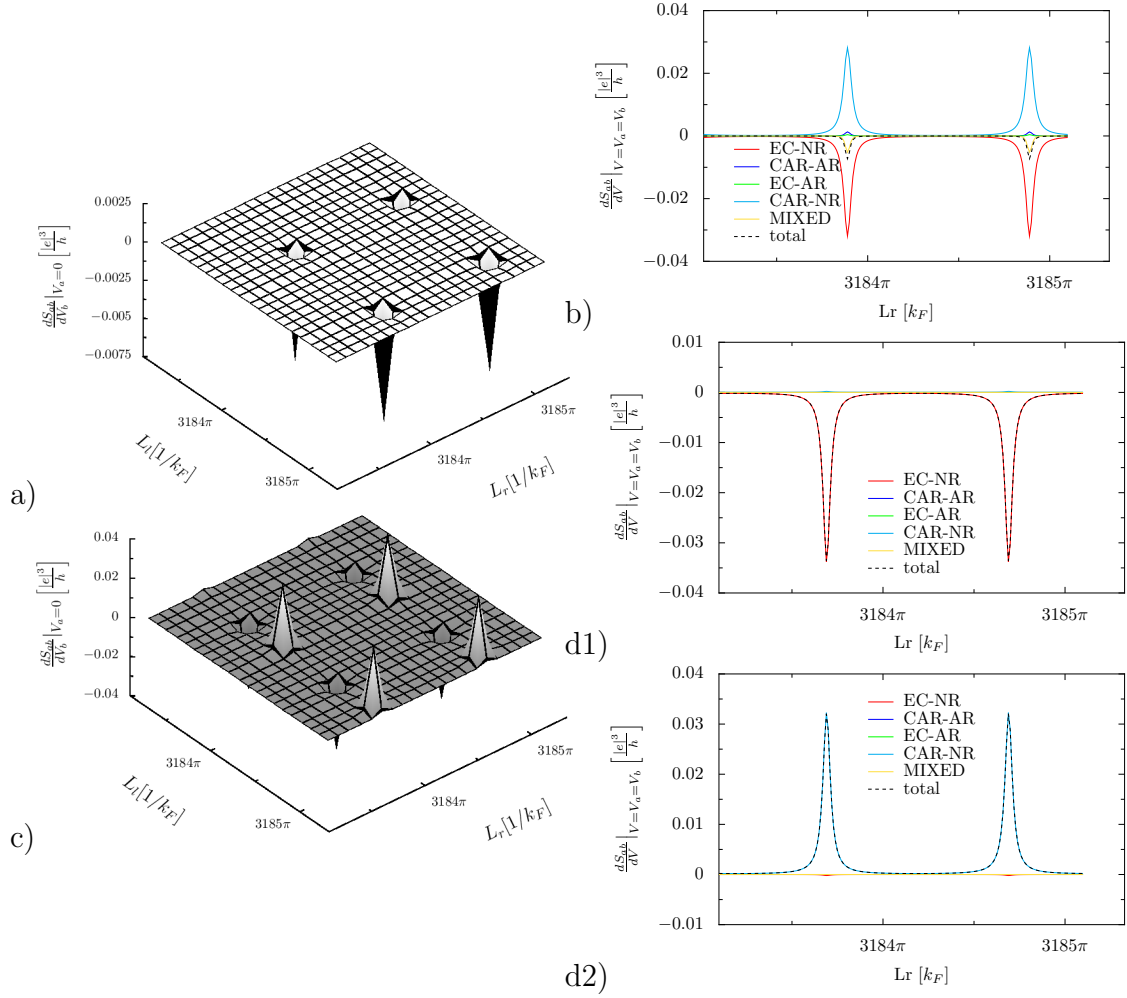


Figure 7.6.: Differential current cross-correlations for $V_a = 0$ in the tunneling limit $T_{lrs} = T_{rsn} = 0.01$, $T_{lnn} = T_{rnn} = 0.26$,
 a) as a function of L_r and L_l at low voltage $|e|V_b = 1 \cdot 10^{-4} \Delta$,
 b) cut through a) at $L_l = 3183.9\pi/k_F$ at higher resolution,
 c) as a function of L_r and L_l at higher voltage $|e|V_b = 6.25 \cdot 10^{-2} \Delta$,
 d1) cut through c) at $L_l = 3183.7\pi/k_F$ at higher resolution,
 d2) cut through c) at $L_l = 3184.1\pi/k_F$ at higher resolution.

7.3. Increasing the Interface Transparency

In the last section, we have studied the ballistic system in the tunnel regime where all resonance peaks are sharp. However, the systems in which electronic Fabry-Perot interferences have already been observed, for example [126, 127], were in the opposite regime of high interface transparency. For increased barrier transparencies, we expect the resonance peaks to become broader and the separation of the different peaks to become less pronounced. In this section, we want to clarify, if it is necessary to stay in the tunnel regime or if the filtering effect survives to higher interface transparencies.

To investigate systematically what happens when the interface transparency is increased, the non-local conductance at $eV_b = 6.25 \cdot 10^{-2} \Delta$ and $V_a = 0$ was calculated for different barrier transparencies, at constant L_r value, which was chosen to be in resonance so that the conductance in function of L_l would feature CAR and EC peaks. Figure 7.7 shows this conductance for a short superconducting electrode $R = 0.25\xi$ and for different values of $T_{lnn} = T_{lns} = T_{rsn} = T_{rnn} = T$. The CAR peak shows an interesting feature: It splits up into two peaks. One possible explanation is that two kinds of CAR resonances can occur. In the present voltage configuration CAR is carried by electrons on the left hand side. The first possibility is that the electron oscillates between the barriers T_{lnn} and T_{lns} as in the tunnel regime. The second possibility is that the electron enters the superconductor as quasi-particle and the (quasi-)electron oscillates between the barriers T_{lnn} and the T_{rsn} . The average over the superconductor does not destroy this resonance because the integral is the same for the electron oscillating at the left hand side and for the hole oscillating at the right hand side. This two possibilities lead to two different resonance lengths. As a consequence of this splitting, the CAR peak vanishes rapidly with increasing barrier transparency, and if one wants to observe it, one should not choose barriers more transparent than $T \approx 0.3$.

The amplitude of quasi-particles decreases exponentially with the superconducting length. Therefore, one can hope to suppress the second resonance between the T_{lnn} and the T_{rsn} barrier by elongating the superconducting electrode. This works indeed, as the plots in figure 7.8 where $R = \xi$ show: The EC and CAR peaks are sharper than in the case of the extremely short superconducting electrode and there is no splitting. Even for barrier transparencies as high as $T = 0.7$, the signature of the EC and the CAR contribution is clearly visible. Against the general trend, we have here a situation where a longer distance in the superconductor leads to a larger signal.

In conclusion, it is not necessary to operate the NNSNN device in the tunnel regime in order to filter the different processes. Surprisingly, CAR resonances are better resolved if the distance in the superconducting electrode is not too short.

Let us now study a system for intermediate interface transparencies $T = T_{lnn} = T_{lns} = T_{rsn} = T_{rnn} = 0.5$ and $R = \xi$, which is clearly outside the tunnel regime but has still a good resolution between the different processes, in more detail. We

7. The Ballistic System

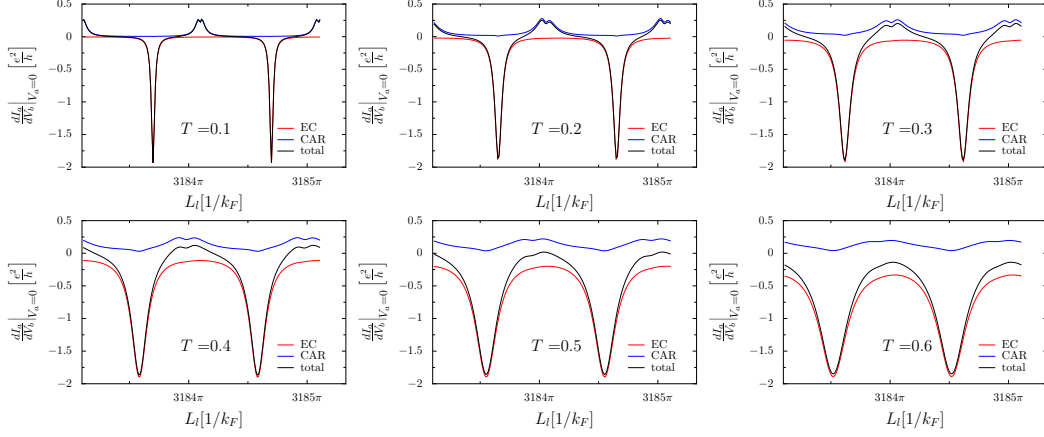


Figure 7.7.: Non-local conductance at $|e|V_b = 6.25 \cdot 10^{-2}\Delta$ and $V_a = 0$ for $T_{l_{nn}} = T_{l_{ns}} = T_{r_{sn}} = T_{r_{nn}} = T$ as indicated in the figure, for a very short superconducting electrode $R = 0.25\xi$, at constant L_r value, chosen to be in resonance so that the conductance in function of L_l features CAR and EC peaks. The CAR peak splits up in two peaks. For $T = 0.5$ and larger, the CAR peak has completely disappeared.

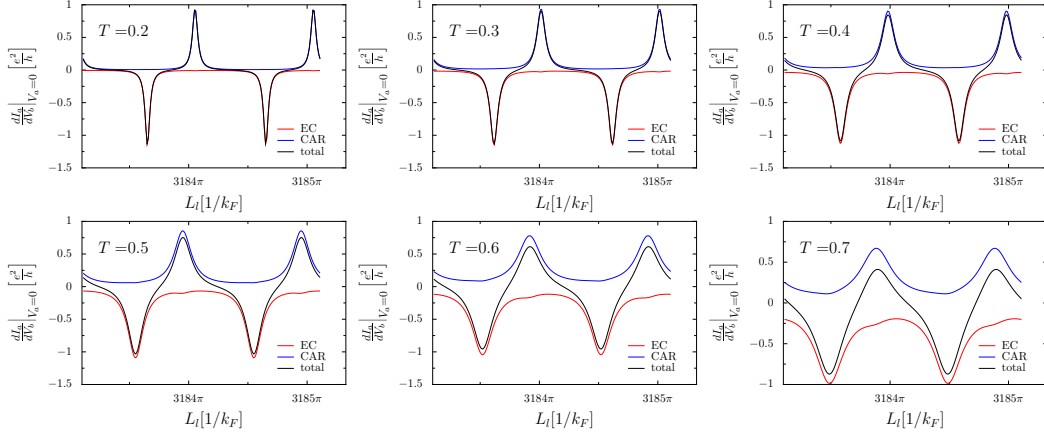


Figure 7.8.: Non-local conductance at $eV_b = 6.25 \cdot 10^{-2}\Delta$ and $V_a = 0$ for $T_{l_{nn}} = T_{l_{ns}} = T_{r_{sn}} = T_{r_{nn}} = T$ as indicated in the figure, for a slightly longer superconducting electrode $R = \xi$, at constant L_r value, chosen to be in resonance so that the conductance in function of L_l features CAR and EC peaks. The EC and CAR peaks are sharper than in the case of the extremely short superconducting electrode depicted in figure 7.7 and there is no splitting. Even for barrier transparencies as high as $T = 0.7$ the signature of the EC and the CAR contribution is clearly visible.

proceed in the same way as in the tunnel regime and analyze the conductance and the current cross-correlations in two different voltage configurations.

Conductance for a symmetrically biased system

Figure 7.9 shows the differential conductance for a symmetrically biased system. At low energies (figure 7.9a) the predominant structures are again the AR mountain ranges. But in difference to the situation in the tunnel regime, there are no CAR peaks on top of the mountain ranges. Instead, at the positions we would have expected them, there are depressions. The cut along the mountain range (figure 7.9b) shows that the AR component features a deep depression where $L_r = L_l$. This depression exists already in the tunnel regime (figure 7.3), but is much less pronounced there. The CAR component increases when L_r approaches L_l as if a peak was to form, but falls back to zero at $L_r = L_l$. In the symmetrical biased case, the differential conductance has no EC component, not because the scattering matrix elements for EC processes are zero, but because there are no free states in the reservoirs. The non-local differential conductance (figure 7.11b) shows that EC processes are very likely to occur at $L_r = L_l = 3183.7\pi/k_F$ with respect to the scattering matrix. As the probabilities for the four possible processes have to sum up to one, a large EC scattering matrix element is only possible at the cost of the CAR and AR scattering matrix elements. In the tunnel regime, the most probable process is normal reflection. The EC scattering matrix element can be increased at the cost of the NR scattering matrix element which has no signature in the conductance. But here, the AR contribution is as high as $3.3e^2/h$, while the maximal possible value in a four channel system is $4e^2/h$.

If higher voltages are applied (see figure 7.9c), each mountain range splits up into two less high mountain ranges. In the tunnel regime, the AR contribution disappeared at higher voltage. Electrons and holes have different wave vectors and therefore different resonance lengths and if the resonances are narrow, electrons and holes are not in resonance at the same time. Here with the higher interface transparencies, the resonances are wider and if the electron is in resonance the hole part is still large enough to form a peak and vice versa. At higher applied voltage, the mountain ranges are surmounted by CAR peaks. The resonance of the EC elements of the scattering matrix occur at different values of L_r and CAR and EC are not in direct competition. The AR contribution (figure 7.9 d1 and d2) features at higher voltage two depressions, where there was only one at lower voltage. In one case AR is decreased in favor of CAR and in the second case, on the diagonals where $L_r = L_l \bmod \pi/k_F$, it is decreased, as in the low energy case, in favor of EC.

Non-local conductance for $V_a = 0$, $V_b > 0$

Figure 7.10 shows the non-local conductance. The peaks position at both studied voltages have the same symmetry as for the non-local conductance in the tunnel regime. But the peaks and depressions are less sharp and higher. In the tunnel

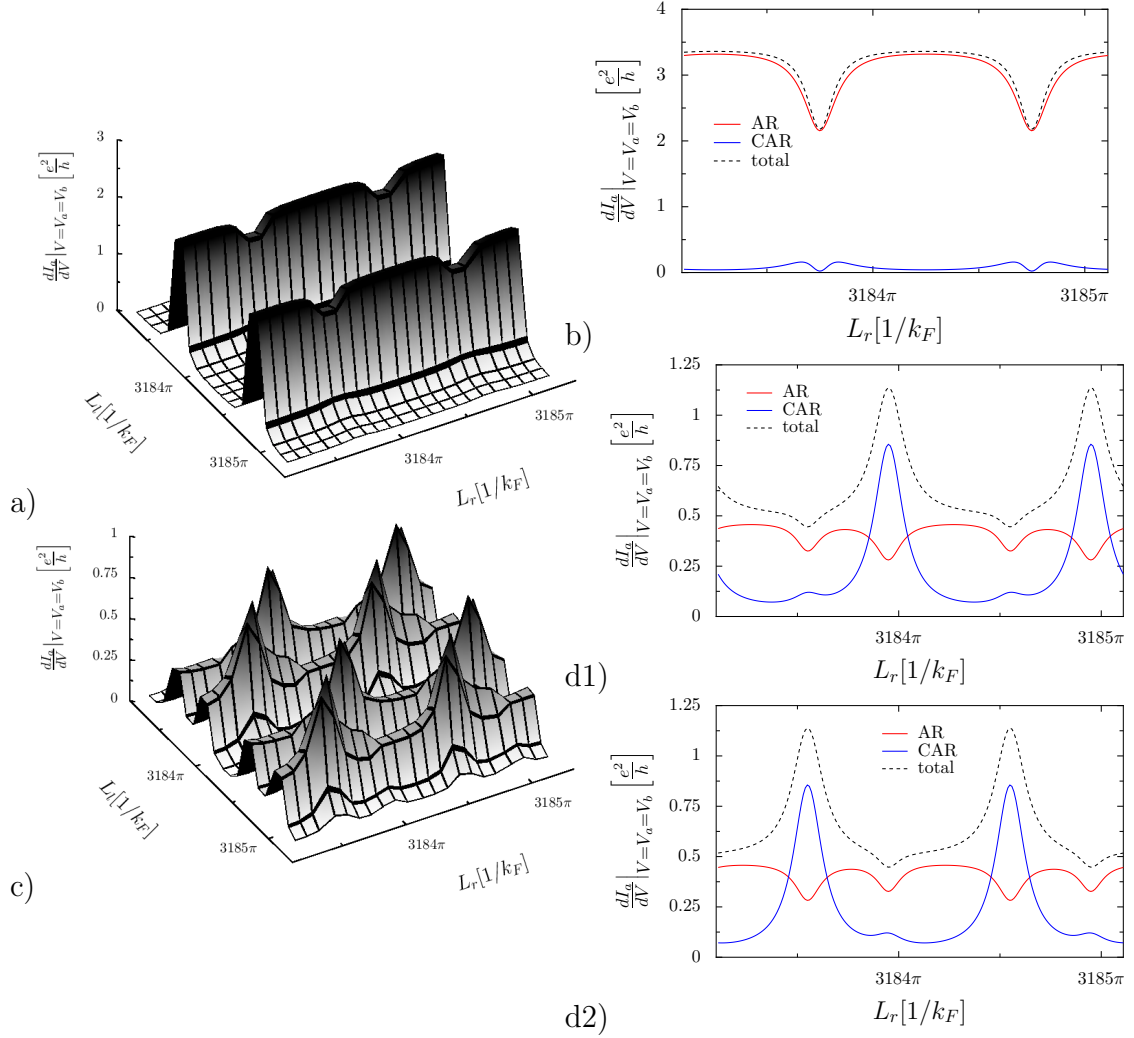


Figure 7.9.: Differential conductance for symmetrically applied bias $V = V_a = V_b$ for intermediate interface transparency $T = T_{lnn} = T_{lns} = T_{rsn} = T_{rnn} = 0.5$ and $R = \xi$,

a) as a function of L_r and L_l at low voltage $|e|V = 1 \cdot 10^{-4} \Delta$,

b) cut through a) along one of the mountain ranges (at $L_l = 3183.7\pi/k_F$) at higher resolution,

c) as a function of L_r and L_l at higher voltage $|e|V = 6.25 \cdot 10^{-2} \Delta$,

d1) cut through c) at $L_l = 3183.5\pi/k_F$ at higher resolution,

d2) cut through c) at $L_l = 3183.9\pi/k_F$ at higher resolution.

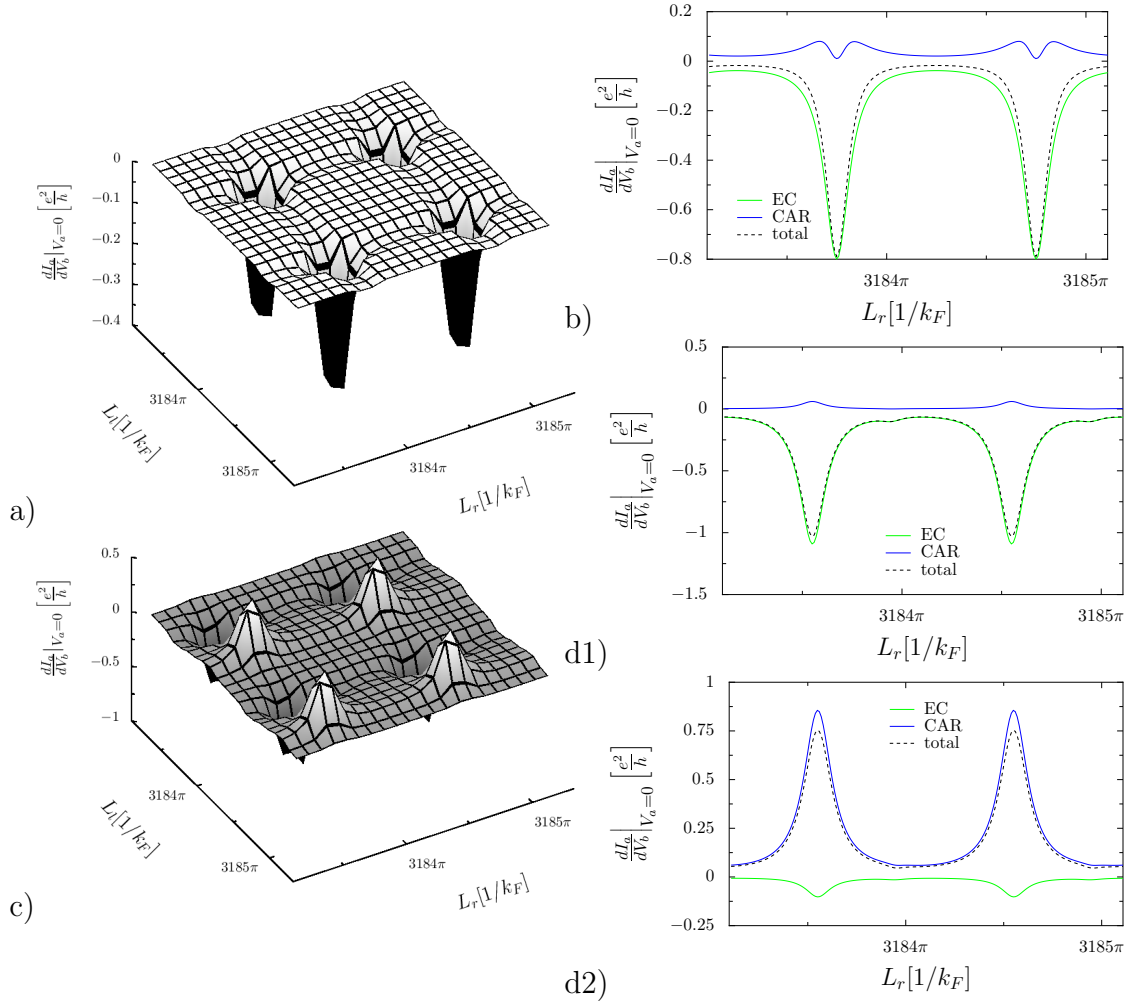
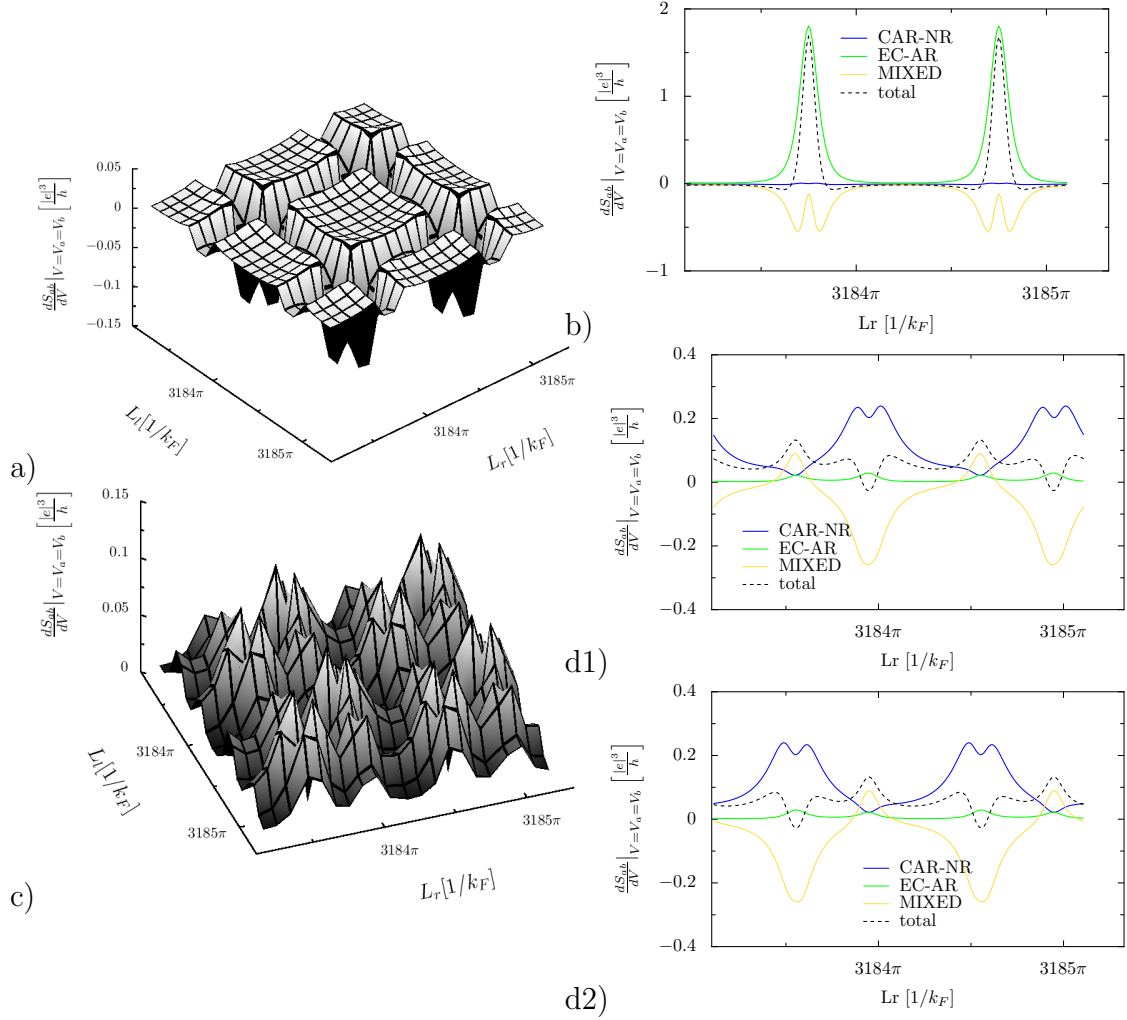


Figure 7.10.: Differential non-local conductance $V_a = 0$ for intermediate interface transparency $T = T_{l_{nn}} = T_{l_{ns}} = T_{r_{sn}} = T_{r_{nn}} = 0.5$ and $R = \xi$,
 a) as a function of L_r and L_l at low voltage $|e|V_b = 1 \cdot 10^{-4}\Delta$,
 b) cut through a) at $L_l = 3183.7\pi/k_F$ at higher resolution,
 c) as a function of L_r and L_l at higher voltage $|e|V_b = 6.25 \cdot 10^{-2}\Delta$,
 d1) cut through c) at $L_l = 3183.5\pi/k_F$ at higher resolution,
 d2) cut through c) at $L_l = 3183.9\pi/k_F$ at higher resolution.



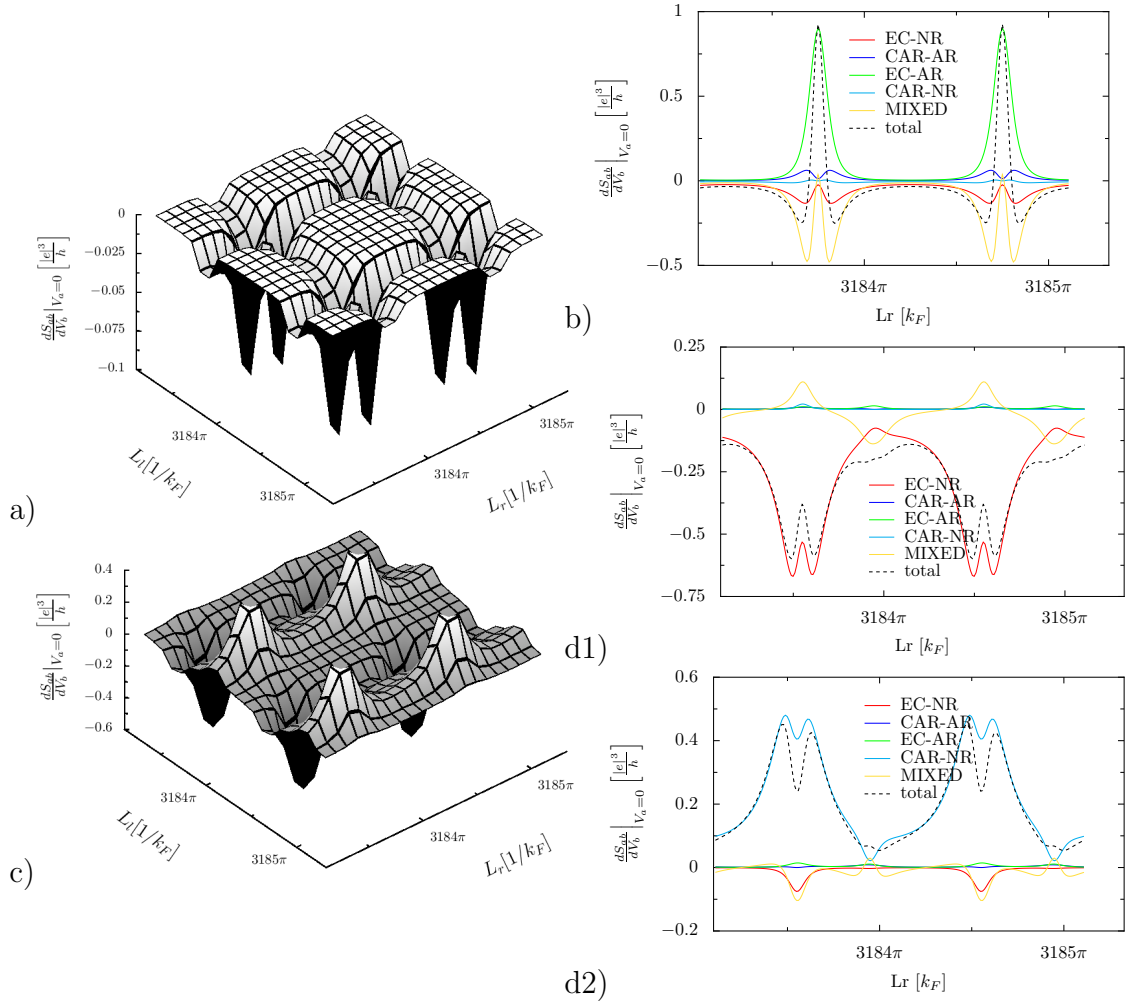


Figure 7.12.: Differential current cross-correlations for $V_a = 0$ for intermediate interface transparency $T = T_{l_{nn}} = T_{l_{ns}} = T_{r_{sn}} = T_{r_{nn}} = 0.5$ and $R = \xi$,
 a) as a function of L_r and L_l at low voltage $|e|V_b = 1 \cdot 10^{-4} \Delta$,
 b) cut through a) at $L_l = 3183.7\pi/k_F$ at higher resolution,
 c) as a function of L_r and L_l at higher voltage $|e|V_b = 6.25 \cdot 10^{-2} \Delta$,
 d1) cut through c) at $L_l = 3183.5\pi/k_F$ at higher resolution,
 d2) cut through c) at $L_l = 3183.9\pi/k_F$ at higher resolution.

regime, the EC and the CAR peak being superimposed at low voltage were similar in magnitude. On figure 7.10b however, the EC amplitude is much larger than the CAR amplitude. As in the symmetrically biased case, there is no CAR peak, but the forming peak features a crater. This figure illustrates that the dip in the CAR contribution occurs exactly at the peak-position in the EC contribution, indicating that the competition between CAR and EC at the level of the scattering matrix is at the origin of the crater in the CAR peak.

Differential current cross-correlations for a symmetrically applied bias

Figure 7.11 shows the current cross-correlations for the symmetric bias case. In the tunnel regime the current cross-correlations were dominated by CAR-NR and EC-NR as those processes depend only quadratic on the interface transparency, while MIXED has cubic and CAR-AR and EC-AR even a bi-quadratic dependence on the interface transparency. For the current cross-correlations at intermediate interface transparency, this restriction does no longer exist. The current cross-correlations in figure 7.11a feature trenches in L_r and in L_l direction. Their spatial extension lets us conclude that they are connected to the AR amplitude which is independent of L_r respectively L_l . From figure 7.11b, we see that the trenches are due to MIXED. Figure 7.11b shows also that the EC-AR component leads to sharp peaks at the positions where $L_r = L_l \bmod \pi/k_F$. These peaks are too narrow to be resolved in the surface plot 7.11a. Here we have again an example for positive current cross-correlations which are not due to CAR. The CAR-NR component which was dominant in the tunnel regime is almost zero here which is consistent with the small amplitude of the CAR process observed in the differential conductance.

At higher energies (figures 7.11d1 and d2), the CAR-NR contribution gains importance as the scattering matrix elements for CAR and EC are no longer in resonance at the same position. In difference to the tunnel regime and as in the case of lower energies, the MIXED processes play an important role.

Differential current cross-correlations for $V_a = 0$, $V_b > 0$

The current cross-correlations in the non-local conductance bias configuration shown in figure 7.12 feature, as the ones in the symmetrically biased case, at low energy trenches where the AR parts of the scattering matrix are in resonance. The MIXED component of the current cross-correlations plays an important role and leads together with the EC-NR-component to mainly negative current cross-correlations. At the points where $L_r = L_l \bmod \pi/k_F$ and the EC elements of the scattering matrix are in resonance, the EC-AR component leads to positive peaks. At higher applied voltage, there is again the separation of the L_l values where CAR and where EC is in resonance and MIXED becomes less important.

Conclusion

These figures show that it is not necessary to be in the tunneling limit in order to separate the different components of the conductance. Against the general trend,

the distance in the superconductor should not be too short. The width and the height of the resonances in the conductance are wider than in the tunnel regime which could even facilitate their observation. As far as the current cross-correlations are concerned, they are richer but also more difficult to interpret in the regime of intermediate interface transparencies because more components play a role.

7.4. Could these Effects Be Observed Experimentally?

What are the possibilities and obstacles for an experimental observation of the phenomena discussed in this chapter? The Fabry-Perot effect needs ballistic transport in a system with only a few (one) channels. The authors of the pioneering paper [126] observed Fabry-Perot interferences in single-walled nanotubes. Instead of varying the length of the nanotube, they change the Fermi-level position in the nanotube by tuning the voltage applied to a gate under the nanotube. As the resonance position depends on the product of wave number and length, changing the Fermi-wave length has the same effect as changing the distance between barriers. This strategy is more realistic than to imagine to vary the distances L_l and L_r . However, if the electrons in the nanotube are sensitive to the electrostatic potential of a gate, they cannot be perfectly screened. One would have to find a regime where the Coulomb interaction is small enough to be neglected in comparison to the, at least in the tunnel regime, also very small coupling energy between the nanotube and the reservoir, but high enough that the Fermi wave vector can be influenced by a gate.

One could imagine a device consisting of two normal conducting and a superconducting electrode connected by one long carbon nanotube with a symmetry similar to devices (see figure 5.4) used in recent experiments [105–108] where the normal and superconducting electrodes are connected over quantum dots. But while there the system was operated in the Coulomb blockade regime, we need the other extreme of very small Coulomb energy. On both sides of the superconductor, there has to be a gate that can be tuned separately so that several periods of Fabry-Perot interferences can be swept in order to obtain plots similar to the one presented in the last section.

The next problem are the interfaces. In reference [126], where Fabry-Perot interferences are observed, the nanotube is connected with near-perfect ohmic contacts to the electrodes. This means, it is in the regime of high interface transparencies ($T \approx 1$), not in the tunnel regime. If the interface transparency is high, the requirement to have the charging energy much smaller than the coupling energy is easier to meet, but in the extreme case of $T \approx 1$ the contrast is too small. In the example of [126] the minimal measured conductance is $dI/dV \approx 3.1e^2/h$ and the maximal measured one $dI/dV \approx 3.3e^2/h$. The last section showed that it is not necessary to be in the tunnel regime to obtain a separation of the different contributions to the conductance. This

can let us hope that an intermediate value of interface transparency can be found. The next problem will then be to achieve this interface transparency experimentally. For sharp Fabry-Perot interferences, the length of the nanotube has to be well defined. If one uses only one long nanotube the superconducting region is created by the proximity effect in the nanotube. So one cannot really speak of a sharp interface.

In conclusion, it will be very challenging to construct a device where the separation of the different components of the conductance and of the current cross-correlations by interference effects in absence of electron-electron interaction are observable. It could, however, be possible to reach experimentally a regime where Fabry-Perot interference effects are in competition to Coulomb blockade effects. The present analysis of a simplified model describing an extreme case could help to explain such experiments in an intermediate regime and it is a good basis for a more complete theory.

7.5. Summary

The insertion of additional tunnel barriers into ballistic NSN-devices leads to Fabry-Perot like oscillations of the differential conductance and of the current cross-correlations. While at low energies the resonances for the CAR and the EC contribution to the non-local conductance occur for the same distances between the barriers, those resonances are well separated at higher energies, because of the different energy dependence of electron and hole wave vectors. In the tunnel regime, the shape of the differential current cross-correlations is very similar to the shape of the differential conductance.

If the central superconducting electrode is not too short, the Fabry-Perot-like oscillations survive to intermediate interface transparencies. In the semi-transparent regime, the competition between the AR, CAR and EC components plays a role on the level of the scattering matrix, because it has to stay unitary. The current cross-correlations are not only composed of EC-NR and CAR-NR, but EC-AR, CAR-AR and MIXED play also an important role.

The experimental realization of a system governed by Fabry-Perot oscillations only will be at least challenging if not impossible. But the detailed study of the Fabry-Perot regime presented here could help to understand an intermediate regime where both Fabry-Perot effects and electron-electron interaction play a role.

Conclusion and Outlook

Transport in the Regime of the Quantum Hall Effect

We have developed a diagrammatic formalism based on a local conductivity model which allowed us to calculate the effective longitudinal conductivity in the high temperature regime of the quantum Hall effect. Our formalism is able to bridge the regime of small fluctuations, which is already well described by first order perturbation theory, to the so far inaccessible regime of strong fluctuations, where quantum Hall samples are typically classed. For transport in a two dimensional electron gas under a strong perpendicular magnetic field, two effects play an important role: The drift motion of electrons along equipotential lines percolating the entire sample and electron-phonon scattering which allows to pass saddle points forming transport-bottle-necks. Both effects enter our formalism via the form of the local conductivity tensor. A signature of the percolation effect is the critical exponent κ . The value of κ has been previously conjectured using qualitative geometrical arguments. Our formalism allowed us to calculate it microscopically.

So far, our formalism is limited to temperatures higher than the typical fluctuations of disorder. It would be worthwhile to extend the calculation of the effective conductivity to temperatures lower than the typical fluctuations of the disorder potential, down to temperatures where the onset of quantum tunneling naively sets a lower bound for the validity of the local conductivity approach. Below the temperature scale associated to the typical disorder strength, the linearization of the Fermi-Dirac distribution will no longer be possible. Additionally, first quantum corrections have to be included in the Hall component of the local conductivity. Both effects mean that we can no longer assume the conductivity fluctuations to follow a Gaussian distribution. Wick's theorem cannot be used and an alternative way to calculate the correlators has to be found. This will certainly not be easy, but the effort would pay in the description of the experimentally observed maximum of the effective longitudinal conductivity reaching values close to e^2/h .

We have compared our result to recent experiments and found overall a very good agreement. For this comparison it was important to know the temperature and magnetic field dependence of the ohmic conductivity σ_0 . So far we used an estimation based on the electron-phonon scattering time found by [4] with Fermi's Golden Rule. However, the estimations at the end of section 3.1 show that first order perturbation theory in the electron-phonon coupling is probably not enough. The phonon contribution to σ_0 should be studied in more detail. A first step would be to

perform the calculation of the electron-phonon scattering time in a self-consistent way.

Another interesting question is whether it is possible to apply the effective medium approach to graphene instead of to ordinary two dimensional electron gases. It has to be clarified whether there is a regime where the local conductivity approach is justified and what are the relevant mechanisms for decoherence. Due to the anomalous quantum Hall effect, the Hall conductivity will have a slightly different form, but the main part of the calculation will stay unchanged.

In the last chapter on the quantum Hall effect, we have turned from the quasi-classical high temperature to the fully quantum mechanical low temperature regime and have studied tunneling over saddle points from the scattering of semi-coherent state wave packets. We have analytically calculated the transmission through a saddle point in the scalar potential in graphene and have found that asymmetric saddle points break particle-hole symmetry in the conductance.

It was natural to start with the scalar potential, as a quantum point contact defined by charged electrodes as well as disorder in form of charged impurities lead to saddle points in the scalar potential. But one of the peculiarities of graphene is the random mass potential due to the coupling to the substrate and it would be interesting to calculate the transmission through a saddle point in this case. The Green's functions for a quadratic mass potential and a flat scalar potential are given in [70]. A calculation of the transmission in analogy to the one developed for the scalar potential should be possible.

Conductance and Differential Current Cross-Correlations in Three-Terminal Normal Conductor-Superconductor-Normal Conductor Hybrid Structures

We have studied the influence of additional barriers on the (non-local) conductance and differential current cross-correlations in three-terminal normal conductor-superconductor-normal conductor (NSN) hybrid structures in order to answer two questions: Can an effect similar to reflectionless tunneling enhance positive current cross correlations in metallic, phase averaged systems? Can the Fabry-Perot interference effects occurring in ballistic systems be used to distinguish the different contributions to the conductance and to the current cross-correlations?

An important tool for this research was to divide the current cross-correlations into different parts. This analysis allowed us to refute the hypothesis that positive current cross-correlations in NSN structures are always a consequence of CAR processes. Additional barriers in metallic, phase averaged systems lead to an enhancement of local processes by reflectionless tunneling but have little influence on non-local processes. The positive current cross-correlations expected for a symmetrically biased system in the tunneling limit are not enhanced by the additional barriers. This negative conclusion is important for experiments, as it shows that the use of diffusive normal metals will probably not simplify the experimental observation of positive current cross-correlation.

In ballistic systems, additional barriers lead to Fabry-Perot oscillations and allow to filter the different contributions of the conductance and of the current cross-correlations, using the different energy dependence of the wave vectors for electrons and holes.

All calculations of the conductance and the differential current cross-correlations were performed in the zero temperature limit. Apart from making calculations simpler this was justified because we wanted to study quantum and not thermal noise. As experiments are always performed at finite temperature, it could be interesting to include finite temperature effects, at least in order to estimate how low temperature has to be so that thermal noise can be neglected. The generalization to finite temperature is straightforward in the used scattering theory: Instead of the Heaviside-Theta functions the full Fermi-Dirac distributions have to be used. At finite temperature, there are additional contributions to the current cross-correlations.

An interesting extension of this work would be to include interaction effects, especially in the ballistic system, as the Fabry-Perot effects will always be in competition with Coulomb blockade. Will the filtering of the different processes still be possible in the presence of interactions?

List of Publications

Published Papers

1. A. Freyn, M. Flöser, and R. Mélin, *Positive current cross-correlations in a highly transparent normal-superconducting beam splitter due to synchronized Andreev and inverse Andreev reflections*, Phys. Rev. B **82**, 014510 (2010).
2. M. Flöser, S. Florens, and T. Champel, *Transmission coefficient through a saddle-point electrostatic potential for graphene in the quantum Hall regime*, Phys. Rev. B **82**, 161408 (2010).
3. M. Flöser, S. Florens, and T. Champel, *Diagrammatic Approach for the High-Temperature Regime of Quantum Hall Transitions*, Phys. Rev. Lett. **107**, 176806 (2011).
4. M. Flöser, S. Florens, and T. Champel, *Transport via classical percolation at quantum Hall plateau transitions*, International Journal of Modern Physics Conference Series (IJMPCS) **11**, 49 (2012).

In Preparation

1. B. Piot, M. Flöser, D. K. Maude, S. Florens, and T. Champel *Classical percolation fingerprints in the high-temperature regime of the quantum Hall effect*, in preparation.
2. M. Flöser, R. Mélin, and D. Feinberg *Does reflectionless tunneling enhance Cooper pair splitting?*, in preparation.

A. Self-Consistent Diagrammatic Approach to the Effective Longitudinal Conductivity

In the main part of my thesis, the effective longitudinal conductivity is first calculated perturbatively and then extrapolated to the regime of strong fluctuations. This is a quite unusual method and in view of the diagrammatic representation, it would perhaps seem more natural to calculate $\langle\chi\rangle$ in self consistent Born approximation. We will try to do that in this appendix. It turns out that the first order of our self-consistent diagrammatic scheme, equivalent to the self consistent Born approximation, is not enough to reach the regime of very small dissipation and to extract the critical exponent κ . Going to second order, we find that such an expansion has a very slow convergence and cannot allow the determination of the critical exponent κ .

Derivation of the Dyson Equation

Our goal is to calculate the tensor $\langle\hat{\chi}\rangle$ given by equation 2.66 with the graphical representation

$$\langle\hat{\chi}\rangle = \text{diagram 1} + \text{diagram 2} + \text{diagram 3} + \dots \quad (\text{A.1})$$

Let us define the full propagator \hat{G} as $\langle\hat{\chi}\rangle$ without the outermost arc and without diagrams which do not have one arc which connects the first and the last dot.:

$$\hat{G} = \text{diagram 1} = \text{diagram 2} + \text{diagram 3} + \text{diagram 4} + \text{diagram 5} + \dots \quad (\text{A.2})$$

The expansion of \hat{G} has the form of a geometric series. It can be resummed

$$\hat{G} = \hat{G}_0 + \hat{G}_0\langle\hat{\chi}\rangle\mathcal{G}_0 + \hat{G}_0\langle\hat{\chi}\rangle\mathcal{G}_0\langle\hat{\chi}\rangle\mathcal{G}_0 + \dots = \hat{G}_0(1 - \langle\hat{\chi}\rangle\mathcal{G}_0)^{-1} \quad (\text{A.3})$$

and yields a Dyson equation in matrix form, where $\langle \hat{\chi} \rangle$ plays the role of the self-energy:

$$\boxed{\hat{\mathcal{G}}(\mathbf{p}) = \hat{\mathcal{G}}_0(\mathbf{p}) + \hat{\mathcal{G}}(\mathbf{p}) \langle \hat{\chi}(\mathbf{p}) \rangle \hat{\mathcal{G}}_0(\mathbf{p})}. \quad (\text{A.4})$$

The special form of the free propagator $\hat{\mathcal{G}}_0(\mathbf{p}) = -\mathbf{p}\mathbf{p}^t/(\sigma_0 p^2) = \mathbf{p}G_0(p)\mathbf{p}^t$ with $G_0(p) = -1/(\sigma_0 p^2)$ gives us hope, that it could be possible to derive a scalar Dyson equation which depends on the norm of \mathbf{p} only. Let us suppose that the full Green's function has the same form as the free one, *i. e.* $\hat{\mathcal{G}}(\mathbf{p}) = \mathbf{p}G(p)\mathbf{p}^t$ and plug this ansatz into the Dyson equation:

$$\mathbf{p}G(p)\mathbf{p}^t = \mathbf{p}G_0(p)\mathbf{p}^t + \mathbf{p}G(p)\mathbf{p}^t \langle \hat{\chi}(\mathbf{p}) \rangle \mathbf{p}G_0(p)\mathbf{p}^t. \quad (\text{A.5})$$

Let us define $S(p) = \mathbf{p}^t \langle \hat{\chi}(\mathbf{p}) \rangle \mathbf{p}$ (as G_0 and G depend only on the norm of \mathbf{p} , the Dyson equation implies that S depends also on the norm only), then

$$\mathbf{p}G(p)\mathbf{p}^t = \mathbf{p}G_0(p)\mathbf{p}^t + \mathbf{p}G(p)S(p)G_0(p)\mathbf{p}^t \quad (\text{A.6})$$

and after multiplication with \mathbf{p}^t/p^2 from the left hand side and with \mathbf{p}/p^2 from the right hand side, we get the desired scalar Dyson equation:

$$G(p) = G_0(p) + G(p)S(p)G_0(p). \quad (\text{A.7})$$

As $G_0(p) = -1/(\sigma_0 p^2)$ it is convenient to define $s(p) = S(p)/p^2$ and $g(p) = p^2 G(p)$, then the Dyson equation reads:

$$\boxed{g(p) = \frac{-1}{\sigma_0 + s(p)}}. \quad (\text{A.8})$$

First Order Self Consistent Scheme

The first order self consistent scheme, analogous to the self consistent Born approximation, consists in neglecting all diagrams with crossings. So we approximate $\langle \hat{\chi} \rangle$ by

$$\hat{\Sigma}_1 = \text{diagram 1} + \text{diagram 2} + \text{diagram 3} + \text{diagram 4} + \dots \quad (\text{A.9})$$

$\hat{\mathcal{G}}$ is now defined as $\hat{\Sigma}_1$ without the outermost arc and from this definition follows that $\hat{\Sigma}_1$ can be represented as

$$\hat{\Sigma}_1 = \text{diagram 1} = \int \frac{d^2 p}{(2\pi)^2} K(p) \hat{e} \hat{\mathcal{G}} \hat{e} \quad (\text{A.10})$$

($K(p)$ and ϵ have been defined in equations (2.71) and (2.72)). In the scalar Dyson equation (A.8) s is replaced by

$$\begin{aligned}
s_1(q) &= \frac{\mathbf{q}^t \Sigma_1(q) \mathbf{q}}{q^2} = \frac{1}{q^2} \int \frac{d^2 p}{(2\pi)^2} K(\mathbf{p} - \mathbf{q}) \mathbf{q}^t \hat{\epsilon} \hat{\mathcal{G}}(\mathbf{p}) \hat{\epsilon} \mathbf{q} \\
&= \frac{1}{q^2} \int \frac{d^2 p}{(2\pi)^2} G(p) K(\mathbf{p} - \mathbf{q}) \mathbf{q}^t \hat{\epsilon} \mathbf{p} \mathbf{p}^t \hat{\epsilon} \mathbf{q} \\
&= \frac{-1}{q^2} \int \frac{d^2 p}{(2\pi)^2} G(p) K(\mathbf{p} - \mathbf{q}) (\mathbf{p} \times \mathbf{q})^2 \\
&= \frac{-1}{q^2} \int \frac{d^2 p}{(2\pi)^2} G(p) K(\mathbf{p} - \mathbf{q}) p^2 q^2 \sin^2(\phi) \\
&= -k_0^2 \xi \int \frac{dp}{4\pi} p g(p) e^{-\frac{\xi^2}{4}(p^2+q^2)} \int d\phi \sin^2(\phi) e^{-\frac{\xi^2}{2} p q \cos(\phi)} \\
&= -\frac{k_0^2 \xi}{4} \int dp p g(p) e^{-\frac{\xi^2}{4}(p^2+q^2)} \left[I_0\left(\frac{pq\xi^2}{2}\right) - I_2\left(\frac{pq\xi^2}{2}\right) \right]
\end{aligned} \tag{A.11}$$

where I_n are the modified Bessel functions of the first kind.

Equation (A.8) and equation (A.11) form a set of self consistent equations. We solve them numerically with the following steps: First a start function g_a for g is guessed, then a first version of s_1 is calculated from this start function and a new function g_b for g is calculated from the first version of s_1 . If $g_a \neq g_b$, g_a is set to $g_a = 1/2(g_a + g_b)$ and the process is repeated until self consistency is reached, *i. e.* until $g_a = g_b$. The desired value of the diagonal elements of $\langle \hat{\chi} \rangle$ is then given by

$$\langle \chi \rangle = s_1(q=0) = -\frac{k_0^2 \xi}{4} \int dp p g(p) e^{-\frac{p^2}{4}}. \tag{A.12}$$

Mixing in each step the new and the old version of g instead of replacing directly g_a by g_b increases the numerical stability. The functions g_a , g_b and s_1 are represented as arrays of sampling points. Due to the exponential function in equation (A.11), it is enough to know these functions for small arguments. For large values of σ_0 the equations converge fast for arbitrary choices of the start function. A good strategy is to calculate first g for large values of σ_0 and decrease then step by step σ_0 , where in each step the final result of g of the preceding step is used as start function.

Figure (A.1) shows the effective longitudinal conductivity $\sigma_L = \sigma_0 + \langle \hat{\chi} \rangle$ in function of σ_0 calculated in the first order self consistent approximation in comparison to σ_L calculated in bare first order perturbation theory and with four-loop order resummation. The first order self consistent Born approximation does not diverge for small values of σ_0 , in difference to plain perturbation theory, but it tends towards a finite value instead of going to zero with a power law. The regime of large conductivity fluctuations is therefore not well described and it is impossible to extract the critical exponent κ from the first order self consistent Born approximation. However, this

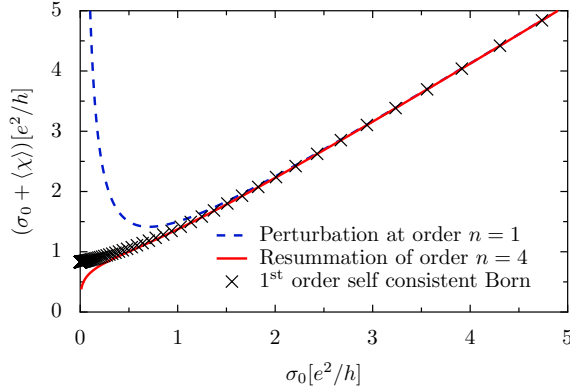


Figure A.1: Comparison of first order self consistent Born approximation with first order perturbation theory and with the four-loop order resummation. The first order self consistent Born approximation does not diverge for small values of σ_0 , but it tends towards a finite value instead of going to zero.

scheme allows to push the validity of the perturbation theory to smaller σ_0 values (down to $\sigma_0 \approx 1$).

Second Order Self Consistent Scheme

As the first order self consistent Born approximation is not sufficient, let us go on and include all diagrams where every arc crosses at most one other arc. This means approximating $\langle \hat{\chi} \rangle$ by $\langle \hat{\chi} \rangle \approx \hat{\Sigma}_2^a + \hat{\Sigma}_2^b$, where $\hat{\Sigma}_2^a$ includes all diagrams where the first and the last dot are connected by one arc, *i. e.* the diagrams of Σ_1 and additionally diagrams where the inner arcs are crossed

$$\hat{\Sigma}_2^a = \hat{\Sigma}_1 + \text{diagram with one arc and crossed inner arcs} + \dots \quad (\text{A.13})$$

and Σ_2^b contains diagrams where the first and the last point are connected to different points and the corresponding arcs cross each other

$$\hat{\Sigma}_2^b = \text{diagram 1} + \text{diagram 2} + \text{diagram 3} + \text{diagram 4} + \dots \quad (\text{A.14})$$

In the Dyson equation (A.8) we have now to set $s = s_2^a + s_2^b$, where $s_2^a = \mathbf{q}^t \Sigma_2^a \mathbf{q} / q^2$ and $s_2^b = \mathbf{q}^t \Sigma_2^b \mathbf{q} / q^2$. s_2^a is calculated in the same way as s_1 . The difference between s_1 and s_2^a is that the function $\hat{\mathcal{G}}$ includes more diagrams in the later case. $\hat{\Sigma}_2^b$ can be represented as

$$\hat{\Sigma}_2^b = \text{diagram with two arcs and crossed inner arcs} \quad (\text{A.15})$$

and therefore

$$\begin{aligned}
s_2^b(q) &= \frac{\mathbf{q}^t \Sigma_2^b(q) \mathbf{q}}{q^2} \tag{A.16} \\
&= \frac{1}{q^2} \int \frac{d^2 p_1}{(2\pi)^2} \int \frac{d^2 p_2}{(2\pi)^2} K(\mathbf{p}_1 - \mathbf{q}) K(\mathbf{p}_2 - \mathbf{p}_1) \mathbf{q}^t \hat{\mathcal{G}}(\mathbf{p}_1) \hat{\mathcal{G}}(\mathbf{p}_2) \hat{\mathcal{G}}(\mathbf{q} - \mathbf{p}_1 + \mathbf{p}_2) \hat{\mathcal{G}} \mathbf{q} \\
&= \frac{1}{q^2} \int \frac{d^2 p_1}{(2\pi)^2} \int \frac{d^2 p_2}{(2\pi)^2} G(p_1) G(p_2) G(|\mathbf{q} - \mathbf{p}_1 + \mathbf{p}_2|) K(\mathbf{p}_1 - \mathbf{q}) K(\mathbf{p}_2 - \mathbf{p}_1) \\
&\quad \mathbf{q}^t \hat{\mathbf{e}}_{\mathbf{p}_1} \mathbf{p}_1^t \hat{\mathbf{e}}_{\mathbf{p}_2} \mathbf{p}_2^t \hat{\mathbf{e}}(\mathbf{q} - \mathbf{p}_1 + \mathbf{p}_2) (\mathbf{q}^t - \mathbf{p}_1^t + \mathbf{p}_2^t) \hat{\mathbf{e}} \mathbf{q} \\
&= \frac{1}{q^2} \int \frac{d^2 p_1}{(2\pi)^2} \int \frac{d^2 p_2}{(2\pi)^2} G(p_1) G(p_2) G(|\mathbf{q} - \mathbf{p}_1 + \mathbf{p}_2|) K(\mathbf{p}_1 - \mathbf{q}) K(\mathbf{p}_2 - \mathbf{p}_1) \\
&\quad (\mathbf{q} \times \mathbf{p}_1)(\mathbf{p}_1 \times \mathbf{p}_2) [\mathbf{p}_2 \times \mathbf{q} - \mathbf{p}_2 \times \mathbf{p}_1] [-\mathbf{p}_1 \times \mathbf{q} + \mathbf{p}_2 \times \mathbf{q}] \\
&= \int \frac{d^2 p_1}{(2\pi)^2} \int \frac{d^2 p_2}{(2\pi)^2} G(p_1) G(p_2) G(|\mathbf{q} - \mathbf{p}_1 + \mathbf{p}_2|) K(\mathbf{p}_1 - \mathbf{q}) K(\mathbf{p}_2 - \mathbf{p}_1) \frac{qp_1 \sin(\phi_1)}{q^2} \\
&\quad (p_1 p_2 \sin(\phi_2 - \phi_1)) [p_2 q \sin(\phi_2) - p_2 p_1 \sin(\phi_2 - \phi_1)] [-p_1 q \sin(\phi_1) + p_2 q \sin(\phi_2)] \\
&= \frac{\xi^2 k_0^4}{16\pi^2} \int d^2 p_1 \int d^2 p_2 g(p_1) g(p_2) g(|\mathbf{q} - \mathbf{p}_1 + \mathbf{p}_2|) \\
&\quad e^{-\frac{\xi^2(q^2 + p_1^2 - 2p_1 q \cos(\phi_1))}{4}} e^{-\frac{\xi^2(p_1^2 + p_2^2 - 2p_1 p_2 \cos(\phi_2 - \phi_1))}{4}} \sin(\phi_1) \sin(\phi_2 - \phi_1) \\
&\quad \frac{-qp_1 \sin(\phi_2) \sin(\phi_1) + qp_2 \sin(\phi_2)^2 + p_1^2 \sin(\phi_2 - \phi_1) \sin(\phi_1) - p_1 p_2 \sin(\phi_2 - \phi_1) \sin(\phi_2)}{q^2 + p_1^2 + p_2^2 - 2qp_1 \cos(\phi_1) + 2qp_2 \cos(\phi_2) - 2p_1 p_2 \cos(\phi_2 - \phi_1)} \\
&= \frac{\xi^2 k_0^4}{16\pi^2} \int dp_1 p_1 \int d\phi_1 \int dp_2 p_2 \int d\phi_2 g(p_1) g(p_2) g(|\mathbf{q} - \mathbf{p}_1 + \mathbf{p}_2|) \\
&\quad e^{-\frac{\xi^2(q^2 + p_1^2 - 2p_1 q \cos(\phi_1))}{4}} e^{-\frac{\xi^2(p_1^2 + p_2^2 - 2p_1 p_2 \cos(\phi_2 - \phi_1))}{4}} \sin(\phi_1) \sin(\phi_2 - \phi_1) \\
&\quad \frac{-qp_1 \sin(\phi_2) \sin(\phi_1) + qp_2 \sin(\phi_2)^2 + p_1^2 \sin(\phi_2 - \phi_1) \sin(\phi_1) - p_1 p_2 \sin(\phi_2 - \phi_1) \sin(\phi_2)}{q^2 + p_1^2 + p_2^2 - 2qp_1 \cos(\phi_1) + 2qp_2 \cos(\phi_2) - 2p_1 p_2 \cos(\phi_2 - \phi_1)}.
\end{aligned}$$

Again, we calculate g self consistently. For the first order self consistent approximation, we had to do only one integral, as the angular integral could be done analytically and it was enough to use the Euler formula. To do the four dimensional integral needed here, we use the Monte Carlo integration routine from the **GNU scientific library**. The continuous values of g have to be interpolated from the sampling points. Once self consistency is reached, the diagonal value of $\langle \hat{\chi} \rangle$ is given by $\langle \chi \rangle = s_2^a(q=0) + s_2^b(q=0)$.

Again, $\langle \chi \rangle$ is first calculated for large values of σ_0 and then σ_0 is stepwise decreased. The result is shown in figure A.2. The result found in second order self consistent Born approximation is closer to the result found with the resummation technique than the first order one, but for $\sigma_0 \lesssim 0.5$ the second order self consistent result is still clearly larger than the four-loop order resummation result. From the points in the interval $0.2e^2/h < \sigma_0 < 0.5e^2/h$ it seems unlikely that the second order self

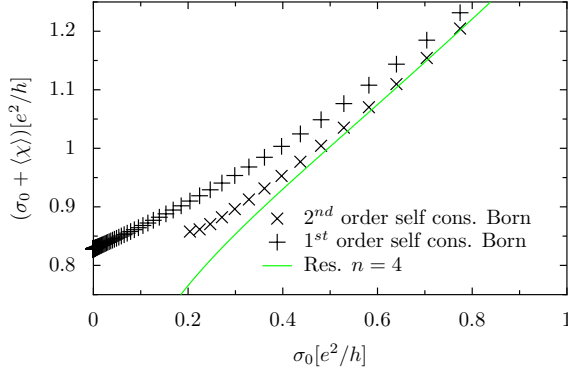


Figure A.2: Comparison of the second order self consistent Born approximation with the first order result and with the four-loop order resummation. The second order self consistent Born approximation is closer to the result found with the resummation technique than the first order one. The second order self consistent Born approximation does not converge for $\sigma_0 \lesssim 0.2e^2/h$

consistent Born result will reach zero in the limit $\sigma_0 \rightarrow 0$. For $\sigma_0 \lesssim 0.2e^2/h$ the second order self consistent calculation does not converge anymore. We could not clarify if the reason is a mathematical one or a lack of numerical accuracy. We tried to increase the number of the sampling points, to reduce σ_0 more slowly or to decrease the mixing of g_a and g_b in order to make the self consistent calculation converge, but without success.

The self consistent approximation seems thus unable to capture the behavior of the longitudinal effective conductivity in the limit of strong spatial fluctuations. In order to extract the critical exponent κ one has to use the non-perturbative Padé resummation technique presented in the main part of this thesis. A possibly more satisfactory approach would be a systematic Monte Carlo resummation of the diagrams. But our results indicate that such a methodology may be poorly convergent in the limit of small dissipation.

B. Components of Current Cross-Correlations

Components of the current cross-correlations:

$$\begin{aligned}
S_{ab}(T=0, V_a, V_b) &= \frac{2e^2}{h} \int dE \left(\right. \\
&2\Re \left[s_{ab}^{ee} s_{ba}^{ee} s_{aa}^{ee\dagger} s_{bb}^{ee\dagger} \right] (\theta(|e|V_a - E) - 2\theta(|e|V_a - E)\theta(|e|V_b - E) + \theta(|e|V_b - E)) \\
&+ 2\Re \left[s_{ab}^{hh} s_{ba}^{hh} s_{aa}^{hh\dagger} s_{bb}^{hh\dagger} \right] (\theta(-|e|V_a - E) - 2\theta(-|e|V_a - E)\theta(-|e|V_b - E) + \theta(-|e|V_b - E)) \left. \right\} EC - NR \\
&+ 2\Re \left[s_{ba}^{eh} s_{ab}^{he} s_{aa}^{hh\dagger} s_{bb}^{ee\dagger} \right] (-\theta(-|e|V_a - E) + 2\theta(-|e|V_a - E)\theta(|e|V_b - E) - \theta(|e|V_b - E)) \\
&+ 2\Re \left[s_{ab}^{eh} s_{ba}^{he} s_{aa}^{ee\dagger} s_{bb}^{hh\dagger} \right] (-\theta(|e|V_a - E) + 2\theta(|e|V_a - E)\theta(-|e|V_b - E) - \theta(-|e|V_b - E)) \left. \right\} CAR - NR \\
&+ 2\Re \left[s_{ab}^{hh} s_{ba}^{ee} s_{bb}^{eh\dagger} s_{aa}^{he\dagger} \right] (-\theta(|e|V_a - E) + 2\theta(|e|V_a - E)\theta(-|e|V_b - E) - \theta(-|e|V_b - E)) \\
&+ 2\Re \left[s_{ab}^{ee} s_{ba}^{hh} s_{aa}^{eh\dagger} s_{bb}^{he\dagger} \right] (-\theta(-|e|V_a - E) + 2\theta(-|e|V_a - E)\theta(|e|V_b - E) - \theta(|e|V_b - E)) \left. \right\} EC - AR \\
&+ 2\Re \left[s_{ba}^{he} s_{ab}^{eh} s_{aa}^{he\dagger} s_{bb}^{eh\dagger} \right] (\theta(|e|V_a - E) - 2\theta(|e|V_a - E)\theta(|e|V_b - E) + \theta(|e|V_b - E)) \\
&+ 2\Re \left[s_{ba}^{eh} s_{ab}^{he} s_{aa}^{eh\dagger} s_{bb}^{he\dagger} \right] (\theta(-|e|V_a - E) - 2\theta(-|e|V_a - E)\theta(-|e|V_b - E) + \theta(-|e|V_b - E)) \left. \right\} CAR - AR \\
&+ 2\Re \left[s_{ab}^{eh} s_{ba}^{hh} s_{bb}^{eh\dagger} s_{aa}^{eh\dagger} + s_{ab}^{hh} s_{ba}^{ee} s_{aa}^{hh\dagger} s_{bb}^{ee\dagger} \right] (-\theta(-|e|V_a - E) + 2\theta(-|e|V_a - E)\theta(-|e|V_b - E) - \theta(-|e|V_b - E)) \\
&+ 2\Re \left[s_{ab}^{ee} s_{ba}^{hh} s_{bb}^{ee\dagger} s_{aa}^{hh\dagger} + s_{ab}^{hh} s_{ba}^{ee} s_{bb}^{hh\dagger} s_{aa}^{ee\dagger} \right] (-\theta(|e|V_a - E) + 2\theta(|e|V_a - E)\theta(|e|V_b - E) - \theta(|e|V_b - E)) \left. \right\} MIXED1 \\
&+ 2\Re \left[s_{ab}^{ee} s_{ba}^{eh} s_{bb}^{ee\dagger} s_{aa}^{eh\dagger} + s_{ab}^{eh} s_{ba}^{ee} s_{bb}^{eh\dagger} s_{aa}^{ee\dagger} \right] (\theta(-|e|V_a - E) - 2\theta(-|e|V_a - E)\theta(|e|V_b - E) + \theta(|e|V_b - E)) \\
&+ 2\Re \left[s_{ab}^{eh} s_{ba}^{ee} s_{bb}^{eh\dagger} s_{aa}^{ee\dagger} + s_{ab}^{ee} s_{ba}^{eh} s_{bb}^{ee\dagger} s_{aa}^{eh\dagger} \right] (\theta(-|e|V_a - E) - 2\theta(-|e|V_a - E)\theta(|e|V_b - E) + \theta(|e|V_b - E)) \left. \right\} MIXED2 \\
&+ 2\Re \left[s_{aa}^{hh} s_{aa}^{ee} s_{aa}^{eh\dagger} s_{aa}^{he\dagger} + s_{aa}^{ee} s_{aa}^{hh} s_{aa}^{he\dagger} s_{aa}^{eh\dagger} \right] (-\theta(|e|V_a - E) + 2\theta(|e|V_a - E)\theta(-|e|V_a - E) - \theta(-|e|V_a - E)) \left. \right\} MIXED3a \\
&+ 2\Re \left[s_{ab}^{eh} s_{bb}^{he} s_{ab}^{ee\dagger} s_{bb}^{hh\dagger} + s_{ab}^{hh} s_{bb}^{ee} s_{ab}^{he\dagger} s_{bb}^{eh\dagger} \right] (-\theta(|e|V_b - E) + 2\theta(|e|V_b - E)\theta(-|e|V_b - E) - \theta(-|e|V_b - E)) \left. \right\} MIXED3b \\
&+ 2\Re \left[s_{aa}^{eh} s_{ba}^{ee} s_{aa}^{eh\dagger} s_{ba}^{ee\dagger} + s_{ba}^{hh} s_{aa}^{ee} s_{aa}^{hh\dagger} s_{ba}^{ee\dagger} \right] (\theta(|e|V_a - E) - 2\theta(|e|V_a - E)\theta(-|e|V_a - E) + \theta(-|e|V_a - E)) \left. \right\} MIXED4a \\
&+ 2\Re \left[s_{ab}^{ee} s_{ba}^{eh} s_{ab}^{ee\dagger} s_{ba}^{eh\dagger} + s_{ab}^{eh} s_{ba}^{ee} s_{ab}^{eh\dagger} s_{ba}^{ee\dagger} \right] (\theta(|e|V_b - E) - 2\theta(|e|V_b - E)\theta(-|e|V_b - E) + \theta(-|e|V_b - E)) \left. \right\} MIXED4b
\end{aligned}$$

Differential current cross-correlations in the non-local conductance setup:

$$\begin{aligned} \frac{dS_{ab}(T=0, V_a=0, V_b)}{dV_b} &= \frac{2|e|^3}{h} \text{sgn}(V_b) \left(\right. \\ &2\Re \left[s_{ab}^{ee}(|e|V_b) s_{ba}^{ee}(|e|V_b) s_{aa}^{ee\dagger}(|e|V_b) s_{bb}^{ee\dagger}(|e|V_b) \right] + 2\Re \left[s_{ab}^{hh}(-|e|V_b) s_{ba}^{hh}(-|e|V_b) s_{aa}^{hh\dagger}(-|e|V_b) s_{bb}^{hh\dagger}(-|e|V_b) \right] \Big\} EC - NR \\ &- 2\Re \left[s_{ba}^{eh}(|e|V_b) s_{ab}^{eh}(|e|V_b) s_{aa}^{hh\dagger}(|e|V_b) s_{bb}^{ee\dagger}(|e|V_b) \right] - 2\Re \left[s_{ab}^{eh}(-|e|V_b) s_{ba}^{eh}(-|e|V_b) s_{aa}^{ee\dagger}(-|e|V_b) s_{bb}^{hh\dagger}(-|e|V_b) \right] \Big\} CAR - NR \\ &- 2\Re \left[s_{ab}^{ee}(|e|V_b) s_{ba}^{hh}(|e|V_b) s_{aa}^{eh\dagger}(|e|V_b) s_{bb}^{eh\dagger}(|e|V_b) \right] - 2\Re \left[s_{ab}^{hh}(-|e|V_b) s_{ba}^{ee}(-|e|V_b) s_{bb}^{eh\dagger}(-|e|V_b) s_{aa}^{eh\dagger}(-|e|V_b) \right] \Big\} EC - AR \\ &+ 2\Re \left[s_{ba}^{he}(|e|V_b) s_{ab}^{he}(|e|V_b) s_{aa}^{eh\dagger}(|e|V_b) s_{bb}^{eh\dagger}(|e|V_b) \right] + 2\Re \left[s_{ab}^{he}(-|e|V_b) s_{ba}^{he}(-|e|V_b) s_{aa}^{eh\dagger}(-|e|V_b) s_{bb}^{eh\dagger}(-|e|V_b) \right] \Big\} CAR - AR \\ &- 2\Re \left[s_{ab}^{ee}(|e|V_b) s_{ba}^{he}(|e|V_b) s_{aa}^{ee\dagger}(|e|V_b) s_{bb}^{he\dagger}(|e|V_b) + s_{ba}^{ee}(|e|V_b) s_{ab}^{he}(|e|V_b) s_{bb}^{ee\dagger}(|e|V_b) s_{aa}^{he\dagger}(|e|V_b) \right] \\ &- 2\Re \left[s_{ab}^{eh}(-|e|V_b) s_{ba}^{hh}(-|e|V_b) s_{aa}^{hh\dagger}(-|e|V_b) s_{bb}^{eh\dagger}(-|e|V_b) + s_{ab}^{hh}(-|e|V_b) s_{ba}^{eh}(-|e|V_b) s_{aa}^{hh\dagger}(-|e|V_b) s_{bb}^{eh\dagger}(-|e|V_b) \right] \Big\} MIXED1 \\ &+ 2\Re \left[s_{ab}^{eh}(|e|V_b) s_{ba}^{ee}(|e|V_b) s_{aa}^{ee\dagger}(|e|V_b) s_{bb}^{eh\dagger}(|e|V_b) + s_{ab}^{hh}(|e|V_b) s_{ba}^{he}(|e|V_b) s_{bb}^{hh\dagger}(|e|V_b) s_{aa}^{he\dagger}(|e|V_b) \right] \\ &+ 2\Re \left[s_{ab}^{ee}(-|e|V_b) s_{ba}^{eh}(-|e|V_b) s_{bb}^{ee\dagger}(-|e|V_b) s_{aa}^{eh\dagger}(-|e|V_b) + s_{ba}^{hh}(-|e|V_b) s_{ab}^{he}(-|e|V_b) s_{aa}^{hh\dagger}(-|e|V_b) s_{bb}^{he\dagger}(-|e|V_b) \right] \Big\} MIXED2 \\ &- 2\Re \left[s_{ab}^{eh}(|e|V_b) s_{bb}^{he}(|e|V_b) s_{aa}^{ee\dagger}(|e|V_b) s_{bb}^{hh\dagger}(|e|V_b) + s_{ab}^{hh}(|e|V_b) s_{bb}^{ee}(|e|V_b) s_{aa}^{he\dagger}(|e|V_b) s_{bb}^{eh\dagger}(|e|V_b) \right] \\ &- 2\Re \left[s_{ab}^{eh}(-|e|V_b) s_{bb}^{he}(-|e|V_b) s_{aa}^{ee\dagger}(-|e|V_b) s_{bb}^{hh\dagger}(-|e|V_b) + s_{ab}^{hh}(-|e|V_b) s_{bb}^{ee}(-|e|V_b) s_{aa}^{he\dagger}(-|e|V_b) s_{bb}^{eh\dagger}(-|e|V_b) \right] \Big\} MIXED3b \end{aligned}$$

B. Components of Current Cross-Correlations

$$\left. \begin{aligned} &+2\Re \left[s_{ab}^{ee}(|e|V_b)s_{ab}^{eh}(|e|V_b)s_{bb}^{ee\dagger}(|e|V_b)s_{ab}^{eh\dagger}(|e|V_b) + s_{ab}^{eh}(|e|V_b)s_{bb}^{he}(|e|V_b)s_{bb}^{hh\dagger}(|e|V_b)s_{ab}^{he\dagger}(|e|V_b) \right] \\ &+2\Re \left[s_{ab}^{ee}(-|e|V_b)s_{ab}^{eh}(-|e|V_b)s_{bb}^{ee\dagger}(-|e|V_b)s_{ab}^{eh\dagger}(-|e|V_b) + s_{ab}^{eh}(-|e|V_b)s_{bb}^{he}(-|e|V_b)s_{bb}^{hh\dagger}(-|e|V_b)s_{ab}^{he\dagger}(-|e|V_b) \right] \end{aligned} \right\} MIXED4b$$

Differential current cross-correlations in the symmetrical setup:

$$\begin{aligned} \frac{dS_{ab}(T=0, V_a+V, V_b=V)}{dV} &= \frac{2|e|^3}{h} \text{sgn}(|e|V) \left(\begin{aligned} &-2\Re \left[s_{ba}^{eh}(|e|V)s_{ab}^{he}(|e|V)s_{aa}^{hh\dagger}(|e|V)s_{bb}^{ee\dagger}(|e|V) + s_{ab}^{eh}(|e|V)s_{ba}^{he}(|e|V)s_{aa}^{ee\dagger}(|e|V)s_{bb}^{hh\dagger}(|e|V) \right] \\ &-2\Re \left[s_{ba}^{eh}(-|e|V)s_{ab}^{he}(-|e|V)s_{aa}^{hh\dagger}(-|e|V)s_{bb}^{ee\dagger}(-|e|V) + s_{ab}^{eh}(-|e|V)s_{ba}^{he}(-|e|V)s_{aa}^{ee\dagger}(-|e|V)s_{bb}^{hh\dagger}(-|e|V) \right] \end{aligned} \right\} CAR - NR \\ &\left. \begin{aligned} &-2\Re \left[s_{ab}^{hh}(|e|V)s_{ba}^{ee}(|e|V)s_{bb}^{eh\dagger}(|e|V)s_{aa}^{he\dagger}(|e|V) + s_{ab}^{ee}(|e|V)s_{ba}^{hh}(|e|V)s_{aa}^{eh\dagger}(|e|V)s_{bb}^{he\dagger}(|e|V) \right] \\ &-2\Re \left[s_{ab}^{hh}(-|e|V)s_{ba}^{ee}(-|e|V)s_{bb}^{eh\dagger}(-|e|V)s_{aa}^{he\dagger}(-|e|V) + s_{ab}^{ee}(-|e|V)s_{ba}^{hh}(-|e|V)s_{aa}^{eh\dagger}(-|e|V)s_{bb}^{he\dagger}(-|e|V) \right] \end{aligned} \right\} EC - AR \\ &\left. \begin{aligned} &+2\Re \left[s_{ab}^{ee}(|e|V)s_{ba}^{eh}(|e|V)s_{bb}^{ee\dagger}(|e|V)s_{aa}^{eh\dagger}(|e|V) + s_{ba}^{eh}(|e|V)s_{ab}^{ee}(|e|V)s_{aa}^{hh\dagger}(|e|V)s_{bb}^{he\dagger}(|e|V) \right] \\ &+2\Re \left[s_{ab}^{ee}(-|e|V)s_{ba}^{eh}(-|e|V)s_{bb}^{ee\dagger}(-|e|V)s_{aa}^{eh\dagger}(-|e|V) + s_{ba}^{eh}(-|e|V)s_{ab}^{ee}(-|e|V)s_{aa}^{hh\dagger}(-|e|V)s_{bb}^{he\dagger}(-|e|V) \right] \\ &+2\Re \left[s_{ab}^{eh}(|e|V)s_{ba}^{ee}(|e|V)s_{aa}^{ee\dagger}(|e|V)s_{bb}^{eh\dagger}(|e|V) + s_{ab}^{eh}(|e|V)s_{ba}^{ee}(|e|V)s_{bb}^{hh\dagger}(|e|V)s_{aa}^{he\dagger}(|e|V) \right] \\ &+2\Re \left[s_{ab}^{eh}(-|e|V)s_{ba}^{ee}(-|e|V)s_{aa}^{ee\dagger}(-|e|V)s_{bb}^{eh\dagger}(-|e|V) + s_{ab}^{eh}(-|e|V)s_{ba}^{ee}(-|e|V)s_{bb}^{hh\dagger}(-|e|V)s_{aa}^{he\dagger}(-|e|V) \right] \end{aligned} \right\} MIXED2 \\ &\left. \begin{aligned} &-2\Re \left[s_{aa}^{hh}(|e|V)s_{ba}^{ee}(|e|V)s_{bb}^{eh\dagger}(|e|V)s_{aa}^{he\dagger}(|e|V) + s_{aa}^{ee}(|e|V)s_{ba}^{hh}(|e|V)s_{bb}^{eh\dagger}(|e|V)s_{aa}^{he\dagger}(|e|V) \right] \\ &-2\Re \left[s_{aa}^{hh}(-|e|V)s_{ba}^{ee}(-|e|V)s_{bb}^{eh\dagger}(-|e|V)s_{aa}^{he\dagger}(-|e|V) + s_{aa}^{ee}(-|e|V)s_{ba}^{hh}(-|e|V)s_{bb}^{eh\dagger}(-|e|V)s_{aa}^{he\dagger}(-|e|V) \right] \end{aligned} \right\} MIXED3a \\ &\left. \begin{aligned} &-2\Re \left[s_{ab}^{eh}(|e|V)s_{bb}^{he}(|e|V)s_{ab}^{ee\dagger}(|e|V)s_{bb}^{hh\dagger}(|e|V) + s_{ab}^{hh}(|e|V)s_{bb}^{ee}(|e|V)s_{ab}^{he\dagger}(|e|V)s_{bb}^{eh\dagger}(|e|V) \right] \\ &-2\Re \left[s_{ab}^{eh}(-|e|V)s_{bb}^{he}(-|e|V)s_{ab}^{ee\dagger}(-|e|V)s_{bb}^{hh\dagger}(-|e|V) + s_{ab}^{hh}(-|e|V)s_{bb}^{ee}(-|e|V)s_{ab}^{he\dagger}(-|e|V)s_{bb}^{eh\dagger}(-|e|V) \right] \end{aligned} \right\} MIXED3b \\ &\left. \begin{aligned} &+2\Re \left[s_{aa}^{eh}(|e|V)s_{ba}^{ee}(|e|V)s_{aa}^{ee\dagger}(|e|V)s_{ba}^{eh\dagger}(|e|V) + s_{ba}^{eh}(|e|V)s_{aa}^{ee}(|e|V)s_{aa}^{hh\dagger}(|e|V)s_{ba}^{he\dagger}(|e|V) \right] \\ &+2\Re \left[s_{aa}^{eh}(-|e|V)s_{ba}^{ee}(-|e|V)s_{aa}^{ee\dagger}(-|e|V)s_{ba}^{eh\dagger}(-|e|V) + s_{ba}^{eh}(-|e|V)s_{aa}^{ee}(-|e|V)s_{aa}^{hh\dagger}(-|e|V)s_{ba}^{he\dagger}(-|e|V) \right] \end{aligned} \right\} MIXED4a \\ &\left. \begin{aligned} &+2\Re \left[s_{ab}^{ee}(|e|V)s_{ab}^{eh}(|e|V)s_{bb}^{ee\dagger}(|e|V)s_{ab}^{eh\dagger}(|e|V) + s_{ab}^{eh}(|e|V)s_{bb}^{he}(|e|V)s_{bb}^{hh\dagger}(|e|V)s_{ab}^{he\dagger}(|e|V) \right] \\ &+2\Re \left[s_{ab}^{ee}(-|e|V)s_{ab}^{eh}(-|e|V)s_{bb}^{ee\dagger}(-|e|V)s_{ab}^{eh\dagger}(-|e|V) + s_{ab}^{eh}(-|e|V)s_{bb}^{he}(-|e|V)s_{bb}^{hh\dagger}(-|e|V)s_{ab}^{he\dagger}(-|e|V) \right] \end{aligned} \right\} MIXED4b \end{aligned}$$

Bibliography

- [1] D. Stroud, *Generalized effective-medium approach to the conductivity of an inhomogeneous material*, Phys. Rev. B **12**, 3368 (1975).
- [2] S. H. Simon and B. I. Halperin, *Explanation for the Resistivity Law in Quantum Hall Systems*, Phys. Rev. Lett. **73**, 3278 (1994).
- [3] M. B. Isichenko *et al.*, *Diffusion in a medium with vortex flow*, JETP **69**, 517 (1989), [ZETF **96**, 913 (1989)].
- [4] H. L. Zhao and S. Feng, *Electron-phonon scattering in strong magnetic fields and the temperature scaling between quantum Hall plateaus*, Phys. Rev. Lett. **70**, 4134 (1993).
- [5] B. Piot *et al.*, *Classical percolation fingerprints in the high-temperature regime of the quantum Hall effect*, in preparation .
- [6] V. Renard, Z. D. Kvon, G. M. Gusev, and J. C. Portal, *Large positive magnetoresistance in a high-mobility two-dimensional electron gas: Interplay of short- and long-range disorder*, Phys. Rev. B **70**, 033303 (2004).
- [7] H. A. Fertig and B. I. Halperin, *Transmission coefficient of an electron through a saddle-point potential in a magnetic field*, Phys. Rev. B **36**, 7969 (1987).
- [8] T. Champel and S. Florens, *Quantum transport properties of two-dimensional electron gases under high magnetic fields*, Phys. Rev. B **75**, 245326 (2007).
- [9] T. Champel, S. Florens, and L. Canet, *Microscopics of disordered two-dimensional electron gases under high magnetic fields: Equilibrium properties and dissipation in the hydrodynamic regime*, Phys. Rev. B **78**, 125302 (2008).
- [10] T. Champel and S. Florens, *Electron quantum dynamics in closed and open potentials at high magnetic fields: Quantization and lifetime effects unified by semicoherent states*, Phys. Rev. B **80**, 125322 (2009).
- [11] G. E. Blonder, M. Tinkham, and T. M. Klapwijk, *Transition from metallic to tunneling regimes in superconducting microconstrictions: Excess current, charge imbalance, and supercurrent conversion*, Phys. Rev. B **25**, 4515 (1982).

- [12] M. P. Anantram and S. Datta, *Current fluctuations in mesoscopic systems with Andreev scattering*, Phys. Rev. B **53**, 16390 (1996).
- [13] J. A. Melsen and Beenakker C. W. J., *Reflectionless tunneling through a double-barrier NS junction*, Physica B **203**, 219 (1994).
- [14] B. Kramer, T. Ohtsuki, and S. Kettemann, *Random network models and quantum phase transitions in two dimensions*, Physics Reports **417**, 211 (2005).
- [15] W. Poirier *et al.*, *Application of the quantum Hall effect to resistance metrology*, Comptes rendus physique **12**, 347 (2011).
- [16] K. Hashimoto *et al.*, *Quantum Hall Transition in Real Space: From Localized to Extended States*, Phys. Rev. Lett. **101**, 256802 (2008).
- [17] G. F. Giuliani and Vignale G., *Quantum Theory of the Electron Liquid* (Cambridge University Press, Cambridge, 2005).
- [18] B. Douçot and V. Pasquier, *Physics in a Strong Magnetic Field*, Séminaire Poincaré 17 (2004).
- [19] S. Adachi, *GaAs, AlAs, and AlXGa1-XAs - Material parameters for use in research and device applications*, J. Appl. Phys. **58**, R1 (1985).
- [20] M. M. Fogler and B. I. Shklovskii, *Collapse of spin splitting in the quantum Hall effect*, Phys. Rev. B **52**, 17366 (1995).
- [21] B. A. Piot *et al.*, *Quantum Hall ferromagnet at high filling factors: A magnetic-field-induced Stoner transition*, Phys. Rev. B **72**, 245325 (2005).
- [22] C. W. J. Beenakker, *Edge channels for the fractional quantum Hall effect*, Phys. Rev. Lett. **64**, 216 (1990).
- [23] D. B. Chklovskii, B. I. Shklovskii, and L. I. Glazman, *Electrostatics of edge channels*, Phys. Rev. B **46**, 4026 (1992).
- [24] N. R. Cooper and J. T. Chalker, *Coulomb interactions and the integer quantum Hall effect: Screening and transport*, Phys. Rev. B **48**, 4530 (1993).
- [25] K. Lier and R. R. Gerhardts, *Self-consistent calculations of edge channels in laterally confined two-dimensional electron systems*, Phys. Rev. B **50**, 7757 (1994).
- [26] T. Ando and Y. Uemura, *Theory of quantum transport in a two-dimensional electron system under magnetic fields. I. Characteristics of level broadening and transport under strong fields*, J. Phys. Soc. Jpn **36**, 959 (1974).

-
- [27] T. Ando, A. B. Fowler, and F. Stern, *Electronic properties of two-dimensional systems*, Rev. Mod. Phys. **54**, 437 (1982).
 - [28] M. Janßen, O. Viehweger, U. Fastenrath, and J. Hajdu, *Introduction to the Theory of the Integer Quantum Hall Effect* (VCH, Weinheim, 1994).
 - [29] K. Hashimoto *et al.*, *Robust Nodal Structure of Landau Level Wave Functions Revealed by Fourier Transform Scanning Tunneling Spectroscopy*, ArXiv e-prints (2012), arXiv:1201.2235.
 - [30] M. E. Raikh and T. V. Shahbazyan, *High Landau levels in a smooth random potential for two-dimensional electrons*, Phys. Rev. B **47**, 1522 (1993).
 - [31] S. Hikami *et al.*, *Anderson localization in a spatially correlated random potential under a strong magnetic field*, Journal de Physique **46**, 2021 (1985).
 - [32] R. R. Gerhardts, *Path-integral approach to the two-dimensional magneto-conductivity problem, I. General Formulation of the Approach*, Zeitschrift für Physik B Condensed Matter **21**, 275 (1975).
 - [33] R. R. Gerhardts, *Path-integral approach to the two-dimensional magneto-conductivity problem, II. Application to n-Type (100)-Surface Inversion Layers of p-Silicon*, Zeitschrift für Physik B Condensed Matter **21**, 285 (1975).
 - [34] K. A. Benedict and J. T. Chalker, *An exactly solvable model of the disordered two-dimensional electron-gas in a strong magnetic-field*, J. Phys. C: Solid State Phys. **19**, 3587 (1986).
 - [35] M. R. Geller and G. Vignale, *Currents in the compressible and incompressible regions of the two-dimensional electron gas*, Phys. Rev. B **50**, 11714 (1994).
 - [36] T. Champel, S. Florens, and M. E. Raikh, *Nonlocal correlations of the local density of states in disordered quantum Hall systems*, Phys. Rev. B **83**, 125321 (2011).
 - [37] J. T. Chalker and P. Coddington, *Percolation, Quantum Tunnelling and the Integer Hall-Effect*, J. Phys. C: Solid State Phys. **21**, 2665 (1988).
 - [38] H. A. Fertig and B. I. Halperin, *Transmission coefficient of an electron through a saddle-point potential in a magnetic field*, Phys. Rev. B **36**, 7969 (1987).
 - [39] K. Slevin and T. Ohtsuki, *Critical exponent for the quantum Hall transition*, Phys. Rev. B **80**, 041304 (2009).
 - [40] H. P. Wei, D. C. Tsui, M. A. Paalanen, and A. M. M. Pruisken, *Experiments on Delocalization and Universality in the Integral Quantum Hall Effect*, Phys. Rev. Lett. **61**, 1294 (1988).

- [41] W. Li *et al.*, *Crossover from the nonuniversal scaling regime to the universal scaling regime in quantum Hall plateau transitions*, Phys. Rev. B **81**, 033305 (2010).
- [42] Y. J. Zhao *et al.*, *Experimental studies of scaling behavior of a quantum Hall system with a tunable Landau level mixing*, Phys. Rev. B **78**, 233301 (2008).
- [43] A. M. Dykhne and I. M. Ruzin, *Theory of the fractional quantum Hall effect: The two-phase model*, Phys. Rev. B **50**, 2369 (1994).
- [44] M. Flöser, S. Florens, and T. Champel, *Diagrammatic Approach for the High-Temperature Regime of Quantum Hall Transitions*, Phys. Rev. Lett. **107**, 176806 (2011).
- [45] M. Flöser, S. Florens, and T. Champel, *Transport via classical percolation at quantum Hall plateau transitions*, International Journal of Modern Physics Conference Series (IJMPCS) **11**, 49 (2012).
- [46] M. B. Isichenko, *Percolation, statistical topography, and transport in random-media*, Reviews of modern physics **64**, 961 (1992).
- [47] S. A. Trugman and A. Weinrib, *Percolation with a threshold at zero: A new universality class*, Phys. Rev. B **31**, 2974 (1985).
- [48] L. D. Landau and E. M. Lifchitz, *Physique théorique: Electrodynamique des milieux continus* (Editions Mir, Moscou, 1990).
- [49] C. Timm, M. E. Raikh, and F. von Oppen, *Disorder-Induced Resistive Anomaly Near Ferromagnetic Phase Transitions*, Phys. Rev. Lett. **94**, 036602 (2005).
- [50] Y. A. Dreizin and A. M. Dykhne, *Anomalous conductivity of inhomogeneous media in a strong magnetic field*, JETP **36**, 127 (1973), [ZETF **63**, 242 (1972)].
- [51] I. V. Kukushkin, S. V. Meshkov, and V. B. Timofeev, *Two-dimensional electron density of states in a transverse magnetic field*, Sov. Phys. Usp. **31**, 511 (1988), [Usp. Fiz. Nauk **155**, 219 (1988)].
- [52] D. Stauffer and A. Aharony, *Introduction To Percolation Theory* (Taylor & Francis, London, 1992).
- [53] D. M. Basko and V. E. Kravtsov, *Coulomb blockade in quantum dots under ac pumping*, Phys. Rev. B **71**, 085311 (2005).
- [54] The GSL-team, *gsl-ref.info*, (2010), <http://www.gnu.org/software/gsl/>.
- [55] G. Peter Lepage, *A new algorithm for adaptive multidimensional integration*, Journal of Computational Physics **27**, 192 (1978).

-
- [56] G. A. Baker, *Essentials of Padé Approximants* (Academic Press, New York, 1975).
- [57] R. R. P. Singh and S. Chakravarty, *High-temperature series expansion for spin glasses. II. Analysis of the series*, Phys. Rev. B **36**, 559 (1987).
- [58] M. G. Watts, in *Application of the method of Pade approximants to the excluded volume problem*, J. Phys. A: Math. Gen. **8**, 61 (1975).
- [59] M. Ferer and M. J. Velgakis, *Hyperscaling in the three-dimensional Ising model*, Phys. Rev. B **27**, 2839 (1983).
- [60] H. Bruus and K. Flensberg, *Many-body quantum theory in condensed matter physics: an introduction* (Oxford University Press, Oxford, 2004).
- [61] Preden Roulleau *et al.*, *Direct Measurement of the Coherence Length of Edge States in the Integer Quantum Hall Regime*, Phys. Rev. Lett. **100**, 126802 (2008).
- [62] A. A. Abrikosov, *Fundamentals of the theory of metals* (North-Holland, Amsterdam, 1988).
- [63] I. S. Gradshteyn and I. M. Ryzhik, *Tabel of Integrals, Series, and Products* (Elsevier Academic Press, Amsterdam, 2007).
- [64] M. M. Fogler, A. Y. Dobin, V. I. Perel, and B. I. Shklovskii, *Suppression of chaotic dynamics and localization of two-dimensional electrons by a weak magnetic field*, Phys. Rev. B **56**, 6823 (1997).
- [65] D. G. Polyakov, F. Evers, A. D. Mirlin, and P. Wölfle, *Quasiclassical magneto-transport in a random array of antidots*, Phys. Rev. B **64**, 205306 (2001).
- [66] D. G. Polyakov and B. I. Shklovskii, *Universal Prefactor of Activated Conductivity in the Quantum Hall Effect*, Phys. Rev. Lett. **74**, 150 (1995).
- [67] M. M. Fogler, D. G. Polyakov, and B. I. Shklovskii, *Activated conductivity in the quantum Hall effect*, Surface science **361**, 255 (1996).
- [68] H. P. Wei, S. Y. Lin, D. C. Tsui, and A. M. M. Pruisken, *Effect of long-range potential fluctuations on scaling in the integer quantum Hall effect*, Phys. Rev. B **45**, 3926 (1992).
- [69] I. Neder *et al.*, *Interference between two indistinguishable electrons from independent sources*, Nature **448**, 333 (2007).

- [70] T. Champel and S. Florens, *High magnetic field theory for the local density of states in graphene with smooth arbitrary potential landscapes*, Phys. Rev. B **82**, 045421 (2010).
- [71] M. Flöser, S. Florens, and T. Champel, *Transmission coefficient through a saddle-point electrostatic potential for graphene in the quantum Hall regime*, Phys. Rev. B **82**, 161408 (2010).
- [72] C. Zachos, D. Fairlie, and T. Curtright, *Quantum mechanics in phase space: an overview with selected papers* (World Scientific Pub Co Inc, Singapore, 2005), Vol. 34.
- [73] C. Zachos, *Geometrical evaluation of star products*, Journal of Mathematical Physics **41**, 5129 (2000).
- [74] M. Büttiker, *Quantized transmission of a saddle-point constriction*, Phys. Rev. B **41**, 7906 (1990).
- [75] A. H. Castro Neto *et al.*, *The electronic properties of graphene*, Rev. Mod. Phys. **81**, 109 (2009).
- [76] K. S. Novoselov *et al.*, *Two-dimensional gas of massless Dirac fermions in graphene*, Nature **438**, 197 (2005).
- [77] M. Flöser, Master's thesis, *Positive Cross Correlations of Noise in a Three Terminal Normal Metal-Superconductor-Normal Metal Hybrid Structure*, Université Joseph Fourier, Grenoble, France, 2009.
- [78] P. G. De Gennes and D. Saint-James, *Elementary excitations in the vicinity of a normal metal-superconducting metal contact*, Phys. Letters **4**, (1963).
- [79] D. Saint-James, *Excitations élémentaires au voisinage de la surface de séparation d'un métal normal et d'un métal supraconducteur*, Journal de Physique **25**, 899 (1964).
- [80] A. F. Andreev, *Thermal conductivity of the intermediate state of superconductors*, JETP **19**, (1964), [ZETF **46**, 1823 (1964)].
- [81] J. M. Byers and M. E. Flatté, *Probing Spatial Correlations with Nanoscale Two-Contact Tunneling*, Phys. Rev. Lett. **74**, 306 (1995).
- [82] A. Einstein, B. Podolsky, and N. Rosen, *Can quantum-mechanical description of physical reality be considered complete?*, Physical review **47**, 777 (1935).
- [83] D. Bohm and Y. Aharonov, *Discussion of experimental proof for the paradox of Einstein, Rosen, and Podolsky*, Physical Review **108**, 1070 (1957).

-
- [84] J.S. Bell, *On the Einstein-Podolsky-Rosen Paradox*, Physics **1**, 195 (1964), reprinted in J. S. Bell, *Speakable and Unspeakable in Quantum Mechanics* (Cambridge University Press, Cambridge, 1989).
- [85] J. F. Clauser, M. A. Horne, A. Shimony, and R. A. Holt, *Proposed Experiment to Test Local Hidden-Variable Theories*, Phys. Rev. Lett. **23**, 880 (1969).
- [86] A. Aspect, J. Dalibard, and G. Roger, *Experimental Test of Bell's Inequalities Using Time-Varying Analyzers*, Phys. Rev. Lett. **49**, 1804 (1982).
- [87] D. Salart *et al.*, *Spacelike Separation in a Bell Test Assuming Gravitationally Induced Collapses*, Phys. Rev. Lett. **100**, 220404 (2008).
- [88] M. Ansmann *et al.*, *Violation of Bell's inequality in Josephson phase qubits*, Nature **461**, 504 (2009).
- [89] P. Recher, E. V. Sukhorukov, and D. Loss, *Andreev tunneling, Coulomb blockade, and resonant transport of nonlocal spin-entangled electrons*, Phys. Rev. B **63**, 165314 (2001).
- [90] G.B. Lesovik, T. Martin, and G. Blatter, *Electronic entanglement in the vicinity of a superconductor*, The European Physical Journal B-Condensed Matter and Complex Systems **24**, 287 (2001).
- [91] G. Deutscher and D. Feinberg, *Coupling superconducting-ferromagnetic point contacts by Andreev reflections*, Applied Physics Letters **76**, 487 (2000).
- [92] N. M. Chtchelkatchev, G. Blatter, G. B. Lesovik, and T. Martin, *Bell inequalities and entanglement in solid-state devices*, Phys. Rev. B **66**, 161320 (2002).
- [93] K. V. Bayandin, G. B. Lesovik, and T. Martin, *Energy entanglement in normal metal-superconducting forks*, Phys. Rev. B **74**, 085326 (2006).
- [94] D. Beckmann, H. B. Weber, and H. v. Löhneysen, *Evidence for Crossed Andreev Reflection in Superconductor-Ferromagnet Hybrid Structures*, Phys. Rev. Lett. **93**, 197003 (2004).
- [95] G. Falci, D. Feinberg, and F. W. J. Hekking, *Correlated tunneling into a superconductor in a multiprobe hybrid structure*, EPL (Europhysics Letters) **54**, 255 (2001).
- [96] R. Mélin and D. Feinberg, *Sign of the crossed conductances at a ferromagnet/superconductor/ferromagnet double interface*, Phys. Rev. B **70**, 174509 (2004).

- [97] S. Russo, M. Kroug, T. M. Klapwijk, and A. F. Morpurgo, *Experimental Observation of Bias-Dependent Nonlocal Andreev Reflection*, Phys. Rev. Lett. **95**, 027002 (2005).
- [98] G. Bignon, M. Houzet, F. Pistolesi, and F. W. J. Hekking, *Current-current correlations in hybrid superconducting and normal-metal multiterminal structures*, EPL (Europhysics Letters) **67**, 110 (2004).
- [99] D. Feinberg, *Andreev scattering and cotunneling between two superconductor-normal metal interfaces: the dirty limit*, The European Physical Journal B-Condensed Matter and Complex Systems **36**, 419 (2003).
- [100] A.L. Yeyati, F. S. Bergeret, A. Martin-Rodero, and TM Klapwijk, *Entangled Andreev pairs and collective excitations in nanoscale superconductors*, Nature Physics **3**, 455 (2007).
- [101] P. Cadden-Zimansky, Z. Jiang, and V. Chandrasekhar, *Charge imbalance, crossed Andreev reflection and elastic co-tunnelling in ferromagnet/superconductor/normal-metal structures*, New Journal of Physics **9**, 116 (2007).
- [102] P. Cadden-Zimansky and V. Chandrasekhar, *Nonlocal Correlations in Normal-Metal Superconducting Systems*, Phys. Rev. Lett. **97**, 237003 (2006).
- [103] R. Mélin, F. S. Bergeret, and A. L. Yeyati, *Self-consistent microscopic calculations for nonlocal transport through nanoscale superconductors*, Phys. Rev. B **79**, 104518 (2009).
- [104] J. Brauer *et al.*, *Nonlocal transport in normal-metal/superconductor hybrid structures: Role of interference and interaction*, Phys. Rev. B **81**, 024515 (2010).
- [105] L. Hofstetter *et al.*, *Finite-Bias Cooper Pair Splitting*, Phys. Rev. Lett. **107**, 136801 (2011).
- [106] L. Hofstetter, S. Csonka, J. Nygård, and C. Schönenberger, *Cooper pair splitter realized in a two-quantum-dot Y-junction*, Nature **461**, 960 (2009).
- [107] L. G. Herrmann *et al.*, *Carbon Nanotubes as Cooper-Pair Beam Splitters*, Phys. Rev. Lett. **104**, 026801 (2010).
- [108] A. Das *et al.*, *Entangling electrons by splitting Cooper pairs: Two-particle conductance resonance and time coincidence measurements*, Arxiv preprint arXiv:1205.2455 (2012).

-
- [109] S. Kogan, *Electronic noise and fluctuations in solids* (Cambridge Univ Pr, Cambridge, 2008).
 - [110] Y.M. Blanter and M. Büttiker, *Shot noise in mesoscopic conductors*, Physics Reports **336**, 1 (2000).
 - [111] M. Büttiker, *Scattering theory of current and intensity noise correlations in conductors and wave guides*, Phys. Rev. B **46**, 12485 (1992).
 - [112] M. Büttiker, *Reversing the sign of current-current correlations*, Quantum noise in mesoscopic physics 3 (2003).
 - [113] J. Wei and V. Chandrasekhar, *Positive noise cross-correlation in hybrid superconducting and normal-metal three-terminal devices*, Nature Physics **6**, 494 (2010).
 - [114] O. Coupiac, Ph.D. thesis, *Réalisation d'un dispositif à trois SQUIDSs pour la mesure de corrélations de bruit de grenaille*, Université Joseph-Fourier - Grenoble I, 2007.
 - [115] B. Kaviraj, O. Coupiac, H. Courtois, and F. Lefloch, *Noise Correlations in Three-Terminal Diffusive Superconductor-Normal-Metal-Superconductor Nanostructures*, Phys. Rev. Lett. **107**, 077005 (2011).
 - [116] J. Torrès and T. Martin, *Positive and negative Hanbury-Brown and Twiss correlations in normal metal-superconducting devices*, The European Physical Journal B-Condensed Matter and Complex Systems **12**, 319 (1999).
 - [117] J. Torrès, T. Martin, and G. B. Lesovik, *Effective charges and statistical signatures in the noise of normal metal-superconductor junctions at arbitrary bias*, Phys. Rev. B **63**, 134517 (2001).
 - [118] A. Freyn, M. Flöser, and R. Mélin, *Positive current cross-correlations in a highly transparent normal-superconducting beam splitter due to synchronized Andreev and inverse Andreev reflections*, Phys. Rev. B **82**, 014510 (2010).
 - [119] S. Duhot, Ph.D. thesis, *Transport électronique non local dans des structures hybrides supraconductrices*, 2008.
 - [120] P. De Gennes, *Superconductivity of metals and alloys* (Addison-Wesley New York, New York, 1989).
 - [121] T. Martin and R. Landauer, *Wave-packet approach to noise in multichannel mesoscopic systems*, Phys. Rev. B **45**, 1742 (1992).

- [122] M. Büttiker, *Scattering theory of thermal and excess noise in open conductors*, Phys. Rev. Lett. **65**, 2901 (1990).
- [123] A. Kastalsky *et al.*, *Observation of pair currents in superconductor-semiconductor contacts*, Phys. Rev. Lett. **67**, 3026 (1991).
- [124] B. J. van Wees, P. de Vries, P. Magnée, and T. M. Klapwijk, *Excess conductance of superconductor-semiconductor interfaces due to phase conjugation between electrons and holes*, Phys. Rev. Lett. **69**, 510 (1992).
- [125] S. Duhot and R. Mélin, *Thouless energy of a superconductor from non local conductance fluctuations*, European Physical Journal B **53**, 257 (2006).
- [126] W. Liang *et al.*, *Fabry-Perot interference in a nanotube electron waveguide*, Nature **411**, 665 (2001).
- [127] H. I. Jørgensen *et al.*, *Electron Transport in Single-Wall Carbon Nanotube Weak Links in the Fabry-Perot Regime*, Phys. Rev. Lett. **96**, 207003 (2006).

Abstract

This thesis consists of two independent parts. The first one deals with transport in two dimensional electron gases in the regime of the quantum Hall effect. In the second part, current and current cross-correlations are studied in normal conductor-superconductor-normal conductor (NSN) hybrid structures.

In the high temperature regime of the quantum Hall effect, the longitudinal conductance is calculated in a diagrammatic formalism based on a local conductivity approach. It takes the interplay between electron-phonon scattering and the drift motion along equipotential lines of the disorder potential into account and provides a microscopic derivation of the universal transport critical exponent that was up to now only conjectured from qualitative geometrical arguments. Microscopic expressions for the dependence in temperature and magnetic field of the longitudinal conductance are derived and compared to recent experiments.

In the low temperature regime of the quantum Hall effect, tunneling over saddle points is studied from the scattering of semi-coherent state wave packets. We derive analytically the transmission coefficient of saddle-points in the scalar potential in graphene and find that asymmetric saddle-points break particle-hole symmetry in the conductance.

In three-terminal NSN hybrid structures the influence of additional barriers on the (non-local) conductance and on current cross-correlations is studied with scattering theory. In metallic, phase averaged systems additional barriers lead to an enhancement of local processes by reflectionless tunneling but have little influence on non-local processes and on current cross-correlations. In ballistic systems, additional barriers lead to Fabry-Perot oscillations and allow to distinguish the different contributions to the conductance and to the current cross-correlations.

Key-Words: Quantum Transport, Quantum Hall Effect, Superconducting Hybrid Structures, Tunneling, Scattering Theory, Percolation

Résumé

Cette thèse est constituée de deux parties indépendantes. La première partie traite du transport dans des gaz d'électrons bidimensionnels dans le régime de l'effet Hall quantique. Dans la deuxième partie, le courant et les corrélations croisées en courant sont étudiées pour des structures hybrides conducteur normal- supraconducteur- conducteur normal (NSN).

Dans le régime de haute température de l'effet Hall quantique, la conductance longitudinale est calculée par un formalisme diagrammatique basé sur une approche de conductivité locale. Ce calcul prend en compte l'effet de dérive des électrons sur les lignes équipotentielles du potentiel de désordre et permet la dérivation microscopique de l'exposant critique de transport qui était auparavant seulement conjecturé à partir d'arguments géométriques qualitatifs. Des expressions microscopiques pour la dépendance en température et en champ magnétique de la conductance longitudinale sont dérivées et comparées avec des expériences récentes.

Dans le régime de basse température de l'effet Hall quantique, le passage du courant par effet tunnel sur des points selles est étudié à partir de la diffusion de paquets d'onde d'états semi-cohérents. Nous dérivons analytiquement le coefficient de transmission d'un point selle pour le potentiel scalaire dans le graphène et trouvons que les points selles asymétriques brisent la symétrie particule-trou de la conductance.

Dans des structures hybrides NSN, nous étudions l'influence de barrières additionnelles sur la conductance (non-locale) et sur les corrélations croisées en courant avec la théorie de diffusion. Dans les systèmes métalliques, où la phase est moyennée, des barrières additionnelles augmentent les processus locaux par réflexion d'Andreev résonante (reflectionless tunneling), mais ont peu d'influence sur les processus non-locaux et sur les corrélations croisées en courant. Dans les systèmes balistiques, des barrières additionnelles causent des oscillations Fabry-Pérot et permettent de distinguer les différents processus contribuant à la conductance et aux corrélations croisées en courant.

Mots clés : Transport quantique, Effet Hall quantique, Structures hybrides supraconductrices, Effet tunnel, Théorie de diffusion, Percolation